Stow, D.A.V., Hernández-Molina, F.J., Alvarez Zarikian, C.A., and the Expedition 339 Scientists
Proceedings of the Integrated Ocean Drilling Program, Volume 339

Site U1386[1]

Expedition 339 Scientists[2]

Chapter contents

Background and objectives

An extensive contourite depositional system (CDS) was generated during the Pliocene and Quaternary by the action of Mediterranean Outflow Water (MOW) on the middle slope of the Gulf of Cádiz. In total, this CDS extends ~300 km alongslope from the exit of the Strait of Gibraltar (or Gibraltar Gateway) and a further 100 km around the West Iberian margin (e.g., Kenyon and Belderson, 1973; Gonthier et al., 1984; Nelson et al., 1999; Alves et al., 2003; Llave et al., 2007; Stow et al., 2002; Mulder et al., 2003; Habgood et al., 2003; Hernández-Molina et al., 2003; Hanquiez et al., 2007; Marchès et al., 2007; Roque et al., 2012). One of the main depositional features of this CDS is the Faro-Albufeira Drift (Gonthier et al., 1984; Faugères et al., 1985a), which is located at ~500–700 meters below sea level (mbsl) within Sector 4 (Fig. **F1** and Fig. **F12** in the "Expedition 339 summary" [Expedition 339 Scientists, 2013a]) of the CDS (defined by Hernández-Molina et al., 2003, and Llave et al., 2007) and has been generated by the upper core of MOW. This corresponds to an elongated, mounded, and separated drift (hereafter referred to as Faro Drift for simplicity), following the nomenclature of Faugéres et al. (1993), with a total length of 100 km, a maximum width of 20 km, and a maximum thickness of ~700 m.

The Faro Drift represents a classic example of middle-slope contourite deposits with a well-layered internal acoustic structure and an internal reflection configuration that onlaps and downlaps in an oblique upslope direction (Fig. **F12** in the "Expedition 339 summary" [Expedition 339 Scientists, 2013a]). It is mainly composed of muddy, silty, and sandy sediments with mixed terrigenous and biogenic composition (Gonthier et al., 1984; Stow et al., 1986, 2002). The stratigraphic architecture of this drift and its relationship with the major structural features in the area has been described in some detail by previous authors (Faugères et al., 1985a, 1985b; Stow et al., 2002; Llave et al., 2001, 2006, 2007, 2011; Roque et al., 2012). In general, the drift shows laterally extensive, aggradational to progradational seismic depositional units with widespread discontinuities (Fig. **F2**).

Faro Drift has been developing along the midslope over the past 5 m.y. under the direct influence of MOW. It therefore contains the signal of MOW through the Strait of Gibraltar, reopened following tectonic adjustments at the end of the Messinian salinity crisis (Hsü et al., 1973; Sierro et al., 2008) and hence a clear record of

---

[1] Expedition 339 Scientists, 2013. Site U1386. *In* Stow, D.A.V., Hernández-Molina, F.J., Alvarez Zarikian, C.A., and the Expedition 339 Scientists, *Proc. IODP,* 339: Tokyo (Integrated Ocean Drilling Program Management International, Inc.). doi:10.2204/iodp.proc.339.104.2013
[2] **Expedition 339 Scientists' addresses.**

Mediterranean Sea and MOW influence on the North Atlantic Ocean (Stow et al., 2011). The high rates of accumulation and expanded sedimentary records of drift deposits permit high-resolution examination of past environmental change (climatic and eustatic) (Llave et al., 2006; Voelker et al., 2006; Toucanne et al., 2007). On a smaller timescale, identified grain-size cyclicity is interpreted as representing cyclic changes in MOW strength (Fig. **F3**), suggesting MOW intensification during cold intervals in the Gulf of Cádiz (Llave et al., 2006; Voelker et al., 2006). During glacial periods, strengthened MOW sank to depths ~700 m deeper than today, impinging on the continental slope at 1600–2200 mbsl (Schönfeld and Zhan, 2000; Rogerson et al., 2005; Llave et al., 2007; Voelker et al., 2006; García et al., 2009). This enhancement of MOW also occurred during Heinrich events, Dansgaard/Oeschger stadials, and the Younger Dryas (Sierro et al., 2005; Llave et al., 2006; Voelker et al., 2006). Furthermore, post-Miocene tectonic activity has also played an important part in the morphological development of the seafloor, controlling multiple current pathways for MOW at each evolutionary stage (Nelson et al., 1999; Llave et al., 2007, 2011; García et al., 2009; Roque et al., 2012).

All the aforementioned work has demonstrated the importance of the Faro Drift for both paleoceanographic and contourite studies. However, despite this significance and despite it being one of the largest drifts in the world, it has never before been drilled for scientific purposes. Therefore, drilling the Faro Drift was a unique challenge for Expedition 339. Site U1386 (36°49.685′N, 7°45.321′W) on the Faro Drift (Figs. **F1**, **F4**) is a very important site and represents an opportunity for recovering a key Pleistocene and Holocene sedimentary succession formed under the influence of the upper core of MOW. This site is complementary to Site U1387, which is ~4.1 km southeast and targets a Pliocene and lower Pleistocene sedimentary record also formed by the upper core of MOW (Fig. **F6** in the "Expedition 339 summary" chapter [Expedition 339 Scientists, 2013a]).

Objectives

The major objective for Site U1386 was to recover at least a complete sedimentary contourite record deposited under the influence of the upper core of MOW for the last 1.8–2 m.y. on the Faro Drift. This record will allow us to investigate

- The influence of the Gibraltar Gateway through the Quaternary,
- MOW paleoceanography and its global climate significance during at least the last 1.8–2 m.y., and
- The effects of climate and sea level changes on the sediment architecture of the contourite drift.

To achieve these major scientific objectives, it is essential to integrate the results at Site U1386 with a dense network of existing high- and medium-resolution seismic reflection profiles.

Specific objectives for Site U1386 include

- Documenting the possible effects of the Gibraltar Gateway through the Pleistocene and hence determining the input variation of the influx of warm, saline intermediate water into the North Atlantic Ocean and the nature of change in the patterns of sedimentation and microfauna;
- Reconstructing the main MOW paleoceanographic events for the Pleistocene and identifying the role of salt injection from MOW in the dynamics of North Atlantic Deep Water;
- Focusing on high-resolution calibration of late Pleistocene–Holocene facies and the inferred environmental changes in terms of global rapid climatic events;
- Evaluating the correlation and influence of cold periods (glaciations, terminations, and ice-rafting events) with MOW variation, testing the concept of cold period intensification of MOW;
- Determining the sedimentary stacking pattern of Faro Drift in relation to changes in sea level and other forcing mechanisms, which can determine the potential role of variations in cross-sectional area of the Gibraltar Gateway;
- Evaluating periods of drift construction, nondeposition (hiatuses), and erosion. The nature of sedimentation and timing of principal unconformities is one of the important objectives, especially for the mid-Pleistocene;
- Determining the timing and extent of hiatuses and condensed sequences and attempting paleodepth reconstruction;
- Evaluating the contourite deposition in relation to sea level variation and to the further development of a sequence stratigraphic model;
- Quantifying the sediment budget and source for the contourite deposits; and
- Calibrating and hence understanding the sedimentary cyclicity evident on the deposits, which can characterize their sedimentary expression and regional extent.

Operations

After a 150 nmi transit from Site U1385, the R/V *JOIDES Resolution* arrived at Site U1386 (proposed Site GC-01A; 560.4 mbsl) at 0415 h on 30 November 2011. We deployed the camera system and conducted a ~2 h survey of the seabed on a 30 m grid pattern to ensure that the seafloor was free of man-made obstructions. No obstructions were observed on the seafloor, but many shallow linear furrows were seen that were assumed to be the result of fishing trawls.

Three holes were drilled at Site U1386 (Table T1). Hole U1386A was cored using the advanced piston corer (APC) system to 183.1 meters below seafloor (mbsf) and then cored with the extended core barrel (XCB) system to 349.3 mbsf. Similarly, Hole U1386B was cored with the APC to 162.3 mbsf and then with the XCB to 464.9 mbsf. Hole U1386C was drilled to 405 mbsf and then cored using the rotary core barrel (RCB) system to the target depth of 526 mbsf. Two cores were taken in the initial drilled interval (Core 339-U1386C-2R, 165–174.6 mbsf, 40% recovery; Core 4R, 205–214.6 mbsf, 93% recovery) to try to fill in short gaps in APC cores recovered from Holes U1386A and U1386B. Downhole logging was carried out in Hole U1386C using the triple combination (triple combo), Formation MicroScanner (FMS)-sonic, and Versatile Sonic Imager (VSI) tool strings (see **"Downhole logging at Site U1386"**). Overall recovery at Site U1386 was 351 m (101.62%) with the APC, 417.63 m (89.1%) with the XCB, and 82 m (58.5%) with the RCB. The total cored interval for Site U1386 was 954.4 m, and total recovery was 850.64 m (89.1%).

Hole U1386A

Once the camera system was recovered at 1255 h, 30 November, we began piston coring in Hole U1386A. APC coring continued to refusal at 183.1 mbsf (Cores 1H through 21H). Recovery for this interval was 101%. Temperature measurements were obtained at 32.3 (Core 4H), 60.8 (Core 7H), 89.3 (Core 10H), 117.8 (Core 13H), 114.0 (Core 16H), and 167.2 (Core 19H) mbsf. Cores were oriented starting with Core 4H. The corer was advanced by recovery on Cores 16H to 19H and 21H. Nonmagnetic hardware was used on all cores. At 183.1 mbsf, the coring system was switched to the XCB and coring continued to a total depth of 349.3 mbsf (Cores 22X through 39X) by 0415 h, 2 December. The 166.2 m interval was cored with a recovery of 97%. The total recovery in Hole U1386A was 346.2 m, which represented 99% of the cored interval. The bit cleared the seafloor at 0620 h on 2 December, and the vessel offset 20 m east of Hole U1386A.

Hole U1386B

Piston coring in Hole U1386B began at 0825 h, 2 December, and advanced to an APC refusal depth of 162.3 mbsf (Cores 1H through 18H). Recovery for the APC interval was 100%. The calculated water depth from the recovery of the first core was 562 mbsl. Temperature measurements using the advanced piston corer temperature tool (APCT-3) were taken at 16.8 (Core 2H), 45.3 (Core 5H), 73.8 (Core 8H), 102.8 (Core 11H), 130.8 (Core 14H), and 157.6 (Core 17H) mbsf. The cores were oriented starting with Core 3H. There were partial strokes with Cores 15H, 16H, and 18H. Nonmagnetic hardware was used to obtain all cores. At 2200 h, 2 December, the coring system was switched to XCB and coring continued to 455.4 mbsf (Cores 19X through 49X), where XCB refusal was reached. Recovery for the XCB interval was 293.5 m (100%).

Hole U1386C

The third hole of Site U1386 was offset 20 m south of Hole U1386B and spudded with the RCB at 0345 h on 5 December. This hole was drilled with a wash barrel to 405 mbsf except for RCB coring of two intervals that eluded recovery in the two previous XCB holes (Cores 2R and 4R from 165.0–174.6 and 205.0–214.6 mbsf, respectively). Continuous RCB coring started at 405 mbsf at 0545 h, 6 December, and reached the depth objective of 526 mbsf by 0200 h, 7 December. RCB interval (140 m) recovery was 59%. The drilled interval was 386 m. The total cored interval for all holes at this site was 954 m with a recovery of 89% (104 cores).

Downhole logging at Site U1386

Following a wiper trip and hole conditioning, Hole U1386C was displaced with 172 bbl of 10.5 ppg mud to prepare the hole for downhole logging. The open end of the pipe was placed at a logging depth of 102.4 mbsf. During rig up of the wireline cable, the cable jumped from the lower left most sheave wheel in the wireline heave compensator and became jammed between the wheel and the frame. Because of the possibility of damage to the cable, it was cut above the crimped section.

The triple combo tool string descended through the seafloor at 2003 h and was successful in reaching the bottom of the hole (526 mbsf). The tool string was back on deck by 0100 h, 8 December. Subsequently, the FMS-sonic tool suite was run into the hole at 0410 h. The tool suite was blocked from further downhole progress by a bridge at 948 mbrf (375 mbsf), the lowermost of the tight sections observed in the triple combo run. Rig down of the FMS-sonic tool string was completed by 0930 h, 8 December.

The marine mammal watch for conducting the vertical seismic profile (VSP) experiment started at 0800 h, 8 December. The VSI tool started its descent in Hole U1386C at ~1030 h and reached a bridge at 940 mbrf

(367 mbsf) at 1105 h. The slightly shallower penetration for this tool run indicated that the hole was closing with time. The seismic source (two-gun cluster; 7 mbsl on the port side) had been ramped up in soft start mode. It was difficult to get a good clamp with the VSI, and consequently noisy waveforms were obtained that were attributed to the rugose borehole and soft formation. Only a fraction of the shots produced clean first arrivals, but there were enough at most stations to stack the waveforms. The upper part of the hole was especially difficult. The tool was back on deck at 1440 h and rigged down by 1530 h, 8 December. The drill string was recovered and the vessel departed for the next site at 1730 h, 8 December. Total time at Site U1386 was 8.6 days.

Lithostratigraphy

The shipboard lithostratigraphic program at Site U1386 involved detailed visual logging of all archive sections, visual assessment of sediment color, petrographic analysis of smear slides and a limited number of thin sections, and selected X-ray diffraction (XRD) analyses of powdered bulk samples. Sediment in Hole U1386A, Hole U1386B below Core 339-U1386B-39X, and Hole U1386C below Core 339-U1386C-4R was sampled regularly for smear slides during visual core description. Relatively few smear slides were made from other intervals in Holes U1386B and U1386C, except to investigate lithologies and features of particular interest or difference from Hole U1386A. Fifty-two samples were selected from Holes U1386A–U1386C for powder XRD analysis in order to gain a general indication of bulk mineralogy. Hand-drawn logs showing the recovered sediment sequence, including the distribution and structure of bedding, are included in the DRAWLOG folder in **"Supplementary material."**

Total carbonate content from these cores, based on shipboard analyses, ranges from 10.9 to 40.7 wt%, with an average of 25.9 wt% (Table T2). These results are consistent with abundances of biogenic and detrital carbonate estimated from smear slides, so the lithologic names determined from smear slide analyses have been used without modification through this text, the accompanying summary diagrams, and the visual core description sheets.

The sediment at Site U1386 is separated into two lithologic units, I and II (Figs. F5, F6). Unit I is a Holocene–Pleistocene sequence dominated by nannofossil mud, calcareous silty mud, and silty sand with biogenic carbonate. These three lithologies are generally organized as bi-gradational sequences (following the conceptual model of Gonthier et al., 1984), the most complete of which coarsens upward from nannofossil mud to calcareous silty mud to silty sand with biogenic carbonate and then fines upward through calcareous silty mud into nannofossil mud. Unit I is divided into three subunits (IA–IC) based on the relative abundance of the silty muds and silty sands. Subunits IA–IC have been defined in Holes U1386A and U1386B but not in Hole U1386C. Unit II is a Pleistocene–Pliocene sequence dominated by the same three lithologies but with a higher abundance of shelly sand and evidence for submarine mass flows. Because of their relatively similar major lithologies, lithologic Units I and II are distinguished on the basis of the patterns and inferred modes of sediment deposition, rather than on the basis of major compositional changes.

The character of sediment physical properties, including natural gamma radiation (NGR), magnetic susceptibility, color reflectance parameters, and density, records the distribution of these various lithologies and sediment components (see **"Physical properties"**). Characteristics of the sedimentary sequence cored at Site U1386, together with some of these additional properties, are summarized in Figure F7.

Unit descriptions

Unit I

Intervals: 339-U1386A-1H-1, 0 cm, through 39X-CC, 48.5 cm; 339-U1386B-1H-1, 0 cm, through 46X-4, 70 cm; 339-U1386C-2R-1, 0 cm, through 7R-3, 133 cm

Depths: Hole U1386A = 0–349.5 mbsf (bottom of hole), Hole U1386B = 0–422 mbsf, Hole U1386C = 0–419.9 mbsf

Age: Holocene–Pleistocene

The sediments of Unit I are composed of varying mixtures of terrigenous and biogenic components (primarily clay minerals, nannofossils, detrital and biogenic carbonate, and quartz; see Site U1386 smear slides in **"Core descriptions"**) (Fig. F8). The three most common lithologies in Unit I are nannofossil mud, calcareous silty mud, and silty sand with biogenic carbonate (Figs. F5, F6; Table T3). Less common lithologies include calcareous mud, biogenic silty mud, and calcareous sandy silt.

Unit I is divided into three subunits on the basis of the relative abundances of nannofossil mud versus calcareous silty mud and silty sand with biogenic carbonate (Fig. F6). Subunits IA and IC are relatively enriched in calcareous silty muds and silty sands with biogenic carbonate, whereas Subunit IB contains a higher proportion of nannofossil mud.

Subunit IA

Intervals: 339-U1386A-1H-1, 0 cm, through 12H-6, 115 cm; 339-U1386B-1H-1, 0 cm, through 12H-6, 31 cm

Depths: Hole U1386A = 0–107.5 mbsf, Hole U1386B = 0–109.8 mbsf
Age: Holocene to Pleistocene

Lithologies and bedding: The major lithologies in Subunit IA are nannofossil mud (Figs. F5, F6, F9), calcareous silty mud, and silty sand with biogenic carbonate. The primary differences between these lithologies are changes in the abundance and grain size of the detrital component with correspondingly inverse variations in the abundance of biogenic carbonate. Subunit IA is distinguished from Subunit IB by the greater importance of silty sand with biogenic carbonate in Subunit IA.

Minor lithologies are subtle variations on several of the major lithologies. These include sandy silt with biogenic carbonate (a slight grain-size variant of silty sand with biogenic carbonate) and calcareous mud (a slight compositional variant of nannofossil mud).

In relatively long intervals of nannofossil mud (multiple meters or more in length), bedding is very indistinct; features that may be beds are distinguished primarily by subtle changes in color, bioturbation intensity, or silt/clay ratio. In intervals that contain several major lithologies, the most common bedding style is the bi-gradational sequence, which ranges from a few decimeters to several meters in thickness. The most complete of these bi-gradational sequences coarsen upward from nannofossil mud to calcareous silty mud to silty sand with biogenic carbonate, and then fine upward through calcareous silty mud into nannofossil mud (Fig. F10). Some of these sequences are less complete, lacking the silty sand with biogenic carbonate; these sequences coarsen upward from nannofossil mud into calcareous silty mud and then fine upward into nannofossil mud. Several bi-gradational sequences in the upper ~30 m of Subunit IA are incomplete because subsequent erosion has removed part or all of the upper nannofossil mud, as indicated by the presence of a sharp to irregular upper contact.

The contacts between all lithologies, and between subjacent beds of nannofossil mud, primarily are gradational and bioturbated. Exceptions are sharp upper contacts and some sharp and inclined bases of calcareous silty mud and/or silty sand with biogenic carbonate.

Structures and texture: Few to no primary sedimentary structures were observed in Subunit IA, except for indistinct and discontinuous silty laminae and lenses in some beds.

Bioturbation is the most obvious secondary sedimentary structure that is present throughout Subunit IA. The most common indicators of bioturbation are diffuse centimeter-scale mottling and millimeter-scale pyritic burrow fills. Black iron sulfide mottling is also common. Discrete burrows and recognizable ichnofossils are rare; those present occur in a few beds with discrete burrows of *Chondrites*. The bioturbation index ranges from sparse to slight, based on observation of beds with slight color changes.

The sediment is fine grained through most of lithologic Subunit IA, with an average grain size of clay to silt. Exceptions are the intervals of silty sand with biogenic carbonate, in which the average grain size is very fine sand and the maximum grain size is medium to coarse sand.

Composition: All lithologies in Subunit IA are dominated by terrigenous material (siliciclastic components of clay minerals, quartz, feldspars, mica, and volcanic glass, plus detrital carbonate) (Table T3; Fig. F8). The biogenic fraction is dominated by nannofossils, with rare to common foraminifers and rare pteropods and sponge spicules. Authigenic components are dominated by pyrite, dolomite, and glauconite. Abundances of terrigenous components, as estimated from smear slides (Fig. F8; Table T3), are 8%–50% siliciclastics (including quartz, feldspars, accessory minerals, and clay minerals), 8%–50% detrital carbonate, and 1%–5% glauconite. No discrete ash layers and no dropstones were observed. Abundances of biogenic components, as estimated from smear slides, are 20%–81% biogenic carbonate (primarily nannofossils, and foraminifers for the silty sand lithology) and 0%–1% biogenic silica (primarily diatoms and radiolarians). Total carbonate contents range from 19.94 to 38.24 wt% (average = 28.4 wt%) in Subunit IA (Table T2). Abundances of authigenic components, as estimated from smear slides, are 1%–5% pyrite (usually associated with burrows) and 1%–5% authigenic dolomite. Glauconite and dolomite can be abundant in the silty sand beds (Fig. F11).

Whole and nearly whole macrofossils are very poorly represented in Subunit IA. The few specimens found include gastropods, bivalves, and a cold-water coral. Macrofossil fragments, however, are distributed through most of the subunit; recognizable fragments include gastropods, bivalves, and echinoderms (i.e., sea urchin spines). Examples of macrofossils are an almost complete cold-water coral (Sample 339-U1386A-1H-1, 5–6 cm; Fig. F12), coral branches (Samples 339-U1386A-9H-6, 122 cm, and 339-U1386B-8H-3, 144 cm; Fig. F13), a nearly complete pectinid valve (Sample 339-U1386A-2H-6, 70–72 cm; Fig. F14), bivalve shells (Samples 339-U1386A-3H-5, 87–89 cm [Fig. F15], and 339-U1386B-8H-CC, 28 cm), and gastropod shells (Samples 339-U1386B-5H-4, 8–9 cm [Fig. F16], and 10H-1, 53–54 cm).

Color: The principal colors of the lithologies in Subunit IA, as noted during visual description of the core, range from olive-gray (5Y 4/2) to dark gray (5Y 4/1) and greenish gray to dark greenish gray. In general, sediments with higher sand and/or carbonate contents have lighter colors.

Bulk mineralogy: Twelve bulk XRD samples were taken from Subunit IA. Diffraction peaks from quartz, calcite, and illite contribute 81% of the total peak intensities identified (Fig. F17; Table T4). Quartz accounts for 43.7% of the total intensity, calcite for 23.0%, and illite for 14.7%. Quartz and calcite contributions in Subunit IA are somewhat less than their average values for the entire succession at Site U1386, whereas the illite contribution in Subunit IA is considerably higher than its average value for the site (10.5%). K-feldspar, plagioclase, and kaolinite each account for 1%–5% of the sample, and minor amounts (<1%) of hornblende, augite, or pyrite were recognized based on peaks thought to be diagnostic. Additional observations based on the XRD patterns are that the ratio of plagioclase to K-feldspar peak intensities is 3.1 in Subunit IA and that dolomite is an average of 20% of the calcite peak intensity. These are both higher than the whole-site average values of 2.5 and 15%, respectively.

Subunit IB

Intervals: 339-U1386A-12H-6, 115 cm, through 26X-2, 96 cm; 339-U1386B-12H-6, 31 cm, through 25X-1, 40 cm; 339-U1386C-2R and 4R

Depth: Hole U1386A = 107.5–217.7 mbsf, Hole U1386B = 109.8–216.3 mbsf, Hole U1386C = 165–213.9 mbsf

Age: Pleistocene

Lithologies and bedding: Subunit IB is distinguished from Subunit IA by the reduced abundance of coarser grained lithologies, as shown in Figures F5 and F6. As a result, the major lithologies in Subunit IB are nannofossil mud and calcareous silty mud. Silty sand with biogenic carbonate is a minor lithology.

As was described for Subunit IA, relatively long intervals of nannofossil mud in Subunit IB (several meters or more in length) are characterized by very indistinct bedding. In intervals that contain both major lithologies, the most common bedding style is a less complete bi-gradational sequence, which coarsens upward from nannofossil mud into calcareous silty mud and then fines upward into nannofossil mud (Fig. F18). Because of the scarcity of silty sand with biogenic carbonate, more complete bi-gradational sequences are rare. One example of a normally graded bed (interval 339-U1386A-13H-5, 100–118 cm), with a sharp irregular base, does not appear to be part of a bi-gradational sequence and its depositional origin is unclear.

The contacts between all lithologies and between subjacent beds of nannofossil mud are primarily gradational and bioturbated. Exceptions are a few beds of calcareous silty mud and/or silty sand with biogenic carbonate with irregular bases.

Structures and texture: No primary sedimentary structures were observed in Subunit IB, except for indistinct and discontinuous silty laminations and lenses in some beds.

Bioturbation is the most obvious secondary sedimentary structure and is present throughout the observed section. Characteristics of the bioturbation are similar to those of the bioturbation in Subunit IA. The bioturbation index in Subunit IB ranges from sparse to slight.

The sediment is fine-grained through most of Subunit IB, with an average grain size of clay to silt. Exceptions are the very few beds of silty sand with biogenic carbonate in Hole U1386A, where the average grain size is very fine sand and the maximum grain size is medium to coarse sand.

Composition: As is true for Subunit IA, all lithologies in Subunit IB are dominated by terrigenous material (siliciclastic components of clay minerals, quartz, feldspars, and mica, plus detrital carbonate) (Table T3; Fig. F8). The biogenic fraction is dominated by nannofossils, with rare to common foraminifers and rare pteropods and sponge spicules. Authigenic components include pyrite, dolomite, and glauconite.

Abundances of terrigenous, biogenic, and authigenic components, as estimated from smear slides (Fig. F8; Table T3), are similar to those of Subunit IA. No discrete ash layers and no dropstones were observed. Total carbonate contents range from 17.03 to 40.71 wt% (average = 27.8 wt%) (Table T2).

Whole and nearly whole macrofossils are very poorly represented in Subunit IB. The few specimens found include recognizable coral fragments and a gastropod (Sample 339-U1386B-21X-1, 113–115 cm; Fig. F19). Macrofossil fragments, however, are distributed through most of the subunit, including fragments of bivalves, echinoderms, corals, and *Arenaria*.

Color: The principal colors of lithologies in Subunit IB, as noted during visual description of the core, range from dark gray (5Y 4/1) to greenish gray (10Y 5/1) to dark greenish gray (10Y 4/1) and very dark gray (2.5Y 3/1). In general, sediments with higher sand and/or carbonate contents have lighter colors.

Bulk mineralogy: Fourteen bulk XRD samples were analyzed from Subunit IB. Diffraction intensities from the minerals quartz, calcite, and illite make up 85.2% of the total mineral diffraction intensities identified (Fig. F17; Table T4). Similar to Subunit IA, quartz accounts for 44.4% of the total intensity, but calcite contributions (31.9%) are somewhat higher and illite contributions (8.9%) are somewhat lower than both the whole-site averages and their respective contributions in Subunit IA. Minor mineral contributions are similar to those in Subunit IA, although the plagioclase/K-feldspar ratio is lower than in Subunit IA and the whole-site average, and dolomite averages 10.8% of the calcite peak intensity.

Subunit IC

Intervals: 339-U1386A-26X-2, 96 cm, through 39X-CC, 48.5 cm (bottom of hole); 339-U1386B-25X-1, 40 cm, through 46X-4, 70 cm; 339-U1386C-6R-1, 0 cm, through 7R-3, 133 cm

Depths: Hole U1386A = 217.7–349.5 mbsf (bottom of hole), Hole U1386B = 216.3–422.4 mbsf, Hole U1386C = 405–418.9 mbsf

Age: Pleistocene

Lithologies and bedding: Subunit IC is distinguished from Subunit IB by the increased abundance of coarser lithologies downhole. As a result, the major lithologies in Subunit IC are the same as those in Subunit IA (nannofossil mud, calcareous silty mud, and silty sand with biogenic carbonate). As in Subunit IA, the primary differences between these lithologies are changes in the abundance and grain size of the detrital component, with correspondingly inverse variations in the abundance of biogenic carbonate.

Subunit IC contains a wider range of minor lithologies than Subunits IA and IB. These minor lithologies include biogenic mud, calcareous sandy silt, calcareous silty sand, and pebbly sand (Fig. F20).

As is observed elsewhere in Unit I, relatively long intervals of nannofossil mud in Subunit IC (several meters or more in length) exhibit very indistinct bedding, defined primarily by subtle changes in color, bioturbation intensity, or silt/clay ratio. In intervals that contain multiple major lithologies, bigradational sequences are common; both more complete sequences (nannofossil mud–calcareous silty mud–silty sand with biogenic carbonate–calcareous silty mud–nannofossil mud) and less complete sequences (nannofossil mud–calcareous silty mud–nannofossil mud) are present.

A few beds located near the base of Subunit IC have sharp erosional bases, fine upward from silty sand with biogenic carbonate to calcareous silty mud, and exhibit bioturbated tops. One of these beds, enriched in rock fragments and glauconite, is illustrated in Figure F21. The pebbly sand comprises subrounded to rounded pebbles in a matrix of very fine to fine sand; however, this bed was recovered only in a core catcher (Sample 339-U1386B-45X-CC), so its texture may be an artifact of drilling. The pebbles are sandstone with calcareous cement (Table T5).

The contacts between most lithologies and between subjacent beds of nannofossil mud are primarily gradational or bioturbated. Exceptions are sharp bases, irregular bases, and some sharp and inclined bases on silty sand or sandy silt beds.

Structures and texture: No primary sedimentary structures were observed in Subunit IC, except for indistinct and discontinuous silty laminations and lenses in some beds.

Bioturbation is the most obvious secondary sedimentary structure in this subunit and is present throughout the observed section. Characteristics of the bioturbation are similar to those of the bioturbation in the rest of Unit I. The bioturbation index in Subunit IC ranges from sparse to slight.

The sediment is fine grained through most of Subunit IC, with an average grain size of clay to silt. Exceptions are the intervals of sandy silt, silty sand, and pebbly sand, where the average grain size ranges from coarse silt to fine sand and the maximum grain size ranges from medium sand to pebble.

Composition: As is true for the rest of Unit I, all lithologies in Subunit IC are dominated by terrigenous material (siliciclastic components of clay minerals, quartz, and mica plus detrital carbonate) (Table T3; Fig. F8). The biogenic fraction is dominated by nannofossils with rare to common foraminifers and rare pteropods and sponge spicules. Diatom fragments are also present at several levels. Authigenic components are dominated by pyrite, dolomite, and glauconite.

Abundances of terrigenous, biogenic, and authigenic components, as estimated from smear slides (Fig. F8; Table T3), generally are similar to their abundances in Subunits IA and IB. The primary difference is the presence of diatom fragments, at abundances <20%, in several smear slides from Subunit IC. No discrete ash layers and no dropstones were observed. Total carbonate contents range from 14.88 to 32.86 wt% (average = 24.33 wt%) (Table T2).

Whole and nearly whole macrofossils are very poorly represented in Subunit IC. The few specimens found include recognizable coral fragments in Section 339-U1386B-35X-6. Macrofossil fragments, however, are distributed through most of the subunit; recognizable fragments include bivalves, echinoderms, and corals.

Color: The principal colors of the lithologies, as noted during visual description of the core, range from gray (5Y 5/1) to greenish gray (5GY 5/1, 5Y 4/1, and 10Y 5/1) to dark greenish gray (10Y 4/1). In general, sediments with higher sand and/or carbonate contents have lighter colors.

Bulk mineralogy: Twenty bulk XRD samples were analyzed from Subunit IC. Diffraction intensities from quartz, calcite, and illite account, on average, for 82.9% of the total identified mineral diffraction intensities (Fig. F17; Table T4). Quartz accounts for 50.1% of the intensities observed, which is more than in Subunits IA and IB, whereas the calcite contribution (23.4%) is similar to Subunit IA and the illite contribution (9.4%) is elevated but not as high as in Subunit IA. Minor minerals observed are the same as in Subunit IA, but the plagioclase/K-feldspar ratio is 2.35 and dolomite is 17.3% of calcite peak intensity in Subunit IC.

Unit II

Intervals: 339-U1386B-46X-4, 70 cm, through 50X-CC, 38 cm (bottom of hole); 339-U1386C-7R-3, 133 cm, through 18R-CC, 13 cm (bottom of hole)

Depth: Hole U1386B = 422.4–465.4 mbsf (bottom of hole), Hole U1386C = 418.9–525.2 mbsf (bottom of hole)

Age: Pleistocene–Pliocene

Lithologies and bedding

The dominant lithologies in Unit II are the same as the major lithologies in Unit I—silty sand with biogenic carbonate, calcareous silty mud, and nannofossil mud—although the relative importance of nannofossil mud decreases significantly downhole through Unit II (Figs. F5, F6). Because of their relatively similar major lithologies, Units I and II are distinguished on the basis of the patterns and inferred modes of sediment deposition rather than on the basis of major compositional changes. Minor lithologies include biogenic mud, a compositional variant of nannofossil mud, and calcareous sandy silt, a compositional and grain size intermediate between silty sand with biogenic carbonate and calcareous silty mud.

In Unit II, major lithologies are organized into sequences that begin with a sharp or erosional base, grade upward from silty sand to silty mud, and exhibit a bioturbated or gradational upper contact. This pattern is especially abundant in Cores 339-U1386B-46X through 47X and Core 339-U1386C-7R through Section 8R-2. The remainder of Unit II is composed of this type of normally graded sequence interstratified with thick beds of nannofossil mud (Fig. F22).

An additional bedding style in Unit II is represented by at least three thick, massive beds that contain angular or contorted centimeter- to decimeter-scale intraclasts of nannofossil mud embedded in a shelly silty sand matrix. Each of these beds has a sharp to erosional base and a sharp upper contact. The intraclasts are randomly dispersed in the matrix and are not graded by size. Three of these beds are found in Hole U1386C: from interval 339-U1386C-12R-1, 130 cm, to 13R-2, 83 cm (at least 666 cm thick); from interval 13R-3, 144 cm, to 14R-1, 16 cm (at least 181 cm thick); and from interval 15R-4, 142 cm, to 15R-5, 97 cm (122 cm thick) (Fig. F23).

Note that Unit II lithologies generally were lithified enough to require cutting by saw rather than by wire.

Structures and texture

Parallel lamination, low-angle inclined lamination, and normally graded bedding are the only primary sedimentary structures reported from Unit II. The lamination is present in a few of the normally graded beds and in almost all silty mud beds.

Bioturbation is a relatively common secondary sedimentary structure in Unit II, especially in the nannofossil muds and the calcareous silty muds. In those lithologies, bioturbation intensity generally is sparse to slight. The sandy silt and silty sand, however, have lower bioturbation intensities, with bioturbation effects generally not observable in the sandy portions of the graded beds. Where bioturbation is present, the most common indicators are diffuse centimeter-scale mottling and millimeter-scale pyritic burrow fills. Discrete burrows and identifiable ichnofauna are rare.

Small-scale subvertical faults (Fig. F24), fault sets, and contorted beds are present at several levels in Unit II. Dewatering structures are associated with at least one of these subvertical faults. The contorted beds are characterized by soft-sediment deformation, with convolute bedding and excellent examples of small-scale recumbent folds (Fig. F23A). The orientation of shell fragments in parts of these beds illustrates the pattern of soft-sediment deformation (Fig. F23A, F23B). Angular intraclasts of nannofossil mud are randomly dispersed in the matrix of shelly silty sand (Fig. F23C) and range from 5 mm to 4 cm in diameter. Millimeter-scale intraclasts are observed at the bases of several normally graded beds (interval 339-U1386C-6R-1, 55 cm, and 7R-1, 26 and 96 cm).

The average sediment grain size in Unit II is slightly larger than the average in Unit I because of the increased abundance of sandy silt and silty sand beds. The maximum grain sizes in Unit II also are larger than those in Unit I, especially when including the larger intraclasts of nannofossil mud, the shell fragments, and the pebbly sand (Core 339-U1386C-7R-2).

Composition

Because the major lithologies in Unit II are the same as the major lithologies in Unit I, the compositions of these two units are relatively similar (Fig. F8). The important terrigenous components continue to be siliciclastics (clay minerals, quartz, feldspars, mica, and accessory minerals) and detrital carbonate, and the important authigenic components continue to be pyrite, dolomite, and glauconite. Biogenic components in the finer grained lithologies continue to be dominated by nannofossils, but shell fragments, including fragments of displaced shallower water taxa, are an important component in the sandier lithologies. Total carbonate contents range from 10.96 to 33.56 wt% (average = 21.39 wt%) (Table T2). Wood fragments are also relatively common in the silty muds, silty sands, and sandy silts between 415 and 425 mbsf. A 1 cm thick wood-rich layer is present in interval 339-U1386C-8R-1, 40.5–41.5 cm.

Relatively complete macrofossils are rare in Unit II. Several are present, however, including an articulated bivalve (Sample 339-U1386C-13R-2, 53–54 cm; Fig. F25) and a gastropod shell (Sample 339-U1386C-12R-4, 77–78 cm; Fig. F26).

In order to compare the composition of the sand fraction from Units I and II, a series of 16 samples of sand separated from core catcher samples were resin-impregnated and made into thin sections. Results of this petrographic study are shown in Table T5.

Color

The principal colors of the lithologies in Unit II, as noted during visual description of the core, range from greenish gray (5GY 5/1 and 5Y 5/1) to dark greenish gray (10Y 4/1) and very dark greenish gray (10Y 3/1 and 5GY 3/1). In general, sediments with higher carbonate and/or sand content have lighter colors.

Bulk mineralogy

Six bulk XRD samples were analyzed in Unit II. Bulk mineralogies are somewhat similar to those of Unit I, and quartz, calcite, and illite account for 85.2% of the total identified mineral diffraction intensities. Quartz contributes 50.1% of the total peak intensity, which is more than the whole-site average. Calcite contributes 25.9%, which matches the whole-site average, and illite contributes 9.2%, which is slightly less than the whole-site average (Fig. F17; Table T4). Minor minerals in Unit II are similar to those in Unit I, the plagioclase/K-feldspar intensity ratio is 2.55, and dolomite is 10.7% of the calcite intensity.

Discussion

Given the setting of Site U1386, several lines of evidence for current transport and changing flow speeds support the interpretation of Unit I as a sequence of contourite deposits. Among these lines of evidence are

- The major lithologies present in Unit I,
- The relative abundances of these lithologies, and
- The organization of these lithologies into bi-gradational sequences with a predominance of gradational contacts and extensive bioturbation.

Subunits IA (~110 m thick) and IC (~205 m thick) are typical examples of a mixed sandy and muddy contourite succession (Fig. F10), whereas Subunit IB (~105 m thick) is a typical example of a muddy/silty contourite succession (Fig. F18). Subunits IA and IC also contain a few turbidites, but these represent a very minor portion of the section.

In comparison to the sediments of Unit I, Unit II is a relatively coarser grained succession of normally graded or massive deposits. The normally graded beds have sharp to erosional bases, generally are a few centimeters to a few decimeters thick, and have gradational bioturbated upper contacts. These characteristics support the interpretation that the beds are turbidites. Between 485 and 508 mbsf, most of the turbidites are sandy and composed of shelly sand, but silty turbidites also are present. At least three very thick massive beds in Unit II have sharp bases, contain intraclasts of nannofossil mud in a matrix of shelly sand, include zones with contorted bedding, and exhibit sharp upper contacts. Based on these characteristics, these beds are interpreted as the deposits of higher concentration sediment mass gravity flows (debris flows), and therefore are considered to be debrites.

The interpretation that Unit II records a significant component of downslope transport, whereas Unit I mainly records alongslope transport, indicates at least one significant change in the depositional regime at Site U1386 since ~5.54 Ma (Fig. F27; ages based on preliminary biostratigraphy; see "Biostratigraphy"). From ~5.54 Ma to sometime between 1.2 and 1.6 Ma (Unit I/II boundary based on calcareous nannofossil biostratigraphy), deposition at this site included downslope sediment mass gravity flows, both as turbidity currents and as higher concentration debris flows. Sediment was sourced from upslope regions that likely extended onto the continental shelf, as evidenced by the abundance of shallower water fauna in the shelly sands in the middle of Unit II. Unfortunately, the depositional history of this site between ~5.54 and ~1.2 Ma cannot be reconstructed in detail because of the presence of an extensive hiatus (3.2–1.9 Ma) and gaps in core recovery. However, the sediment record represented by Unit II indicates that downslope processes dominated deposition at this site, both prior to and immediately following the hiatus. Turbidite processes around this time were considered previously in the Faro Drift region by Roque et al. (2012), but debrites have been identified here for the first time.

Beginning at the transition from Unit II to I, sometime between 1.2 and 1.6 Ma, clearly recognizable bottom current processes are inferred to have dominated sediment transport and deposition (Fig. F27). The onset of clear bottom current influence at Site U1386 is recorded by interbedding of contourites with sandy and silty turbidites in the lowermost 30 m of Subunit IC. This interstratification indicates that episodes of downslope transport continued even as alongslope transport became more important. Occasional sediment input by downslope processes continued through the rest of Subunit IC, as evidenced by the rock fragment- and glauconite-rich turbidites at ~218 mbsf in Hole U1386A and ~253 mbsf in Hole U1836B.

After this transitional interval, alongslope transport processes appear to have strengthened significantly, as recorded by thick sandy contourite beds in the overlying remainder of Subunit IC (Fig. F27). These are the thickest sandy contourites in Unit I, suggesting a sustained time of strong and persistent flow at this site. Deposition at Site U1386 subsequently shifted to a muddy/silty mode, as recorded by the muddy/silty contourites of Subunit IB. This shift suggests a weakening of alongslope transport at this site, with one or more of the following as possible causes:

- Overall weakening of the bottom current system,
- The core of the bottom current migrated upslope from this location (northward), or
- The proximity of the site to turbidite channels changed from more proximal during deposition of Subunits IA and IC to more distal during deposition of Subunit IB.

A large (2–4 km wide) channel previously described by Llave et al. (2001, 2007) and Hernández-Molina et al. (2006) was located just to the south of Site U1386 during deposition of Subunits IA and IC, but this channel was not present (or at least nearby) during Subunit IB deposition. From their more proximal location, downslope flows in these channels could have supplied sand material during deposition of the coarser grained Subunits 1A and 1C. Based on preliminary biostratigraphic information, the episode of decreased sand deposition represented by Subunit IB persisted from >580 ka to at least 470 ka, (subject to uncertainties in the present age-depth model for Site U1386).

Alongslope depositional processes appear to have strengthened sometime between 470 and 270 ka at Site U1386, producing the change from the predominantly muddy/silty contourites of Subunit IB to the sandier contourites of Subunit IA. The sandy contourites of Subunit IA also are thinner than those of Subunit IC, suggesting that flow was weaker or more variable or sand supply was reduced since ~580–700 ka relative to conditions prior to that time (Fig. F27). Physical property data apparently resolve cyclicity in Subunit IA at inferred glacial–interglacial timescales (see **"Physical properties"**), suggesting that variations in bottom current strength were important at Site U1386 during that time.

The apparent Pleistocene cyclicity might also indicate that Site U1386 could be considered a mixed system, with downslope processes (turbidity currents) dominant during sea level lowstands and alongslope processes (contour currents) dominant during highstands. Equally, however, tectonic activity might be considered a prime control on downslope deposition. Further work and comparison with other sites is required in order to resolve these controls.

The complexities of changes in sediment source and/or current flow are seen in the XRD data that show higher illite percentages, higher dolomite/calcite ratio, and a possibly higher plagioclase/K-feldspar ratio in Subunit IA. This may indicate a sediment source or current flow change when compared with older subunits. These differences are greater between Subunits IA and IB than between IA and IC.

Another highlighted observation is the importance of authigenic dolomite and glauconite throughout the succession. What is their potential source? What are the implications for transport through currents? What is the importance of numerous shallow-water shells, corals, and glauconite? How were they transported to this site?

Biostratigraphy

The sedimentary record recovered at Site U1386 is continuous for most of the Holocene and Pleistocene (Fig. F28; Table T6). However, from the Gelasian (1.8–2.588 Ma) to the Zanclean (3.6–5.3 Ma), the record seems to be discontinuous and is strongly affected by debris flows and other downslope transport processes that significantly influence the planktonic and benthic microfossil assemblages. The record of Messinian (5.3–7.2 Ma) deposits at the base of Hole U1386C is not confirmed by the planktonic foraminifer data, as many of the bioevents recorded at this site, especially last occurrence (LO) events, can be affected by reworking and redeposition in younger levels. Nevertheless, characteristic Pliocene/Miocene boundary marker species were identified, and the age of first occurrence (FO) events can constrain and provide a maximum age for the lowermost cores recovered at this site. In particular, the oldest sediments recovered must be younger than 5.8 Ma.

During the Quaternary, sedimentation rates range from 35 cm/k.y. between 0 and 384 mbsf to 15 cm/k.y. between 384 and 453 mbsf (Fig. **F28**) and are in perfect agreement with the sedimentation rate estimated for the Brunhes interval based on the paleomagnetic records (see **"Paleomagnetism"**).

Preservation of microfossils is, in general, moderate to good, and calcareous nannofossils and foraminifers are abundant. In contrast to Site U1385, benthic foraminifers are much more abundant and can be equal to or even more abundant than planktonic foraminifers in some samples. Ostracods are also much more abundant at Site U1386 than at Site U1385. Pteropods were not observed at Site U1386.

Pollen and spores are abundant in all analyzed samples, ranging from ~3,000 to 46,500 grains/cm^3 (two to four times higher than the concentrations at Site U1385) and good to moderately well preserved in the upper 300 mbsf. Below this depth, the pollen is poorly preserved, and in particular a relatively high amount of conifer pollen is corroded (Fig. **F29**). Microcharcoal and dinocysts were also observed in all the samples.

Calcareous nannofossils

We examined all core catcher samples from Holes U1386A–U1386C for calcareous nannofossil biostratigraphy. Additionally, selected samples from Holes U1386A and U1386C were analyzed to constrain biohorizons, paying attention only to marker species. Calcareous nannofossil assemblages are abundant and diverse, and preservation is good to moderate, with weak dissolution in some samples. Small placolith species (<3 µm) dominate most of the assemblages. Inorganic input and reworking of pre-Pleistocene (mainly Neogene and Paleogene) species vary from few to common throughout all sections (Table **T7**).

Seventeen nannofossil datums defined and/or calibrated by Raffi et al. (2006 and references therein) and Flores et al. (2010) were identified in all holes (Table **T6**).

The change in abundance of large *Emiliania huxleyi* (>4 µm) that characterizes Termination 1 in mid- to low-latitude water masses in the Atlantic Ocean has been proven as a useful event by Flores et al. (2010). This change in abundance was recorded between Samples 339-U1386A-1H-3, 5 cm, and 1H-3, 50 cm (3.05–3.50 mbsf), and between the top of Core 339-U1386B-1H and Sample 1H-CC (top of hole–7.32 mbsf), making it possible to distinguish the onset of the Holocene in both holes.

The FO of *E. huxleyi* (0.26 Ma), which marks the base of Zone NN21, was placed between Samples 339-U1386A-11H-CC and 12H-CC (97.18–108.74 mbsf) and between 339-U1386B-8H-CC and 9H-CC (74.22–84.05 mbsf). However, this event should be taken with caution because of dissolution effects and the low proportion of this species. The LO of *Pseudoemiliania lacunosa* (0.46 Ma), considered a globally synchronous event defining the top of Zone NN19, occurs between Samples 339-U1386A-13H-2, 90 cm, and 13H-3, 5 cm (110.70–111.35), and between 339-U1386B-14H-CC and 15H-CC (129.79–141.33 mbsf).

A biohorizon considered useful in Pleistocene sediments is the LO of *Reticulofenestra asanoi* (0.90 Ma), which was placed between Sample 339-U1386A-31X-3, 90 cm, and 31X-4, 30 cm (265.85–266.75), and between 339-U1386B-30X-CC and 31X-CC (273.67–283.43 mbsf), although sporadic specimens of *R. asanoi* were observed after the defined biohorizon. Small discrepancies after comparison with paleomagnetic data can be explained by reworking or possible uncertainties in the magnetostratigraphy (see **"Paleomagnetism"**). However, we also cannot discard diachronism with previous calibrations (e.g., Raffi et al., 2006).

The FO of *R. asanoi* (1.07 Ma), another significant event for the Pleistocene, was recorded between Samples 339-U1386B-41X-CC and 42X-CC (379.34–388.57 mbsf). To define this biohorizons we considered specimens of *R. asanoi* ≥6 µm in size.

The LO of large *Gephyrocapsa* spp. (>5.5 µm; 1.24 Ma) was recorded between Samples 339-U1386B-45X-CC and 46X-CC (407.93–423.66 mbsf). The LO of *Helicosphaera sellii* (1.25 Ma), considered a diachronous event (Raffi et al., 1993; Wei, 1993), was identified in the same interval and in Samples 339-U1386C-6R-CC and 7R-CC (406.43–421.75 mbsf). The occurrence of *H. sellii* at this site is consistent with the ages provided by Raffi et al. (2006) for the Mediterranean Sea when compared with other calibrated events.

The FO of large *Gephyrocapsa* spp. (>5.5 µm; 1.61 Ma) was identified between Samples 339-U1386B-47X-CC and 48X-CC (428.94–446.67 mbsf) and 339-U1386C-8R-CC and 9R-CC (426.08–438.55 mbsf). The LO of *Calcidiscus macintyrei* (1.66 Ma), close in time to the FO of large *Gephyrocapsa* spp., was defined and identified between Samples 339-U1386B-49X-CC and 50X-CC (451.16–455.78 mbsf) and between 339-U1386C-10R-CC and 11R-CC (451.64–454.08 mbsf).

A strong variation in the composition of the calcareous nannofossil assemblage exists between Samples 339-U1386C-11R-CC and 12R-CC. Species such as *Discoaster brouweri, Discoaster pentaradiatus, Discoaster surculus, Sphenolithus* spp., and *Reticulofenestra pseudoumbilicus* (>7 µm) were recorded. The succession of events is complex to establish because of potential reworking and scarcity of some of these taxa. However, the LOs of the mentioned species and/or morphotypes occur between 1.95 and 3.83 Ma, allowing us to infer a hiatus within Zones NN18 and NN14.

The presence of *Discoaster asymmetricus* in Sample 339-U1386C-13R-CC permits placing this sample in Zone NN14, younger than 4.12 Ma (Raffi et al., 2006).

The lower portion of Hole U1386C was analyzed paying attention to sediment intervals richest in fine sediment, in order to avoid sandy portions (see **"Lithostratigraphy"**).

The occurrence of *Ceratolithus acutus* (LO at 5.34 Ma) between Samples 339-U1386C-17R-3, 124 cm, and 17R-4, 71 cm (514.34–515.51 mbsf), is consistent with the succession. This event should, however, be taken with caution because of dissolution effects and the low proportion of this species (Table T7). The LO of *Discoaster quinqueramus,* marker species of Zone NN11 (5.54 Ma), was recorded between Samples 339-U1386C-17R-4, 71 cm, and 17R-5, 66 cm (515.31–516.76 mbsf). However, the record of this taxon below this level is scarce.

Planktonic foraminifers

Planktonic foraminifers are dominant or abundant in all samples from Hole U1386A and the majority of samples from Hole U1386B (Table T8), both of which recovered Holocene to Pleistocene sediment (Table T6). The exceptions in Hole U1386B are Samples 339-U1386B-44X-CC through 47X-CC, in which planktonic foraminifers are absent or very rare in the encountered detrital sand. In Hole U1386C, which reaches further back in time, foraminifer abundance varies between dominant and very few specimens (Table T9). The Holocene and Pleistocene planktonic foraminifer assemblages observed at Site U1386 are typical of temperate waters from the North Atlantic with a mixture of surface and deep-dwelling foraminifers. *Globigerina bulloides, Neogloboquadrina pachyderma* (dextral), and *Globorotalia inflata* are the dominant species in most samples from Holes U1386A and U1386B and in Samples 339-U1386C-2R-CC through 11R-CC (Tables T8, T9). In the Pliocene samples from Hole U1386C, *G. inflata* is replaced by *Globorotalia puncticulata* in the fauna. The polar species *N. pachyderma* (sinistral) dominates in Samples 339-U1386A-37X-CC and 339-U1386B-25X-CC and 41X-CC, indicating that these samples date from glacial periods. *Globigerinoides ruber* and *Orbulina universa* are present in most of the samples from all three holes. In the Pliocene section of Hole U1386C (Samples 339-U1386C-12R-CC through 18R-CC), *Globigerina apertura, Globigerina decoraperta,* and *Globigerinoides extremus* regularly contribute to the fauna, and *Globigerinoides trilobus* is present, sometimes in higher abundance, from Core 339-U1385C-15R downhole (Table T9). In the Pleistocene sediment, the deep-dwelling fauna consists mainly of *Globorotalia truncatulinoides* and *Globorotalia scitula,* both dominantly coiling dextral, with minor contributions by *Globorotalia crassaformis* (preferentially sinistral coiling) and *Globorotalia hirsuta.* In the Pliocene samples from Hole U1386C, *G. crassaformis* is sometimes present in low numbers. *Globorotalia miocenica* was observed in Sample 339-U1386C-12R-CC.

Within the Pleistocene sections of Holes U1386B (above 455.8 mbsf) and U1386C (above 454.1 mbsf), three biostratigraphic events were observed. The top of the paracme of *N. pachyderma* (sinistral) (1.21 Ma; Lourens et al., 2004), was placed between Samples 339-U1386B-42X-CC and 43X-CC (388.57–398.08 mbsf; Table T8). Because of the sandy sediment encountered in the core catchers of Cores 339-U1386B-44X through 47X, the bottom of the paracme of *N. pachyderma* (sinistral) (1.37 Ma; Lourens et al., 2004), is less well defined and tentatively placed between Samples 339-U1386B-47X-CC and 48X-CC (428.94–446.67 mbsf). In Hole U1386C, this event occurs between Samples 339-U1386C-8R-CC and 9R-CC (426.08–438.55 mbsf; Table T9).

The large, heavily encrusted specimens of *Neogloboquadrina atlantica* (dextral) that were also observed at Site U1385 (see **"Biostratigraphy"** in the "Site U1385" chapter [Expedition 339 Scientists, 2013c]) were found in Samples 339-U1386B-47X-CC (one specimen) and 48X-CC (428.89–446.67 mbsf; Table T8) and between Samples 339-U1386C-6R-CC and 10R-CC (406.38–451.64 mbsf; Table T9).

A major change in the foraminifer assemblages was observed in Core 339-U1386C-12R, defined by the appearance of a number of species extinct since the early Pleistocene or the late Pliocene such as *G. puncticulata, Sphaeroidinellopsis seminulina,* and *Dentoglobigerina altispira* (Tables T6, T9). These Pliocene foraminifers are very abundant in Samples 339-U1386C-12R-CC through 16R-CC (467.91–508.28 mbsf). Sediment in this interval, however, indicates strong gravitational downslope transport characterized by debrites and turbidites and abundant evidence for slump deposits (see **"Lithostratigraphy"**). Because the LO of *S. seminulina* occurred at 3.19 Ma and Sample 339-U1386C-11R-CC is of Pleistocene age, a major hiatus of at least 1.4 m.y. seems to exist between Samples 11R-CC and 12R-1, 45–47 cm (454.08–462.87 mbsf).

Because of the coincidence in the occurrence of lower Pliocene faunas with evidence of gravitational transport from the slope, the reliability of the LO events in the Pliocene core catcher samples remains ambiguous. In order to confirm the events, discrete samples from hemipelagic and contourite intervals were analyzed. The sequence of foraminifer events in these samples is, in general, the one expected for the early Pliocene, but there are some inconsistencies with comparable sites of this time period (Hilgen, 1991; Lourens et al., 2004; Sierro et al., 2000, 2009). Considering only the samples taken in contourite intervals, the LO of *S. seminulina* (3.19 Ma) was placed between Samples 339-U1386C-13R-3, 43–45 cm, and 14R-1, 62–64 cm (475.45–482.24 mbsf), and the last abundant occurrence (LaO) of *Globorotalia margaritae* (3.98 Ma) should be placed between Samples 16R-5, 0–2 cm, and 16R-6, 46–48 cm (506.52–507.95 mbsf). However, *G. margaritae* is present uphole to Sample 15R-4, 24–26 cm.

The presence of *G. puncticulata* together with *S. seminulina* and the absence of *G. margaritae* in the debrite deposits of Core 339-U1386C-12R also constrain the age of the slope deposits to an interval between 4 and 3.19 Ma.

One of the main inconsistencies observed in Hole U1386C is that the first specimens of *G. puncticulata* were found in Sample 339-U1386C-17R-CC. Although very rare, two specimens of the same species were also found in Sample 339-U1386C-17R-3, 27–29 cm. Throughout the North Atlantic and the Mediterranean, this species is normally very abundant in the foraminifer assemblages since its FO. At Site U1386, this species becomes very abundant between Samples 339-U1386C-16R-6, 43–45 cm, and 16R-5, 0–2 cm (506.52–507.95 mbsf). It is between these two samples where the FO of *G. puncticulata* (4.52 Ma; Lourens et al., 2004) should be placed, but we have no explanation for the presence of rare specimens in deeper sediments. Furthermore, the FO of *G. puncticulata* was identified at exactly the same depth as the LaO of *G. margaritae* (3.98 Ma). Only the presence of a hiatus can explain the coincidence of these two events at this site.

The bottom of Hole U1386C was reached with Sample 339-U1386C-18R-CC. Although it was described as a turbidite bed that contains coarse quartz grains (see **"Lithostratigraphy"**), abundant specimens of *G. margaritae* were found that strongly support an age younger than 5.8 Ma, the age of its first abundant occurrence. Even if the foraminifers were transported, as suggested for the abundant occurrence of shelf benthic foraminifers, the turbidite event had to occur after *G. margaritae* was already deposited. Consequently, the presence of this species constrains the maximum age for the bottom of this hole to an age younger than 5.8 Ma.

The presence of rare specimens of *G. puncticulata* in Sample 339-U1386C-17R-CC, only 6 m above the bottom of the hole, would indicate a maximum age of 4.52 Ma. If these specimens are in situ, a large part of the planktonic foraminifer assemblage was transported downslope.

Benthic foraminifers

Samples 339-U1386A-1H-CC through 39X-CC, 339-U1386B-38X-CC through 50X-CC, and 339-U1386C-2R-CC through 18R-CC were studied for the abundance of benthic foraminifers (Table **T10**). Additionally, selected core catcher samples from Hole U1386B were examined for the "*Stilostomella* extinction" event. The combined information from all studied samples documents the entire succession recovered at Site U1386.

Abundance and preservation of benthic foraminifers are related to grain size and depositional environment. In the contouritic portions of Holes U1386A (Samples 1H-CC through 38X-CC), U1386B (Samples 38X-CC through 42X-CC), and U1386C (Samples 2R-CC through 4R-CC), benthic foraminifers are abundant and preservation is generally good. Moderate preservation only occurs in Samples 339-U1386A-23X-CC and 24X-CC and in 339-U1386C-2R-CC and 4R-CC, in which increased amounts of silt and sand were observed. With the beginning of turbidite and debrite deposition, foraminiferal preservation declines. Benthic foraminifers in Samples 339-U1386B-43X-CC and 46X-CC are moderately preserved, and Samples 339-U1386B-44X-CC, 45X-CC, and 47X-CC are barren or contain only a few poorly preserved tests of the shelf taxon *Elphidium*. In Hole U1386C, preservation declines from moderate to poor between Samples 339-U1386C-6R-CC and 18R-CC, whereas the abundance of foraminiferal shells increases.

Similar to preservation, the composition of the benthic foraminiferal assemblages shows a relation to grain size and the depositional environment. Most of the assemblages in nannofossil ooze and silty mud (Samples 339-U1386A-1H-CC through 43X-CC and 339-U1386B-48X-CC through 50X-CC; see **"Lithostratigraphy"**) consist of species of *Brizalina, Bulimina, Cassidulina, Globobulimina, Melonis, Sigmoilopsis,* and *Uvigerina* in varying proportions.

These taxa characterize upper bathyal environments with increased organic matter flux and reduced ventilation (van Morkhoven et al., 1986; Leckie and Olson, 2003; Murray, 2006). Peak abundances of *Brizalina* spp. and *Globobulimina* spp. (e.g., Sample 339-U1386A-19H-CC) indicate peaks in oxygen depletion of bottom waters related to enhanced input of organic matter and/or a well-stratified water column. This interpretation is in good agreement with the organic geochemistry results in Hole U1386A (see **"Geochemistry"**). Occasional transport from the outer shelf is indicated by abraded shells of *Lenticulina* spp. (e.g., Samples 339-U1386A-4H-CC and 12H-CC; Table **T10**). Shells of inner–middle shelf taxa (*Ammonia beccarii* and *Elphidium* spp.) occur sporadically.

The "epibenthos group," suggested as an indicator for MOW intensity (Schönfeld, 1997, 2002; Schönfeld and Zahn, 2000), is represented by (in order of decreasing contribution) *Planulina ariminensis, Cibicides lobatulus, Textularia* spp., *Hanzawaia concentrica,* and *Epistominella exigua* at Site U1386. In most core catcher samples, these taxa show abundances <5%. Only in Samples 339-U1386A-24X-CC, 27X-CC, 30X-CC, 32X-CC, and 34X-CC were abundances >5% recorded for *P. ariminensis, C. lobatulus,* and *Textularia* spp. In general, an increase in current energy and ventilation is suggested between Samples 23X-CC and 39X-CC, in which the abundances of *Trifarina angulosa, Trifarina bradyi,* and *Cibicidoides* spp. increase (Kaiho, 1999). In most of these samples, a parallel decrease in the abundance of the low-oxygen indicator *Brizalina* spp. is observed (Murray, 2006).

Hyalinea balthica, an indicator for cold-water masses (Bayliss, 1969; van Morkhoven et al., 1986), is abundant to dominant in Samples 339-U1386A-1H-CC, 5H-CC, 18H-CC, 27X-CC, and 28X-CC. A comparison with the abundance of temperature-sensitive taxa in the other microfossil groups and trends in physical properties, as well as the available age constraints, implies a relation of these samples to different glacial intervals. Beginning approximately with the mid-Pleistocene revolution marker horizon in the seismic profiles (Llave et al., 2001, 2011), this taxon occurs only sporadically in the lower part of the succession.

In strong contrast to the assemblages described above, the lower portion of the succession (below Sample 339-U1386B-44X-CC) shows the frequent occurrence of shelf taxa. These are mainly composed of heavily abraded tests of *Elphidium crispum* and *Elphidium* cf. *jenseni,* whereas *A. beccarii* and *Asterigerinata planorbis* occur rarely. Parallel to the increase in shelf taxa, preservation of upper bathyal taxa (mainly *Brizalina, Uvigerina,* and *Cibicidoides*) declines and foraminiferal shells are often abraded and broken.

Between Samples 339-U1386C-10R-CC and 11R-CC, *Cassidulina laevigata/teretis* suddenly disappears. These foraminifers are related to boreal waters and occur frequently in the North Atlantic during the middle–late Pliocene and the Pleistocene. Its disappearance roughly co-occurs with the hiatus indicated by the planktonic microfossil groups and may be related to the warmer climate during the late Miocene and early Pliocene.

Finally, a change in preservation (shells are not pristine/heavily calcified) and species composition (although similar to the generic level) is noticeable in Samples 339-U1386C-17R-CC and 18R-CC. The poor preservation, however, restricts species identification and interpretation.

With respect to biostratigraphy, the *Stilostomella* extinction (0.58–0.7 Ma) (Hayward, 2002; Kawagata et al., 2005) was recognized between Samples 339-U1386A-28X-CC and 29X-CC (244.42–253.73 mbsf), as well as in Samples 339-U1386B-28X-CC and 29X-CC (254.46–263.03 mbsf). The datum agrees well with age estimates from nannoplankton assemblages and paleomagnetic measurements (Fig. **F28**). It has to be noted that nodosariids, pleurostomellids, and stilostomellids are rare at this depth interval and only a few tests have been identified. However, the tests in Samples 339-U1386A-29X-CC and 30X-CC are well preserved and thus considered autochthonous. In contrast, a broken and abraded test of *Siphonodosaria* was found in Sample 28X-CC that is considered reworked. More common occurrences of these foraminiferal groups are recorded below Sample 34X-CC.

Ostracods

Ostracods were examined in most core catcher samples from Holes U1386A–U1386C, providing a low-resolution record of the entire stratigraphic section recovered at Site U1386. Ostracod abundance varies from absent to >160 specimens per sample (average = 21). Abundance maxima (>70 specimens) were observed in Samples 339-U1386A-1H-CC, 2H-CC, and 10H-CC and 339-U1386B-1H-CC (Fig. **F30**). The overall assemblage includes >60 species belonging to 44 genera (Table **T11**). However, species diversity values are underestimated because species of selected genera (i.e., *Krithe* and *Cytheropteron*) were grouped together to facilitate the shipboard preliminary study. Ostracod preservation varies from good in the upper 110 m of the cored section to moderate to poor with increasing depth thereafter. Species diversity increases with overall abundance.

The ostracod fauna at Site U1386 includes shelf and upper slope taxa. *Krithe* is the dominant genus, accompanied by *Cytheropteron, Argilloecia, Henryhowella, Loxoconcha, Cytherella, Buntonia, Parakrithe, Bythoceratina,* and *Pseudocythere*. Four main assemblages were identified based on the ostracod stratigraphic distribution. Assemblage A is characterized by *Krithe* spp., *Argilloecia acuminate,* and *Cytheropteron* spp. (Fig. **F30**). This assemblage is absent from the bottom of the record at Site U1386 (526–400 mbsf), but it quickly increases in relative abundance between 430 and ~270 mbsf, reaching the highest values between Samples 339-U1386A-27X-CC (234 mbsf) and 35X-CC (310 mbsf). Based on calcareous nannofossils and planktonic foraminifer biostratigraphy, the onset of this episode coincides approximately with the mid-Pleistocene revolution (0.9 Ma) horizon (Llave et al., 2001, 2011). Beginning at ~170 mbsf and extending to the top of the stratigraphic section, Assemblage A increases sharply in abundance and shows broad temporal variability.

Assemblage B consists of *Henryhowella sarsii, Bythoceratina scaberrima, Pterigocythereis jonesii, Cytherella serratula, Rectobuntonia inflata, Buntonia sublatissima, Echinocythereis echinata, Eucythere pubera,* and *Paracytheridea* sp. The assemblage displays highest relative abundance between ~125 and 165 mbsf, between ~280 and 350 mbsf, and near the base of the cored section. Notably, *B. scaberrima* and *P. jonesii* are only present in Samples 339-U1386A-1H-CC through 3H-CC (Fig. **F30**).

Assemblage C is characterized by the presence of mid- to inner-shelf taxa *Aurila, Callistocythere, Loxoconcha rhomboidea, Sagmocythere* sp., *Urocythereis sororcula, Actinocythereis* sp., *Cimbaurila ulicznyi,* and *Occultocythereis culter.* This assemblage is observed only in Samples 339-U1386A-24X-CC and 339-U1386C-12R-CC and 13R-CC (Fig. **F30**). These samples correspond to debrites or turbidite layers (see **"Lithostratigraphy"**), and the taxa are considered to be reworked.

Assemblage D includes *Pseudocythere caudata, Paradoxostoma ensiforme, Buntonia dertonensis, Carinocythereis whitei,* and *Costa punctatissima* and is observed only from ~95 to 17 mbsf (Fig. **F30**). The observed variability in ostracod distribution suggests changes in bottom water ventilation, sedimentation, and food availability over the last ~4 m.y. at Site U1386 that are concurrent with similar changes in the benthic foraminifers at this site. Assemblage A is dominated by *Krithe* and *Argilloecia*. As documented by Cronin (1983) and Alvarez Zarikian et al. (2009), the genera can thrive under high surface productivity and in poorly oxygenated waters, whereas *Cytheropteron* has been documented to be closely associated with deglacial transitions in the North Atlantic (Cronin et al., 1999; Alvarez Zarikian et al., 2009). These results are in agreement with those derived from the benthic foraminifers at this site (see above). The taxonomic composition of Assemblage B seems to reveal periods of higher energy and well-ventilated bottom waters. In contrast, Assemblage C indicates reworked material by the presence of moderately to poorly preserved allochthonous inner-shelf taxa. This is supported by the co-occurrence of inner-shelf foraminifers *Elphidium* and *Ammonia* in the same samples.

Palynology

Thirteen samples, eight from Hole U1386A (Samples 1H-CC, 5H-CC, 8H-CC, 15H-CC, 20H-CC, 26X-CC, 32X-CC, and 35X-CC), three from Hole U1386B (Samples 40X-CC, 42X-CC, and 50X-CC), and two from Hole U1386C (Samples 9R-CC and 17R-CC), representing the three kinds of lithology identified at this site (nannofossil mud, silty mud, and silty sand; see **"Lithostratigraphy"**) were analyzed. *Pinus* is well represented in the upper 200 mbsf of the sequence, with the maximum abundance in Sample 339-U1386A-1H-CC (Fig. **F29;** Table **T12**). In Samples 339-U1386A-8H-CC and 20H-CC and in Samples 339-U1386B-40X-CC and 42X-CC, pollen grains from the Mediterranean forest, mainly deciduous and evergreen *Quercus* and *Olea,* along with those from semidesert environments (*Artemisia, Ephedra,* and Chenopodiaceae/Amaranthaceae) and grasslands, mainly *Taraxacum*-type and Poaceae, dominate the assemblage. Few pollen from heathlands were recorded along the sequence.

Semidesert plants peak in Sample 339-U1386A-15H-CC, whereas the Mediterranean trees and shrubs are relatively abundant in Sample 5H-CC, indicating particularly dry/cold and warm climates, respectively. These assemblages highlight different climates that, based on the magnetic susceptibility record, might relate to marine isotope Stages 5 and 12, respectively (see **"Stratigraphic correlation"**). Interestingly, below 350 mbsf and older than 1.6 Ma, we identified the presence of "clam-shell" pollen morphotypes, which are typical from Taxodiaceae plants, although some Cupressaceae pollen look similar (Traverse, 1988). So far, we have preferred to name this morphotype as Taxodiaceae/Cupressaceae, awaiting identification confirmation. The former family is extinct in Europe at present, and neither are recorded in the European pollen records covering the last 0.425 m.y., in particular those from the Western Iberian margin (e.g., Desprat et al., 2007; Tzedakis et al., 2009), nor in the pollen record of Ocean Drilling Program Site 976 in the Alboran Sea, which reflects the vegetation of southeastern Iberia from 1.09 to 0.9 Ma (Joannin et al., 2011). Taxodiaceae/Cupressaceae pollen reach a substantially high concentration in Sample 339-U1386C-9R-CC, dated at ~1.65 Ma (Fig. F29).

Paleomagnetism

Paleomagnetic investigation of the 101 APC, XCB, and RCB cores collected at Site U1386 (excluding the three wash cores from Hole U1386C and two empty cores from Holes U1386A and U1386B) included the measurement of magnetic susceptibility of whole-core and archive-half split-core sections and the natural remanent magnetization (NRM) of archive-half split-core sections. NRM was measured before and after alternating field (AF) demagnetization with 20 mT peak field for all studied cores of the site. The FlexIt tool was used to orient the cores in the APC section of Holes U1386A and U1386B starting with Core 4H (Table **T13**). Although the rubber knob holding the tool in place broke sometime during the operation in Hole U1386B, the results of the reorientation attempt look convincing and the data appear to be usable. Stepwise AF demagnetization on 24 selected discrete samples was performed at successive peak fields of 0, 5, 10, 15, 20, 25, 30, 35, 40, 45, 50, 55, 60, 70, and 80 mT to verify the reliability of the split-core measurements and to help determine the magnetostratigraphy in the XCB-cored sections. The depth levels where the measured discrete samples were taken are indicated by triangles in the first panel of Figure **F31.** We processed data extracted from the Laboratory Information Management System (LIMS) database by removing all measurements collected from disturbed and void intervals, which are listed in Tables **T14** (see **"Stratigraphic correlation"**), and all measurements that were made within 10 cm of the section ends, which are slightly biased by measurement edge effects. The processed NRM inclination, declination, and intensity data after 20 mT peak field AF demagnetization are listed in Tables **T15, T16,** and **T17.**

Natural remanent magnetization and magnetic susceptibility

The intensity of NRM after 20 mT demagnetization is similar in magnitude in the overlapping parts of Holes U1386A and U1386B, ranging from ~10^{-4} to ~10^{-2} A/m (Fig. F31). Below ~450 mbsf, NRM intensity decreases to ~10^{-5} to ~10^{-4} A/m.

In spite of the significant coring disturbance and drill string overprint in the XCB- and RCB-cored sections, a relatively stable magnetic component was preserved in sediment from all three holes, which allows for the determination of magnetic polarity for most parts of the recovered sediment sequences. A magnetic overprint with steep positive inclinations, which was probably acquired during drilling, was usually removed by up to 20 mT peak field AF demagnetization (Fig. F32). However, NRM directions show relatively large scatter in the XCB and RCB sections below ~180 mbsf (Hole U1386A) and ~150 mbsf (Hole U1386B). The XCB cores are heavily biscuited and usually contain as much of the disturbed matrix as the intact material, strongly compromising the quality of the resulting paleomagnetic data. Only discrete samples taken from the biscuits will be able to reveal a better quality paleomagnetic signal.

The AF demagnetization behavior of eight discrete samples from normal and reversed polarity intervals is illustrated in Figure **F32.** All samples exhibit a steep, normal overprint that was generally removed after AF demagnetization at a peak field of ~15–20 mT, demonstrating that the 20 mT magnetic cleaning level is sufficient to eliminate the overprint. The samples also appear to acquire an anhysteretic remanent magnetization during AF demagnetization at high peak fields (>55 mT), possibly because of a bias caused by the ambient magnetic field during demagnetization. We calculated component NRM directions of the discrete samples from data from the 25–50 mT demagnetization steps using principal component analysis (Kirschvink, 1980) and the UPmag software (Xuan and Channell, 2009). Component inclinations of discrete samples with maximum angular deviation less than ~15° are shown as yellow circles in Figure F31 (first panel).

Magnetic susceptibility measurements were made on whole cores from all three holes as part of the Whole-Round Multisensor Logger (WRMSL) analysis and on archive-half split-core sections using the Section Half Multisensor Logger (SHMSL) (see **"Physical properties"**). Magnetic susceptibility is consistent between the two instruments and in general mimics the NRM intensity. The WRMSL acquired susceptibility was stored in the database in raw meter units. These were multiplied by a factor of 0.68×10^{-5} to convert to the dimensionless volume SI unit (Blum, 1997). A factor of $(67/80) \times 10^{-5}$ was multiplied by the SHMSL-acquired susceptibility stored in the database. Magnetic susceptibility varies between 5×10^{-5} and 40×10^{-5} SI (Fig. **F31,** fourth panel). Note that in Figure **F31,** a constant of 25×10^{-5} SI was added to the SHMSL measurements (gray lines) to facilitate the comparison with the WRMSL measurements (black lines).

Magnetostratigraphy

Sedimentation rates at Site U1386 are high, on the order of 350 m/m.y., which result in the occurrence of all magnetic polarity reversals in the highly disturbed XCB and RCB part of the cored section. The lack of core orientation and the significant coring disturbance and drill string overprint in the XCB and RCB cores limit our magnetostratigraphic interpretation to rely entirely on changes in magnetic inclination and on measurements of discrete samples taken from the relatively undisturbed drilling biscuits. The geomagnetic field at the latitude of Site U1386 (36.83°N) has an expected inclination of 56.27°, assuming a geocentric axial dipole field model, which is sufficiently steep to determine magnetic polarity in APC, XCB, and RCB cores that lack horizontal orientation.

The Brunhes–Matuyama polarity transition occurs at ~274.6 mbsf in Hole U1386A (interval 339-U1386A-32X-2, ~90 cm) and at ~273.3 mbsf in Hole U1386B (interval 339-U1386B-30X-7, ~60 cm) (Fig. F31; Table T18). The relatively large scatter of the remanent directions in the XCB cores made it difficult to determine the exact position of the boundary; however, detailed paleomagnetic work on discrete samples from drilling biscuits should resolve the transition relatively well. The termination of the Jaramillo Subchron (C1r.1n) was identified with the help of discrete samples in Hole U1386A at ~344.6 mbsf (Section 339-U1386A-39X-4) and in Hole U1386B at ~347.9 mbsf (Section 339-U1386B-39X-6) (Fig. F31; Table T18). The onset of the Jaramillo Subchron at 1.072 Ma occurs at ~374 mbsf in Hole U1386B. This interpretation is supported by discrete sample results as well as a shift of split-core inclination to more negative values (Fig. F31, first panel). The top of the RCB-cored section in Hole U1386C seems to record part of the Matuyama Chron (C1r.2r). Below Core 339-U1386C-10R (~450 mbsf) magnetostratigraphic interpretation is not possible because of a combination of poor core recovery, very low NRM intensity, sedimentary features such as debris flows and slumps (see **"Lithostratigraphy"**), and an apparent hiatus (see **"Biostratigraphy"**).

With sedimentation rates of ~350 m/m.y. in the APC part of the section, NRM data show several intervals with shallow or negative inclinations that are often accompanied by large changes (~180°) in the FlexIt tool–corrected declination data. Some example intervals are at ~80 and ~168 mbsf in Hole U1386A and at ~17 mbsf in Hole U1386B. Visual inspection of the split-core images and core descriptions indicate no apparent disturbance in these intervals, suggesting these intervals may be associated with geomagnetic excursions. High-resolution measurements with full demagnetization sequence are needed to confirm these interpretations.

Physical properties

Physical properties at Site U1386 were determined in Holes U1386A and U1386B and the cored sections of Hole U1386C (Cores 339-U1386C-2R, 4R, and 6R through 18R). High-resolution scanning at 2.5 cm intervals on whole-round sections was performed with the WRMSL in all holes, whereas the Special Task Multisensor Logger (STMSL) was only used for Hole U1386B for stratigraphic correlation purposes. Thermal conductivity probes were applied to Section 3 of each core in Hole U1386A. *P*-wave velocity measurements on split-core sections (working half) were obtained in Hole U1386A for every section; however, reasonable results were only obtained for the upper ~76 mbsf. Moisture and density measurements were determined for every second section of each core from Hole U1386A, downhole below Core 339-U1386B-37X, and for Cores 339-U1386C-2R, 4R, and 6R through 18R. Color reflectance analysis and split-core point-magnetic measurements were taken on every section at 5 cm intervals.

Whole-Round Multisensor Logger and Special Task Multisensor Logger measurements

The STMSL was not used for Hole U1386A because no immediate acquisition of data for stratigraphic correlation was necessary, but the STMSL was used for Holes U1386B and U13686C. Cores were equilibrated for 3 h before measuring with the WRMSL.

Gamma ray attenuation bulk density

Gamma ray attenuation (GRA) density at Site U1386 is highly variable between 1.6 and 2.2 g/cm^3 (Fig. F33). Some of the scatter could be explained by incomplete filling of core liners, especially in sandy sections and cores for which the more disruptive XCB and RCB drilling techniques were applied. Besides this, the natural variations in the sand content of the sediment and in its texture are also reflected in the GRA density record. Between 400 and 450 mbsf increased densities correspond to an interval rich in sandy turbidite deposits. This relation is opposite to the general trend observed at this site, that low GRA densities often conform to sand-rich intervals. The contrasting correlations between density and lithology reflect the difference in texture and composition of layers generated by bottom current processes (i.e., contourites) and gravitational processes (i.e., turbidites).

Magnetic susceptibility

Of all physical properties, magnetic susceptibility displays the most marked changes (Fig. **F33**). Based on WRMSL data, four physical property units can be distinguished that differ in value range and variability. Physical properties Unit I, between 0 and ~150 mbsf, exhibits declining susceptibilities and distinct fluctuations between 10 × 10^{-5} and 40 × 10^{-5} SI with peaks approaching 55 × 10^{-5} SI. For this unit, a remarkable coherence of susceptibility, NGR counts, and spectral reflectance component a* can be noted (Figs. **F33, F34**). More reddish sediments (i.e., high a*; see Site U1386 visual core descriptions in **"Core descriptions"**) are found in intervals of high susceptibility with no apparent change in grain size. Whether the color change might be attributed to varying amounts of hematite or other mineralogical changes in the composition of the sediments remains unclear. Below in physical properties Unit II (150–420 mbsf), magnetic susceptibility shows less variability (5 × 10^{-5} to 20 × 10^{-5} SI).

The entire interval between 0 and 420 mbsf corresponds to lithologic Unit I (see **"Lithostratigraphy"**). The boundary between lithologic Subunits IA and IB, at ~110 mbsf in Hole U1386B, fits to the general trend of declining magnetic susceptibility. Except for its upper part (110–150 mbsf), the more mud rich Subunit IB has, on average, low and uniform susceptibilities. The top of lithologic Subunit IC, at ~216 mbsf in Hole U1386B, shows a slight increase of susceptibility, which drops to a level similar to that of Subunit IB further downhole. Whereas Subunit IC is very similar to Subunit IA in terms of lithology and mineralogical composition, the latter clearly has the highest and most variable susceptibilities.

Between 420 and 445 mbsf, the very distinct physical properties Unit III can be discerned with highly variable values that markedly increase to maximum peaks of 526 × 10^{-5} SI, corresponding to turbidites. Downhole, below 445 mbsf, physical properties Unit IV is defined by magnetic susceptibility data that is dominated by low values close to 10 × 10^{-5} SI. Here, debrites and turbidites are the dominant lithofacies. In the lithologic units, the entire interval below 420 mbsf corresponds to Unit II (see **"Lithostratigraphy"**).

Because the sulfate reduction zone only extends through the upper 12–13 m of sediment and gas flux is significantly lower than at Site U1385, diagenesis is suspected to have a minor influence on the magnetic susceptibility signal. Hence, we assume that the magnetic susceptibility signal is dominated by the primary sediment composition.

WRMSL and split-core magnetic susceptibility data agree well for cores drilled using the APC. For sediments retrieved with the XCB or RCB, WRMSL values are consistently lower. We assume that this difference can be attributed to the incomplete filling of the liner for those cores with lower values, providing less volume for sensor loop integration.

P-wave velocity

Sonic velocities were measured with the WRMSL for Holes U1386A and U1386B, and an attempt was made to determine *P*-wave velocities on split cores in each section of Hole U1386A (Fig. **F33**). Because of poor sediment to liner coupling, reasonable results from the WRMSL could only be obtained for the upper ~25 m of sediment. The *P*-wave velocity profile can be extended to 77 mbsf by using the *P*-wave determinations on split cores. Although the sediment surface appeared to be smooth and should have provided adequate coupling to the transducers, no clear acoustic signal could be obtained for *P*-wave velocity determinations at greater depth. An explanation for this might be the relatively stiff and brittle nature of the sediment, which promotes the formation of small cracks that negatively affect signal propagation.

P-wave velocities follow the trend of increasing GRA densities in the upper 12 mbsf, beginning with values of 1450–1500 m/s in the uppermost meters, increasing downhole to 1550–1650 m/s for WRMSL and split core data (only accounting for automatically processed data). Both types of measurement agree well, especially when only considering split-core data with high signal quality (solid symbols in Fig. **F33**). One measurement at 22.6 mbsf stands out, with a sonic velocity of 1796 m/s measured on a sandy interval.

Natural gamma radiation

NGR scanning on all cores from Site U1386 was performed mostly at low resolution with one position (usually Position II) of the detector array. Exceptions are Cores 339-U1386A-1H and 2H, which were measured in Positions I and II of the detector array. NGR counts fluctuate between 20 and 60 cps, revealing cyclic patterns throughout all cored sections (Fig. **F34**). Comparatively low NGR counts of not more than 45 cps below 150 mbsf might at least partly be attributed to the lower recovery of core during rotary drilling. A correlation between the dramatic increase in magnetic susceptibility below 420 mbsf and higher NGR counts is apparent, although NGR values start to increase at ~380 mbsf. It is notable that above ~380 mbsf, sandy layers are commonly associated with low NGR values, whereas below ~380 mbsf, coarse-grained sediments are related to intervals dominated by high NGR counts. The change in the depositional style from contouritic to turbiditic apparently affects the mineralogical composition of the sandy layers, which can be interpreted as a change from a silicate-dominated to a carbonate-bearing lithology.

Moisture and density measurements

Determination of moisture and density (MAD) on discrete sediment samples was performed on every section of Hole U1386A (Fig. **F35**). Sampling was preferentially carried out on the dominant lithology of a section, avoiding small interlayers of differing grain size (e.g., centimeter-scale sand layers). Generally, GRA and MAD methods give consistent bulk density results (Fig. **F33**). Compared to Site U1385, a steep compaction-related density increase might only be inferred for the uppermost ~12 mbsf, where porosity and water content of the sediments decrease inversely to the increase of bulk density (Figs. **F33, F35**). Below 12 mbsf, moisture content and porosity slowly decrease toward 20%–25% (moisture content) and ~45% (porosity) at ~460 mbsf, below which no further decrease occurs. This change in consolidation state of the sediment is associated with the significant hiatus identified by biostratigraphic analyses of Cores 339-U1386C-11R and 12R (Fig. **F28**). Cyclic fluctuations are overprinted on the general trends, with marked increases in porosity and moisture content at about 185, 310, and 370–395 mbsf (Fig. **F35**). Increased sand content was noted around 310 and 370–395 mbsf, although a similar relation to coarser sediments is not evident for the high moisture content and porosity at ~185 mbsf.

Grain density is relatively constant for the entire interval drilled at Site U1386, fluctuating between 2.7 and 2.8 g/cm^3 (Fig. **F35**). The only exception is the interval between 400 and 450 mbsf, which has on average slightly higher grain density (constantly above 2.75 g/cm^3) than the other cored intervals. High magnetic susceptibility, characteristic for this interval, might point to a significant contribution of heavy minerals in this turbidite-rich interval (see **"Lithostratigraphy"**). The underlying interval between 460 and 480 mbsf characterized by debrites has grain densities between 2.71 and 2.77 g/cm^3, which are lower than those of the overlying turbidites.

Thermal conductivity

Thermal conductivity was measured once per core using the full-space probe, usually in Section 3 of all cores in Hole U1386A, except Cores 339-U1386A-12H through 17H because of technical problems (Fig. **F36**). Thermal conductivity generally follows reduced porosity and water content in the sediment, with a decrease from ~1.7 W/(m·K) in the uppermost interval to 1.1 W/(m·K) at ~100 mbsf. Because interstitial water is a good thermal conductor, this relation matches expectations. The enhanced scatter below 180 mbsf relates to XCB coring, which generates cracks and core disturbances that affect the accuracy of the thermal conductivity measurements.

Summary of main results

Based on physical property data, distinct intervals were identified that are commonly related to boundaries between the defined lithologic units. The upper ~150 mbsf (physical properties Unit I) are characterized by relatively high, fluctuating NGR and magnetic susceptibility values with a persistent covariation of both parameters with sediment color. Between ~150 and 420 mbsf (physical properties Unit II) this variability decreases and the relation to sediment color is lost. Outstanding, especially in terms of very high magnetic susceptibility, is the interval between 420 and 445 mbsf, physical properties Unit III, corresponding to turbidite-prone deposits. Below 445 mbsf (physical properties Unit IV) low NGR and susceptibility values conform to a shift in the lithology to debrites and turbidites below a major hiatus. The assumed occurrence of the mid-Pleistocene revolution discontinuity at ~250 mbsf is not reflected in a notable change in physical properties.

Geochemistry

Volatile hydrocarbons

Headspace gas analysis was performed as a part of the standard protocol required for shipboard safety and pollution prevention monitoring. In total, 36 headspace samples from Hole U1386A, 9 headspace samples from Hole U1386B, and 10 headspace samples from Hole U1386C (sampling resolution of one per core) were analyzed (Fig. **F37;** Table **T19**). In Hole U1386A, methane (C_1), ethane (C_2), and ethene ($C_{2=}$) were detected. Methane ranges from 6 ppmv near the surface to a maximum of 47,727 ppmv at 41.3 mbsf (Section 339-U1386A-5H-7). At the base of Hole U1386A, methane is 5,963 ppmv. Ethane was first detected also at 41.3 mbsf (Section 5H-7) and ethene at 176.9 mbsf (Section 20H-8). In Hole U1386A, ethane reaches a maximum of 3.5 ppmv at 337.6 mbsf (Section 38X-6). Ethene reaches a maximum of 1.1 ppmv at 337.6 mbsf (Section 38X-6).

In Holes U1386B and U1386C, methane, ethane, and ethene were detected. In Hole U1386B, methane is 11,109 ppmv at 358.1 mbsf, reaches a secondary peak of 8,367.9 ppmv at 428 mbsf, and decreases to 4,691.9 ppmv at the base of Hole U1386B (448.9 mbsf). Ethene ranges between 1.7 ppmv at 358.1 mbsf and 0.5 ppmv at 387.27 mbsf. Ethane was detected in all measured headspace samples from Hole U1386B and ranges between 0.7 and 6 ppmv.

In Hole U1386C, methane is 1191.4 ppmv at 420.6 mbsf and 3968.6 ppmv at the base of the hole at 524.2 mbsf, with a maximum of 5304.3 ppmv at 450.6 mbsf (Section 339-U1386C-10R-6). Ethene varies between 0.4 ppmv and a maximum of 1.3 ppmv at the base of Hole U1386C (524.2 mbsf), whereas ethane varies between 1.3 and 11.5 ppmv.

Sedimentary geochemistry

Sediment samples were collected for analysis of solid-phase geochemistry (inorganic and organic carbon) at a resolution of approximately one sample per core in Holes U1386A–U1386C (Table **T2**). Weight percent $CaCO_3$ varies from 10 to 40 wt% (Fig. **F38;** Table **T2**). Organic carbon is calculated to be between 0.4 and 1.5 wt% (Fig. **F39A;** Table **T2**).

Weight percent nitrogen (Fig. **F39B;** Table **T2**) was measured downhole to 270.8 mbsf and ranges from 0.04 to 0.1 wt%. Total nitrogen variability decreases below ~160 mbsf. The C/N ratio, used to distinguish the origin of organic matter (marine versus terrestrial) in sediment (Emerson and Hedges, 1988; Meyers, 1997), ranges from 7.57 to 25.83 and indicates that the organic carbon is mainly of marine origin with a contribution from terrestrial matter (Fig. **F39C;** Table **T2**). The higher C/N ratios, especially in the uppermost 31 mbsf, are not unexpected given the proximity of Site U1386 to land. Below 31 mbsf, the C/N ratios decrease sharply, ranging from 7.57 to 12.83 and indicating degradation of organic matter at this site (Ruttenberg and Goñi, 1997).

Interstitial water chemistry

Major cations and anions

Whole-round samples were taken downhole for interstitial water analysis from Hole U1386A to 337.5 mbsf and from Hole U1386B to 448.5 mbsf. Biscuiting of XCB cores made proper removal of contamination (i.e., drilling slurry) from whole-round samples progressively more difficult farther downhole. In particular, the presence of sulfate was noted in at least one Hole U1386B sample far below the base of the sulfate reduction zone, which is indicative of contamination by drilling fluid. For this reason, the measurements from Hole U1386B are excluded from the following analysis.

Sulfate concentrations drop markedly in the uppermost part of Hole U1386A, from 28.9 mM for seawater at the seafloor to 20 mM at 3 mbsf to 0 mM at 12.5 mbsf (Fig. **F40A;** Table **T20**), indicating very high rates of sulfate reduction at this site with high sediment accumulation rates. Alkalinity is elevated in the upper 12.5 mbsf, averaging 8–10 meq/L, decreases to ~5 meq/L at 32 mbsf, and remains low downhole to 175 mbsf (Fig. **F40B;** Table **T20**). An alkalinity peak of 8 mM occurs at 187 mbsf followed by a decline to 250 mbsf and an increase to a maximum near the base of Hole U1386A (Fig. **F40B;** Table **T20**). Ammonium concentrations increase rapidly in the upper 32 mbsf and slowly continue to climb to the base of Hole U1386A (Fig. **F40C;** Table **T20**).

The sulfate–methane transition (see discussion in **"Geochemistry"** in the "Site U1385" chapter [Expedition 339 Scientists, 2013c]) is marked by sulfate depletion at 12.5 mbsf and a rise in methane between 12.5 and 22 mbsf (Fig. **F40D**). Methane reaches peak concentrations of 48,000 ppmv at 42 mbsf, decreases downhole to 100 mbsf, and remains relatively low to the bottom of the hole.

Calcium concentrations are 8.5 mM at the surface and decrease rapidly to a minimum of 3.5 mM at 12.5 mbsf (Fig. **F41A;** Table **T20**). Magnesium concentrations decrease from surface values of 50–55 to ~30 mM at 100 mbsf and remain relatively unchanged to the base of Hole U1386A (Fig. **F41B;** Table **T20**). Potassium shows a similar pattern of values decreasing downhole from 11 mM near the surface to ~6 mM near the base of the hole (Fig. **F41C;** Table **T20**).

Chloride concentration decreases downhole from 586 mM near the surface to 569 mM at 60 mbsf. Below 60 mbsf, chloride values are scattered around 570 mM (Fig. U1386-H-F6). Sodium to chloride ratios are all near the seawater value of 0.86, indicating that downhole changes in chloride are not affected by underlying brines (Fig. **F42**).

The observed interstitial water profiles are largely the result of microbially mediated reactions involving organic matter, carbonate diagenesis, and diffusion. Sulfate reduction and methanogenesis are the dominant processes in the upper 100 mbsf. Methane diffusing upward into the sulfate reduction zone is rapidly consumed by anaerobic methane oxidation. Both sulfate reduction and anaerobic methane oxidation produce alkalinity (Gieskes, 1983; Boetius et al, 2000):

$$2CH_2O + SO_4^{2-} \rightarrow 2HCO_3^- + H_2S \text{ and}$$

$$CH_4 + SO_4^{2-} \rightarrow HCO_3^- + HS^- + H_2O.$$

High alkalinity promotes authigenic carbonate precipitation, which explains the minimum in calcium at 12.5 mbsf (Fig. **F41A;** Table **T20**). Calcium and magnesium are negatively correlated with a slope of ~2 (Fig. **F43A;** Table **T20**). Dolomitization of calcite may account for this relationship because one mechanism of dolomite formation involves replacement of half of the Ca^{2+} ions by Mg^{2+}, resulting in removal of magnesium and addition of calcium to interstitial water. Bacterial sulfate reduction can eliminate ion pairing between magnesium and sulfate in sediment pore waters (Katz and Ben-Yaakov, 1980) and create a high-magnesium environment conducive to dolomite formation.

Minor elements

Strontium, barium, and lithium have similar patterns showing increasing concentrations downhole (Fig. **F44A–F44C;** Table **T20**), whereas boron shows an inverse pattern and generally decreases downhole (Fig. **F44D;** Table **T20**). Silicon concentrations range between 100 and 200 µM in the upper 150 m of Hole U1386A and increase to an average of 250 µM below (Fig. **F44E;** Table **T20**). Iron and manganese are below detection limits in all but the uppermost core. Calcium, strontium, barium, and lithium are positively correlated, suggesting they are controlled by similar processes, namely carbonate diagenesis (Figs. **F43B, F44A–F44C**).

Stable isotopes

Samples for stable isotope analysis were collected from the base of each section of every core taken in Hole U1386A for the upper 350 mbsf using a syringe, with the exception of Section 6 in each core where a 5 cm whole-round sample was taken. Rhizon samples were taken from the middle (~75 cm) of Section 6 for comparison. Only the upper 83 mbsf were analyzed shipboard for $\delta^{18}O$ and δD.

Interstitial water $\delta^{18}O$ and δD values increase downhole from bottom water values at the top of Hole U1386A to a broad maximum between ~27 and 55 mbsf (Fig. **F45;** Table **T21**). $\delta^{18}O$ and δD are positively correlated, with a slope that is indistinguishable from the modern $\delta^{18}O$-δD relationship from a nearby hydrographic profile (Fig. **F46**). The downhole peak in $\delta^{18}O$ and δD is suggestive of an increase in the isotopic composition of seawater during the last glacial period, which has been attenuated by diffusion (McDuff, 1984; Schrag and DePaolo, 1993). However, this interpretation is not supported by the downhole chloride profile. Contrary to the expected trend caused by glaciation (Adkins and Schrag, 2001, 2003), chloride concentrations decrease in the upper 50 mbsf where $\delta^{18}O$ and δD increase (Fig. **F45**). The decreasing downhole trend in chloride concentration paired with increases in both $\delta^{18}O$ and δD likely indicates the in situ presence of gas hydrates that dissociated upon sediment recovery (Kastner et al., 1991; Dählmann and de Lange, 2003).

The opposite trends in chloride and water isotopic ratios will need to be investigated further postcruise after chloride measurements are measured at higher resolution.

Summary

The interstitial water profile at Site U1386 is dominated by organic matter diagenesis with a sharp decrease in C/N ratios at ~31 mbsf, a shallow sulfate reduction zone in the uppermost 12.5 mbsf, and methanogenesis below. High alkalinity associated with sulfate reduction and anaerobic methane oxidation has resulted in authigenic calcite and dolomite formation. Iron sulfide minerals formed as a consequence of sulfate reduction. A simultaneous downhole increase in interstitial water $\delta^{18}O$ and δD and decrease in chloride concentration suggests that gas hydrates are present in the sediments at Site U1386 and have dissociated upon core recovery.

Downhole measurements

Logging operations

Downhole logging measurements in Hole U1386C were made after completion of RCB coring to a total depth of 526 m drillers depth below seafloor (DSF). In preparation for logging, the hole was flushed with a 30 bbl sweep of high-viscosity mud and the bit was released at the bottom of the hole. The hole was then displaced with 172 bbl of barite-weighted mud (10.5 ppg), and the pipe was pulled up to 102.4 m DSF. Three tool strings were deployed in Hole U1386C: a modified triple combo, the FMS-sonic, and the VSI (Fig. **F47;** see also **"Downhole measurements"** and Table **T6** in the "Methods" chapter [Expedition 339 Scientists, 2013b] for tool definitions). The triple combo was modified to include both the old phasor dual induction–spherically focused resistivity tool (DIT-SFL) and the new High-Resolution Laterolog Array (HRLA) in order to test the HRLA in low-resistivity formations (see Table **T6** in the "Methods" chapter [Expedition 339 Scientists, 2013b] for tool definitions).

At 1935 h on 7 December 2011, the triple combo tool string (resistivity, density, and NGR tools) descended from the rig floor into the pipe (Fig. **F48**). When the tool string was just below the end of the pipe, the wireline heave compensator (WHC) settings were optimized to minimize downhole tool motion. The downlog proceeded at ~1000 m/h and reached the base of the hole at ~526 mbsf. The hole was logged up to seafloor at 275 m/h. The tool string returned for a short uphole repeat section from 227 to 103 m wireline depth below seafloor.

Rig-up of the FMS-sonic tool string started at 0245 h on 8 December. A downlog was taken at 730 m/h, from which we established the best settings for source frequency and automated *P*-wave velocity picking from the sonic waveforms. The tool string was blocked from further downhole progress by a bridge at 375 mbsf that had been observed in the triple combo run but had now fully closed up. Two uphole passes of the FMS-sonic tool string were run, Pass 1 to the seafloor and Pass 2 to the base of the pipe, both at 550 m/h. Rig-down was completed at 0930 h.

Marine mammal watch for the VSP started at 0800 h. The soft-start of the Sercel G. Gun parallel cluster (two 250 in^3 air guns separated by 1 m) started at 0930 h. The air gun cluster was positioned on the port side of the *JOIDES Resolution* at a water depth of ~7 mbsl with a borehole offset of ~45 m. Before reaching the bottom of the hole, a short uplog was taken from 334 to 290 mbsf to ensure depth accuracy by comparing the shape of the VSI gamma curve to those of the other logging runs. The VSI tool string reached the blocked zone at 369 mbsf, a few meters shallower than the previous tool string. Obtaining a good clamp with the VSI caliper arm was difficult, probably because of the rugose borehole and soft formation, and consequently the received sonic waveforms were noisy. The initial plan was to make check shot stations at 25 m intervals, but because of the variability in borehole diameter, station depths were relocated to where the borehole was smooth and in gauge based on examination of the triple combo caliper curve. Only a fraction of the shots produced clean first arrivals, but enough first arrivals were taken at most stations to stack. A good first arrival pick in the upper part of the hole was especially difficult to obtain.

The log data quality was reduced by washouts and bridging of the borehole wall. Although the borehole had a baseline diameter (10–11 inches) close to the bit size, small- to large-scale washouts were pervasive throughout the logged section (Fig. **F49**). The 406–412 mbsf interval was washed out beyond the limit of the Hostile Environment Litho-Density Sonde (HLDS) caliper, and the narrow section at 376–383 mbsf found during the triple combo run subsequently blocked the hole for the next two tool strings. Resistivity, sonic velocity, and NGR logs were generally robust to changes in hole diameter, although there was some reduction in values in the larger washouts. Density was more affected, with lower density values than core measurements in washouts (Fig. **F49**). The photoelectric effect log has anomalously high values, especially in the washouts, because barium in the logging mud swamped the signal. However, barite-weighted mud was a necessity to keep the borehole open. The FMS resistivity images were also dominated by poor contact with the borehole wall in the washed out areas.

Differences were observed in the seafloor depth given by the step in the gamma radiation logs. The triple combo main pass found seafloor at 575 mbrf and FMS-sonic Pass 2 found it at 570 mbrf, compared to the drillers mudline at 573.2 mbrf (Hole U1386A). The differences were partly due to tides; sea level was at +0.8 m for the triple combo main pass, –0.8 m for FMS-sonic Pass 2, and –0.9 m for the drillers mudline in Hole U1386A (Fig. **F48**). Seas were calm (maximum peak-to-peak heave = 40–50 cm), giving little contribution to the offset, and the hole was relatively shallow, so cable stretch was not an issue either. Some variability is typical in choosing the exact point at which the gamma ray log steps up at the seafloor because it can appear as a gradual change. The remaining difference between the triple combo and FMS-sonic tool string seafloor depths can be attributed to the WHC. A ~43 cm difference exists between the upper and lower extents of the "home" window of the WHC flying head, which translates to a 2.6 m difference in cable length because of the six-wheel pulley system of the compensator. However, a reasonably good depth match between the open-hole NGR logs between logging runs and the core data was achieved using a seafloor depth of 573 mbrf for the triple combo tool string main pass and 570 mbrf for the second pass of the FMS-sonic tool string.

Logging units

Hole U1386C downhole logs have moderately high amplitude variability on a several-meter to submeter scale, and the character of the logs changes gradually downhole with no major steps in the base levels. Therefore, the entire logged interval was assigned to one logging unit (Fig. **F49**). At the scale of this unit, the NGR signal typically ranges from 50 to 70 gAPI and is dominated by the radioactivity of potassium and thorium, with uranium contributing a relatively minor component (Fig. **F50**). Potassium and thorium curves are closely correlated. Both elements are found in clay minerals. Quartz, calcite, and illite comprise as much as >80% of the sediment at Site U1386 based on bulk XRD analyses (see **"Lithostratigraphy"**), so the NGR signal is primarily tracking clay content (quartz and calcite contain no radioactive elements). Minerals like K-feldspar and mica also contribute to the NGR signal. Density and sonic velocity logs increase downhole, reflecting sediment compaction with depth. Low density values generally correspond to intervals with borehole enlargements and lower NGR values.

Logging Unit 1 was divided into three subunits based on changes in mineralogy inferred from the potassium log, a change in character of the density log, and the onset of lithification.

Logging Subunit 1A: base of drill pipe to 346 mbsf

The upper logging subunit is characterized by medium-amplitude cyclic swings in bulk density, NGR (including uranium, thorium, and potassium components), resistivity, and sonic velocity values. Several orders of cycles are observed, varying from 1 m to several tens of meters in thickness (Fig. **F49**). The potassium and thorium concentrations co-vary closely, suggesting that clay content controls these logs. The uranium concentrations generally vary independently or are anticorrelated. As expected from downhole compaction, the resistivity, density, and sonic velocity logs have an increasing downhole trend and are generally well correlated.

Logging Subunit 1B: 346–464 mbsf

Logging Subunit 1B is distinguished from the subunit above by its higher potassium content, which reaches a maximum of 2.2% at 382.5 mbsf (Fig. **F50**). The thorium content is relatively comparable to Subunit 1A, suggesting that overall clay content remains similar but additional potassium-bearing minerals are present (see **"Lithostratigraphy"**) (e.g., K-feldspar, mica, and glauconite, which contains potassium but only low levels of thorium compared to other clay minerals). Subunit 1B is also characterized by a reduction in the number of thin washouts, and consequently the short wavelength variability disappears from the density log, but the longer wavelength swings remain. NGR continues to show cyclic variability. A large decrease to anomalously low values in all logs between 406 and 412 mbsf is due to a 6 m thick washed out level, wider than the 18 inch limit of the HLDS caliper arm, that possibly reflects a loose coarse-grained interval (pebbly sand was recovered at the same depth in Section 339-U1386B-45X-CC). An interval of higher resistivity is observed from 422 to 425 mbsf and probably correlates to cores with a cemented sandy interval (Cores 339-U1386B-6R through 8R). Resistivity returns to lower values downhole and corresponds to unconsolidated intervals. The transition between logging Subunits 1A and 1B does not correlate with any major changes in sediment deposits or faunal assemblages (see **"Lithostratigraphy"** and **"Biostratigraphy"**). It is close to the top of the termination of the Jaramillo Subchron (C1r.1n), identified in Hole U1386A at ~344.6 mbsf (Section 339-U1386A-39X-4) and in Hole U1386B at ~347.9 mbsf (Section 339-U1386B-39X-6) (see **"Paleomagnetism"**), providing an age of ~0.988 Ma.

Logging Subunit 1C: 464–526 mbsf

Several intervals of high resistivity values are observed in Subunit 1C at 465–475 and 478–481 mbsf (Fig. **F49**). These high values likely represent the onset of more pervasive lithification and correlate with cemented bioclastic turbidites and debrites (Cores 399-U1386C-12R through 15R; see **"Lithostratigraphy"**). In addition to the presence of sands, the abundance of shell fragments in this interval may dilute the clay fraction and therefore contribute to the lower gamma content observed in the same interval. Potassium contents return to values similar to Subunit 1A. The transition between logging Subunits 1B and 1C corresponds to a major hiatus of at least 1.4 m.y. identified between Sections 339-U1386C-11R-CC and 12R-1 by biostratigraphic analysis (see **"Biostratigraphy"**).

Comparison of the HRLA and DIT-SFL resistivity logs

The Schlumberger HRLA resistivity tool (Griffiths et al., 2000) was run in high-resistivity ocean crust on the two most recent *JOIDES Resolution* IODP expeditions (335 and 336) but until now has not been run in unconsolidated sediments. Previous generations of laterolog, such as the Dual Laterolog, were not designed for low-resistivity unlithified sedimentary formations such as those encountered during IODP expeditions. However, the HRLA measurement range extends to low resistivities and therefore is likely to be suitable for IODP use. In Hole U1386C, we obtained both HRLA and DIT-SFL resistivity logs in order to compare absolute resistivity values, vertical resolutions, and effects of washouts.

Overall, the two sets of logs show the same resistivity trends and fluctuations in Hole U1386C (Figs. **F49, F51**). The higher vertical resolution of the HRLA is apparent in the deep-reading logs from both tools (deep resistivity [RLA5] from the HRLA and deep induction resistivity [IDHP] from the DIT-SFL; Fig. **F49**). RLA5 has a ~30 cm vertical resolution, compared to ~240 cm for IDPH, and IDPH follows almost exactly the lower envelope of RLA5 resistivity values. Zooming in on an example interval, 250–300 mbsf (Fig. **F51**), the shallow-reading logs from both tools have lower resistivity values than the deep-reading logs, as expected, because the shallow-reading logs sample proportionately more seawater and less formation than the deep-reading logs. For the shallowest reading logs (spherically focused resistivity [SFLU] from the DIT-SFL and RLA1 from the HRLA), RLA1 has very slightly higher values and a higher vertical resolution than SFLU. The separation of the shallow and deep HRLA log values is much reduced where the borehole diameter is in gauge (e.g., 285 mbsf) and expanded where the hole is washed out (e.g., 259 mbsf) or rugose (e.g., 268 mbsf), as is also the case for the DIT-SFL. The vertical resolution of the HRLA logs does not appear to drop off for the deeper reading measurements, as is the case for the DIT-SFL logs. The features in the HRLA resistivity logs were cross-checked against the velocity logs. The same features match very well in both (Fig. **F51**).

Formation MicroScanner images

Despite the rugosity of the borehole wall associated with the presence of washout intervals, FMS resistivity images reveal numerous gradual and sharp transitions between alternations of resistive and conductive beds larger than ~5 cm. Most of these alternations correlate well with the resistivity curves from the triple combo tool string (Fig. **F52**), but the FMS images also reveal stratigraphic information at a finer spatial resolution than the standard resistivity logs. Where the silty sand layers correlate with lower values in the gamma ray log (see ~341 and 362 mbsf in Fig. **F52**), the FMS images illustrate smallest scale changes in the sediment electrical properties that may be related to the subtle changes in clay content or in sediment hardness (see for example several-centimeter thick, light–dark alternations from 345 and 354 mbsf in Fig. **F52**). Inclined bedding (appearing as sinusoids) at slight angle is observed at some depths. It will be possible to measure dip directions and angle.

Cyclicity

Figure **F53** illustrates the cyclic nature of the sediment record, which alternates between high and low gamma ray log values at intervals of 5–10 m. As a first rough estimate of the average duration of these alternations, the cycles in Subunit 1A were counted. For the 102–346 mbsf interval, ~35 alternations in the potassium curve (average thickness = ~7 m) occur over an interval of ~700 k.y. (based on a mean sedimentation rate of 0.35 m/k.y., see **"Biostratigraphy"** and **"Paleomagnetism"**). This gives an average duration of approximately 20 k.y. for each cycle, which is close to the orbital precession Milankovitch cycle (~19 and 23 k.y. periodicity). Given the uncertainties in the initial age estimates, the probability that all cycles are not recorded equally well in the sediment record, and the subjective nature of counting cycles, this early estimate requires further verification. However, it certainly seems reasonable that precession-band variability is recorded at Site U1386. Nearby in the Gulf of Cádiz, gamma ray and sonic log cyclic patterns have been observed in lower Pliocene sediments, where they were tuned to eccentricity-modulated precession cycles of the 65°N summer insolation curve (Sierro et al., 2000).

Vertical seismic profile and sonic velocity

One objective of the expedition was to establish the age and lithologic origin of the seismic reflections previously identified in seismic sections. The VSP, traveltime derived from the sonic velocity log, and synthetic seismograms provide three ways of making these correlations between the stratigraphy and the seismic sections.

Although many of the sonic waveforms recorded downhole during the VSP were noisy, 12 out of the 14 stations yielded check shot traveltimes, ranging from 0.9224 s two-way traveltime (TWT) at 143.2 mbsf to 1.1604 s TWT at the deepest station at 369.4 mbsf (Fig. **F54;** Table **T22**). Sonic traveltimes were also calculated from the sonic log velocities, which give two-way traveltimes within 0.01 s of those from the VSP. Sonic velocities (104–354 mbsf) increase downhole with a linear trend of ~0.1 km/s per 100 m. Extrapolating this trend to the base of the hole, the interval velocity yields an estimate for 526 m of 1.309 s TWT (0.569 s below the seafloor reflection). This is not an ideal method, but in the absence of velocity data from the lowermost 172 m of the hole, it is a simple assumption. The boundary between logging Subunits 1B and 1C at 464 m (a hiatus in the core) is at 1.2485 s TWT, which correlates well with a previously defined unconformity by Llave et al. (2001, 2007, 2011). The similarity of the resistivity logs to the sonic velocity log (Fig. **F49**) offers the potential for a "pseudosonic" log to be constructed from the resistivity data to the base of the hole and used as input for a synthetic seismogram.

Heat flow

Twelve APCT-3 downhole temperature measurements in Holes U1386A and U1386B ranged from 13.56°C at 16.8 mbsf to 18.88°C at 167.2 mbsf (Table **T23**), giving a geothermal gradient of 34.3°C/km (Fig. **F36**). The measurements increase linearly with depth, and the trend line intersects the seafloor at 13.1°C. The linearity over this depth range indicates fairly steady temperature conditions on the century scale, and that MOW bottom water at this location and depth has been historically at a steady temperature of ~13°C. Oceanographic measurements indicate that MOW has warmed and become saltier over the last few decades: deep MOW has warmed by 0.3°C over 20 y (Millot et al., 2006) and by 0.5°C over 50 y (Potter and Lozier, 2004). Unfortunately, at Site U1386 the bottom water temperature was difficult to determine accurately from the 12 APCT-3 temperature profiles. The average of the minimum temperature in the profiles differed significantly between Holes U1386A and U1386B (12.79° and 13.65°C, respectively). The traditional method of estimating seafloor temperature, the average temperature while the APCT-3 is held at the mudline, yields 14.06° and 14.00°C for the two holes. Typically, bottom water will be colder than the measured water in the pipe, so the coldest temperature in the APCT-3 profile is normally more representative because of the time needed for temperature equilibration.

Thermal conductivity under in situ conditions was estimated from laboratory-determined thermal conductivity using the method of Hyndman et al. (1974) (see **"Physical properties"** in the "Methods" chapter [Expedition 339 Scientists, 2013b]). The calculated in situ values average 0.5% below the measured laboratory values. Thermal resistance was calculated by integrating the inverse of in situ thermal conductivity over depth (Fig. **F36**). A heat flow of 42.1 mW/m^2 was obtained from the linear fit between temperature and thermal resistance (Fig. **F36**) (Pribnow et al., 2000). This value is in the lower half of the normal range for heat flow on the Portuguese margin (Grevemeyer et al., 2009).

Stratigraphic correlation

The meters composite depth (mcd) scale for Site U1386 was based primarily on correlation of magnetic susceptibility between holes. NGR and GRA density data provided confirmation of the correlation in some intervals and were used as constraints in other intervals where the magnetic susceptibility was low or lacked correlative features. GRA density provided the primary constraint for the first core in each hole. Both cores recovered the mudline, but Core 339-U1386B-1H was shifted (expanded) on average downhole by ~11 cm relative to Core 339-U1386A-1H. The density anomalies could only be correlated well with each other downhole to ~30 mcd.

The correlation is relatively straightforward downhole to 70 mcd but has several uncertain links between cores below this depth (Fig. **F55**). The first of these uncertainties is with the connection between the base of Core 339-U1386A-8H and the top of Core 339-U1386B-8H. The lack of distinct susceptibility or density anomalies and the relatively broad NGR anomaly in this junction only constrain the correlation to within about ±50 cm. The connection between the base of Core 339-U1386B-10H and the top of Core 339-U1386A-11H is uncertain because of coring disturbance, which is severe over most of Core 339-U1386A-11H. Correlation below ~110 mcd, which is just below the interval in Cores 339-U1386A-12H and 339-U1386B-11H that contains a sequence of very distinctive cyclic susceptibility anomalies, is much more uncertain. Part of the uncertainty arises from real coring gaps and part from coring disturbance, as virtually all XCB cores are partially disturbed, with the disturbance often consisting of the ubiquitous occurrence of coring biscuits (see **"Lithostratigraphy"**).

To achieve a composite depth scale beyond 110 mcd, we first shifted the cores with a constant growth factor of 1.11 for the three holes at Site U1386, indicating an 11% increase in mcd values relative to meters below seafloor (mbsf) values (Fig. **F56**). This growth factor fits the upper part of the sequence. Subsequently, we shifted the individual cores upward or downward for the best correlation between both holes, taking into account that successive cores in each hole do not overlap (Table **T24**). When no apparent correlation existed between the base of one core and the top of the next in the parallel hole, the lower core (the one deeper in the mbsf scale) was appended to the base of the one above. Given the lack of evidence for overlap, appending cores to each other improves the odds that the spliced section will contain a complete section, albeit with the possibility of some duplication. Some serious difficulties are posed, however, by incomplete cores or cores with no recovery (e.g., Cores 339-U1386A-25X and 339-U1386B-20X) and conflicting magnetic susceptibility values between parallel cores (e.g., Cores 339-U1386A-24X, 339-U1386B-23X, and 339-U1386C-4R). In these cases, the comparison between NGR and logging HSGR data was used to improve construction of the composite record.

The three holes cored at Site U1386 provide enough material to produce a splice with relatively few gaps within the upper 390 m of the section (Table **T25**). Below this depth, most of the section is single-cored, with coring gaps undoubtedly occurring between each core (Fig. **F55**). Where possible, we avoided including intervals in the splice that were disturbed significantly by drilling, voids, and interstitial water samples (Table **T14**). In addition, all magnetic susceptibility data were cleaned for the top of each section and measurement outliers (Table **T26**).

To facilitate a direct comparison of the highly expanded spliced record of Site U1386 with the original mbsf scale, we transferred the mcd scale to mbsf values (i.e., mbsf*) by applying both a linear regression fit through the core tops of all holes (Fig. **F57**) and forcing the fit line through the origin (i.e., at zero mcd and mbsf*), revealing an average compression factor of 0.9006472906.

Finally, to test the robustness of our spliced record, we compared the NGR core data in Holes U1386A and U1386B with the logging HSGR data of Hole U1386C (Fig. **F58**). Because of its relatively low resolution (~20 cm), we included all NGR measurements in both holes and plotted them on the mbsf* depth scale, using a five-point moving average. The HSGR data are plotted on the logging mbsf scale, which was directly derived from the tool string. Characteristic features within both records between 100 mbsf (top of the logging operations) and 380 mbsf clearly correlate to one another, suggesting that the spliced core data contains an almost continuous stratigraphic succession. The minor misalignment between NGR and HSGR anomalies are caused by very small differences between the logging mbsf and the mbsf* depth scales, which can be resolved using a few tie points (Figs. **F58, F59**). Evidently, the comparison of NGR and HSGR data illustrates that the spliced section is virtually complete downhole to 380 mbsf*, providing a useful guide for postcruise studies to plan sampling strategies.

References

Adkins, J.F., and Schrag, D.P., 2001. Pore fluid constraints on deep ocean temperature and salinity during the Last Glacial Maximum. *Geophys. Res. Lett.,* 28(5):771–774. **doi:10.1029/2000GL011597**

Adkins, J.F., and Schrag, D.P., 2003. Reconstructing Last Glacial Maximum bottom water salinities from deep-sea sediment pore fluid profiles. *Earth Planet Sci. Lett.,* 216(1–2):109–123. **doi:10.1016/S0012-821X(03)00502-8**

Alvarez Zarikian, C.A., Stepanova, A.Y., and Grützner, J., 2009. Glacial–interglacial variability in deep sea ostracod assemblage composition at IODP Site U1314 in the subpolar North Atlantic. *Mar. Geol.,* 258(1–4):69–87. **doi:10.1016/j.margeo.2008.11.009**

Alves, T.M., Gawthorpe, R.L., Hunt, D.W., and Monteiro, J.H., 2003. Cenozoic tectono-sedimentary evolution of the western Iberian margin. *Mar. Geol.*, 195(1–4):75–108. **doi:10.1016/S0025-3227(02)00683-7**

Bayliss, D.D., 1969. The distribution of *Hyalinea balthica* and *Globorotalia truncatulinoides* in the type Calabrian. *Lethaia,* 2(2):133–143. **doi:10.1111/j.1502-3931.1969.tb01632.x**

Blum, P., 1997. Physical properties handbook: a guide to the shipboard measurement of physical properties of deep-sea cores. *ODP Tech. Note,* 26. **doi:10.2973/odp.tn.26.1997**

Boetius, A., Ravenschlag, K., Schubert, C.J., Rickert, D., Widdel, F., Gieseke, A., Amann, R., Jørgensen, B.B., Witte, U., and Pfannkuche, O., 2000. A marine microbial consortium apparently mediating anaerobic oxidation of methane. *Nature (London, U. K.),* 407(6804):623–626. **doi:10.1038/35036572**

Cronin, T.M., 1983. Bathyal ostracodes from the Florida-Hatteras slope, the straits of Florida, and the Blake Plateau. *Mar. Micropaleontol.,* 8(2):89–119. **doi:10.1016/0377-8398(83)90007-5**

Cronin, T.M., DeMartino, D.M., Dwyer, G.S., and Rodriguez-Lazaro, J., 1999. Deep-sea ostracode species diversity: response to late Quaternary climate change. *Mar. Micropaleontol.,* 37(3–4):231–249. **doi:10.1016/S0377-8398(99)00026-2**

Dählmann, A., and de Lange, G.J., 2003. Fluid–sediment interactions at eastern Mediterranean mud volcanoes: a stable isotope study from ODP Leg 160. *Earth Planet. Sci. Lett.,* 212(3–4):377–391. **doi:10.1016/S0012-821X(03)00227-9**

Desprat, S., Sánchez Goñi, M.F., Naughton, F., Turon, J.-L., Duprat, J., Malaizé, B., Cortijo, E., and Peypouquet, J.-P., 2007. Climate variability of the last five isotopic interglacials: direct land-sea-ice correlation from the multiproxy analysis of north-western Iberian margin deep-sea cores. *In* Sirocko, F., Claussen, M., Sánchez Goñi, M.F., and Litt, T. (Eds.), *The Climate of Past Interglacials.* Dev. Quat. Sci., 7:375–386. **doi:10.1016/S1571-0866(07)80050-9**

Egbert, G.D., and Erofeeva, S.Y., 2002. Efficient inverse modeling of barotropic ocean tides. *J. Atmos. Oceanic Technol.,* 19(2):183–204. **doi:10.1175/1520-0426(2002)019<0183:EIMOBO>2.0.CO;2**

Emerson, S., and Hedges, J.I., 1988. Processes controlling the organic carbon content of open ocean sediments. *Paleoceanography,* 3(5):621–634. **doi:10.1029/PA003i005p00621**

Expedition 339 Scientists, 2013a. Methods. *In* Stow, D.A.V., Hernández-Molina, F.J., Alvarez Zarikian, C.A., and the Expedition 339 Scientists, *Proc. IODP,* 339: Tokyo (Integrated Ocean Drilling Program Management International, Inc.). **doi:10.2204/iodp.proc.339.102.2013**

Expedition 339 Scientists, 2013b. Site U1385. *In* Stow, D.A.V., Hernández-Molina, F.J., Alvarez Zarikian, C.A., and the Expedition 339 Scientists, *Proc. IODP,* 339: Tokyo (Integrated Ocean Drilling Program Management International, Inc.). **doi:10.2204/iodp.proc.339.103.2013**

Faugères, J.-C., Frappa, M., Gonthier, E., de Resseguier, A., and Stow, D., 1985a. Modelé et facies de type contourite à la surface d'une ride sédimentaire édifiée par des courants issus de la veine d'eau méditerranéenne (ride du Faro, Golfe de Cadix). *Bull. Soc. Geol. Fr.*, 1(1):35–47.

Faugères, J.-C., Frappa, M., Gonthier, E., and Grousset, F., 1985b. Impact de la veine deau méditerranéenne sur la sedimentation de la marge sud et ouest Iberique au Quaterbaire recent. *Bull. Inst. Geol. Bassin Aquitaine,* 37:259–287.

Faugères, J.C., Mézerais, M.L., and Stow, D.A.V., 1993. Contourite drift types and their distribution in the North and South Atlantic Ocean basins. *Sediment. Geol.,* 82(1–4):189–203. **doi:10.1016/0037-0738(93)90121-K**

Flores, J.-A., Colmenero-Hidalgo, E., Mejía-Molina, A.E., Baumann, K.-H., Hendericks, J., Larsson, K., Prabhu, C.N., Sierro, F.J., and Rodrigues, T., 2010. Distribution of large *Emiliania huxleyi* in the central and northeast Atlantic as a tracer of surface ocean dynamics during the last 25,000 years. *Mar. Micropaleontol.,* 76(3–4):53–66. **doi:10.1016/j.marmicro.2010.05.001**

García, M., Hernández-Molina, F.J., Llave, E., Stow, D.A.V., León, R., Fernández-Puga, M.C., Díaz del Río, V., and Somoza, L., 2009. Contourite erosive features caused by the Mediterranean Outflow Water in the Gulf of Cádiz: Quaternary tectonic and oceanographic implications. *Mar. Geol.*, 257(1–4):24–40 **doi:10.1016/j.margeo.2008.10.009**

Gieskes, J.M., 1983. The chemistry of interstitial waters of deep sea sediments: interpretation of deep sea drilling data. *In* Riley, J.P., and Chester, R. (Eds.), *Chemical Oceanography* (Vol. 8): London (Academic), 221–269.

Gonthier, E.G., Faugeres, J.C., and Stow, D.A.V., 1984. Contourite facies of the Faro Drift, Gulf of Cádiz. *In* Stow, D.A.V., and Piper, D.J.W. (Eds.), *Fine-Grained Sediments: Deep Water Processes and Facies.* Geol. Soc. Spec. Publ., 15:275–292. **doi:10.1144/GSL.SP.1984.015.01.18**

Grevemeyer, I., Kaul, N., and Kopf, A., 2009. Heat flow anomalies in the Gulf of Cadiz and off Cape San Vincente, Portugal. *Mar. Pet. Geol.,* 26(6):795–804. **doi:10.1016/j.marpetgeo.2008.08.006**

Griffiths, R., Barber, T.D., and Faivre, O., 2000. Optimal evaluation of formation resistivities using array induction and array laterolog tools. *Trans. SPWLA Annu. Logging Symp.,* 41:BBB. (Abstract)

Habgood, E.L., Kenyon, N.H., Masson, D.G., Akhmetzhanov, A., Weaver, P.P.E., Gardner, J., and Mulder, T., 2003. Deep-water sediment wave fields, bottom current sand channels, and gravity flow channel-lobe systems: Gulf of Cádiz, NE Atlantic. *Sedimentology,* 50(3):483–510. **doi:10.1046/j.1365-3091.2003.00561.x**

Hanquiez, V., Mulder, T., Lecroart, P., Gonthier, E., Marchès, E., and Voisset, M., 2007. High resolution seafloor images in the Gulf of Cádiz, Iberian margin. *Mar. Geol.,* 246(1):42–59. **doi:10.1016/j.margeo.2007.08.002**

Hayward, B.W., 2002. Late Pliocene to middle Pleistocene extinctions of deep-sea benthic foraminifera ("*Stilostomella* extinction") in the southwest Pacific. *J. Foraminiferal Res.,* 32(3):274–307. **doi:10.2113/32.3.274**

Hernández-Molina, F.J., Llave, E., Somoza, L., Fernández-Puga, M.C., Maestro, A., León, R., Medialdea, T., Barnolas, A., García, M., Díaz del Río, V., Fernández-Salas, L.M., Vázquez, J.T., Lobo, F., Alveirinho Dias, J.M., Rodero, J., and Gardner, J., 2003. Looking for clues to paleoceanographic imprints: a diagnosis of the Gulf of Cádiz contourite depositional systems. *Geology,* 31(1):19–22. **doi:10.1130/0091-7613(2003)031<0019:LFCTPI>2.0.CO;2**

Hernández-Molina, F.J., Llave, E., Stow, D.A.V., García, M., Somoza, L., Vázquez, J.T., Lobo, F.J., Maestro, A., Díaz del Río, V., León, R., Medialdea, T., and Gardner, J., 2006. The contourite depositional system of the Gulf of Cádiz: a sedimentary model related to the bottom current activity of the Mediterranean Outflow Water and its interaction with the continental margin. *Deep-Sea Res., Part II,* 53(11–13):1420–1463. **doi:10.1016/j.dsr2.2006.04.016**

Hilgen, F.J., 1991. Extension of the astronomically calibrated (polarity) time scale to the Miocene/Pliocene boundary. *Earth Planet. Sci. Lett.,* 107(2):349–368. **doi:10.1016/0012-821X(91)90082-S**

Hsü, K.J., Cita, M.B., and Ryan, W.B.F., 1973. The origin of the Mediterranean evaporites. *In* Ryan, W.B.F., Hsü, K.J., et al., *Init. Repts. DSDP,* 13: Washington, DC (U.S. Govt. Printing Office), 1203–1231. **doi:10.2973/dsdp.proc.13.143.1973**

Hyndman, R.D., Erickson, A.J., and Von Herzen, R.P., 1974. Geothermal measurements on DSDP Leg 26. *In* Davies, T.A., Luyendyk, B.P., et al., *Init. Repts. DSDP,* 26: Washington, DC (U.S. Govt. Printing Office), 451–463. **doi:10.2973/dsdp.proc.26.113.1974**

Joannin, S., Bassinot, F., Combourieu Nebout, N., Peyron, O., and Beaudoin, C., 2011. Vegetation response to obliquity and precession forcing during the mid-Pleistocene transition in western Mediterranean region (ODP Site 976). *Quat. Sci. Rev.,* 30(3–4):280–297. **doi:10.1016/j.quascirev.2010.11.009**

Kaiho, K., 1999. Effect of organic carbon flux and dissolved oxygen on the benthic foraminiferal oxygen index (BFOI). *Mar. Micropaleontol.,* 37(1):67–76. **doi:10.1016/S0377-8398(99)00008-0**

Kastner, M., Elderfield, H., and Martin, J.B., 1991. Fluids in convergent margins: what do we know about their composition, origin, role in diagenesis and importance for oceanic chemical fluxes? *Philos. Trans. R. Soc. London, Ser. A,* 335(1638):243–259. **doi:10.1098/rsta.1991.0045**

Katz, A., and Ben-Yaakov, S., 1980. Diffusion of seawater ions, Part II. The role of activity coefficients and ion pairing. *Mar. Chem.,* 8(4):263–280. **doi:10.1016/0304-4203(80)90016-X**

Kawagata, S., Hayward, B.W., Grenfell, H.R., and Sabaa, A., 2005. Mid-Pleistocene extinction of deep-sea foraminifera in the North Atlantic Gateway (ODP Sites 980 and 982). *Palaeogeogr., Palaeoclimatol., Palaeoecol.,* 221(3–4):267–291. **doi:10.1016/j.palaeo.2005.03.001**

Kenyon, N.H., and Belderson, R.H., 1973. Bed forms of the Mediterranean undercurrent observed with side-scan sonar. *Sediment. Geol.,* 9(2):77–99. **doi:10.1016/0037-0738(73)90027-4**

Kirschvink, J.L., 1980. The least-squares line and plane and the analysis of palaeomagnetic data. *Geophys. J. R. Astron. Soc.,* 62(3):699–718. **doi:10.1111/j.1365-246X.1980.tb02601.x**

Leckie, R.M., and Olson, H.C., 2003. Foraminifera as proxies of sea-level change on siliciclastic margins. *In* Olson, H.C., and Leckie, R.M. (Eds.), *Micropaleontologic Proxies of Sea-Level Change and Stratigraphic Discontinuities.* Spec. Publ.—SEPM (Soc. Sediment. Geol.), 75:5–19.

Llave, E., Hernández-Molina, F.J., Somoza, L., Díaz del Río, V., Stow, D.A.V., Maestro, A., and Alveirinho Dias, J.M., 2001. Seismic stacking pattern of the Faro-Albufeira contourite system (Gulf of Cádiz): a Quaternary record of paleoceanographic and tectonic influences. *Mar. Geophys. Res.*, 22(5–6):487–508. **doi:10.1023/A:1016355801344**

Llave, E., Hernández-Molina, F.J., Somoza, L., Stow, D.A.V., and Díaz Del Río, V., 2007. Quaternary evolution of the contourite depositional system in the Gulf of Cádiz. *Geol. Soc. Spec. Publ.*, 276:49–79. **doi:10.1144/GSL.SP.2007.276.01.03**

Llave, E., Matias, H., Hernández-Molina, F.J., Ercilla, G., Stow, D.A.V., and Medialdea, T., 2011. Pliocene–Quaternary contourites along the northern Gulf of Cadiz margin: sedimentary stacking pattern and regional distribution. *Geo-Mar. Lett.*, 31(5–6):377–390. **doi:10.1007/s00367-011-0241-3**

Llave, E., Schönfeld, J., Hernández-Molina, F.J., Mulder, T., Somoza, L., Díaz del Río, V., and Sánchez-Almazo, I., 2006. High-resolution stratigraphy of the Mediterranean outflow contourite system in the Gulf of Cádiz during the late Pleistocene: the impact of Heinrich events. *Mar. Geol.*, 227(3–4):241–262. **doi:10.1016/j.margeo.2005.11.015**

Lourens, L., Hilgen, F., Shackleton, N.J., Laskar, J., and Wilson, D., 2004. The Neogene period. *In* Gradstein, F.M., Ogg, J.G., and Smith, A. (Eds.), *A Geologic Time Scale 2004:* Cambridge (Cambridge Univ. Press), 409–440.

Marchès, E., Mulder, T., Cremer, M., Bonnel, C., Hanquiez, V., Gonthier, E., and Lecroart, P., 2007. Contourite drift construction influenced by capture of Mediterranean Outflow Water deep-sea current by the Portimão submarine canyon (Gulf of Cádiz, South Portugal). *Mar. Geol.*, 242(4):247–260. **doi:10.1016/j.margeo.2007.03.013**

McDuff, R.E., 1985. The chemistry of interstitial waters, Deep Sea Drilling Project Leg 86. *In* Heath, G.R., Burckle, L.H., et al., *Init. Repts. DSDP,* 86: Washington, DC (U.S. Govt. Printing Office), 675–687. **doi:10.2973/dsdp.proc.86.131.1985**

Meyers, P.A., 1997. Organic geochemical proxies of paleoceanographic, paleolimnologic, and paleoclimatic processes. *Org. Geochem.*, 27(5–6):213–250. **doi:10.1016/S0146-6380(97)00049-1**

Millot, C., Candela, J., Fuda, J.-L., and Tber, Y., 2006. Large warming and salinification of the Mediterranean outflow due to changes in its composition. *Deep-Sea Res., Part I,* 53(4):656–666. **doi:10.1016/j.dsr.2005.12.017**

Mulder, T., Voisset, M., Lecroart, P., Le Drezen, E., Gonthier, E., Hanquiez, V., Faugères, J.-C., Habgood, E., Hernandez-Molina, F.J., Estrada, F., Llave-Barranco, E., Poirier, D., Gorini, C., Fuchey, Y., Volker, A., Freitas, P., Lobo Sanchez, F., Fernandez, L.M., and Morel, J., 2003. The Gulf of Cádiz: an unstable giant contouritic levee. *Geo-Mar. Lett.*, 23(1):7–18. **doi:10.1007/s00367-003-0119-0**

Murray, J.W., 2006. *Ecology and Applications of Benthic Foraminifera*: Cambridge (Cambridge Univ. Press).

Nelson, C.H., Baraza, J., Maldonado, A., Rodero, J., Escutia, C., and Barber, J.H., Jr., 1999. Influence of the Atlantic inflow and Mediterranean outflow currents on late Quaternary sedimentary facies of Gulf of Cádiz continental margin. *Mar. Geol.*, 155(1–2):99–129. **doi:10.1016/S0025-3227(98)00143-1**

Nelson, C.H., and Maldonado, A., 1999. The Cadiz margin study off Spain: an introduction. *Mar. Geol.,* 155(1–2):3–8. **doi:10.1016/S0025-3227(98)00138-8**

Potter, R.A., and Lozier, M.S., 2004. On the warming and salinification of the Mediterranean Outflow Waters in the North Atlantic. *Geophys. Res. Lett.,* 31(1):L01202. **doi:10.1029/2003GL018161**

Pribnow, D., Kinoshita, M., and Stein, C., 2000. *Thermal Data Collection and Heat Flow Recalculations for Ocean Drilling Program Legs 101–180:* Hanover, Germany (Inst. Joint Geosci. Res., Inst. Geowiss. Gemeinschaftsauf. [GGA]). **http://www-odp.tamu.edu/publications/heatflow/ODPReprt.pdf**

Raffi, I., Backman, J., Fornaciari, E., Pälike, H., Rio, D., Lourens, L., and Hilgen, F., 2006. A review of calcareous nannofossil astrobiochronology encompassing the past 25 million years. *Quat. Sci. Rev.,* 25(23–24):3113–3137. **doi:10.1016/j.quascirev.2006.07.007**

Raffi, I., Backman, J., Rio, D., and Shackleton, N.J., 1993. Plio–Pleistocene nannofossil biostratigraphy and calibration to oxygen isotope stratigraphies from Deep Sea Drilling Project Site 607 and Ocean Drilling Program Site 677. *Paleoceanography,* 8(3):387–408. **doi:10.1029/93PA00755**

Rogerson, M., Rohling, E.J., Weaver, P.P.E., and Murray, J.W., 2005. Glacial to interglacial changes in the settling depth of the Mediterranean outflow plume. *Paleoceanography,* 20(3):PA3007. **doi:10.1029/2004PA001106**

Roque, C., Duarte, H., Terrinha, P., Valadares, V., Noiva, J., Cachão, M., Ferreira, J., Legoinha, P., and Zitellini, N., 2012. Pliocene and Quaternary depositional model of the Algarve margin contourite drifts (Gulf of Cádiz, SW Iberia): seismic architecture, tectonic control, and paleoceanographic insights. *Mar. Geol.,* 303–306:42–62. **doi:10.1016/j.margeo.2011.11.001**

Ruttenberg, K.C., and Goñi, M.A., 1997. Phosphorus distribution, C:N:P ratios, and $\delta^{13}C_{oc}$ in arctic, temperate, and tropical coastal sediments: tools for characterizing bulk sedimentary organic matter. *Mar. Geol.,* 139(1–4):123–145. **doi:10.1016/S0025-3227(96)00107-7**

Schönfeld, J., 1997. The impact of the Mediterranean Outflow Water (MOW) on benthic foraminiferal assemblages and surface sediments at the southern Portuguese continental margin. *Mar. Micropaleontol.*, 29(3–4):211–236. **doi:10.1016/S0377-8398(96)00050-3**

Schönfeld, J., 2002. Recent benthic foraminiferal assemblages in deep high-energy environments from the Gulf of Cádiz (Spain). *Mar. Micropaleontol.*, 44(3–4):141–162. **doi:10.1016/S0377-8398(01)00039-1**

Schönfeld, J., and Zahn, R., 2000. Late glacial to Holocene history of the Mediterranean outflow. Evidence from benthic foraminiferal assemblages and stable isotopes at the Portuguese margin. *Palaeogeogr., Palaeoclimatol., Pal-*

aeoecol., 159(1–2):85–111. **doi:10.1016/S0031-0182(00)00035-3**

Schrag, D.P., and DePaolo, D.J., 1993. Determination of $\delta^{18}O$ of seawater in the deep ocean during the Last Glacial Maximum. *Paleoceanography,* 8(1):1–6. **doi:10.1029/92PA02796**

Sierro, F.J., Hernandez-Almeida, I., Alonso-Garcia, M., and Flores, J.A., 2009. Data report: Pliocene–Pleistocene planktonic foraminifer bioevents at IODP Site U1313. *In* Channell, J.E.T., Kanamatsu, T., Sato, T., Stein, R., Alvarez Zarikian, C.A., Malone, M.J., and the Expedition 303/306 Scientists, *Proc. IODP,* 303/306: College Station, TX (Integrated Ocean Drilling Program Management International, Inc.). **doi:10.2204/iodp.proc.303306.205.2009**

Sierro, F.J., Hodell, D.A., Curtis, J.H., Flores, J.A., Reguera, I., Colmenero-Hidalgo, E., Bárcena, M.A., Grimalt, J.O., Cacho, I., Frigola, J., and Canals, M., 2005. Impact of iceberg melting on Mediterranean thermohaline circulation during Heinrich events. *Paleoceanography,* 20(2):PA2019. **doi:10.1029/2004PA001051**

Sierro, F.J., Ledesma, S., and Flores, J.A., 2008. Astrobiochronology of late Neogene deposits near the Strait of Gibraltar (SW Spain). Implications for the tectonic control of the Messinian salinity crisis. *In* Briand, F. (Ed.), *The Messinian Salinity Crisis from Mega-deposits to Microbiology—A Consensus Report.* CIESM Workshop Monogr., 33:45–48. **http://www.ciesm.org/online/monographs/Almeria07.pdf**

Sierro, F.J., Ledesma, S., Flores, J.-A., Torrescusa, S., and Martínez del Olmo, W., 2000. Sonic and gamma-ray astrochronology: cycle to cycle calibration of Atlantic climatic to Mediterranean sapropels and astronomical oscillations. *Geology,* 28(8):695–698. **doi:10.1130/0091-7613(2000)28<695:SAGACT>2.0.CO;2**

Stow, D.A.V., Faugères, J.-C., and Gonthier, E., 1986. Facies distribution and textural variation in Faro Drift contourites: velocity fluctuation and drift growth. *Mar. Geol.,* 72(1–2):71–100. **doi:10.1016/0025-3227(86)90100-3**

Stow, D.A.V., Faugères, J.-C., Gonthier, E., Cremer, M., Llave, E., Hernández-Molina, F.J., Somoza, L., and Díaz-del-Río, V., 2002. Faro-Albufeira Drift complex, northern Gulf of Cádiz. *In* Stow, D.A.V., Pudsey, C.J., Howe, J.A., Faugères, J.-C., and Viana, A.R. (Eds.), *Deep-Water Contourite Systems: Modern Drifts and Ancient Series, Seismic and Sedimentary Characteristics.* Mem.—Geol. Soc. London, 22(1):137–154. **doi:10.1144/GSL.MEM.2002.022.01.11**

Stow, D., Hernández-Molina, F.J., Hodell, D., and Alvarez Zarikian, C.A., 2011. Mediterranean outflow: environmental significance of the Mediterranean Outflow Water and its global implications. *IODP Sci. Prosp.,* 339. **doi:10.2204/iodp.sp.339.2011**

Toucanne, S., Mulder, T., Schönfeld, J., Hanquiez, V., Gonthier, E., Duprat, J., Cremer, M., and Zaragosi, S., 2007. Contourites of the Gulf of Cádiz: a high-resolution record of the paleocirculation of the Mediterranean Outflow Water during the last 50,000 years. *Palaeogeogr., Palaeoclimatol., Palaeoecol.,* 246(2–4):354–366. **doi:10.1016/j.palaeo.2006.10.007**

Traverse, A., 1988. *Paleopalynology:* Boston (Unwyn Hyman).

Tzedakis, P.C., Pälike, H., Roucoux, K.H., and de Abreu, L., 2009. Atmospheric methane, southern European vegetation and low–mid latitude links on orbital and millennial timescales. *Earth Planet. Sci. Lett.,* 277(3–4):307–317. **doi:10.1016/j.epsl.2008.10.027**

van Morkhoven, F.P.C.M., Berggren, W.A., and Edwards, A.S., 1986. *Cenozoic Cosmopolitan Deep-Water Benthic Foraminifera.* Bull. Cent. Rech. Explor.—Prod. Elf-Aquitaine, 11.

Voelker, A.H.L., Lebreiro, S.M., Schönfeld, J., Cacho, I., Erlenkeuser, H., and Abrantes, F., 2006. Mediterranean Outflow strengthening during Northern Hemisphere coolings: a salt source for the glacial Atlantic? *Earth Planet. Sci. Lett.,* 245(1–2):39–55. **doi:10.1016/j.epsl.2006.03.014**

Wei, W., 1993. Calibration of upper Pliocene–lower Pleistocene nannofossil events with oxygen isotope stratigraphy. *Paleoceanography,* 8(1):85–99. **doi:10.1029/92PA02504**

Xuan, C., and Channell, J.E.T., 2009. UPmag: MATLAB software for viewing and processing U channel or other pass-through paleomagnetic data. *Geochem., Geophys., Geosyst.,* 10(10):Q10Y07. **doi:10.1029/2009GC002584**

Publication: 17 June 2013
MS 339-104

Figure F1. 3-D bathymetric map showing the northwest end of the Faro elongated, mounded, and separated drift and the location of Sites U1386 (36°49.685′N, 7°45.321′W) and U1387 (36°48.321′N, 7°43.132′W) (made by H. Pereira, Escola Secundária de Loulé, Portugal, using Mirone and iView4D software).

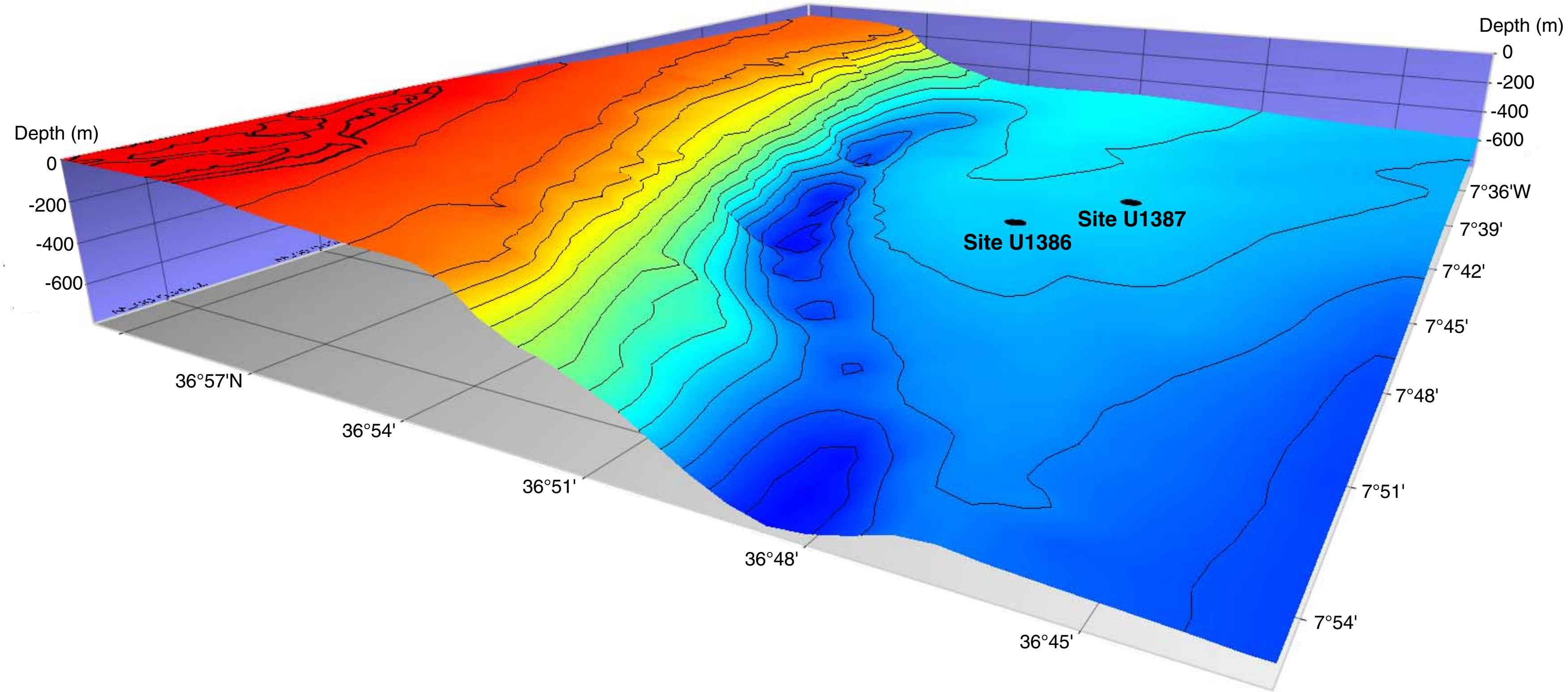

Figure F2. Chronostratigraphic interpretation of different order depositional sequences in the Faro-Albufeira Drift. Legend for seismic horizons after Llave et al. (2011) and Stow et al. (2011). MIS = marine isotope stage, MPR = mid-Pleistocene revolution discontinuity, BQD = base Quaternary discontinuity. **A.** Sparker seismic profile indicating the main seismic units (Q-I and Q-II) within the Quaternary contourite sedimentary record (from Llave et al., 2001). **B.** 3.75 kHz seismic profile across the mounded Faro-Albufeira Drift indicating the main late Pleistocene seismic units (a–d; from Llave et al., 2006). **C.** TOPAS seismic profile across the Faro-Cádiz sheeted drift indicating the main seismic units within the main late Pleistocene seismic units (a–d; from Llave et al., 2006).

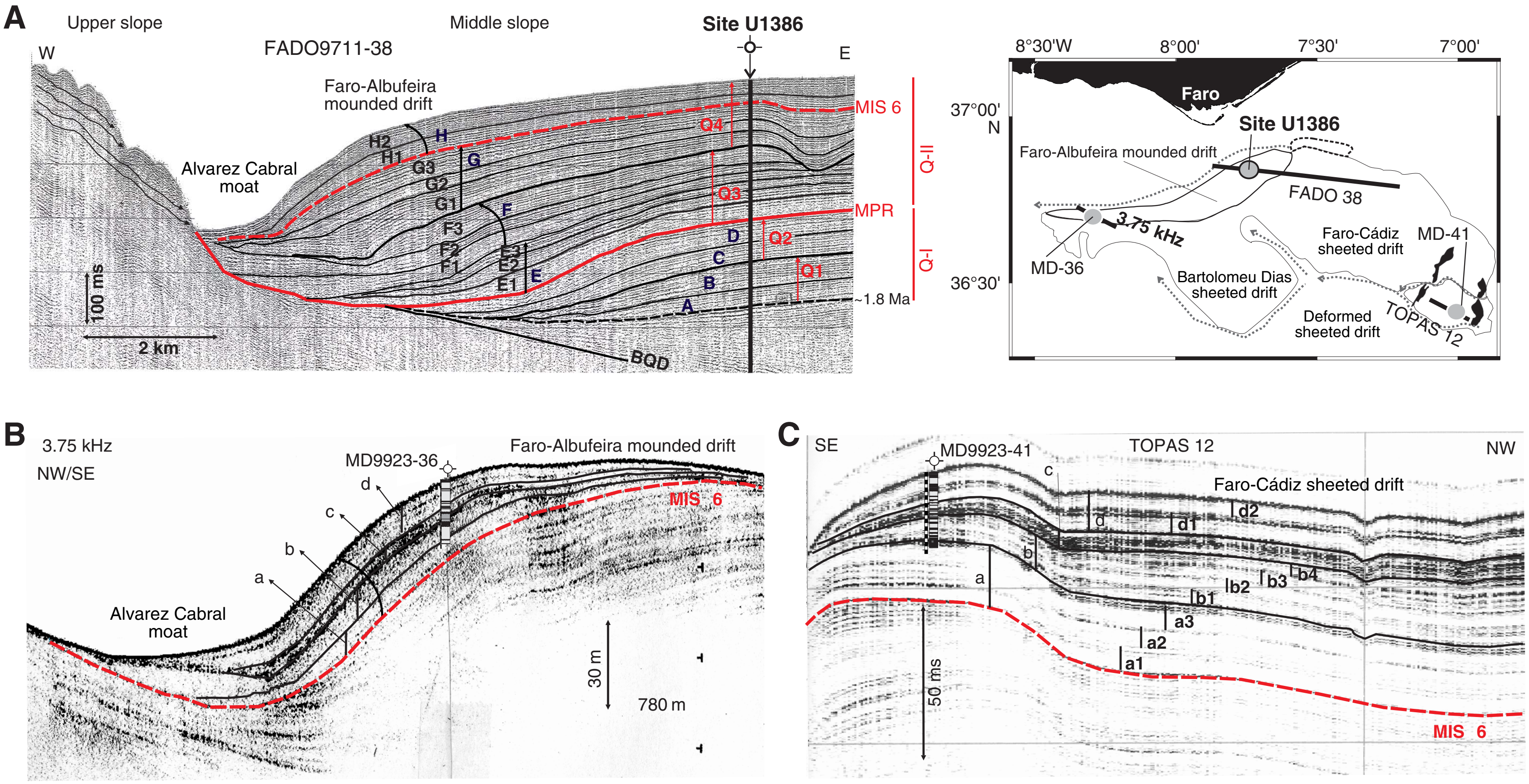

Figure F3. Paleoclimate records of Calypso piston Core MD99-2336 from the Faro-Albufeira Drift, Gulf of Cádiz, from (**A**) Llave et al. (2006) and (**B**) Lebreiro and Voelker (unpubl. data from the MOWFADRI project). Changes in grain size and thereby in the strength of MOW are revealed by the mean grain-size MOW variation exactly correlated with Heinrich events and Dansgaard/Öschger cycles. VPDB = Vienna Peedee belemnite, LGM = Last Glacial Maximum, IRD = ice-rafted debris. BP = before present, MIS = marine isotope stage.

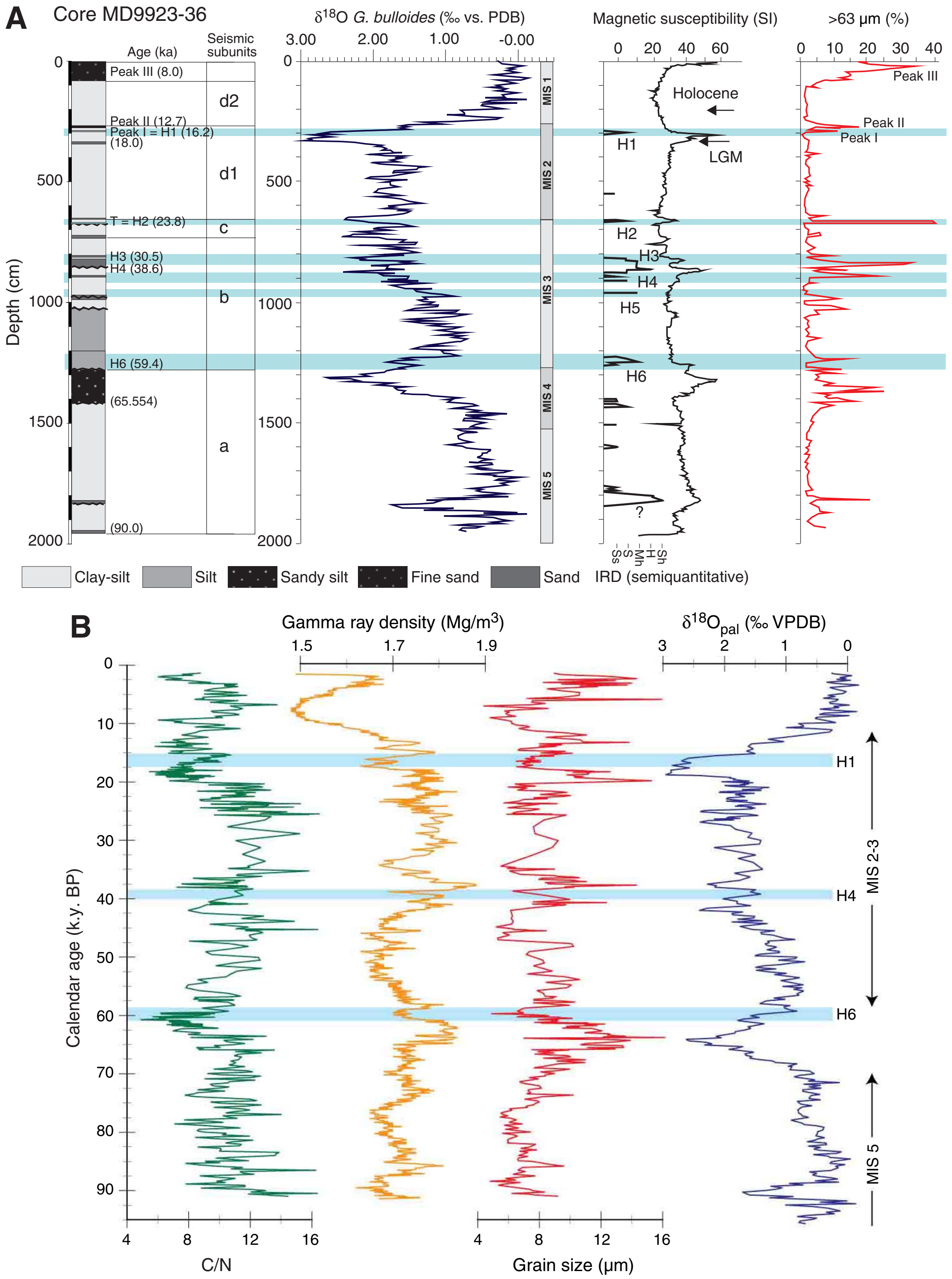

Figure F4. Bathymetric map with seismic track lines and locations of Sites U1386 and U1387 in the contourite depositional system on the middle slope of the Gulf of Cádiz (base map made by R. León, Geological Survey, IGME, Spain).

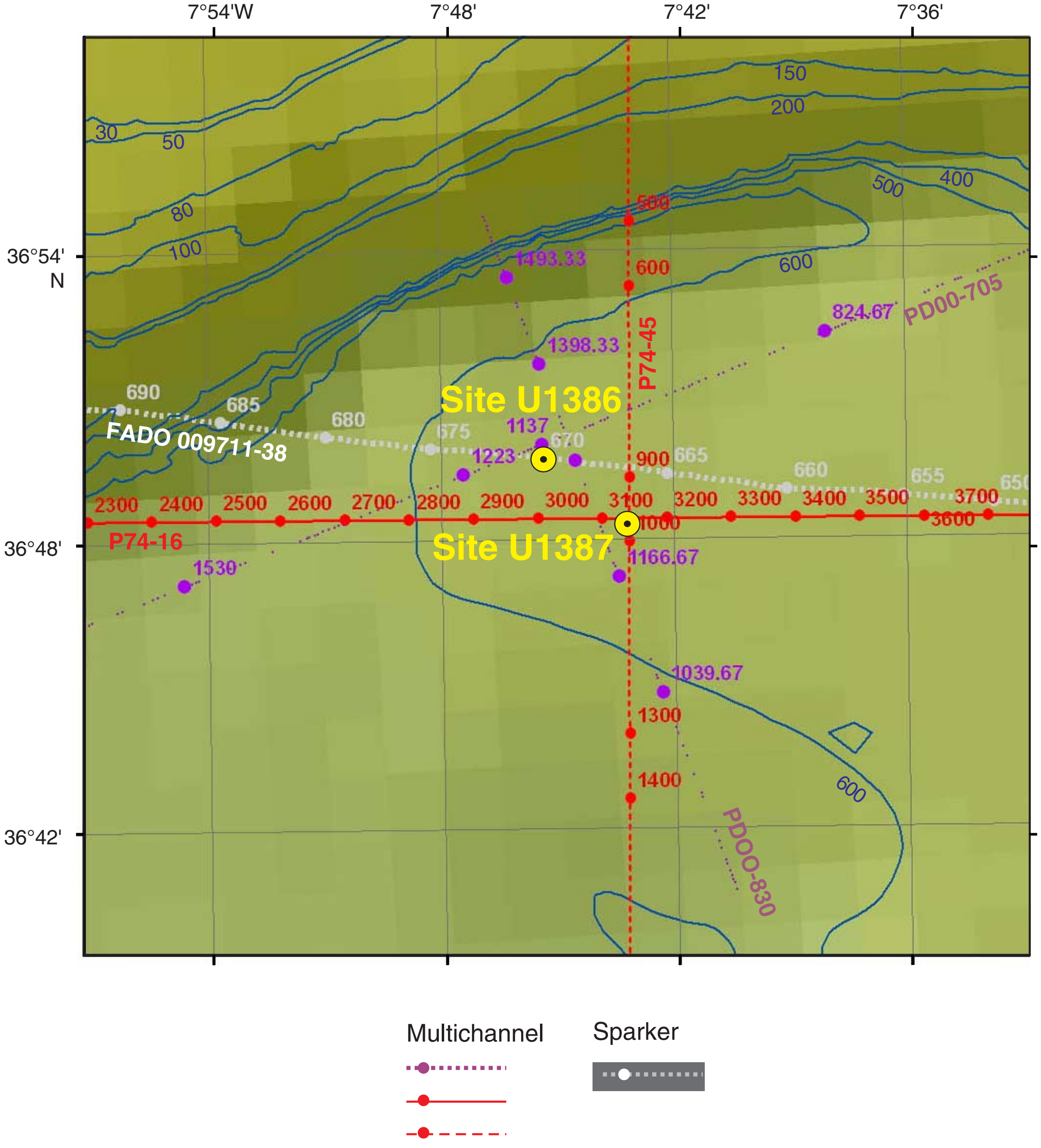

Figure F5. Graphic lithology summary log, Site U1386. MOW = Mediterranean Outflow Water.

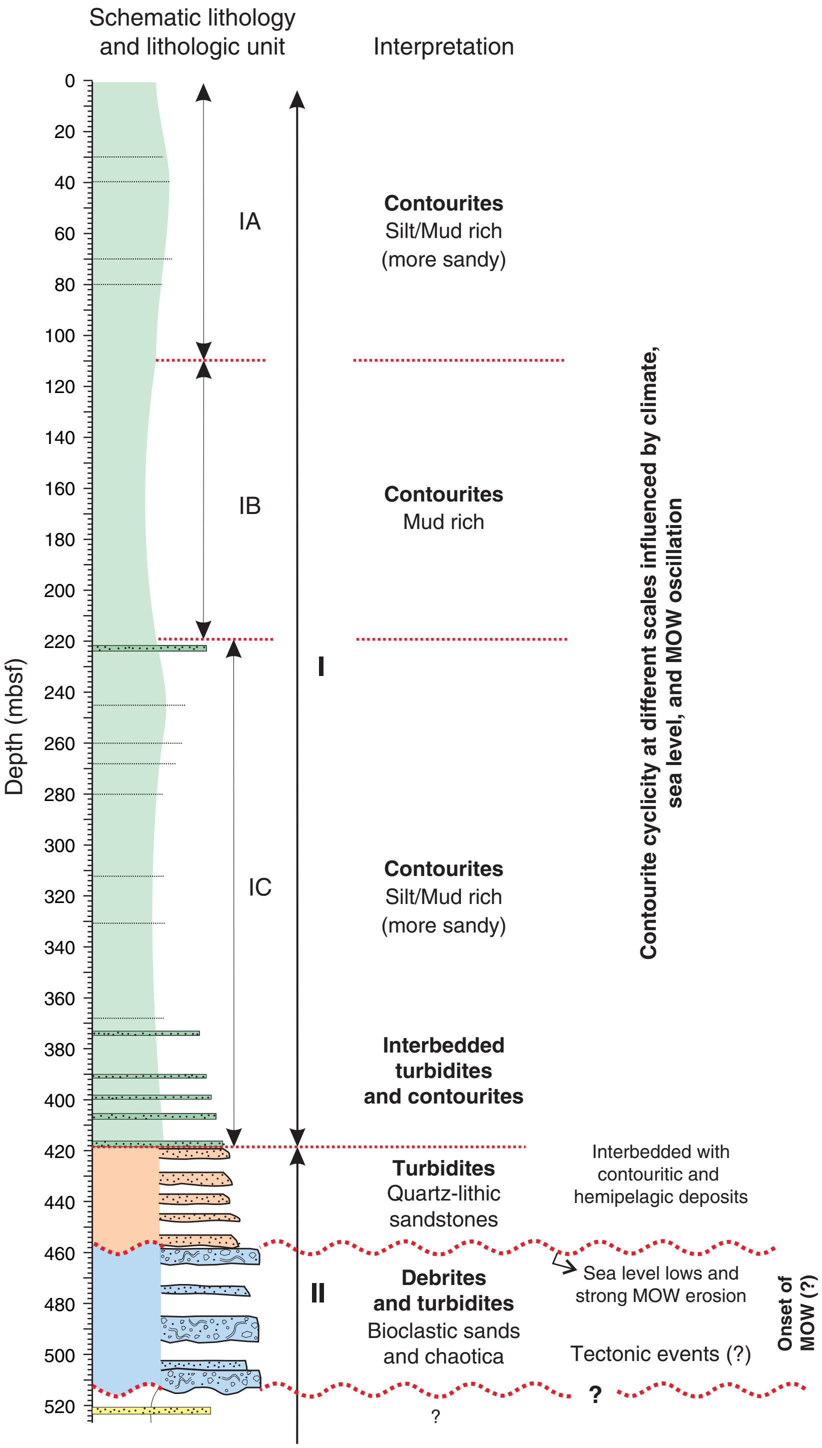

Figure F6. Plots of downhole variations in lithology percentages, Holes U1386A–U1386C.

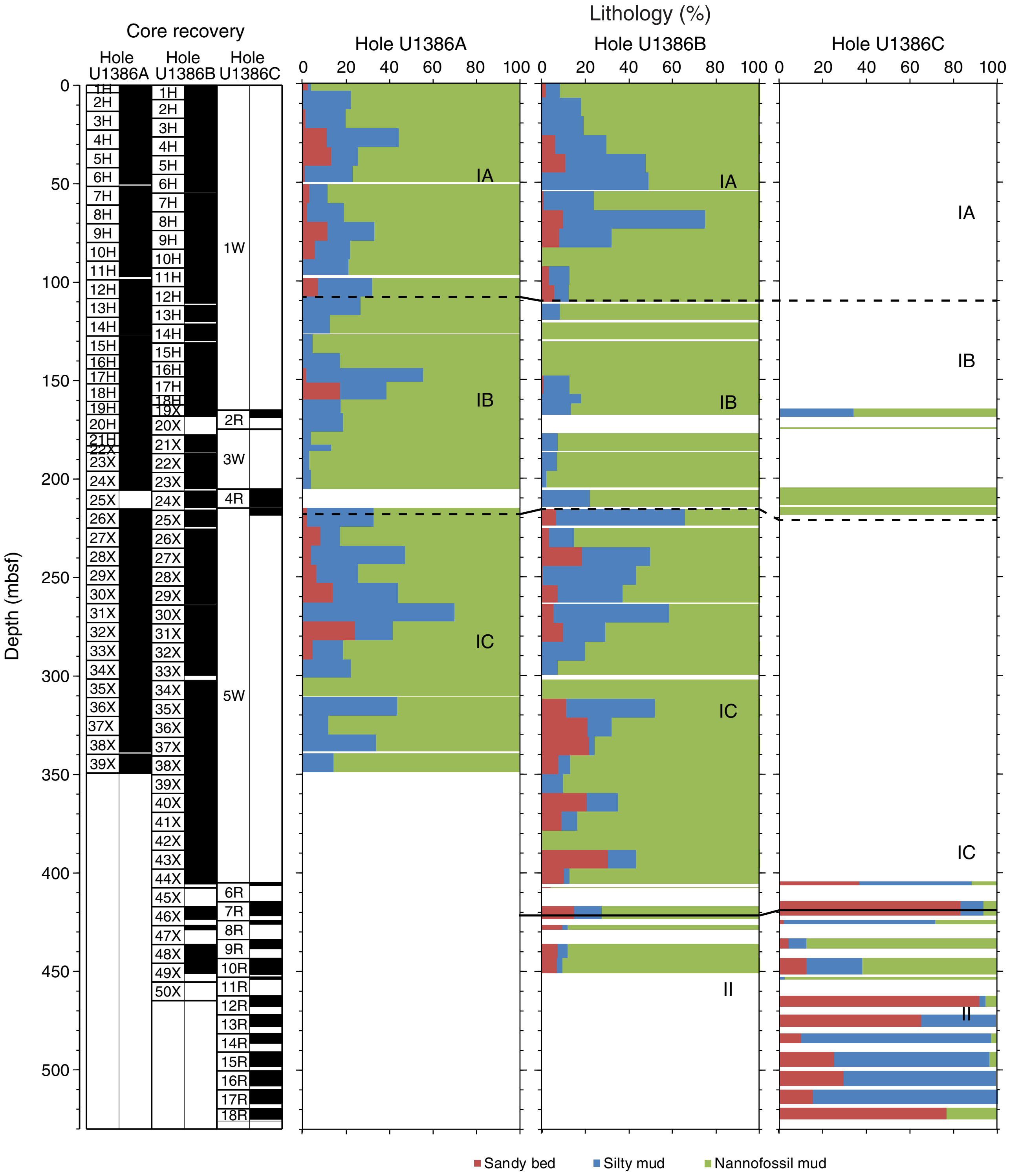

Figure F7. Graphic lithologic summaries, Site U1386. **A.** Hole U1386A. (Continued on next two pages.)

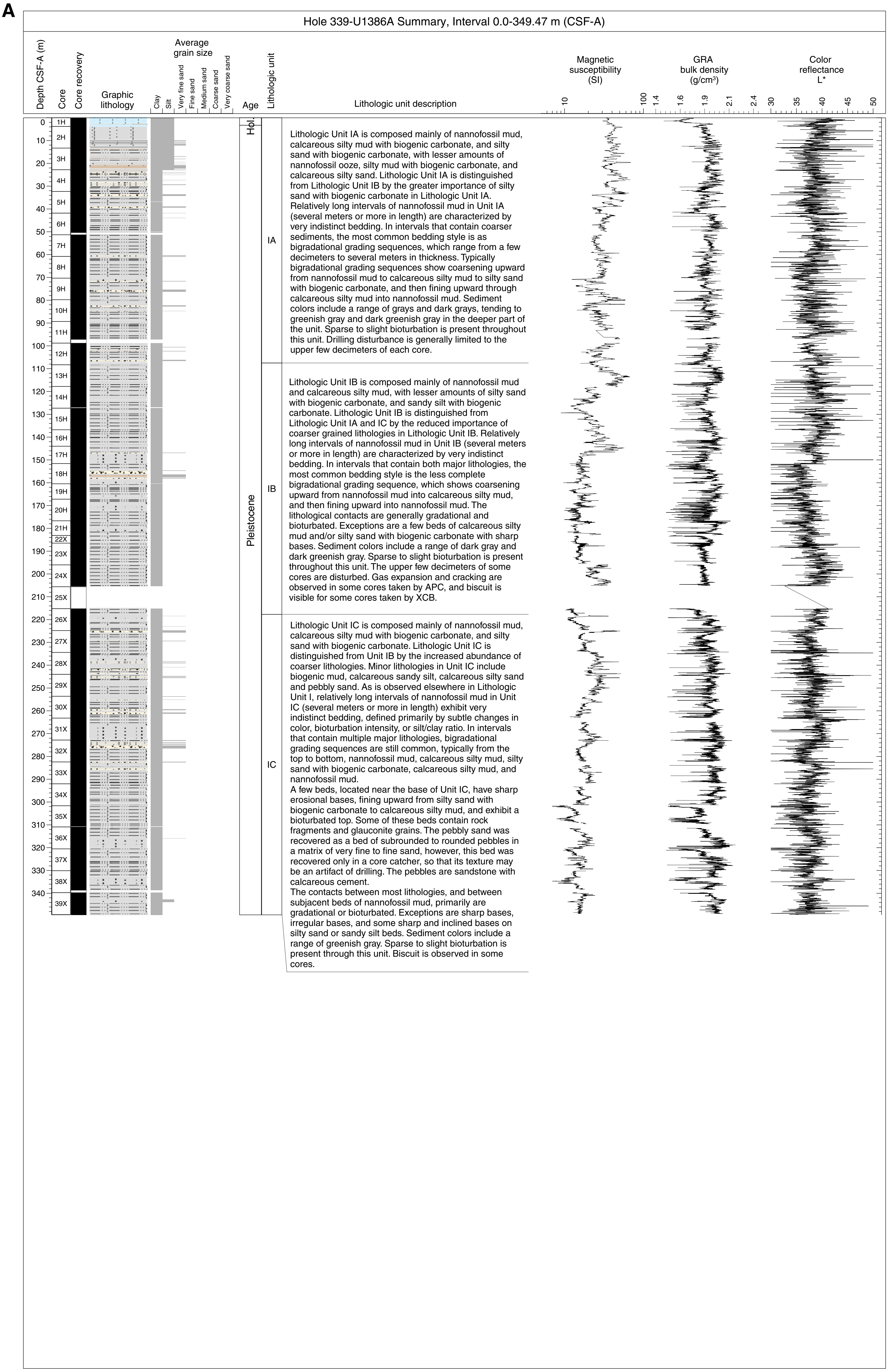

Lithologic Unit IA is composed mainly of nannofossil mud, calcareous silty mud with biogenic carbonate, and silty sand with biogenic carbonate, with lesser amounts of nannofossil ooze, silty mud with biogenic carbonate, and calcareous silty sand. Lithologic Unit IA is distinguished from Lithologic Unit IB by the greater importance of silty sand with biogenic carbonate in Lithologic Unit IA. Relatively long intervals of nannofossil mud in Unit IA (several meters or more in length) are characterized by very indistinct bedding. In intervals that contain coarser sediments, the most common bedding style is as bigradational grading sequences, which range from a few decimeters to several meters in thickness. Typically bigradational grading sequences show coarsening upward from nannofossil mud to calcareous silty mud to silty sand with biogenic carbonate, and then fining upward through calcareous silty mud into nannofossil mud. Sediment colors include a range of grays and dark grays, tending to greenish gray and dark greenish gray in the deeper part of the unit. Sparse to slight bioturbation is present throughout this unit. Drilling disturbance is generally limited to the upper few decimeters of each core.

Lithologic Unit IB is composed mainly of nannofossil mud and calcareous silty mud, with lesser amounts of silty sand with biogenic carbonate, and sandy silt with biogenic carbonate. Lithologic Unit IB is distinguished from Lithologic Unit IA and IC by the reduced importance of coarser grained lithologies in Lithologic Unit IB. Relatively long intervals of nannofossil mud in Unit IB (several meters or more in length) are characterized by very indistinct bedding. In intervals that contain both major lithologies, the most common bedding style is the less complete bigradational grading sequence, which shows coarsening upward from nannofossil mud into calcareous silty mud, and then fining upward into nannofossil mud. The lithological contacts are generally gradational and bioturbated. Exceptions are a few beds of calcareous silty mud and/or silty sand with biogenic carbonate with sharp bases. Sediment colors include a range of dark gray and dark greenish gray. Sparse to slight bioturbation is present throughout this unit. The upper few decimeters of some cores are disturbed. Gas expansion and cracking are observed in some cores taken by APC, and biscuit is visible for some cores taken by XCB.

Lithologic Unit IC is composed mainly of nannofossil mud, calcareous silty mud with biogenic carbonate, and silty sand with biogenic carbonate. Lithologic Unit IC is distinguished from Unit IB by the increased abundance of coarser lithologies. Minor lithologies in Unit IC include biogenic mud, calcareous sandy silt, calcareous silty sand and pebbly sand. As is observed elsewhere in Lithologic Unit I, relatively long intervals of nannofossil mud in Unit IC (several meters or more in length) exhibit very indistinct bedding, defined primarily by subtle changes in color, bioturbation intensity, or silt/clay ratio. In intervals that contain multiple major lithologies, bigradational grading sequences are still common, typically from the top to bottom, nannofossil mud, calcareous silty mud, silty sand with biogenic carbonate, calcareous silty mud, and nannofossil mud.
A few beds, located near the base of Unit IC, have sharp erosional bases, fining upward from silty sand with biogenic carbonate to calcareous silty mud, and exhibit a bioturbated top. Some of these beds contain rock fragments and glauconite grains. The pebbly sand was recovered as a bed of subrounded to rounded pebbles in a matrix of very fine to fine sand, however, this bed was recovered only in a core catcher, so that its texture may be an artifact of drilling. The pebbles are sandstone with calcareous cement.
The contacts between most lithologies, and between subjacent beds of nannofossil mud, are primarily are gradational or bioturbated. Exceptions are sharp bases, irregular bases, and some sharp and inclined bases on silty sand or sandy silt beds. Sediment colors include a range of greenish gray. Sparse to slight bioturbation is present through this unit. Biscuit is observed in some cores.

Figure F7 (continued). B. Hole U1386B. (Continued on next page.)

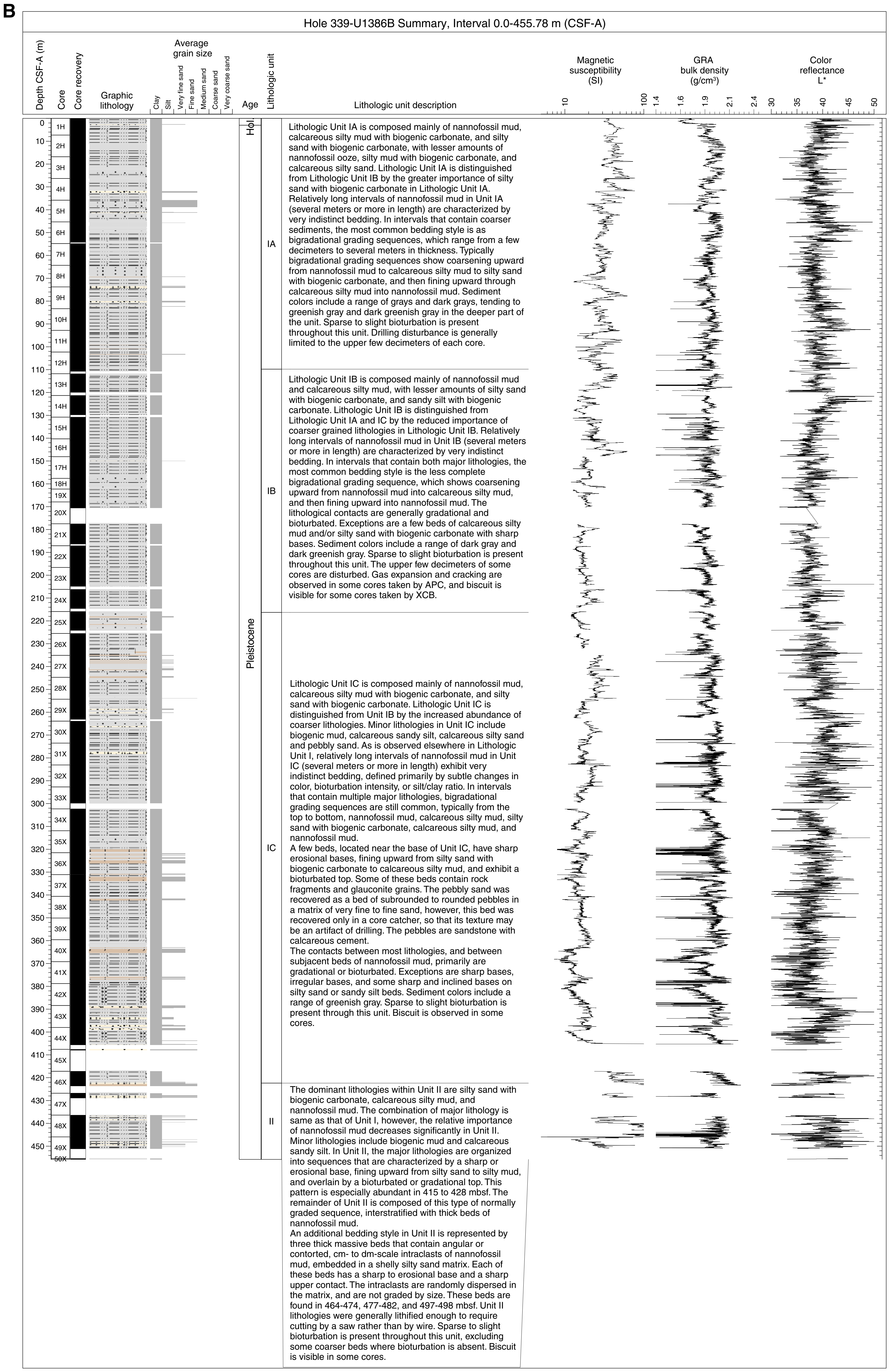

Lithologic Unit IA is composed mainly of nannofossil mud, calcareous silty mud with biogenic carbonate, and silty sand with biogenic carbonate, with lesser amounts of nannofossil ooze, silty mud with biogenic carbonate, and calcareous silty sand. Lithologic Unit IA is distinguished from Lithologic Unit IB by the greater importance of silty sand with biogenic carbonate in Lithologic Unit IA. Relatively long intervals of nannofossil mud in Unit IA (several meters or more in length) are characterized by very indistinct bedding. In intervals that contain coarser sediments, the most common bedding style is as bigradational grading sequences, which range from a few decimeters to several meters in thickness. Typically bigradational grading sequences show coarsening upward from nannofossil mud to calcareous silty mud to silty sand with biogenic carbonate, and then fining upward through calcareous silty mud into nannofossil mud. Sediment colors include a range of grays and dark grays, tending to greenish gray and dark greenish gray in the deeper part of the unit. Sparse to slight bioturbation is present throughout this unit. Drilling disturbance is generally limited to the upper few decimeters of each core.

Lithologic Unit IB is composed mainly of nannofossil mud and calcareous silty mud, with lesser amounts of silty sand with biogenic carbonate, and sandy silt with biogenic carbonate. Lithologic Unit IB is distinguished from Lithologic Unit IA and IC by the reduced importance of coarser grained lithologies in Lithologic Unit IB. Relatively long intervals of nannofossil mud in Unit IB (several meters or more in length) are characterized by very indistinct bedding. In intervals that contain both major lithologies, the most common bedding style is the less complete bigradational grading sequence, which shows coarsening upward from nannofossil mud into calcareous silty mud, and then fining upward into nannofossil mud. The lithological contacts are generally gradational and bioturbated. Exceptions are a few beds of calcareous silty mud and/or silty sand with biogenic carbonate with sharp bases. Sediment colors include a range of dark gray and dark greenish gray. Sparse to slight bioturbation is present throughout this unit. The upper few decimeters of some cores are disturbed. Gas expansion and cracking are observed in some cores taken by APC, and biscuit is visible for some cores taken by XCB.

Lithologic Unit IC is composed mainly of nannofossil mud, calcareous silty mud with biogenic carbonate, and silty sand with biogenic carbonate. Lithologic Unit IC is distinguished from Unit IB by the increased abundance of coarser lithologies. Minor lithologies in Unit IC include biogenic mud, calcareous sandy silt, calcareous silty sand and pebbly sand. As is observed elsewhere in Lithologic Unit I, relatively long intervals of nannofossil mud in Unit IC (several meters or more in length) exhibit very indistinct bedding, defined primarily by subtle changes in color, bioturbation intensity, or silt/clay ratio. In intervals that contain multiple major lithologies, bigradational grading sequences are still common, typically from the top to bottom, nannofossil mud, calcareous silty mud, silty sand with biogenic carbonate, calcareous silty mud, and nannofossil mud.
A few beds, located near the base of Unit IC, have sharp erosional bases, fining upward from silty sand with biogenic carbonate to calcareous silty mud, and exhibit a bioturbated top. Some of these beds contain rock fragments and glauconite grains. The pebbly sand was recovered as a bed of subrounded to rounded pebbles in a matrix of very fine to fine sand, however, this bed was recovered only in a core catcher, so that its texture may be an artifact of drilling. The pebbles are sandstone with calcareous cement.
The contacts between most lithologies, and between subjacent beds of nannofossil mud, primarily are gradational or bioturbated. Exceptions are sharp bases, irregular bases, and some sharp and inclined bases on silty sand or sandy silt beds. Sediment colors include a range of greenish gray. Sparse to slight bioturbation is present through this unit. Biscuit is observed in some cores.

The dominant lithologies within Unit II are silty sand with biogenic carbonate, calcareous silty mud, and nannofossil mud. The combination of major lithology is same as that of Unit I, however, the relative importance of nannofossil mud decreases significantly in Unit II. Minor lithologies include biogenic mud and calcareous sandy silt. In Unit II, the major lithologies are organized into sequences that are characterized by a sharp or erosional base, fining upward from silty sand to silty mud, and overlain by a bioturbated or gradational top. This pattern is especially abundant in 415 to 428 mbsf. The remainder of Unit II is composed of this type of normally graded sequence, interstratified with thick beds of nannofossil mud.
An additional bedding style in Unit II is represented by three thick massive beds that contain angular or contorted, cm- to dm-scale intraclasts of nannofossil mud, embedded in a shelly silty sand matrix. Each of these beds has a sharp to erosional base and a sharp upper contact. The intraclasts are randomly dispersed in the matrix, and are not graded by size. These beds are found in 464-474, 477-482, and 497-498 mbsf. Unit II lithologies were generally lithified enough to require cutting by a saw rather than by wire. Sparse to slight bioturbation is present throughout this unit, excluding some coarser beds where bioturbation is absent. Biscuit is visible in some cores.

Figure F7 (continued). C. Hole U1386C.

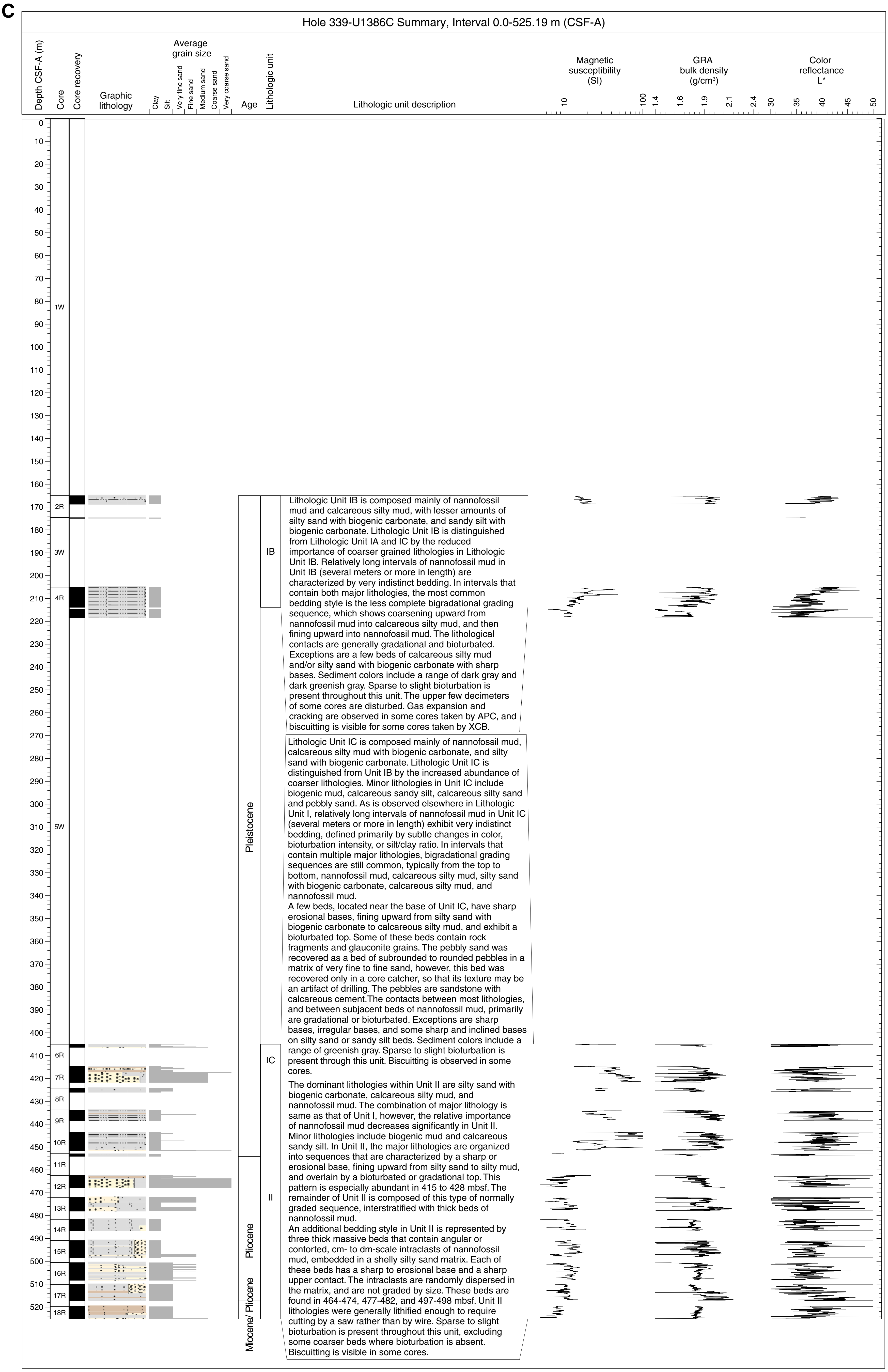

Lithologic Unit IB is composed mainly of nannofossil mud and calcareous silty mud, with lesser amounts of silty sand with biogenic carbonate, and sandy silt with biogenic carbonate. Lithologic Unit IB is distinguished from Lithologic Unit IA and IC by the reduced importance of coarser grained lithologies in Lithologic Unit IB. Relatively long intervals of nannofossil mud in Unit IB (several meters or more in length) are characterized by very indistinct bedding. In intervals that contain both major lithologies, the most common bedding style is the less complete bigradational grading sequence, which shows coarsening upward from nannofossil mud into calcareous silty mud, and then fining upward into nannofossil mud. The lithological contacts are generally gradational and bioturbated. Exceptions are a few beds of calcareous silty mud and/or silty sand with biogenic carbonate with sharp bases. Sediment colors include a range of dark gray and dark greenish gray. Sparse to slight bioturbation is present throughout this unit. The upper few decimeters of some cores are disturbed. Gas expansion and cracking are observed in some cores taken by APC, and biscuitting is visible for some cores taken by XCB.

Lithologic Unit IC is composed mainly of nannofossil mud, calcareous silty mud with biogenic carbonate, and silty sand with biogenic carbonate. Lithologic Unit IC is distinguished from Unit IB by the increased abundance of coarser lithologies. Minor lithologies in Unit IC include biogenic mud, calcareous sandy silt, calcareous silty sand and pebbly sand. As is observed elsewhere in Lithologic Unit I, relatively long intervals of nannofossil mud in Unit IC (several meters or more in length) exhibit very indistinct bedding, defined primarily by subtle changes in color, bioturbation intensity, or silt/clay ratio. In intervals that contain multiple major lithologies, bigradational grading sequences are still common, typically from the top to bottom, nannofossil mud, calcareous silty mud, silty sand with biogenic carbonate, calcareous silty mud, and nannofossil mud.

A few beds, located near the base of Unit IC, have sharp erosional bases, fining upward from silty sand with biogenic carbonate to calcareous silty mud, and exhibit a bioturbated top. Some of these beds contain rock fragments and glauconite grains. The pebbly sand was recovered as a bed of subrounded to rounded pebbles in a matrix of very fine to fine sand, however, this bed was recovered only in a core catcher, so that its texture may be an artifact of drilling. The pebbles are sandstone with calcareous cement. The contacts between most lithologies, and between subjacent beds of nannofossil mud, primarily are gradational or bioturbated. Exceptions are sharp bases, irregular bases, and some sharp and inclined bases on silty sand or sandy silt beds. Sediment colors include a range of greenish gray. Sparse to slight bioturbation is present through this unit. Biscuitting is observed in some cores.

The dominant lithologies within Unit II are silty sand with biogenic carbonate, calcareous silty mud, and nannofossil mud. The combination of major lithology is same as that of Unit I, however, the relative importance of nannofossil mud decreases significantly in Unit II. Minor lithologies include biogenic mud and calcareous sandy silt. In Unit II, the major lithologies are organized into sequences that are characterized by a sharp or erosional base, fining upward from silty sand to silty mud, and overlain by a bioturbated or gradational top. This pattern is especially abundant in 415 to 428 mbsf. The remainder of Unit II is composed of this type of normally graded sequence, interstratified with thick beds of nannofossil mud.

An additional bedding style in Unit II is represented by three thick massive beds that contain angular or contorted, cm- to dm-scale intraclasts of nannofossil mud, embedded in a shelly silty sand matrix. Each of these beds has a sharp to erosional base and a sharp upper contact. The intraclasts are randomly dispersed in the matrix, and are not graded by size. These beds are found in 464-474, 477-482, and 497-498 mbsf. Unit II lithologies were generally lithified enough to require cutting by a saw rather than by wire. Sparse to slight bioturbation is present throughout this unit, excluding some coarser beds where bioturbation is absent. Biscuitting is visible in some cores.

Figure F8. Plots of smear slide abundances, Holes U1386A–U1386C.

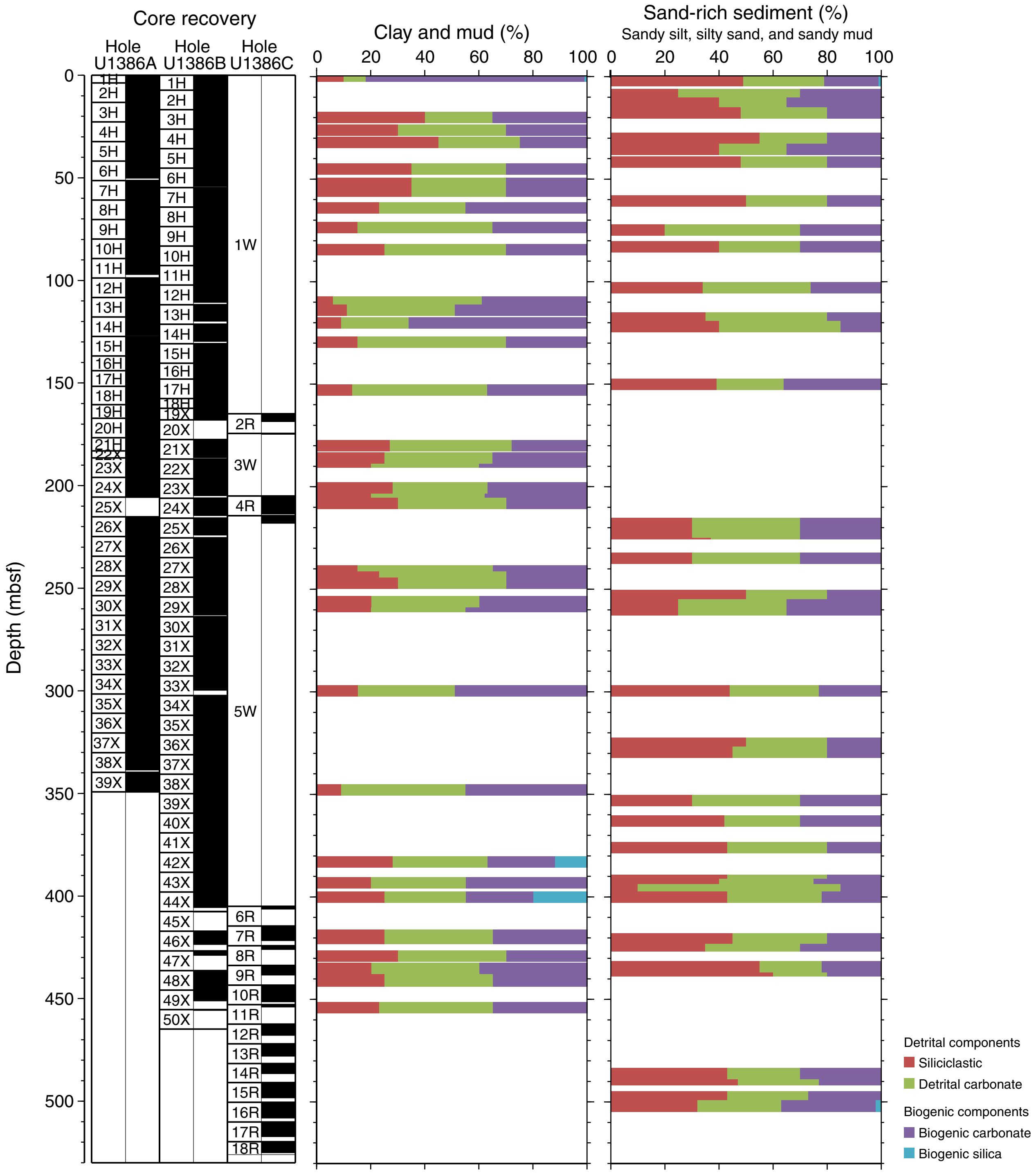

Figure F9. Core images of typical bioturbated nannofossil mud from Unit I (interval 339-U1386A-8H-3A, 0–150 cm).

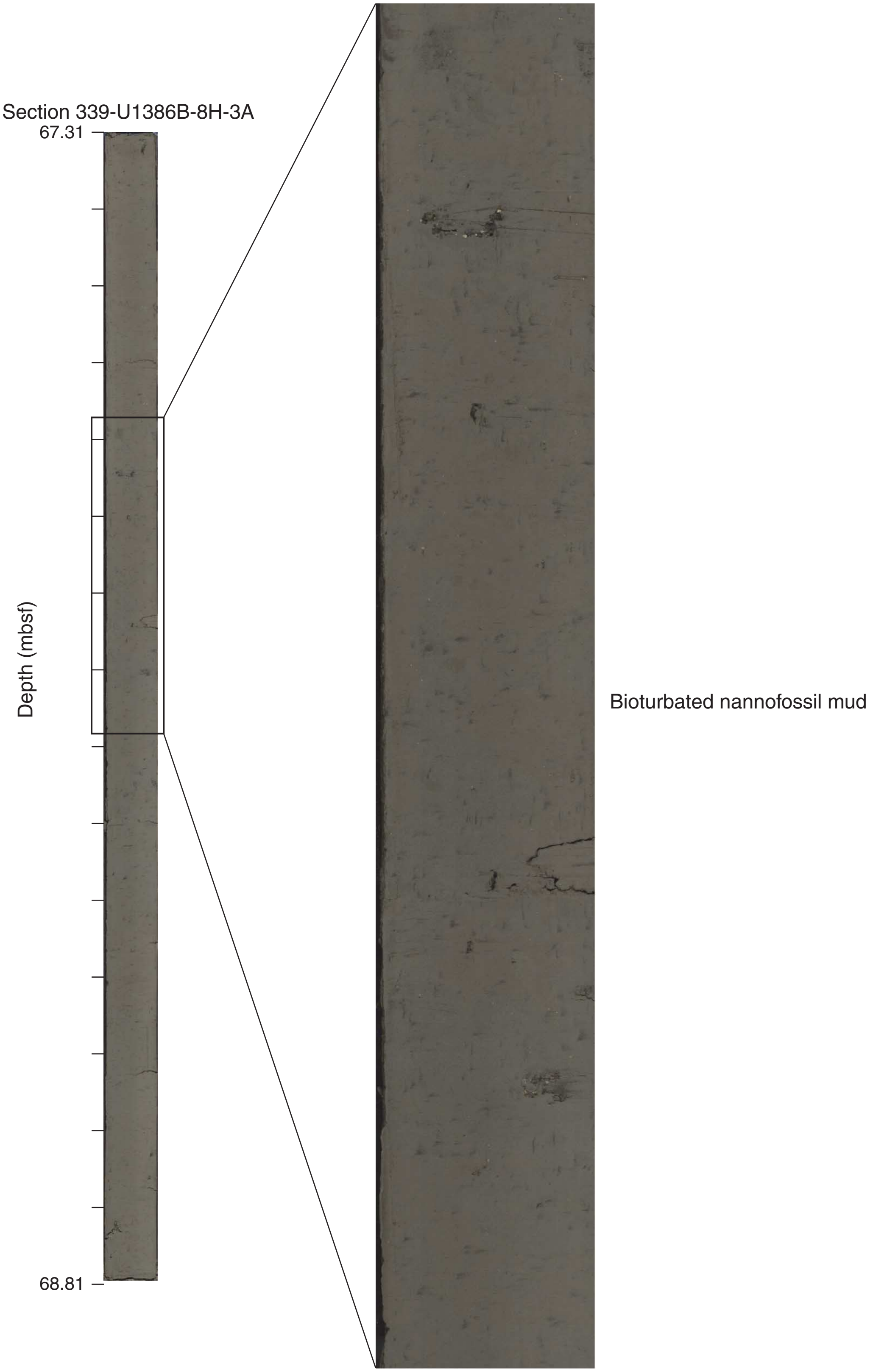

Figure F10. Core images of typical bi-gradational mottled sandy bed from Subunit IA (Sections 339-U1386B-43X-4A and 5A).

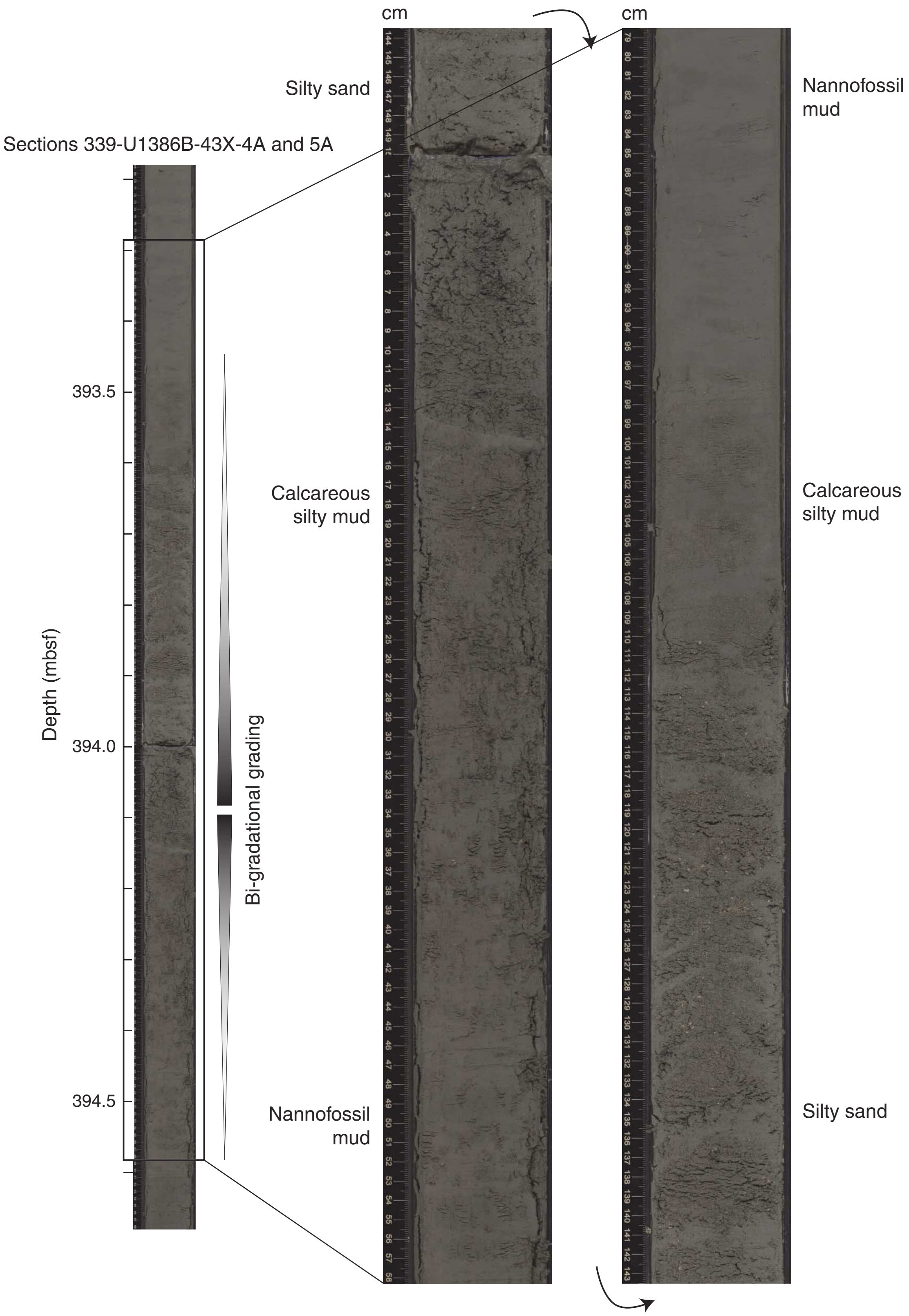

Figure F11. Photomicrographs of smear slides showing authigenic dolomite (rhombic grains) and glauconite (greenish grains) (Samples 339-U1386A-10H-2A, 115 cm, and 339-U1386B-48X-1A, 27 cm).

Sample 339-U1386A-10H-2A, 115 cm

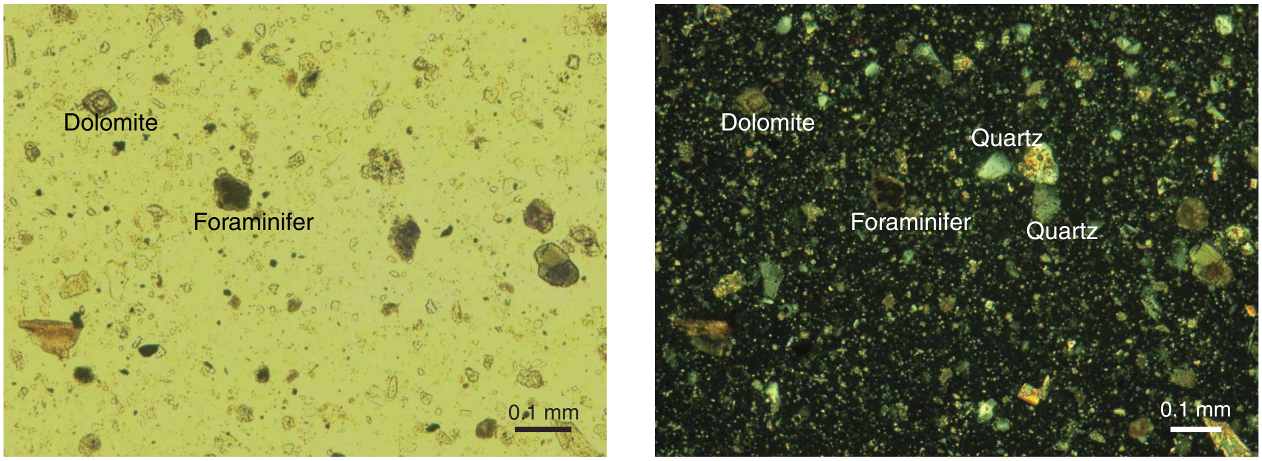

Sample 339-U1386B-48X-1A, 27 cm

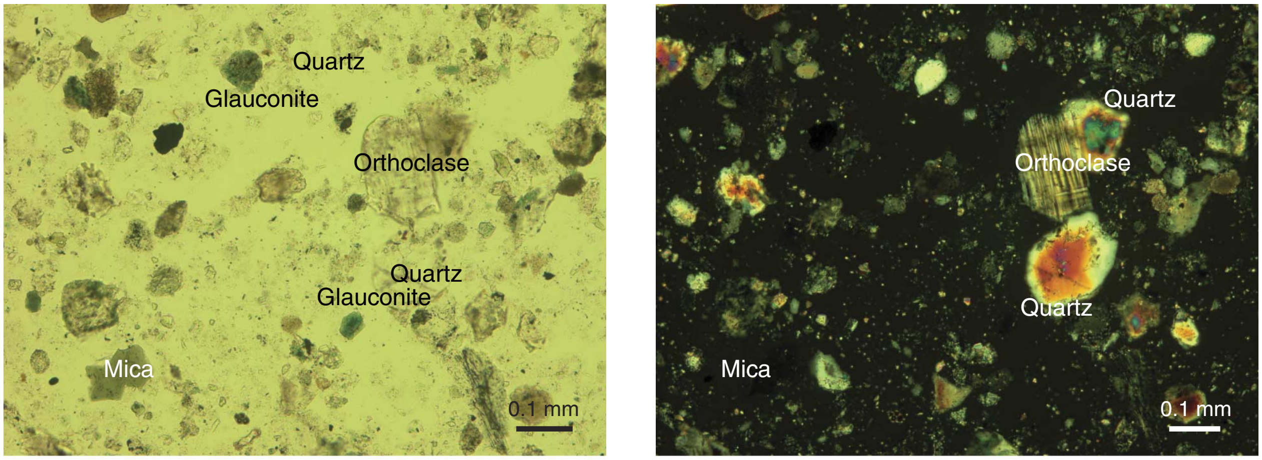

Figure F12. Photograph of almost-whole cold-water coral (Sample 339-U1386A-1H-1, 5–6 cm).

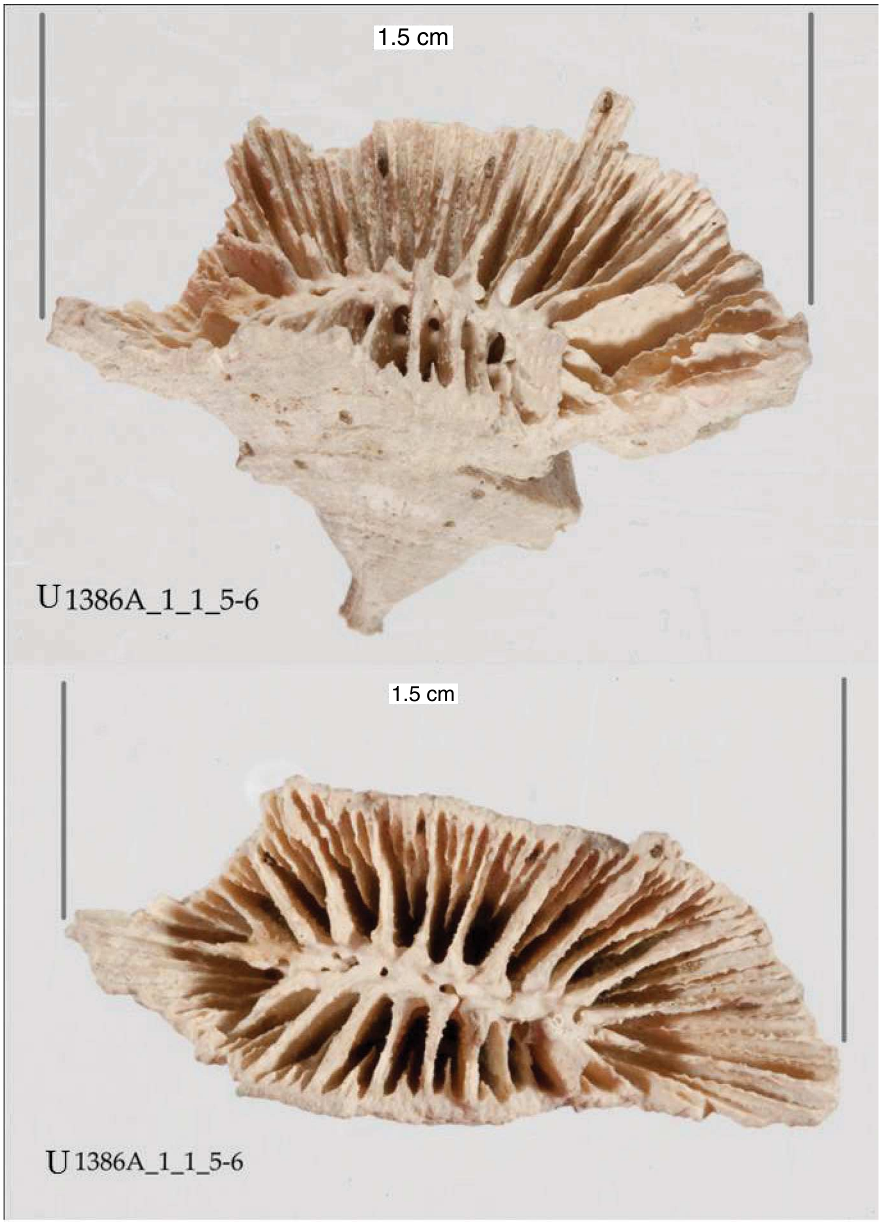

Figure F13. Photograph of coral branch (Sample 339-U1386B-8H-3, 144 cm).

Figure F14. Photograph of almost-whole pectin valve (Sample 339-U1386A-2H-6, 70–72 cm).

Figure F15. Photograph of bivalve shell (Sample 339-U1386A-3H-5, 87–89 cm).

Figure F16. Photograph of gastropod shell (Sample 339-U1386B-5H-4, 8–9 cm).

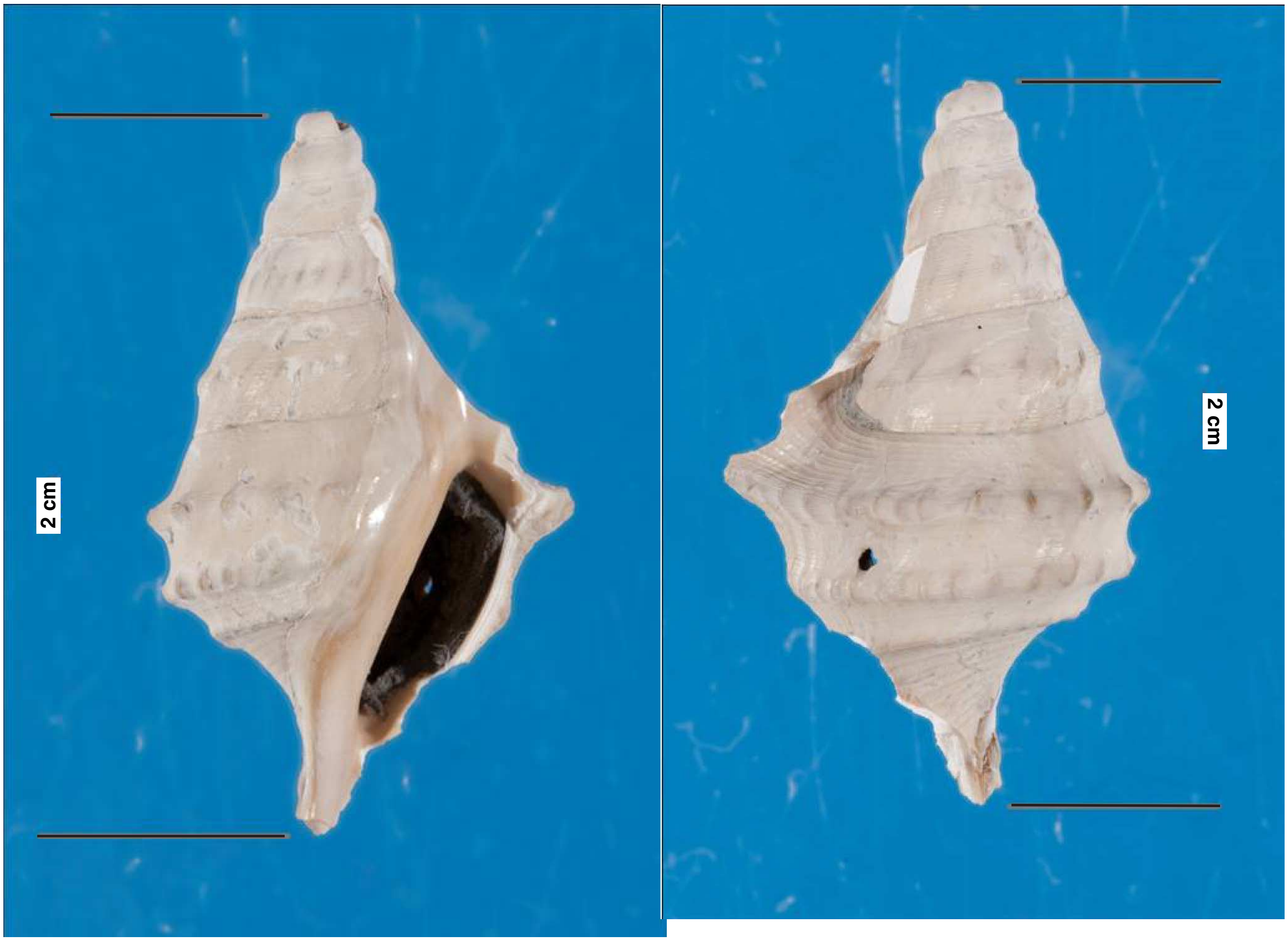

Figure F17. Plots of XRD results and lithologic units, Holes U1386A–U1386C.

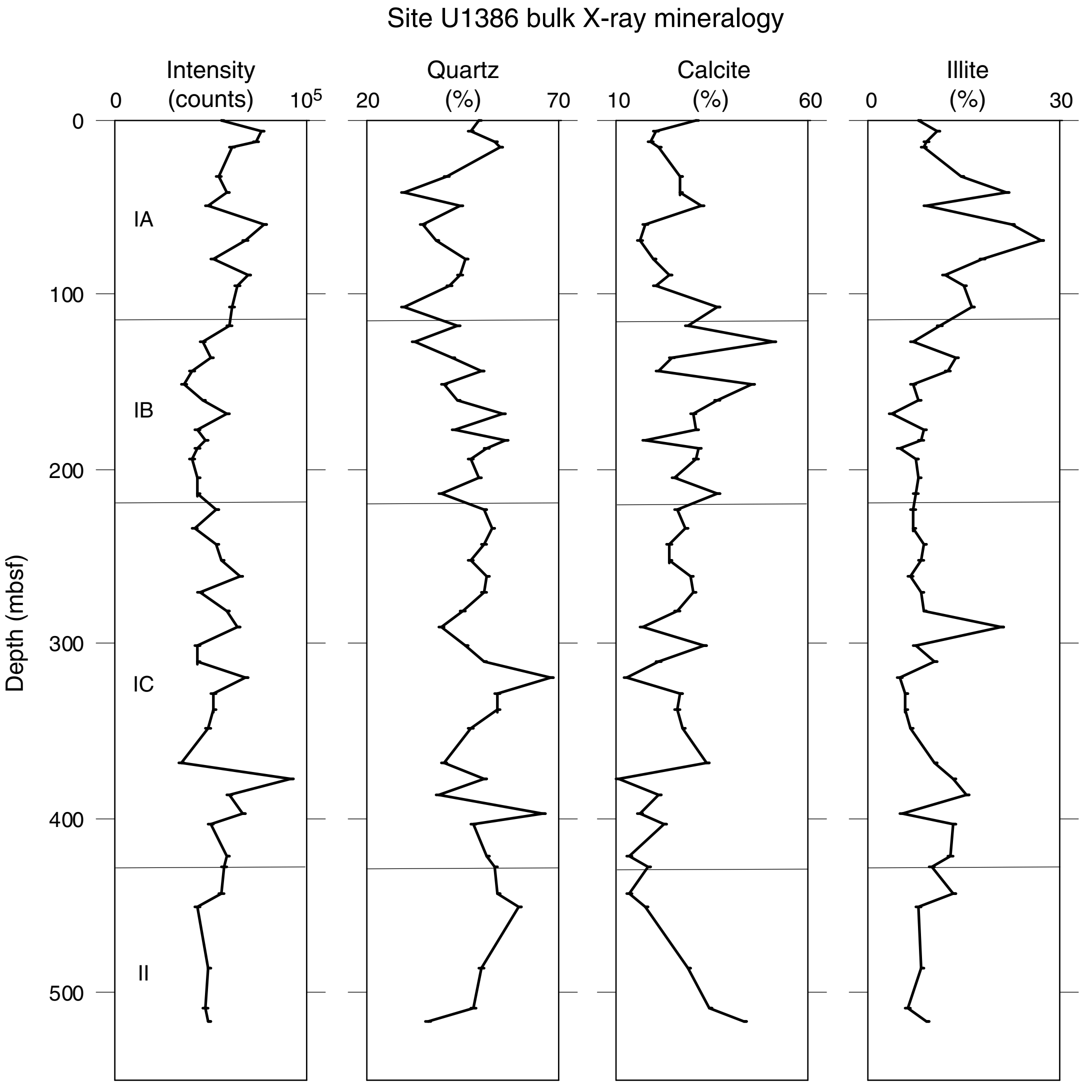

Figure F18. Core images of typical bi-gradational mottled muddy/silty bed from Subunit IB (Section 339-U1386A-13H-3A).

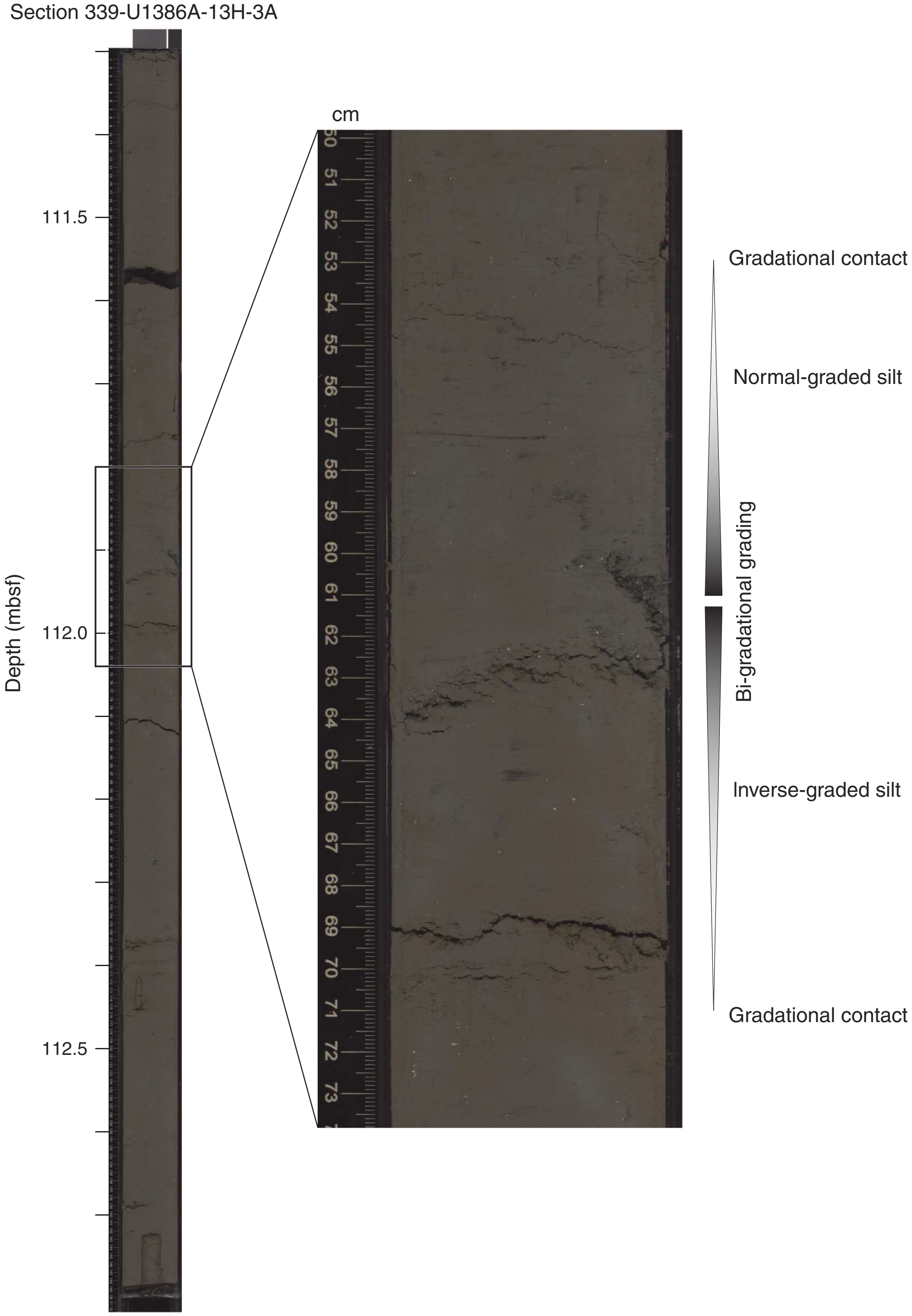

Figure F19. Photograph of gastropod shell (Sample 339-U1386B-21X-1, 113–115 cm).

Figure F20. Core image of pebbly sand from the base of Subunit IC (Section 339-U1386B-45X-CC).

Figure F21. Core images of rock fragments and glauconite-rich thin turbidite (intervals 339-U1386A-26X-3A, 26–30 cm, and 339-U1386B-28X-7A, 118–124 cm).

Figure F22. Core images of typical sandy turbidite from Unit II (Section 339-U1386C-6R-2A).

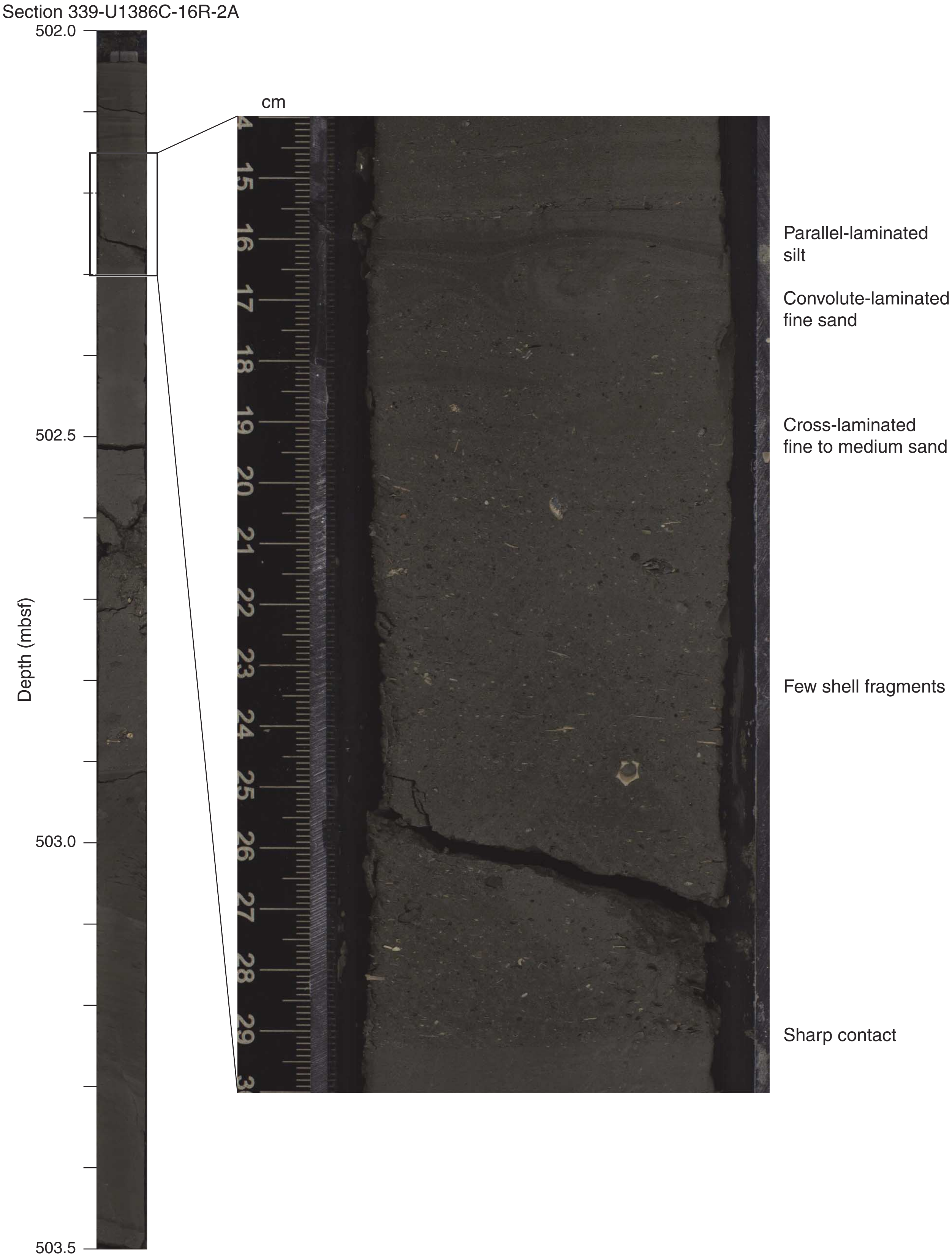

Figure F23. **A.** Core image with location of a typical debrite from Unit II (Section 339-U1386C-15R-5A). **B.** Debrite with convolute bedding (interval 339-U1386C-12R-2A, 77–84 cm). **C.** Mud clast in a shelly sand matrix (interval 339-U1386C-15R-5A, 45–52 cm).

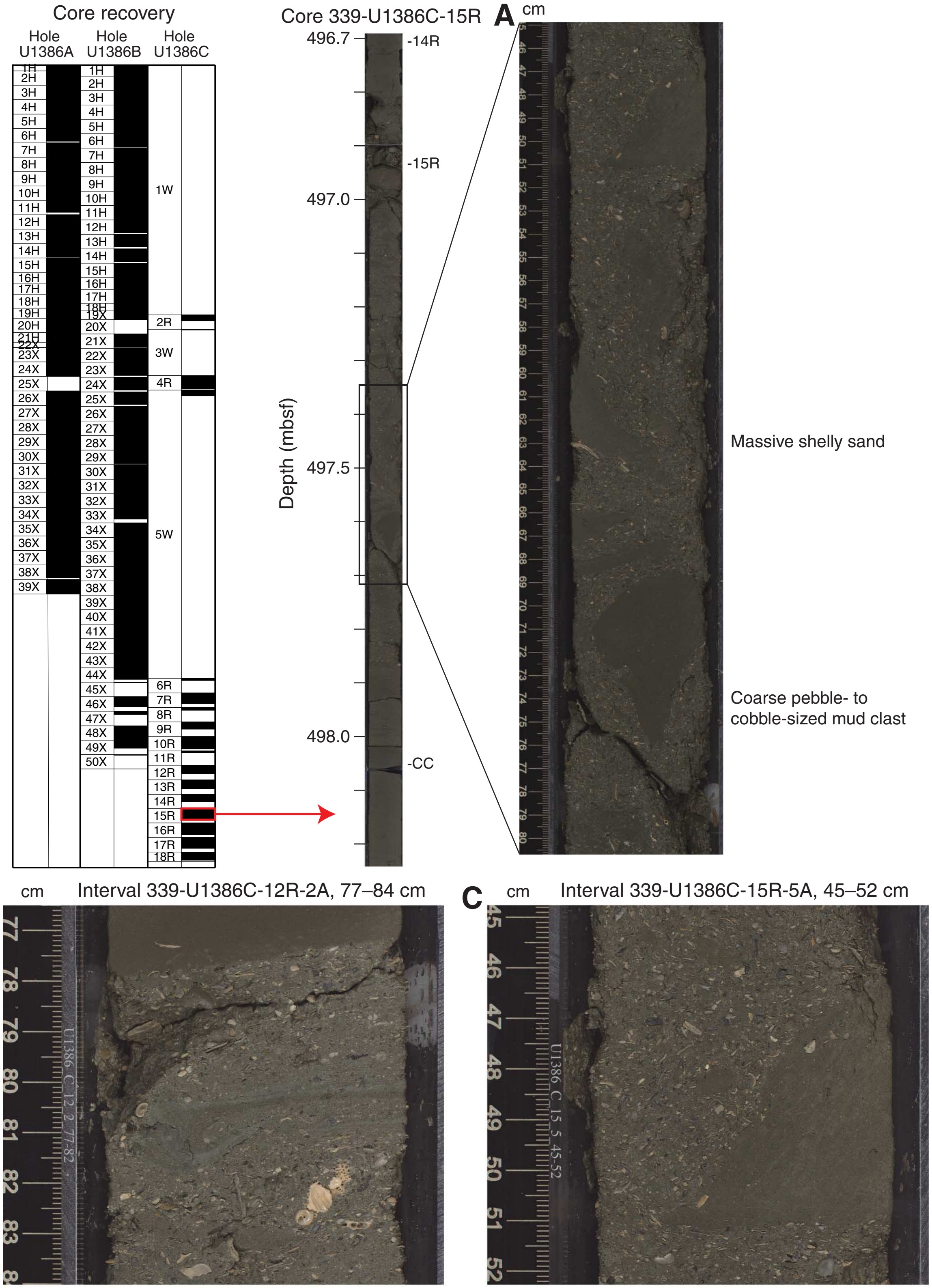

Figure F24. Core images of normal microfaults and dewatering structures associated with the microfaults (Sections 339-U1386C-16R-2).

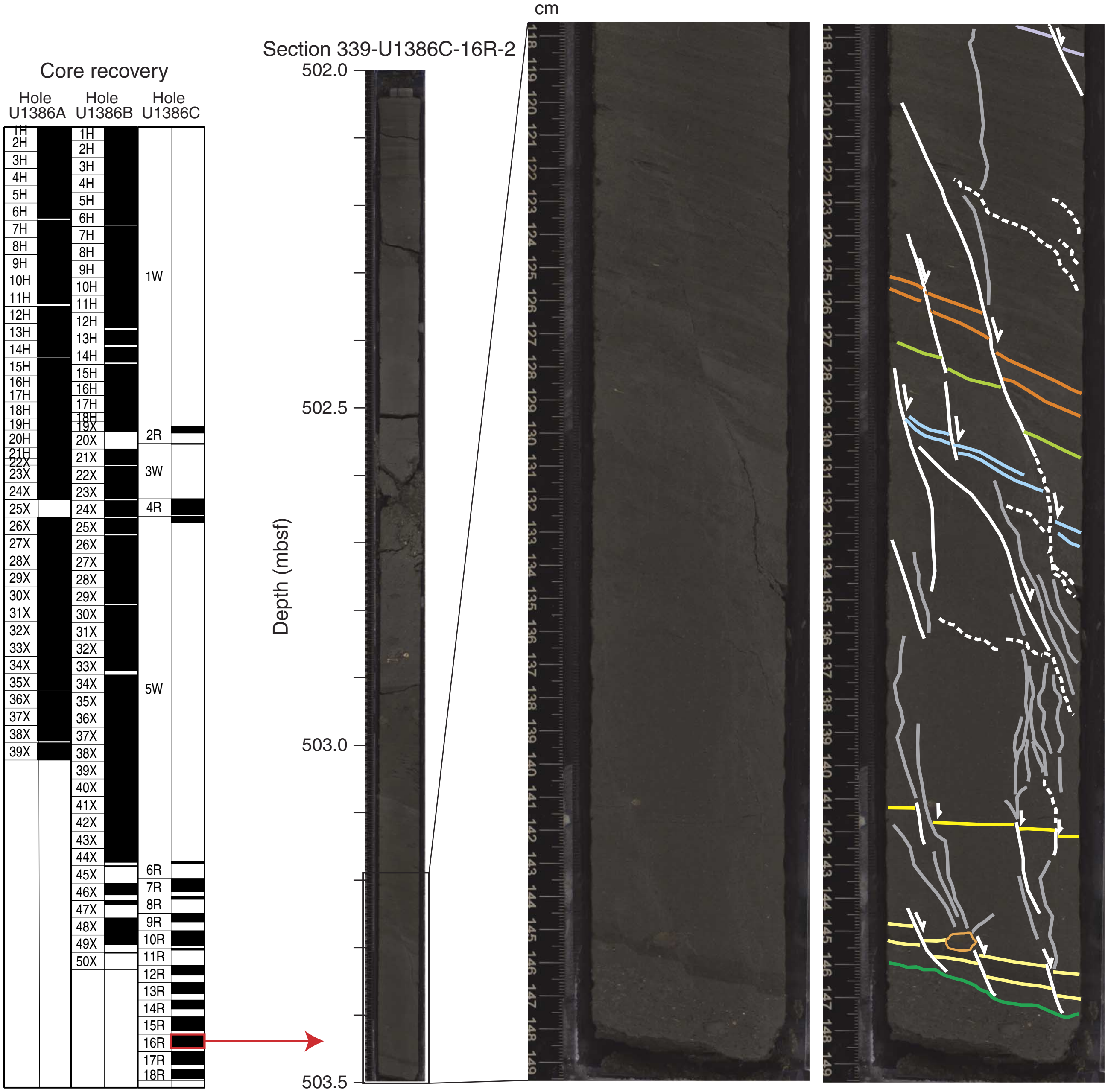

Figure F25. Photograph of bivalve (Sample 339-U1386C-13R-2, 53–54 cm).

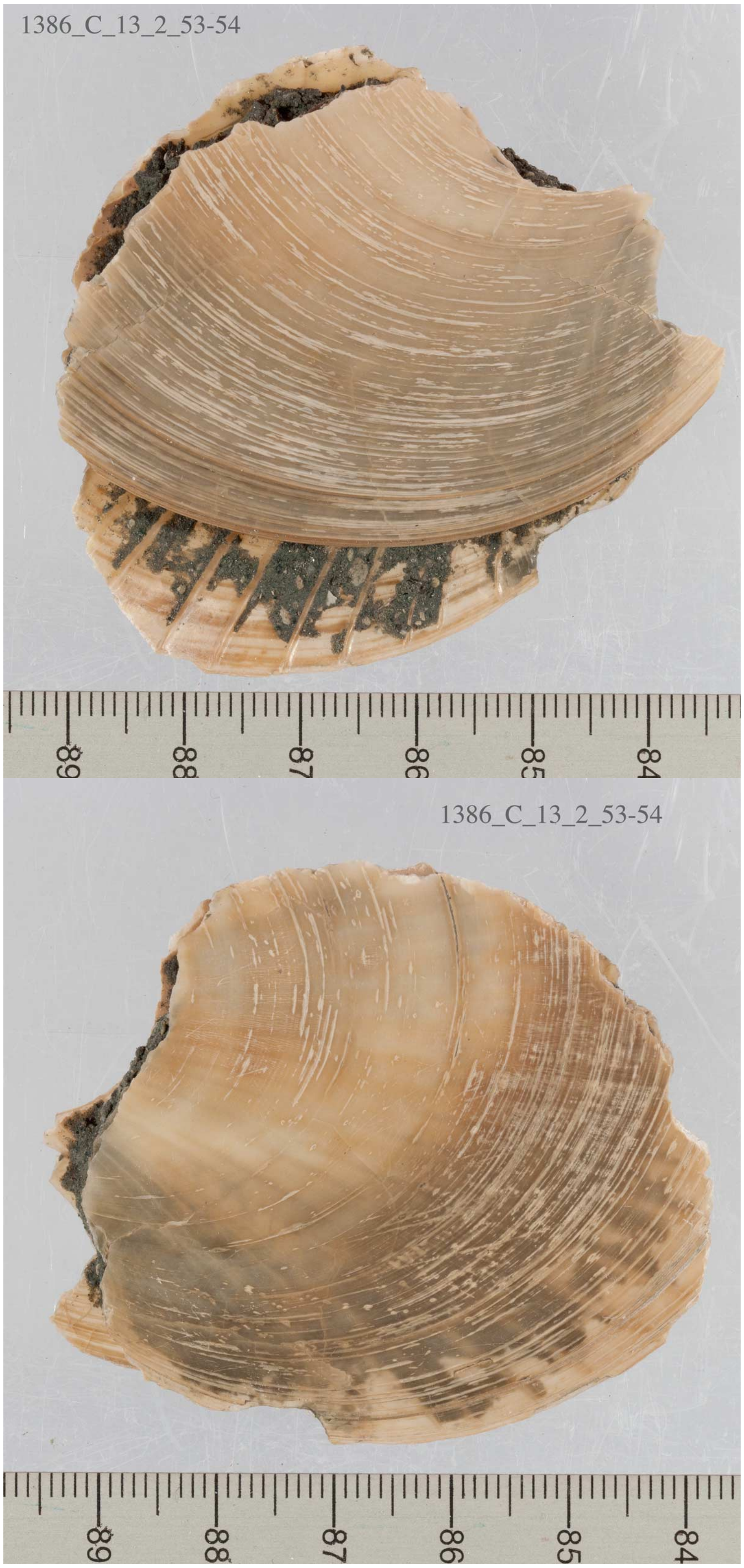

Figure F26. Photograph of gastropod shell (Sample 339-U1386C-12R-4, 77–78 cm). Shell was sawn when core was opened.

Figure F27. Plot of coarse sediment bed thickness and sedimentary process type, Holes U1386A–U1386C. Only beds 40 cm thick or more were considered.

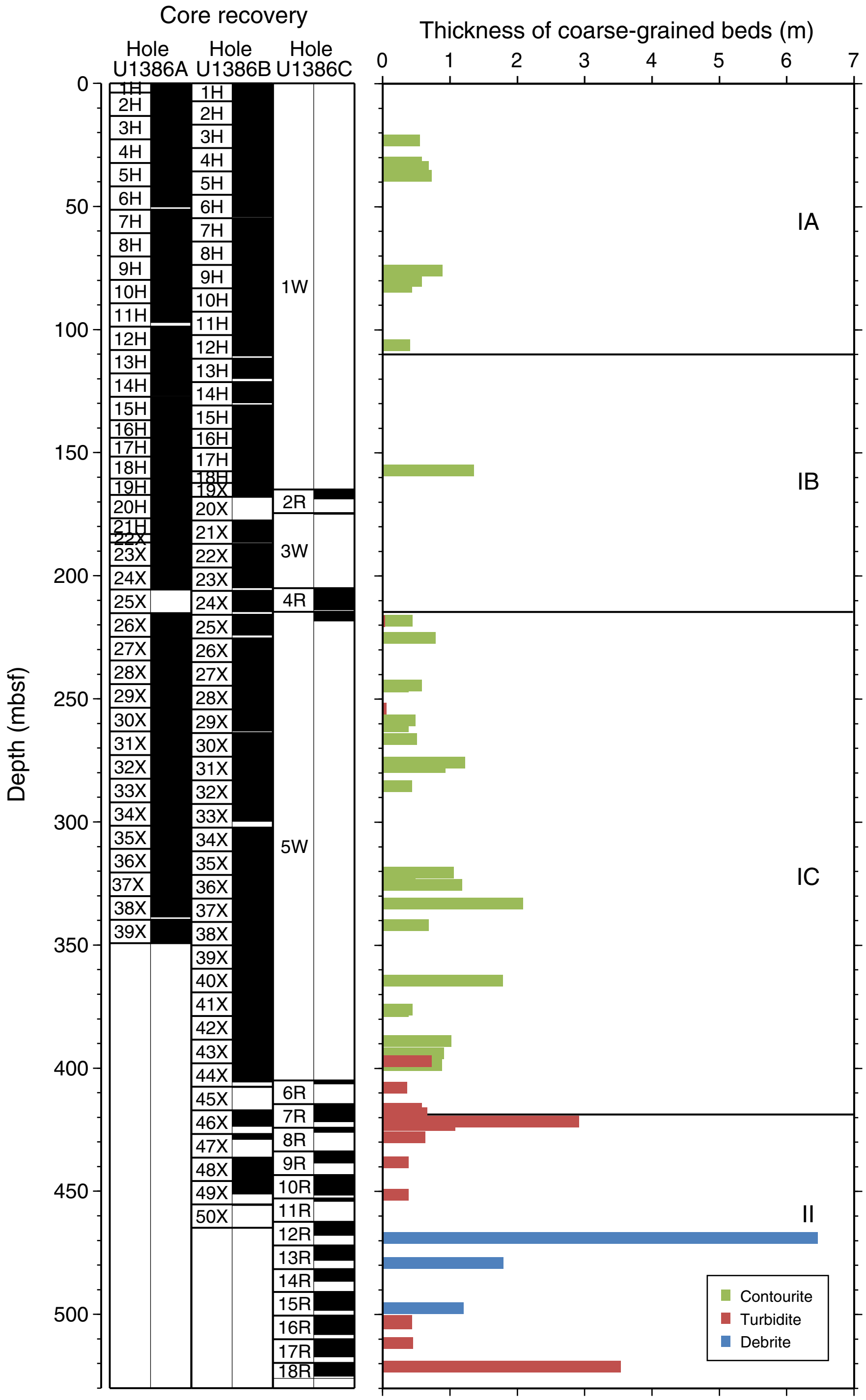

Figure F28. Biostratigraphic events vs. depth, Site U1386. Events are plotted at their mean depth (Table T6). For Hole U1386C, solid symbols are nannofossil datums and open symbols are planktonic foraminifer events.

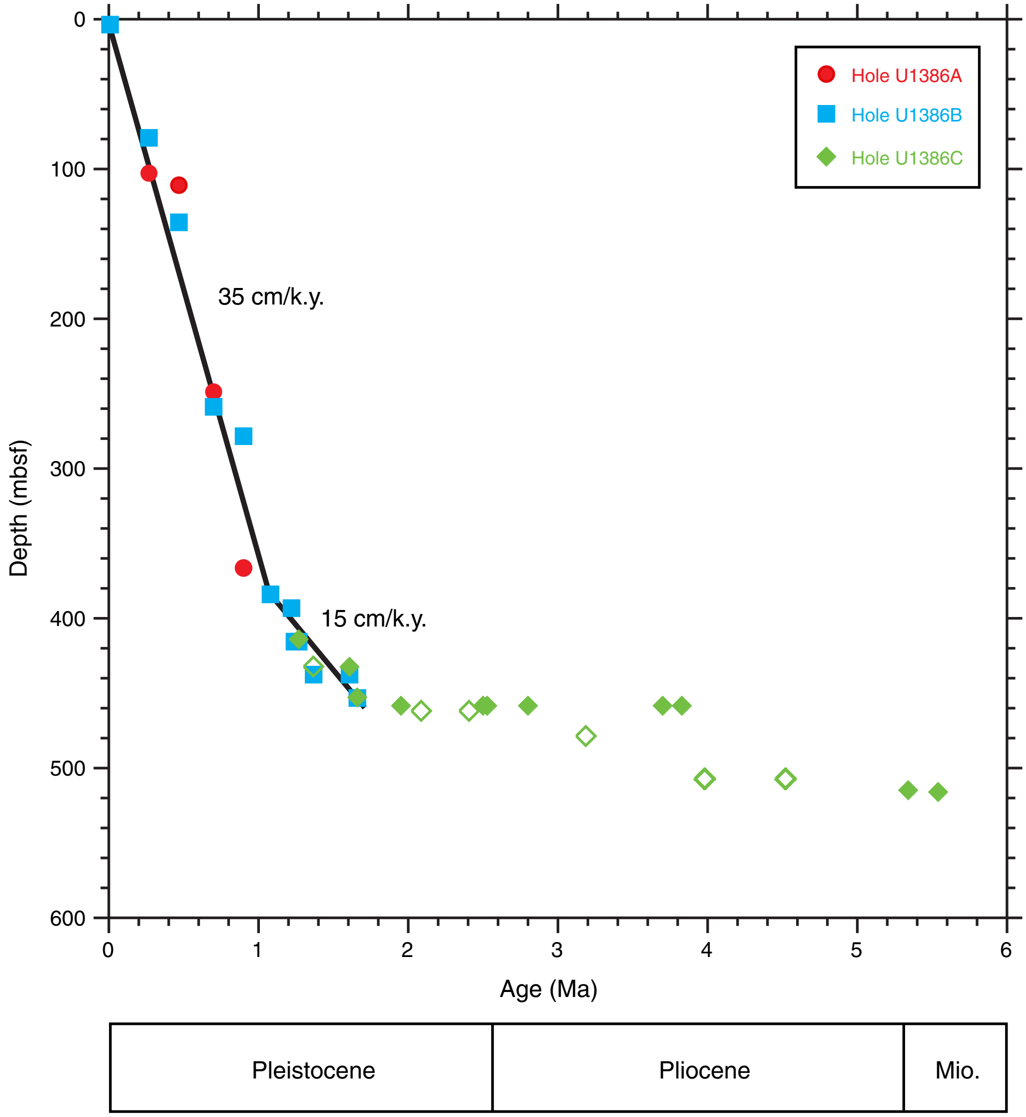

Figure F29. Preliminary pollen results from the analysis of 13 samples from Site U1386. Mediterranean forest is mainly deciduous and evergreen *Quercus, Olea,* and *Pistacia*. Heathland is Ericaceae. Inset photograph (1000×) is of Taxodiaceae/Cupressaceae morphotype, ~30 µm in size, which is abundant in Sample 339-U1386C-9R-CC. Preservation: G = good, M = moderate, P = poor.

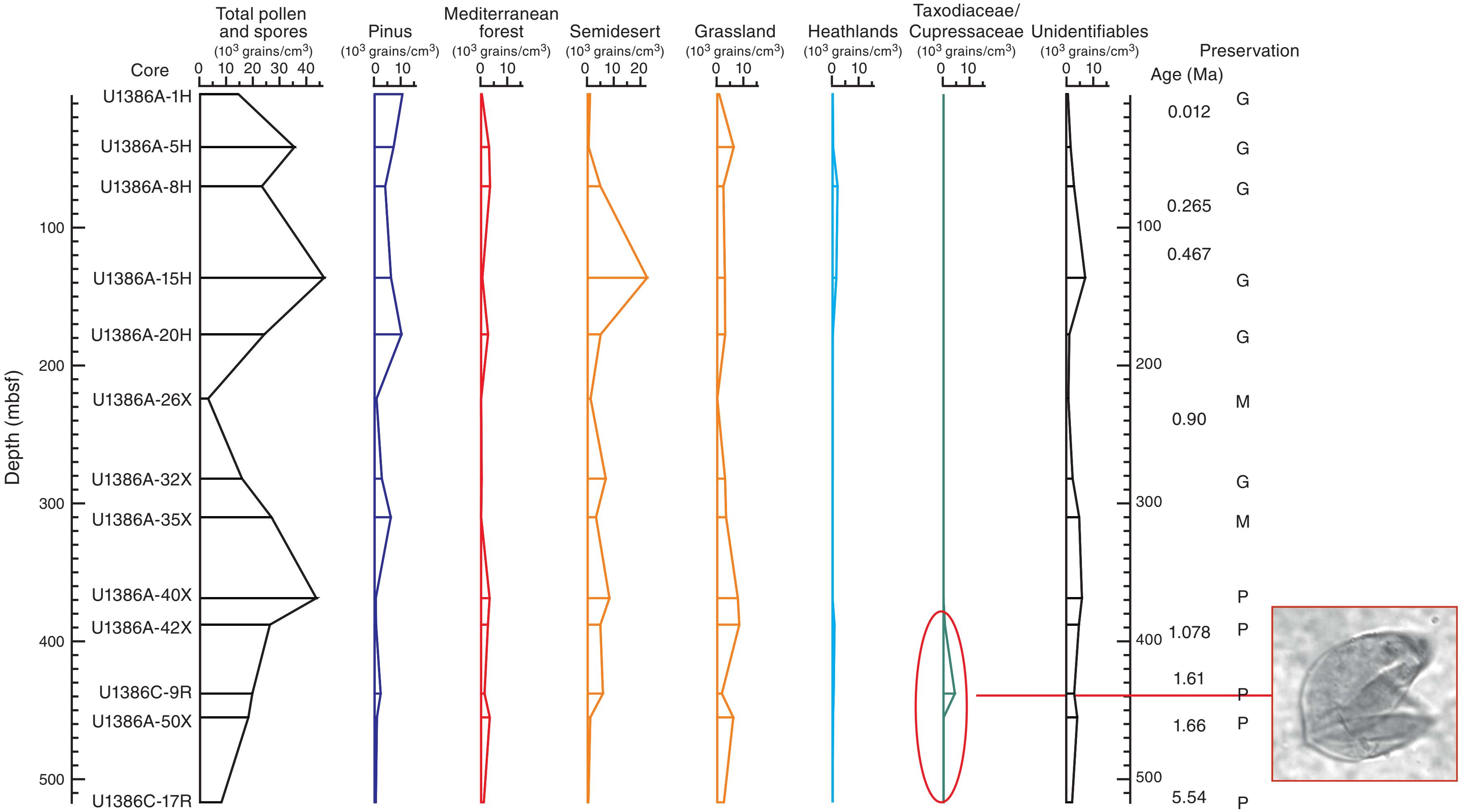

Figure F30. Stratigraphic distribution of ostracod abundance and ostracod assemblages at Site U1386. Downhole relative abundance of Assemblage B is indicated by the light green line and plotted on the scale in the upper *x*-axis. Relative abundances of *Bythoceratina* and *Pterigocythereis* are plotted on the lower *x*-axis. See text for details. Light yellow shaded area = Mid-Pleistocene Transition between 1.2 and 0.6 Ma. MPR = mid-Pleistocene revolution.

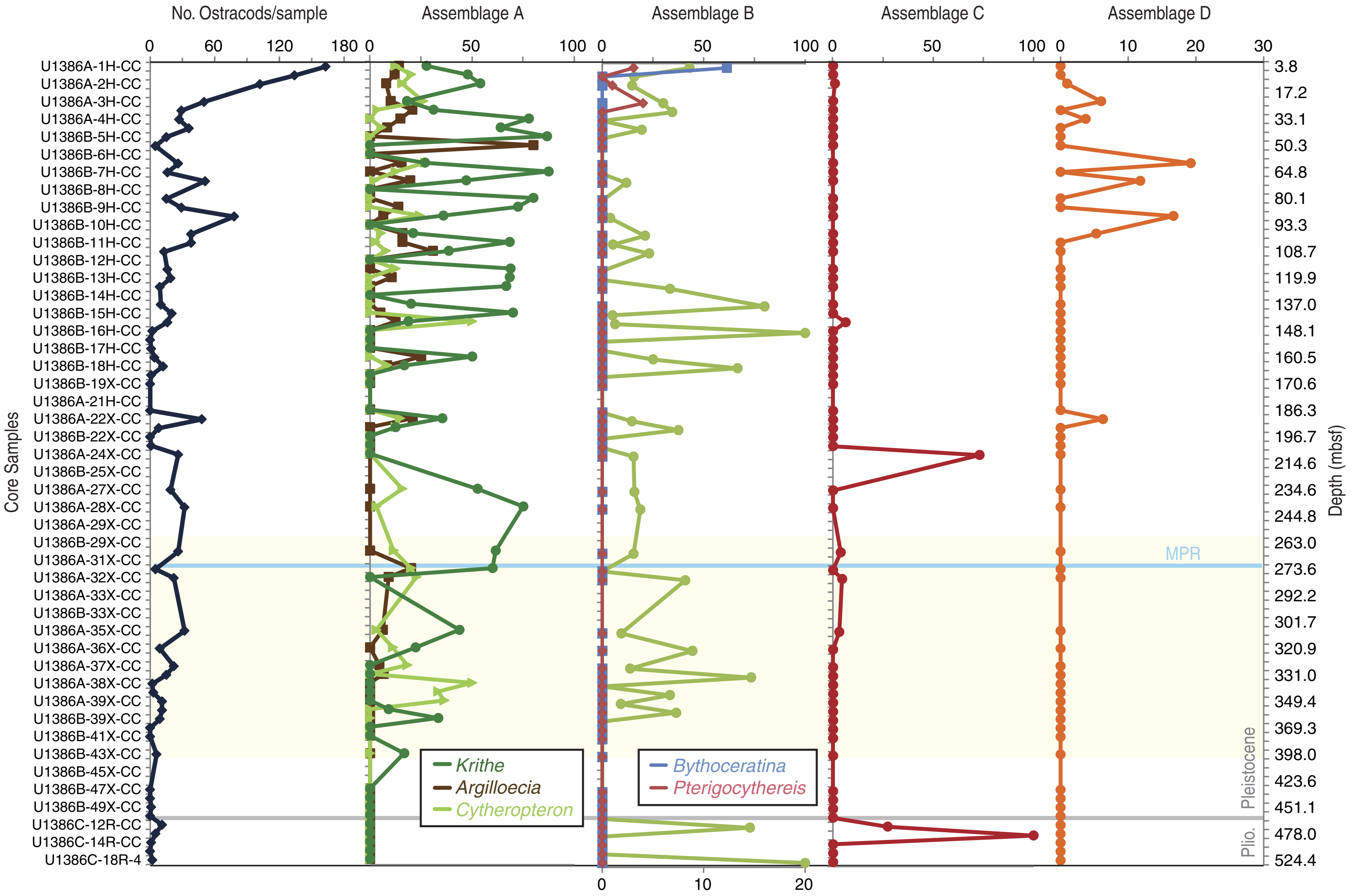

Figure F31. Paleomagnetism after 20 mT AF demagnetization, Site U1386. Blue triangles = discrete sample locations, yellow circles = component inclinations of discrete samples with maximum angular deviation less than ~15°. In the Chron columns, black = normal polarity, white = reversed polarity, and gray = zones without a clear magnetostratigraphic interpretation. In Inclination columns, blue dashed lines = expected geomagnetic axial dipole inclinations at the site latitude during reversed (left) and normal (right) polarities. In Declination columns, light blue circles = original declinations and dark blue squares = FlexIt tool–corrected declinations. In Susceptibility columns, gray lines represent SHMSL susceptibility plus 25 × 10^{-5} volume SI to better show the comparison with WRMSL susceptibility (black lines). **A.** Hole U1386A APC cores. (Continued on next four pages.)

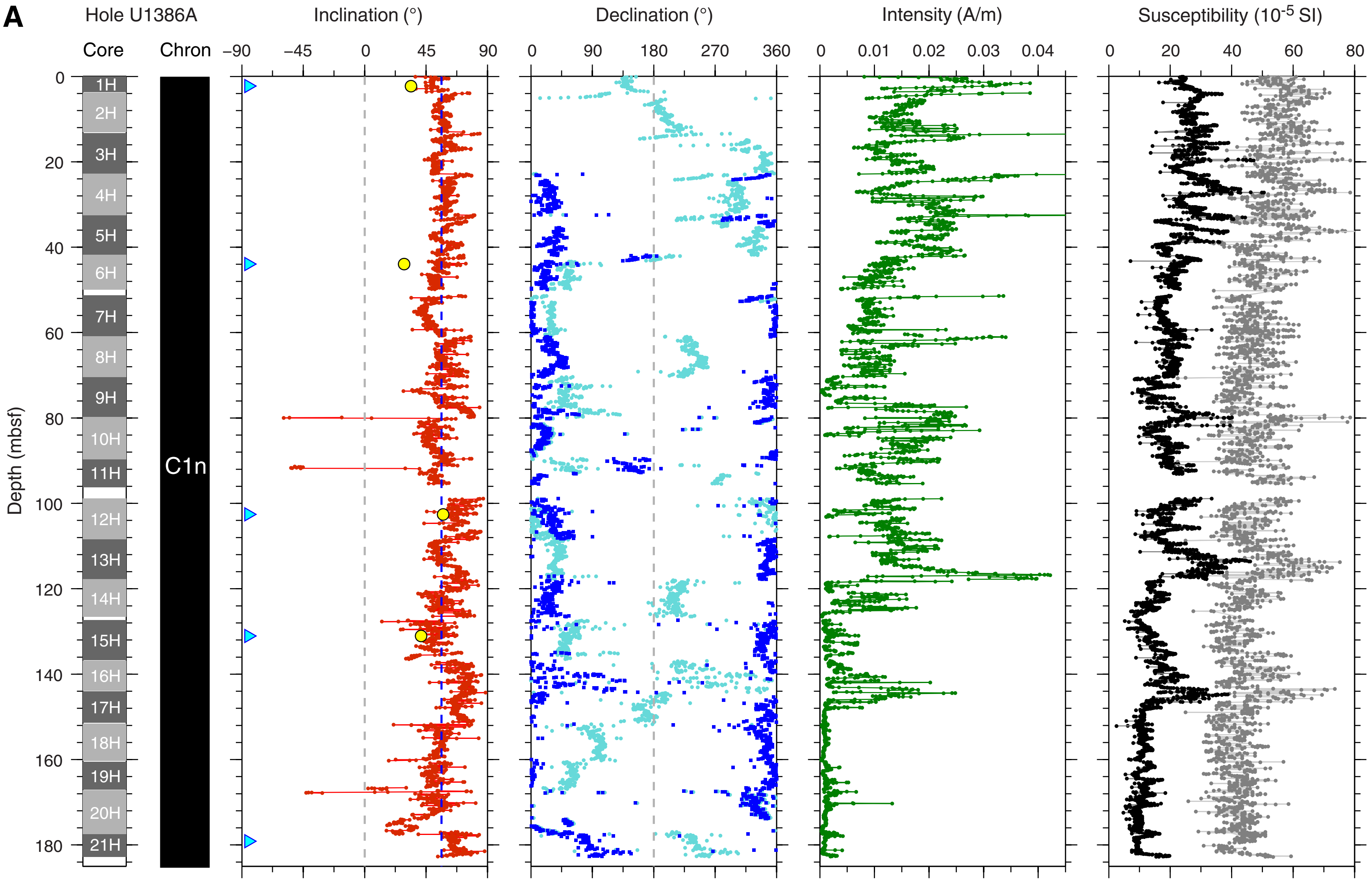

Figure F31 (continued). B. Hole U1386A XCB cores. (Continued on next page.)

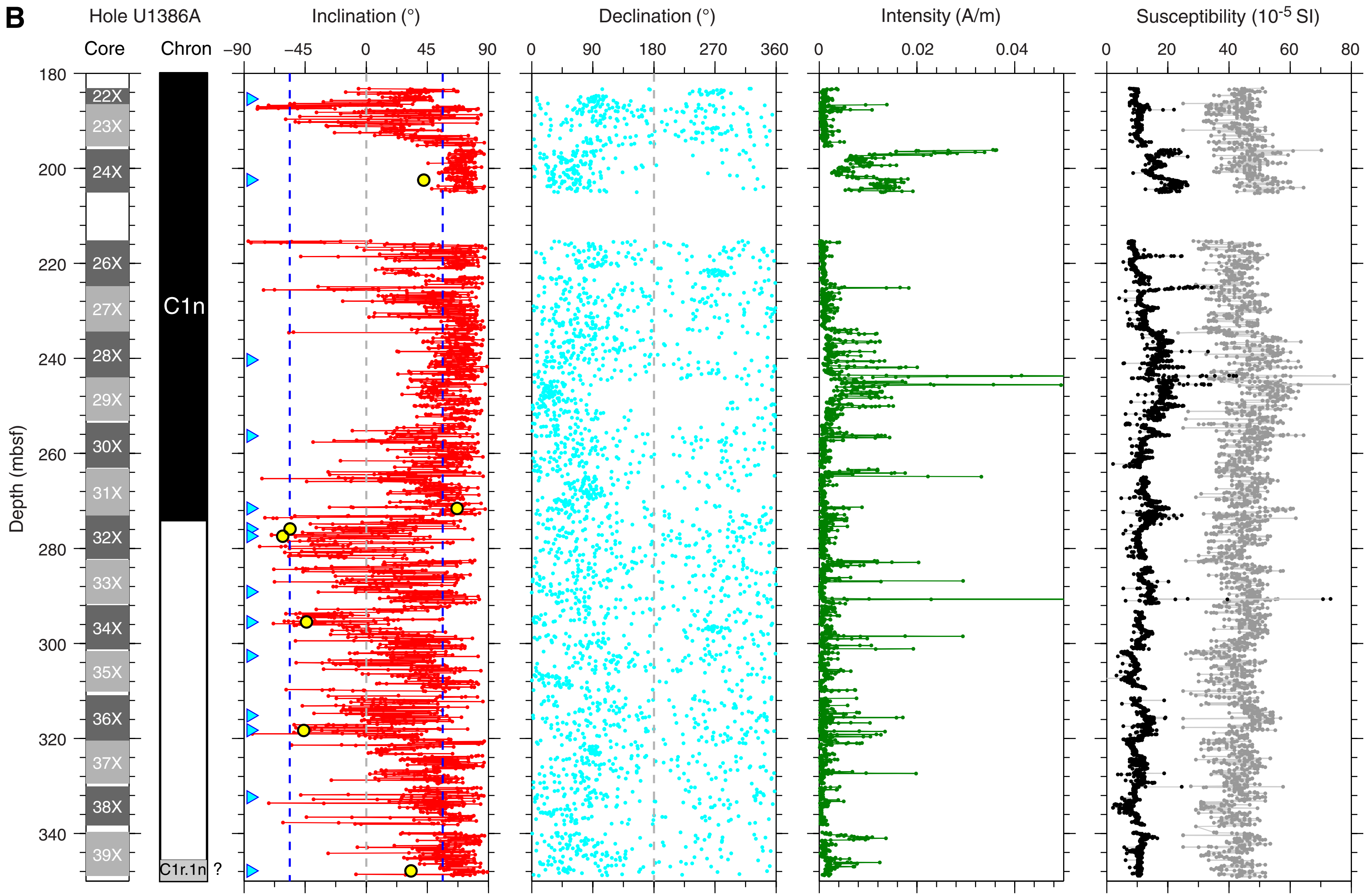

Figure F31 (continued). C. Hole U1386B APC cores. (Continued on next page.)

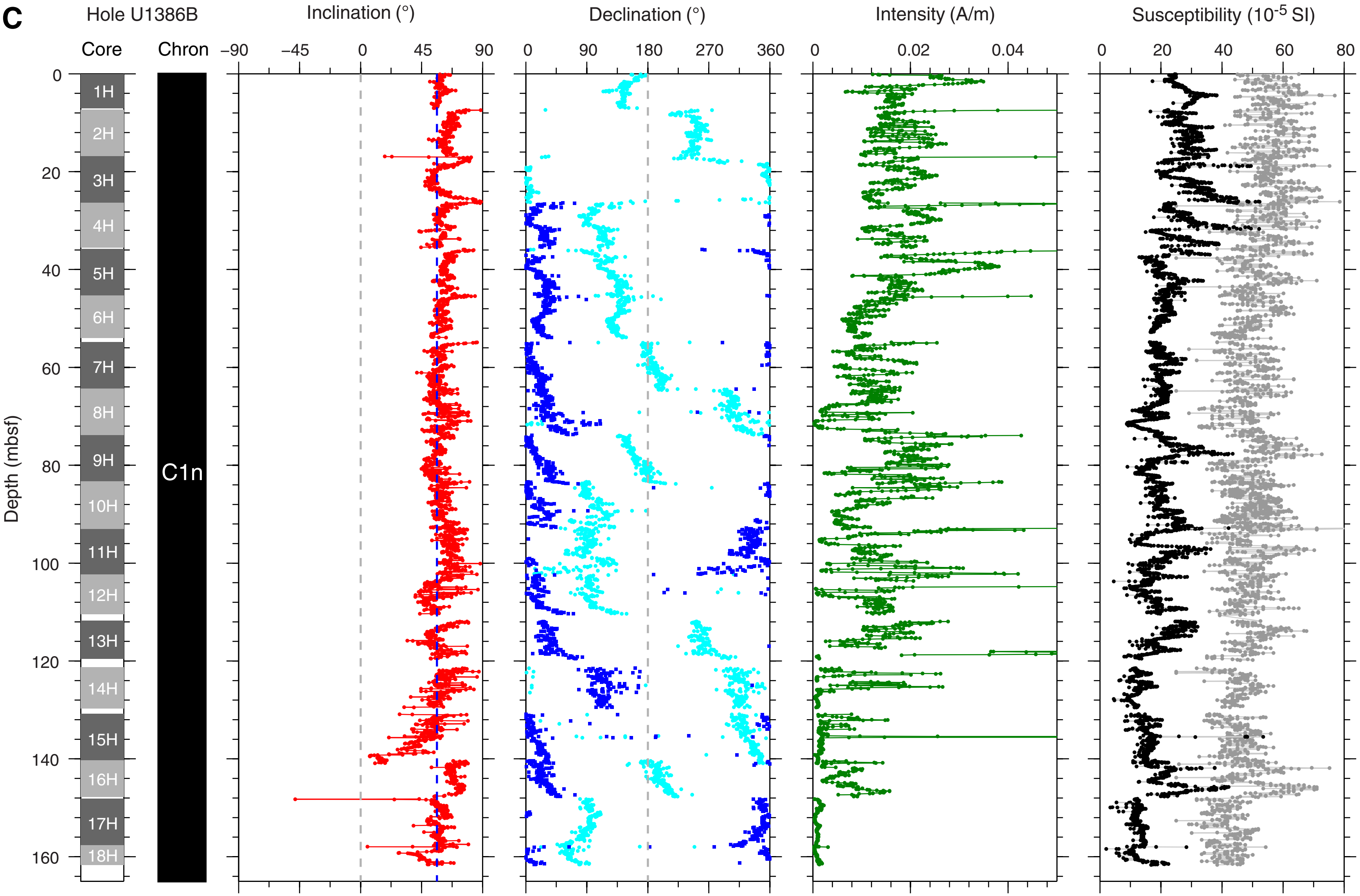

Figure F31 (continued). D. Hole U1386B XCB cores. (Continued on next page.)

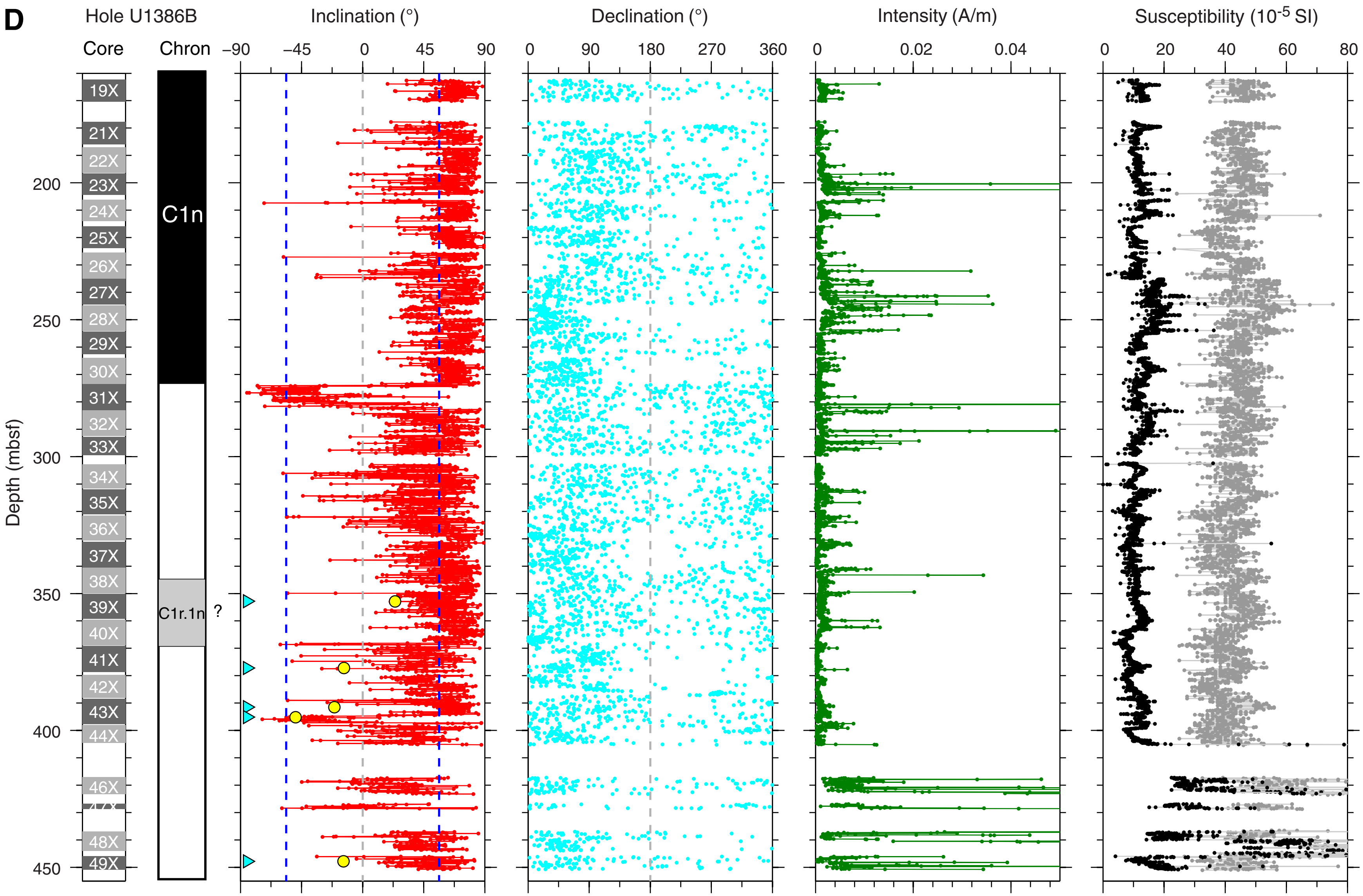

Figure F31 (continued). E. Hole U1386C RCB cores.

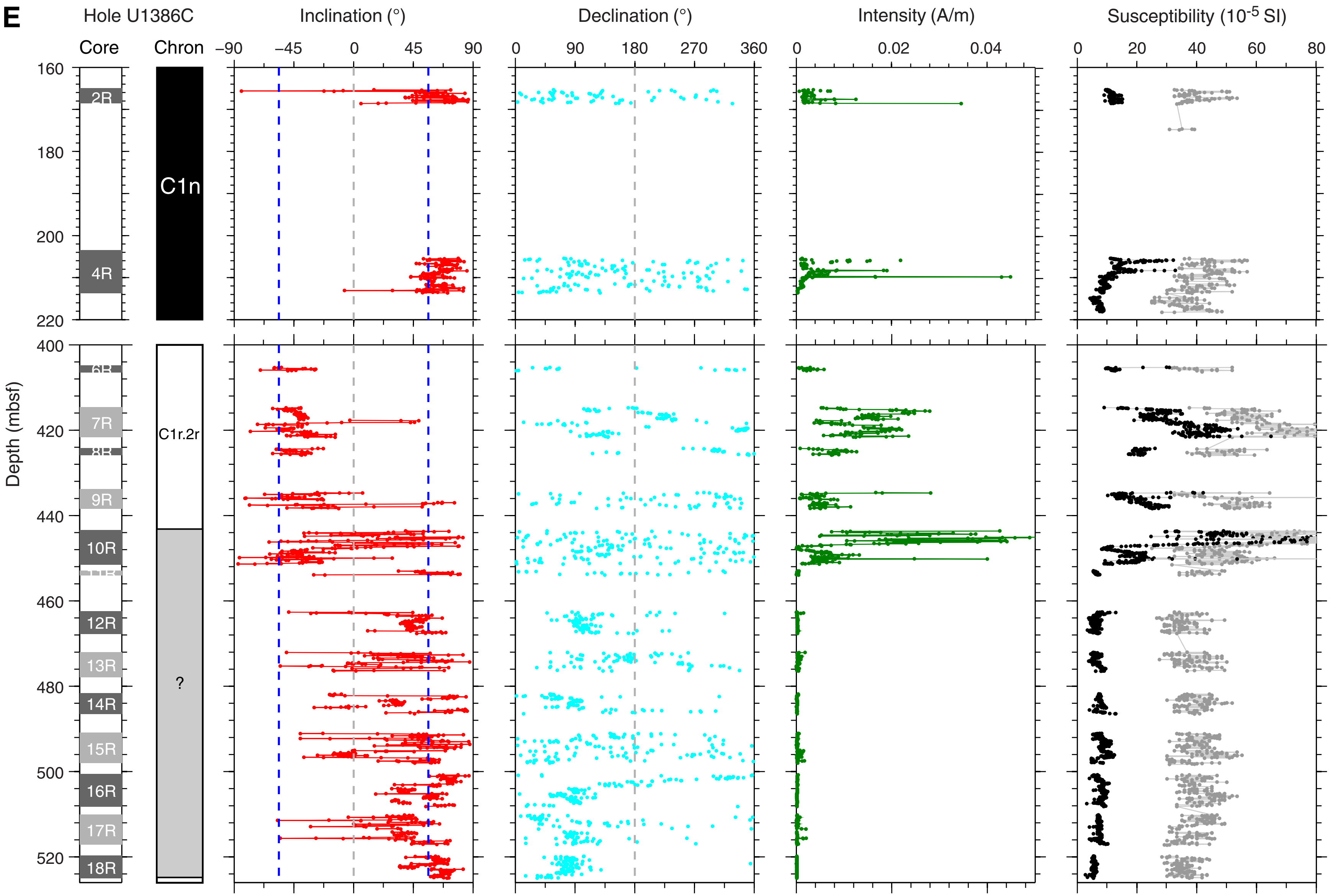

Figure F32. AF demagnetization results for eight discrete samples, Site U1386. For each sample, the right plot shows the vector endpoints of paleomagnetic directions measured after each demagnetization treatment on an orthogonal projection (Zijderveld) plot. Squares = horizontal projections, circles = vertical projections. The left plot shows the intensity variation with progressive demagnetization. Orthogonal projection plots illustrate the removal of a steep drilling overprint by ~15–20 mT peak field AF demagnetization and possible ARM acquisition during high-peak field (>55 mT) AF demagnetization, with the remaining magnetization providing a well-resolved characteristic remanent magnetization.

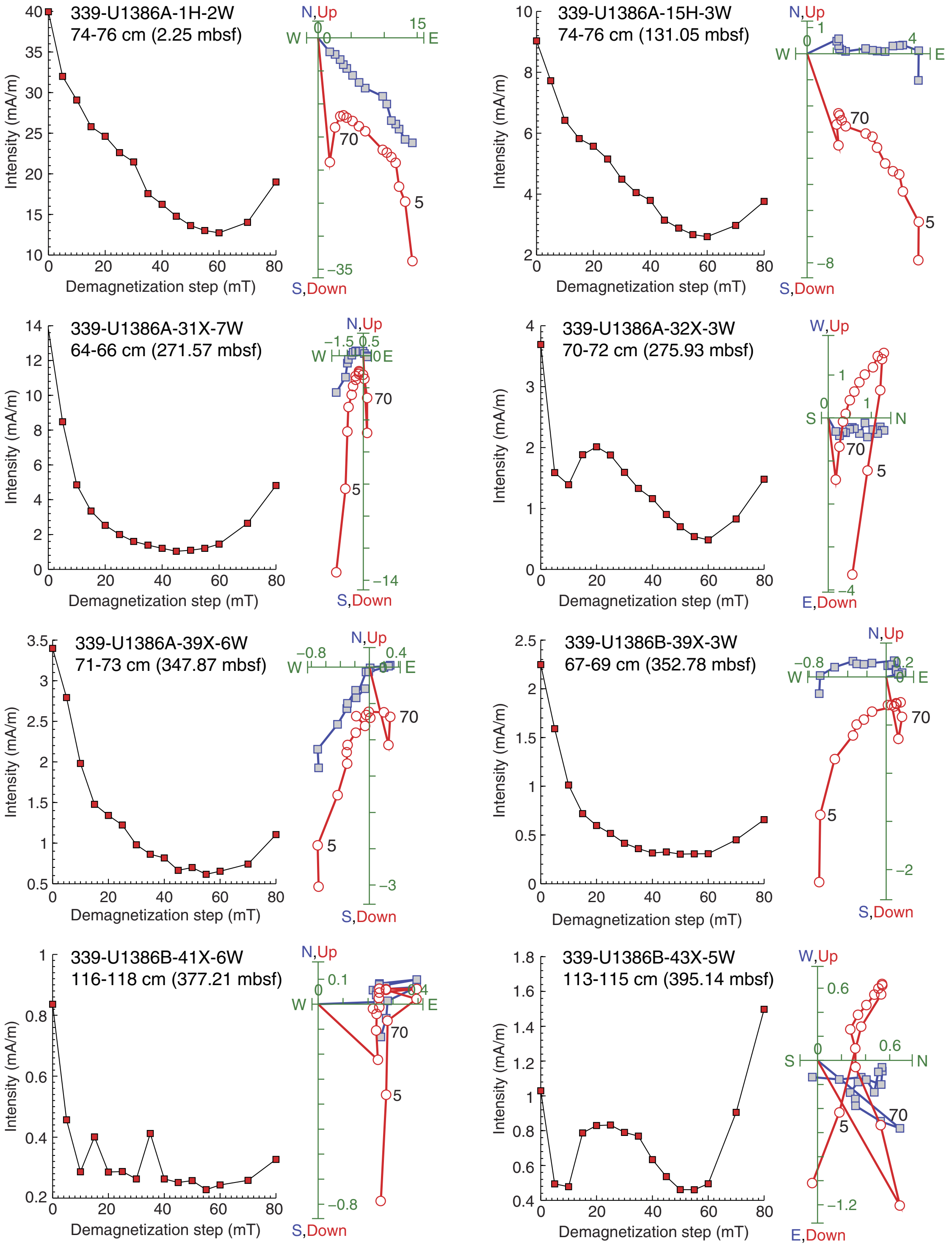

Figure F33. Plots of *P*-wave velocity (PWV) measured in Hole U1386B on the Whole-Round Multisensor Logger (WRMSL; green line) and Section Half Measurement Gantry (discrete samples) in automatic (solid circles) and manual (open circles) mode in Hole U1386A, wet bulk density measurements in Holes U1386A (red diamonds) and U1386B (green diamonds), gamma ray attenuation density measured on the WRMSL in Holes U1386B (black line) and U1386C (gray line), and magnetic susceptibility (MS) measured on the WRMSL in Holes U1386B (black line) and U1386C (gray line) and on split cores in Holes U1386B (green) and U1386C (light green). Note that records were cleaned for outliers and bad data at section ends, and susceptibility is plotted on a logarithmic scale to account for the high range of values. PP = physical properties.

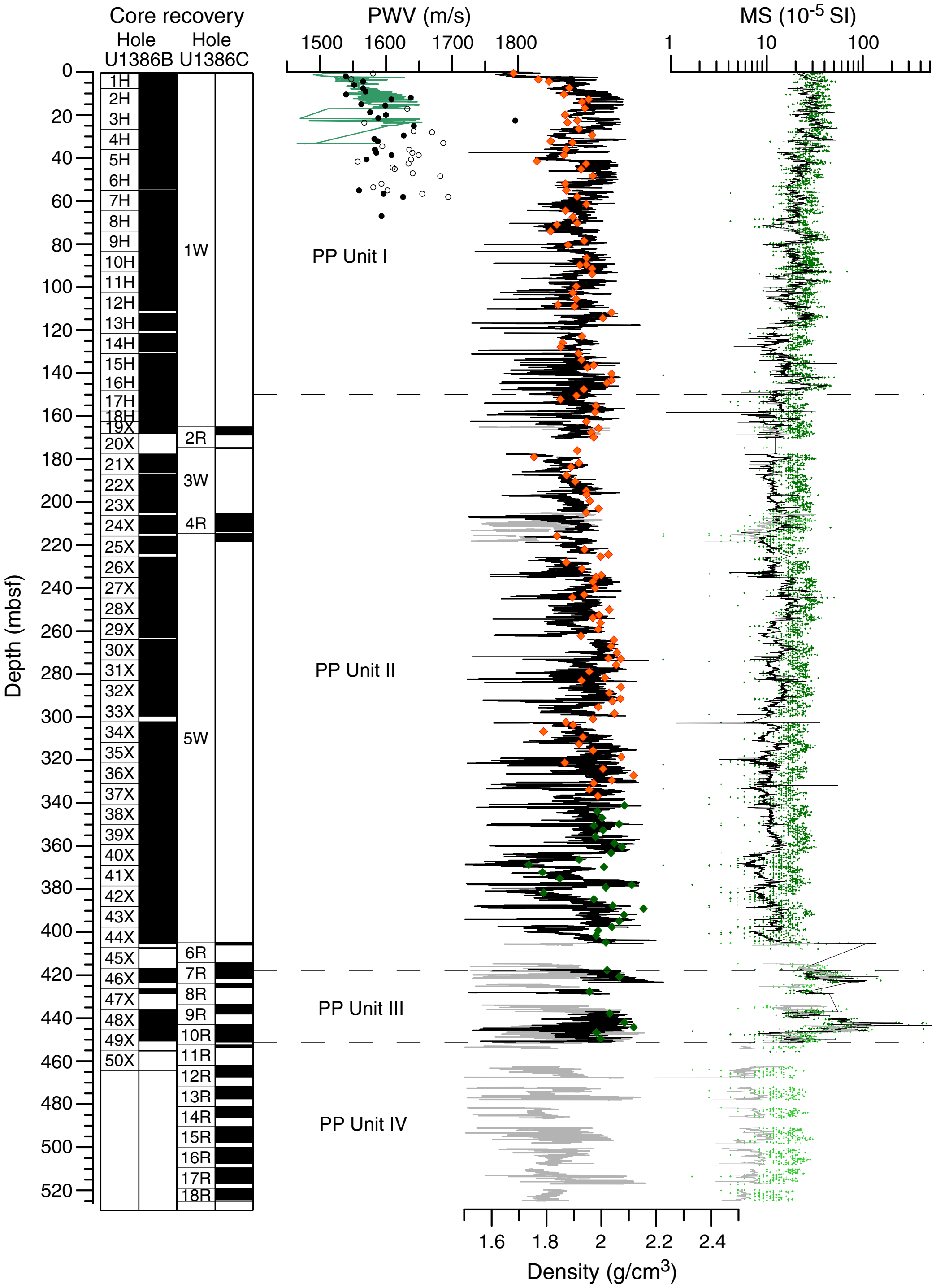

Figure F34. Plots of color reflectance (L* and a*) and natural gamma ray (NGR) measurements in Holes U1386B (black, red, and dark blue lines) and U1386C (gray, orange, and light blue lines). Note that the data have been cleared for outliers and bad data at section ends. PP = physical properties.

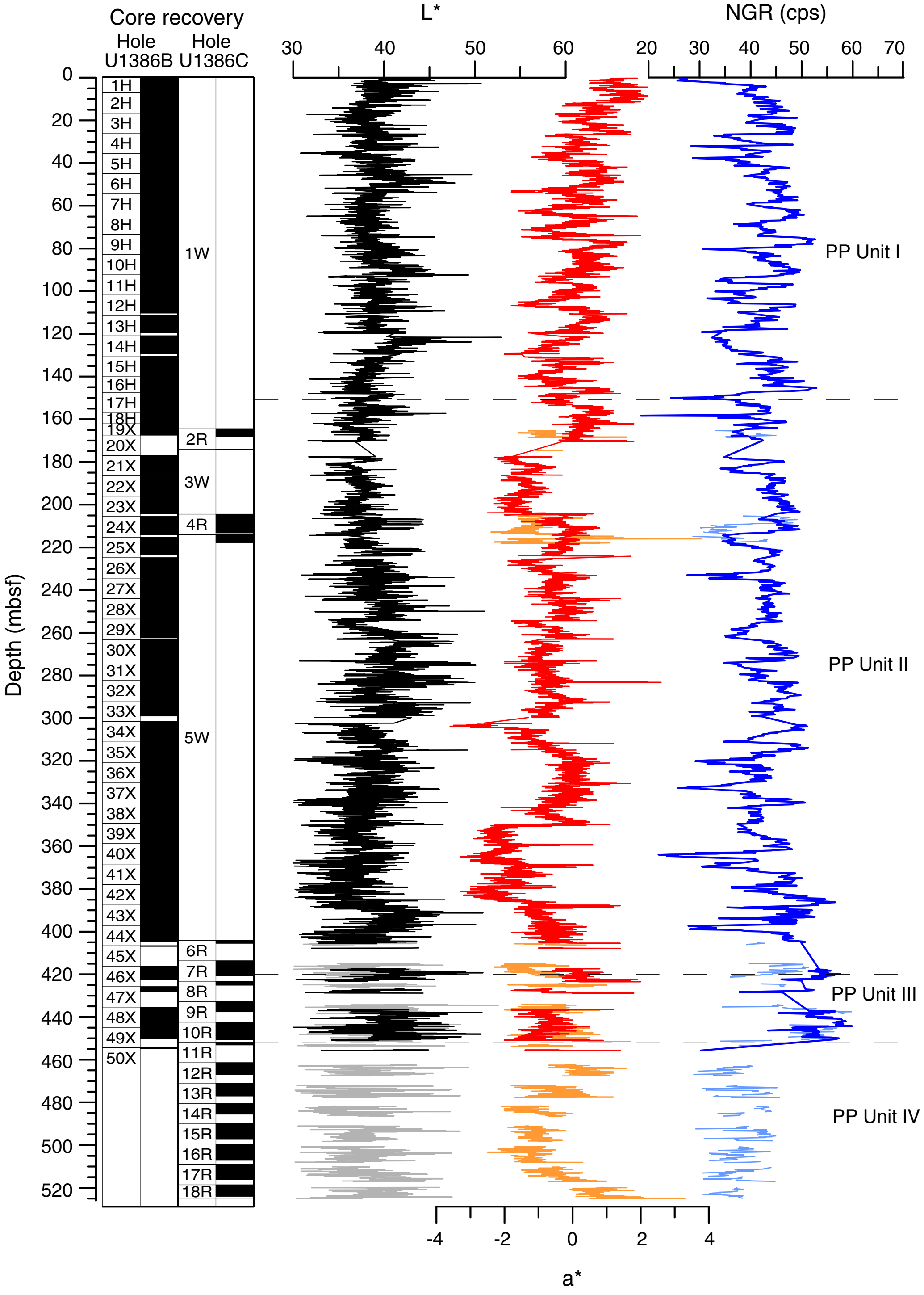

Figure F35. Plots of downhole distribution of discrete measurements of grain density, moisture content, and porosity in Holes U1386A (dark solid symbols), U1386B (light solid symbols), and U1386C (open symbols). PP = physical properties.

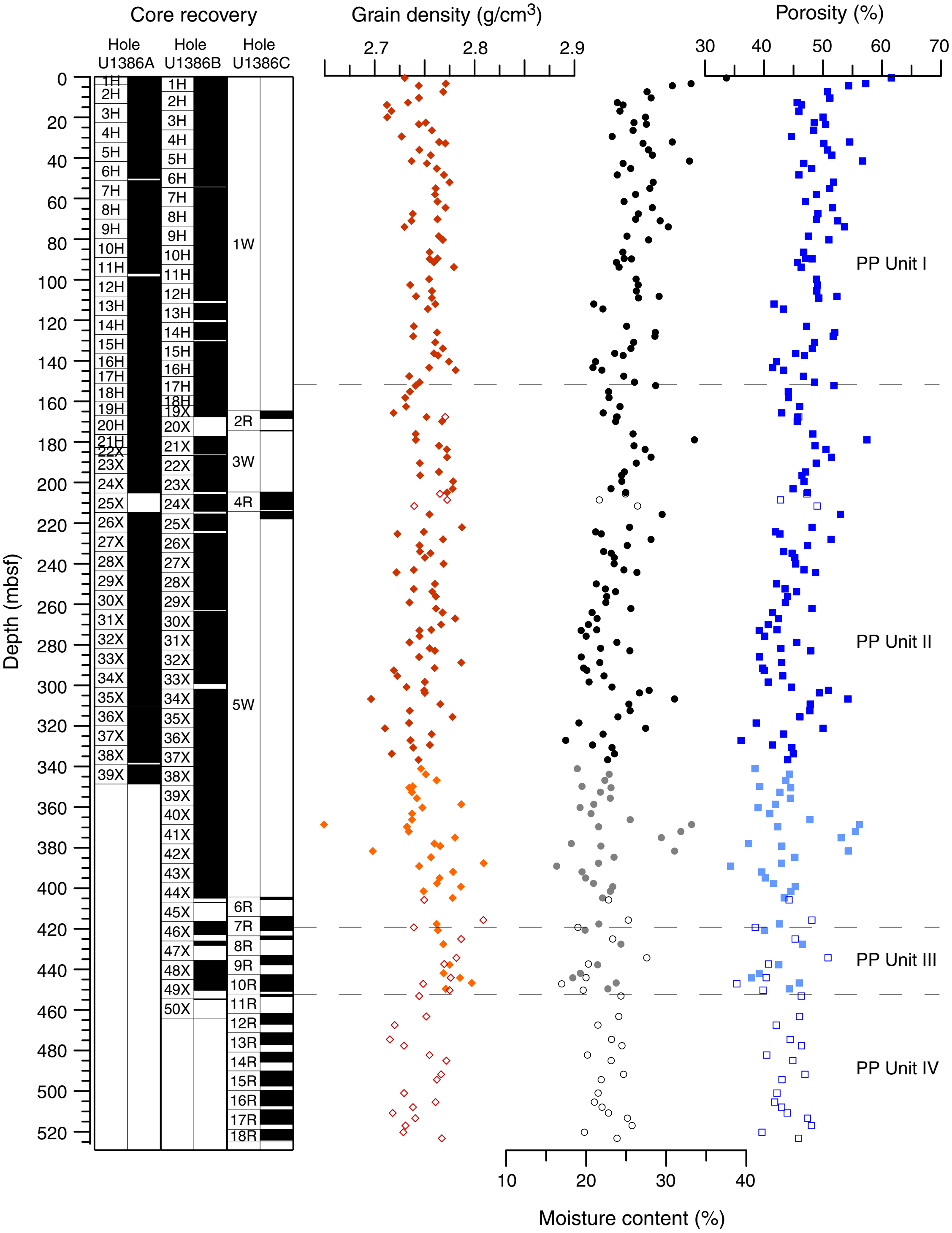

Figure F36. Plots of heat flow calculations, Site U1386. **A.** Sediment temperatures in Holes U1386A and U1386B. **B.** Thermal conductivity data from Hole U1386A (circles) with calculated thermal resistance (solid line). **C.** Bullard plot of heat flow calculated from a linear fit of the temperature data.

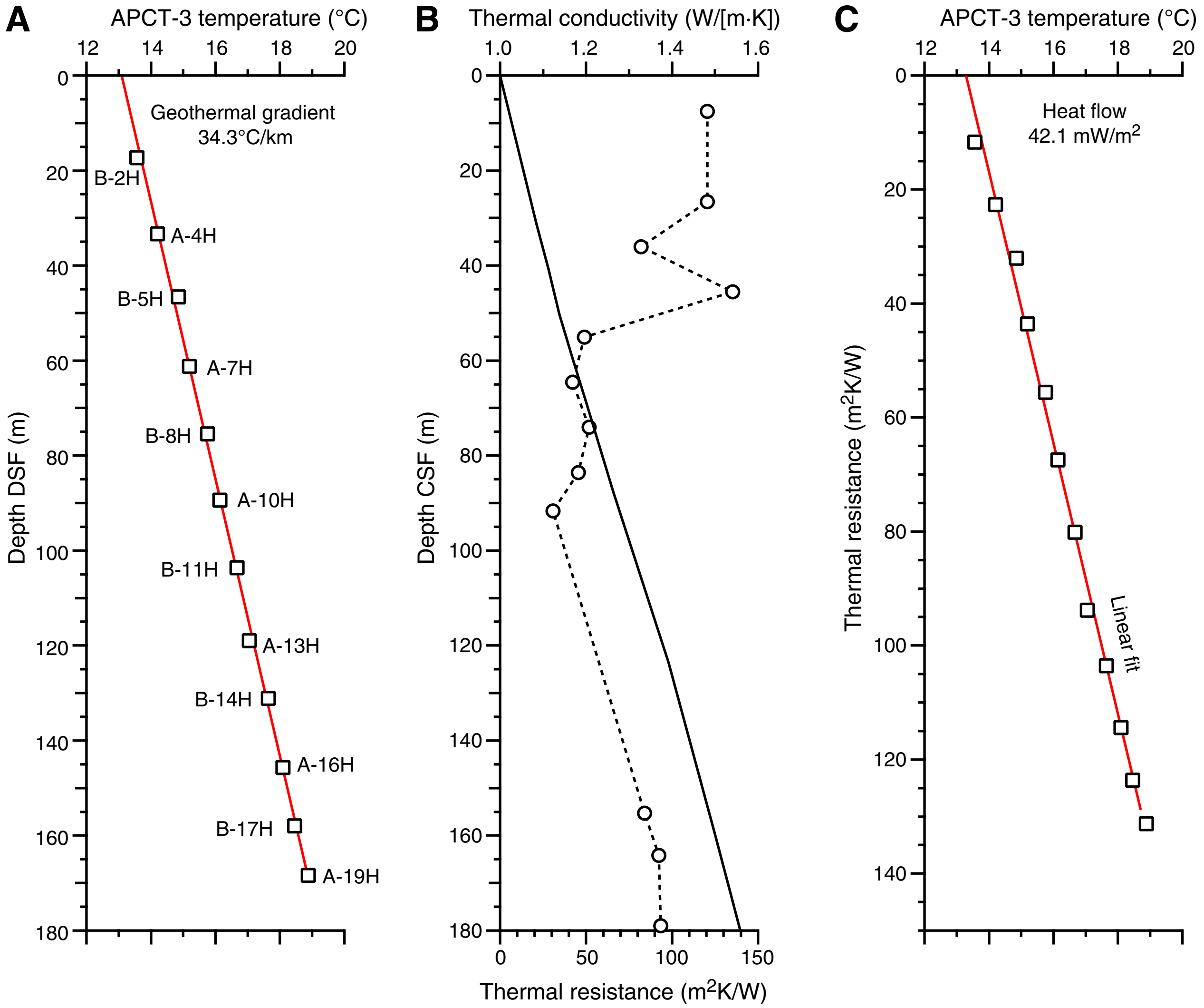

Figure F37. Plot of headspace gas analyses for volatile hydrocarbons, Site U1386.

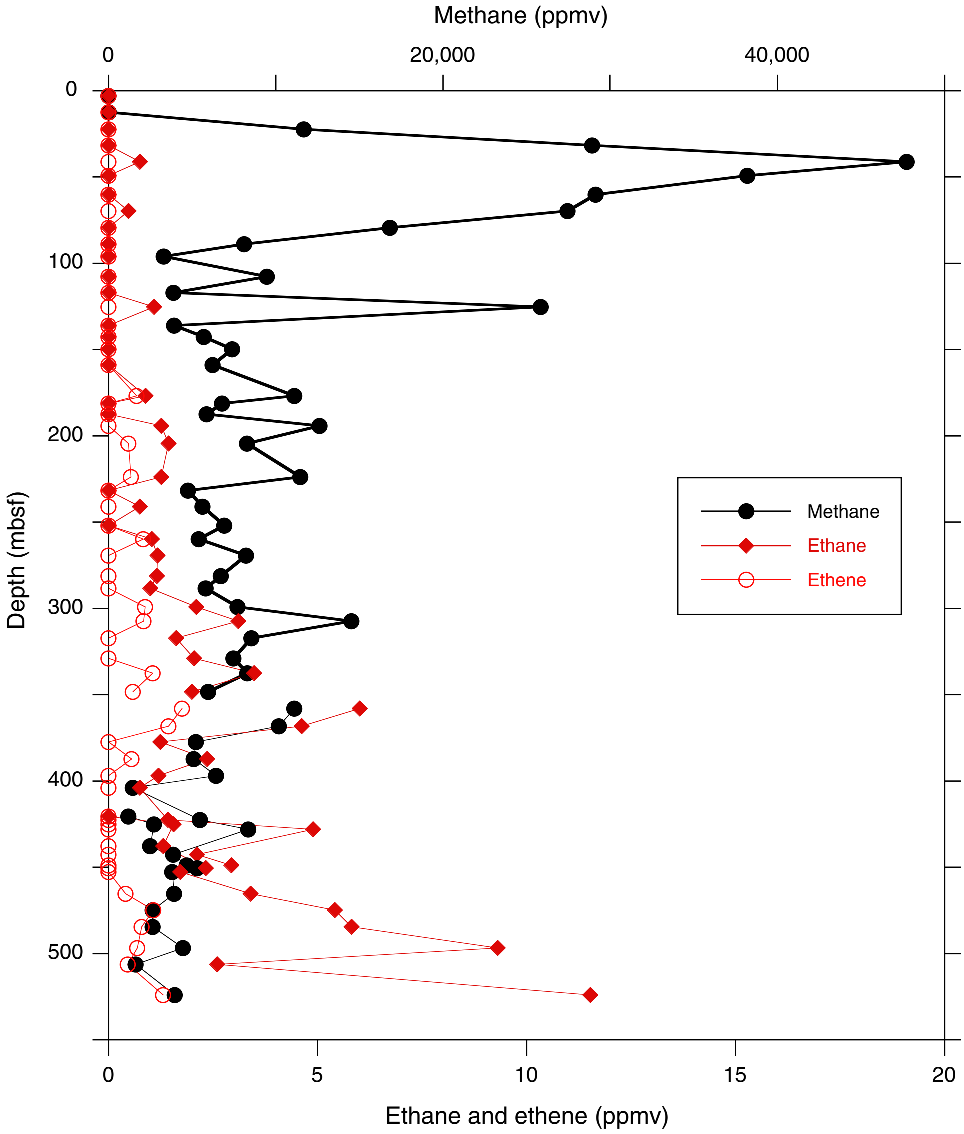

Figure F38. Plot of calcium carbonate, Site U1386. Solid circles = Hole U1386A, open circles = Hole U1386B, red diamonds = Hole U1386C.

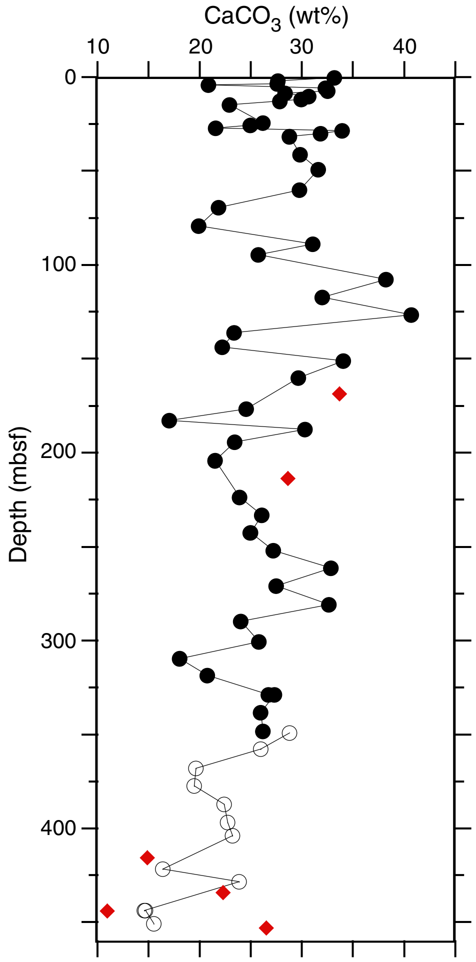

Figure F39. A–C. Plots of calculated total organic carbon (TOC), total nitrogen (TN), and C/N ratio, Hole U1386A.

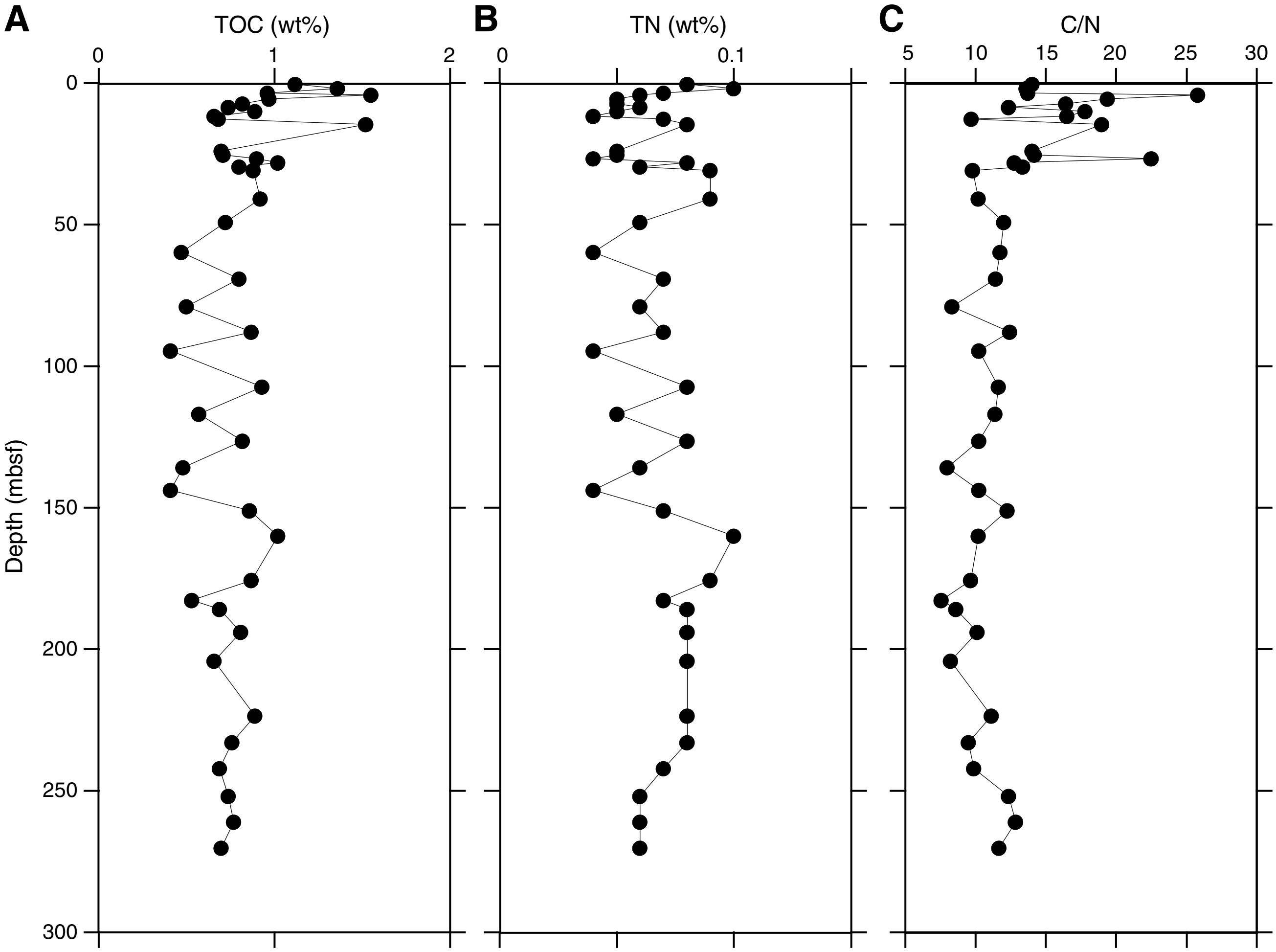

Figure F40. A–D. Plots of interstitial water sulfate, alkalinity, ammonium, and hydrocarbons (open circles = methane, solid circles = ethane), Hole U1386A.

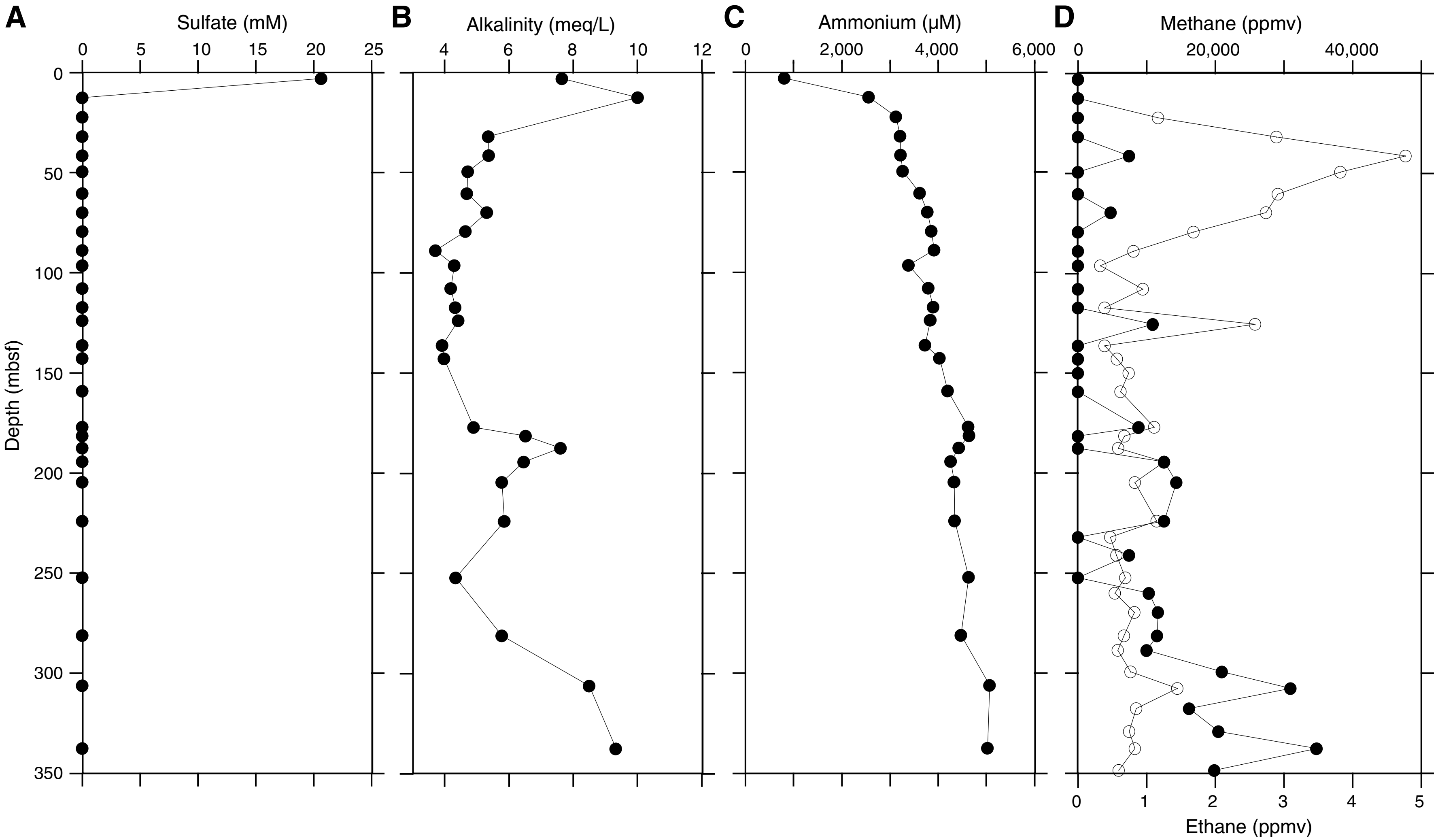

Figure F41. A–C. Plots of interstitial water calcium, magnesium, and potassium, Hole U1386A. Solid circles = inductively coupled plasma–atomic emission spectrometer measurement, open circles = ion chromatograph measurement.

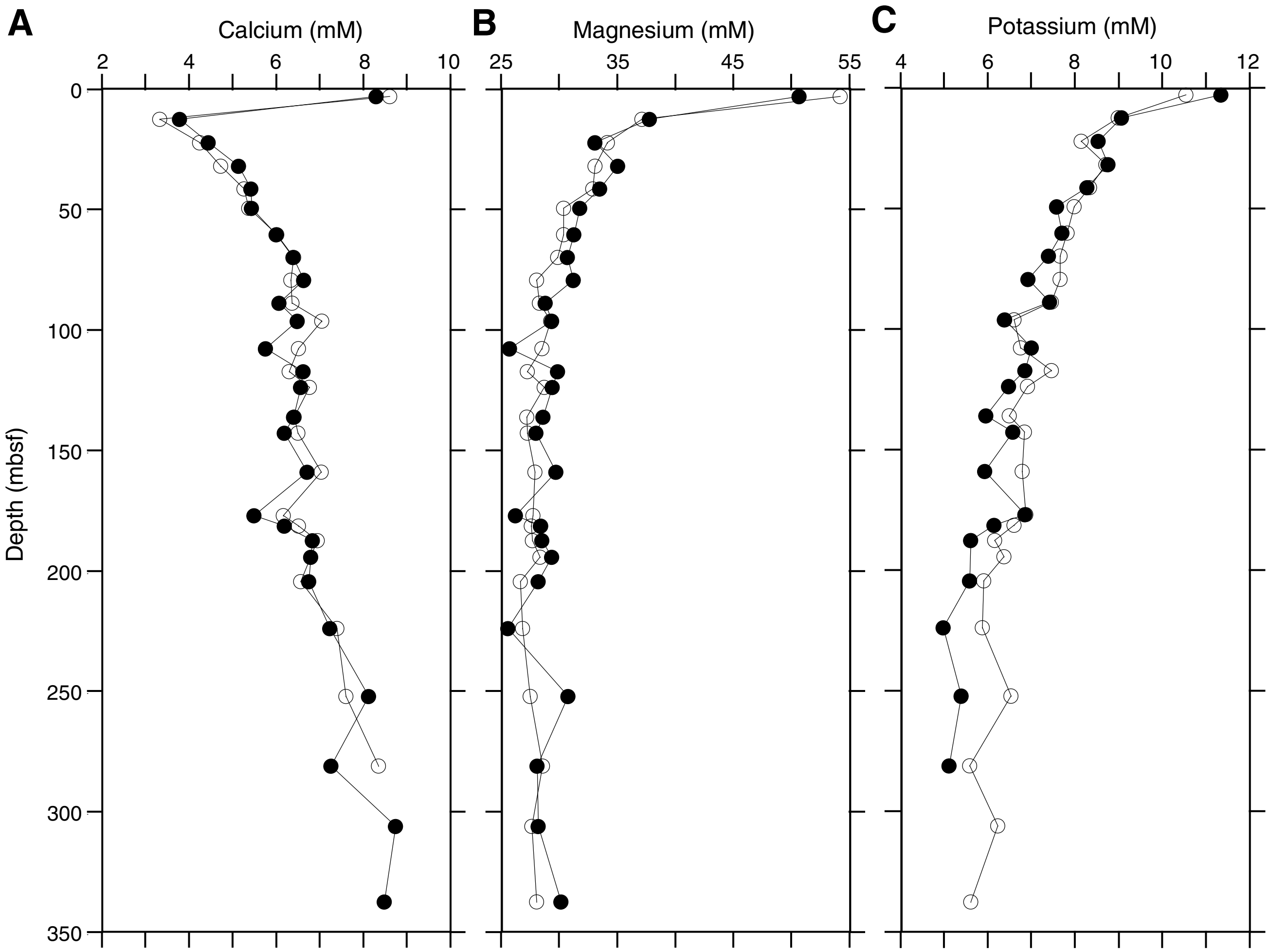

Figure F42. Plots of interstitial water chloride and Na^+/Cl^- ratio, Hole U1386A.

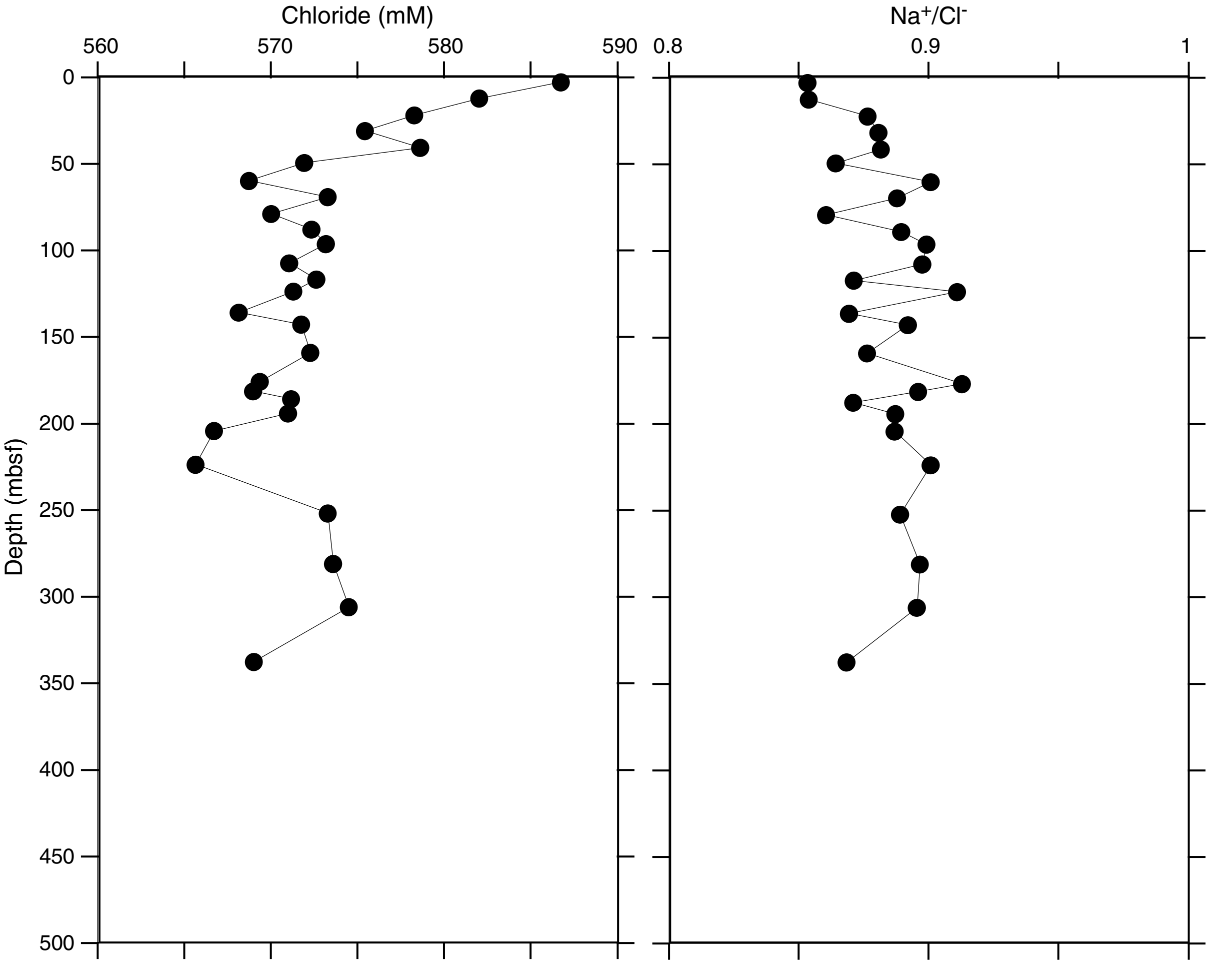

Figure F43. A, B. Plots of calcium vs. magnesium and calcium vs. strontium, Hole U1386A.

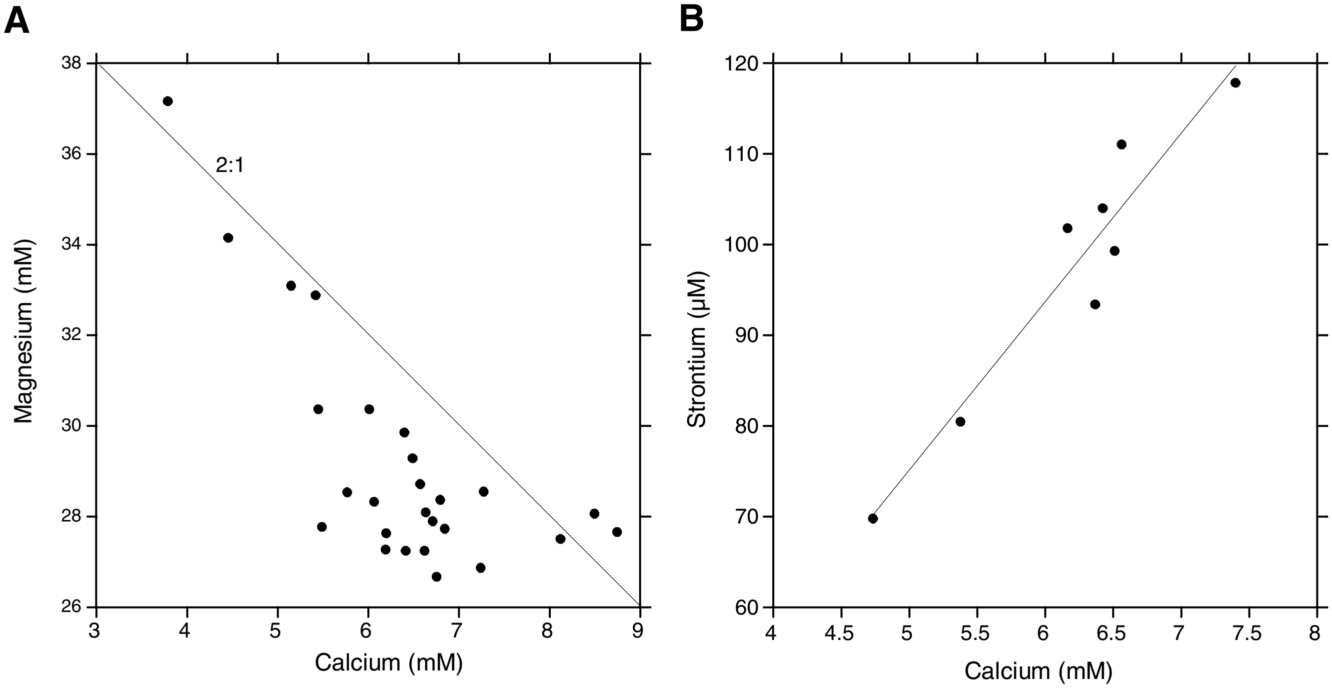

Figure F44. A–E. Plots of interstitial water strontium, barium, lithium, boron, and silicon, Hole U1386A.

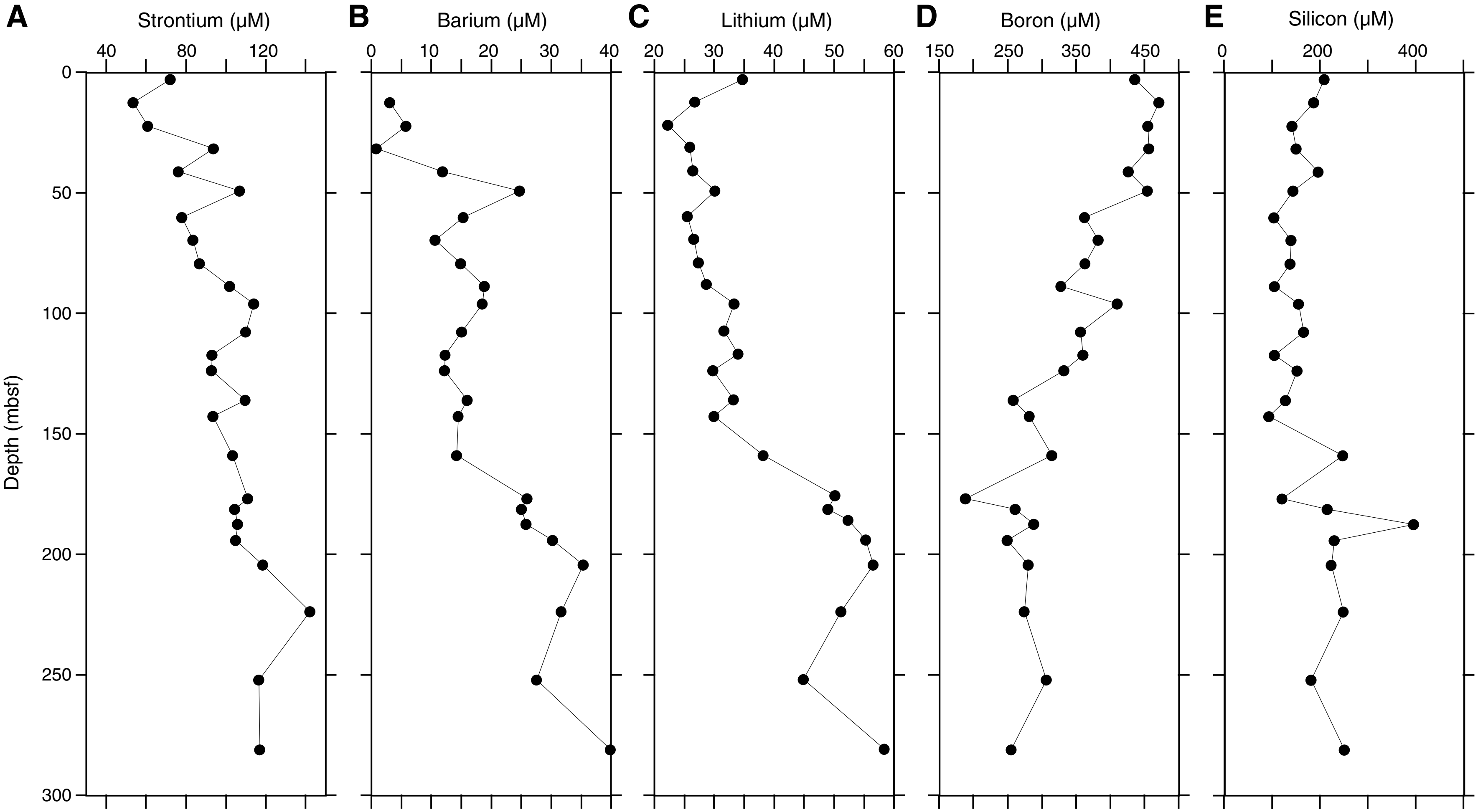

Figure F45. Plots of interstitial water stable isotopes and chloride from whole-round or syringe samples taken at the base of each core, Hole U1386A. Red circles = replicate analyses. VSMOW = Vienna standard mean ocean water.

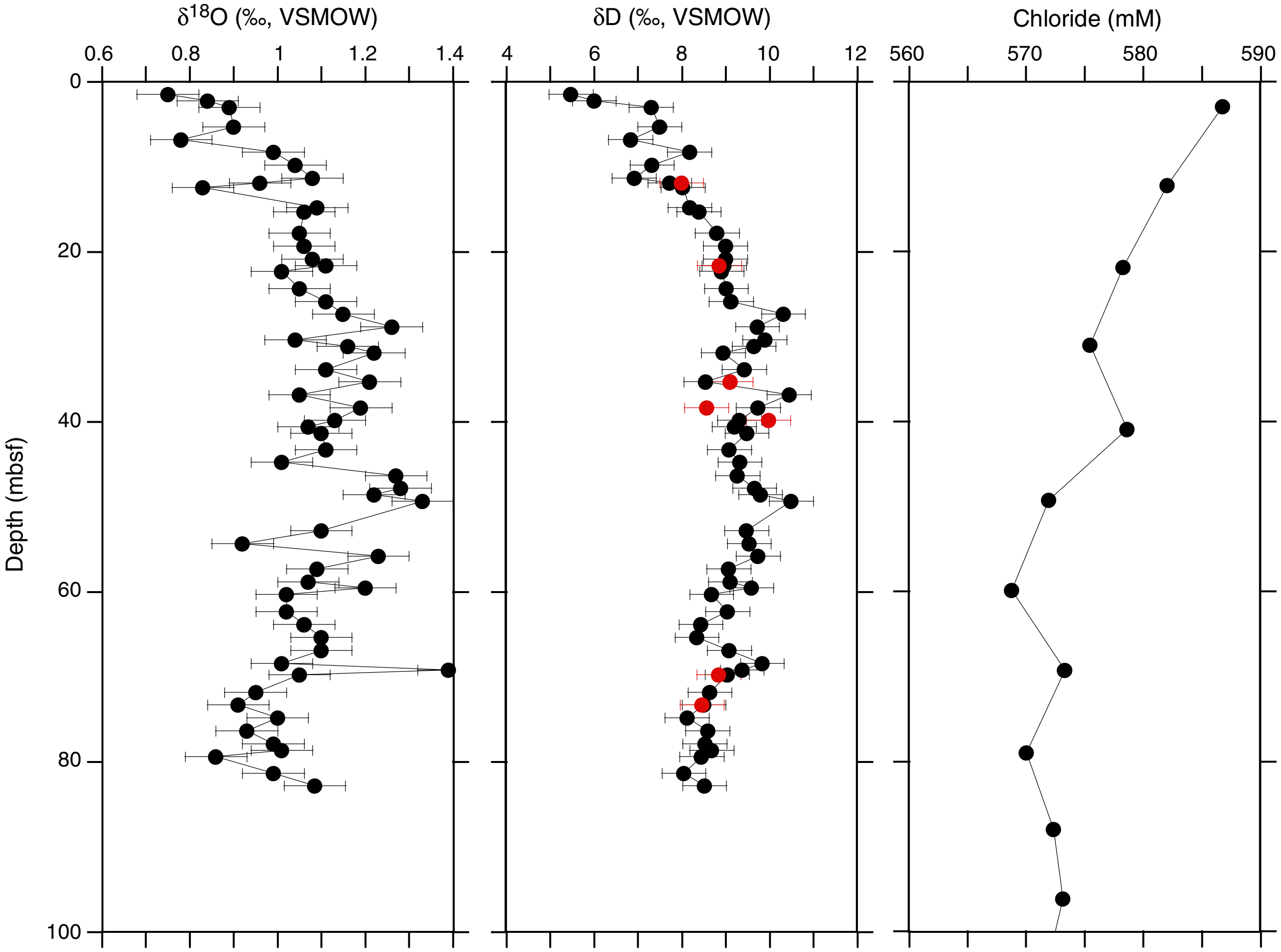

Figure F46. Plot of $\delta^{18}O$ vs. δD, Hole U1386A. Solid circles = data from nearby GEOTRACES Station 1, open circles = data from Site U1386. VSMOW = Vienna standard mean ocean water.

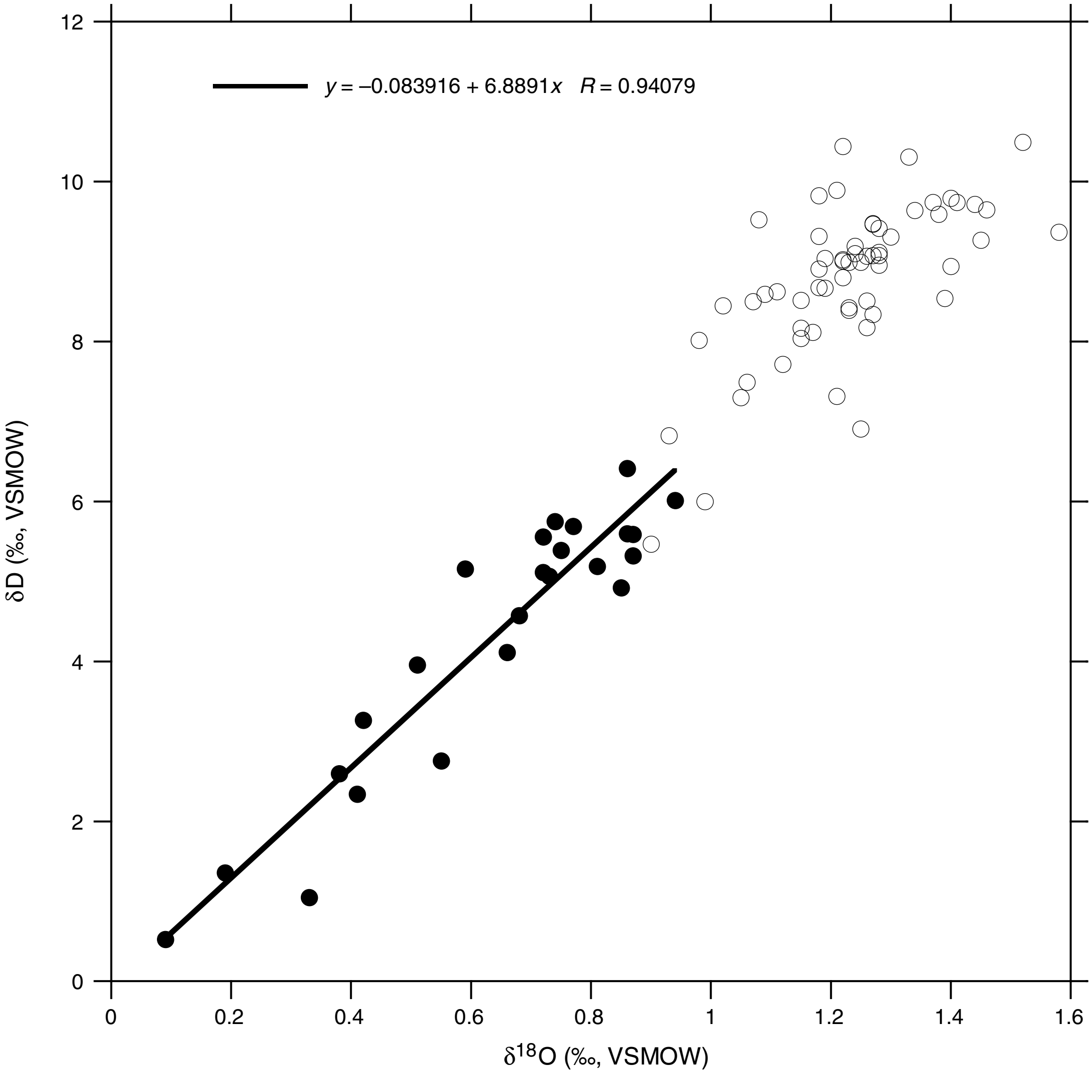

Figure F47. Logging operations summary diagram, Site U1386. FMS = Formation MicroScanner, VSP = vertical seismic profile.

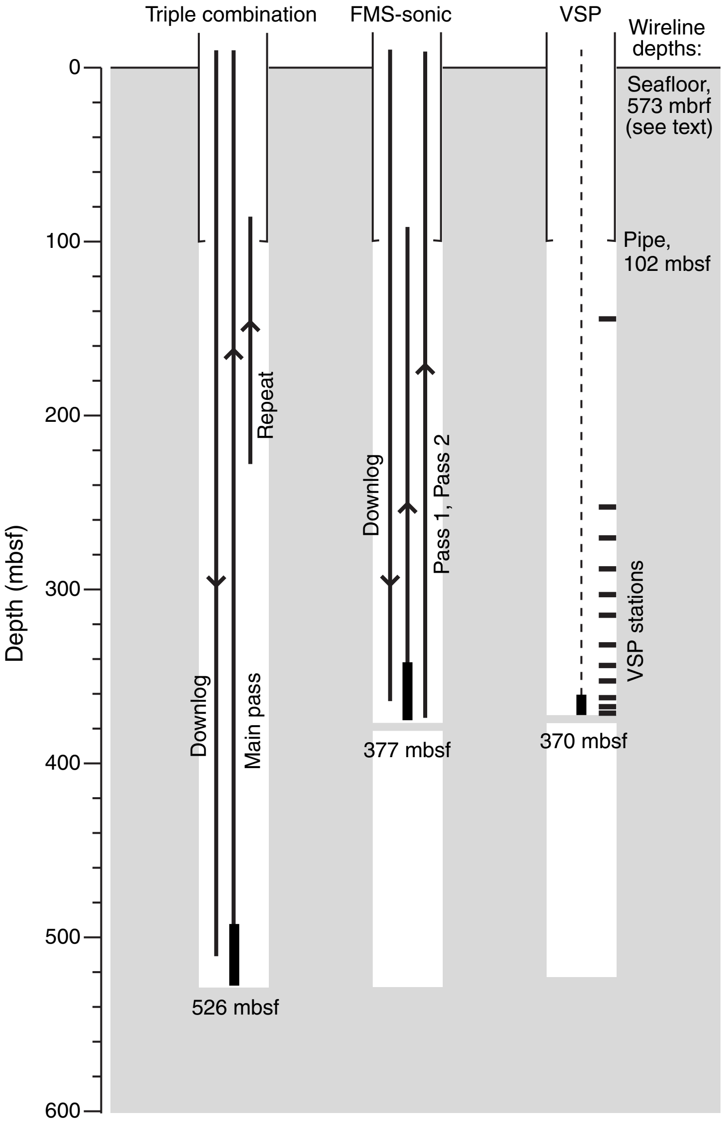

Figure F48. Plots of tides and ship heave, Site U1386. Tides were calculated using Tide Model Driver, a Matlab front-end for the Oregon State University Tidal Data Inversion (Egbert and Erofeeva, 2002). Ship heave was derived from acceleration measured by the motion reference unit in the moonpool area. FMS = Formation MicroScanner, APCT-3 = advanced piston corer temperature tool. RMS = root-mean square.

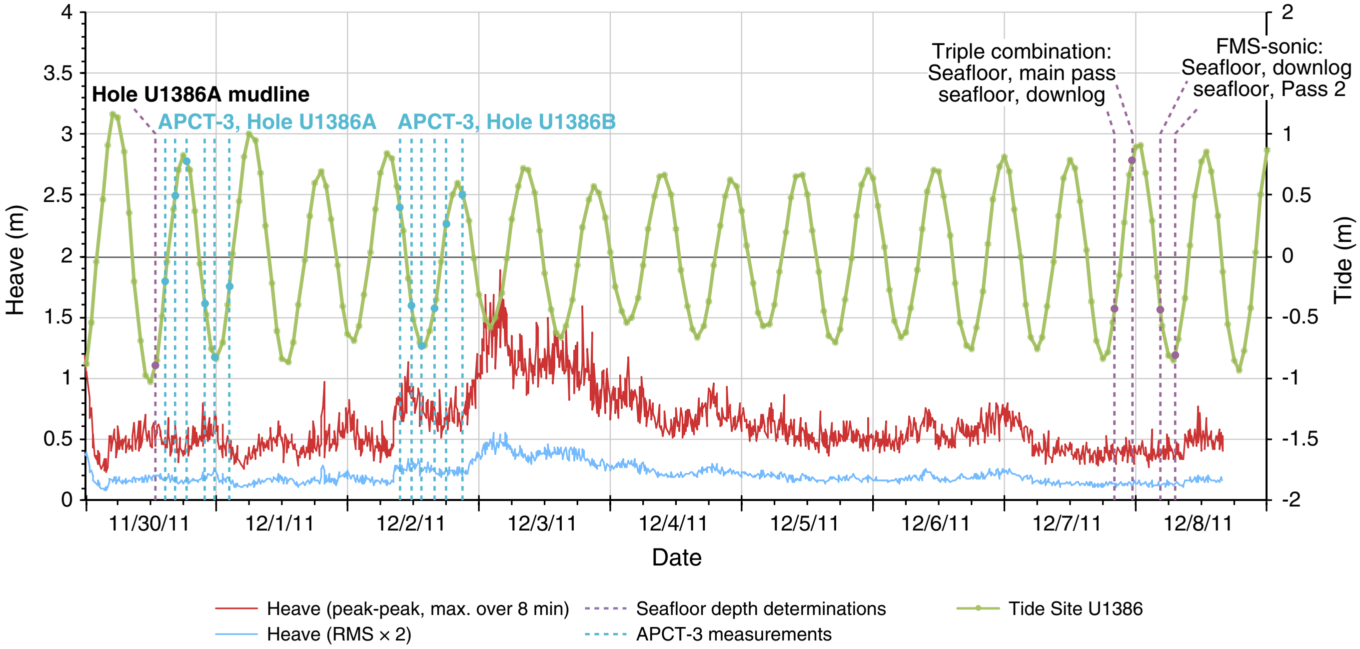

Figure F49. Downhole logs and logging units, Hole U1386C. HSGR = standard (total) gamma radiation, MAD = moisture and density discrete samples, RHOM = bulk density, IDPH = deep induction resistivity, RLA5 = deep apparent resistivity, PWC = *P*-wave caliper.

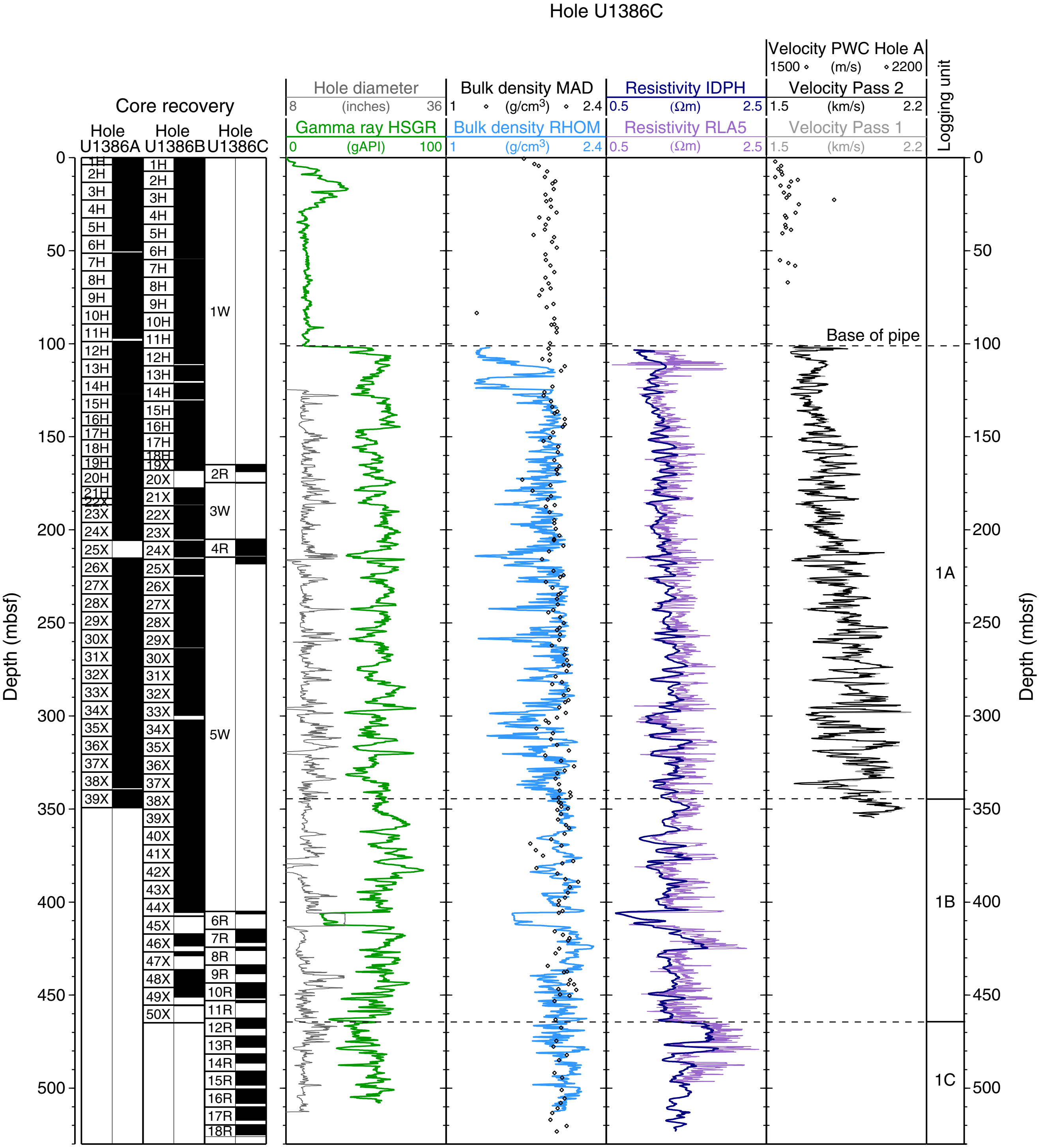

Figure F50. Natural gamma radiation (NGR) logs and logging units, Hole U1386C. HSGR = standard (total) gamma radiation, HCGR = computed gamma radiation.

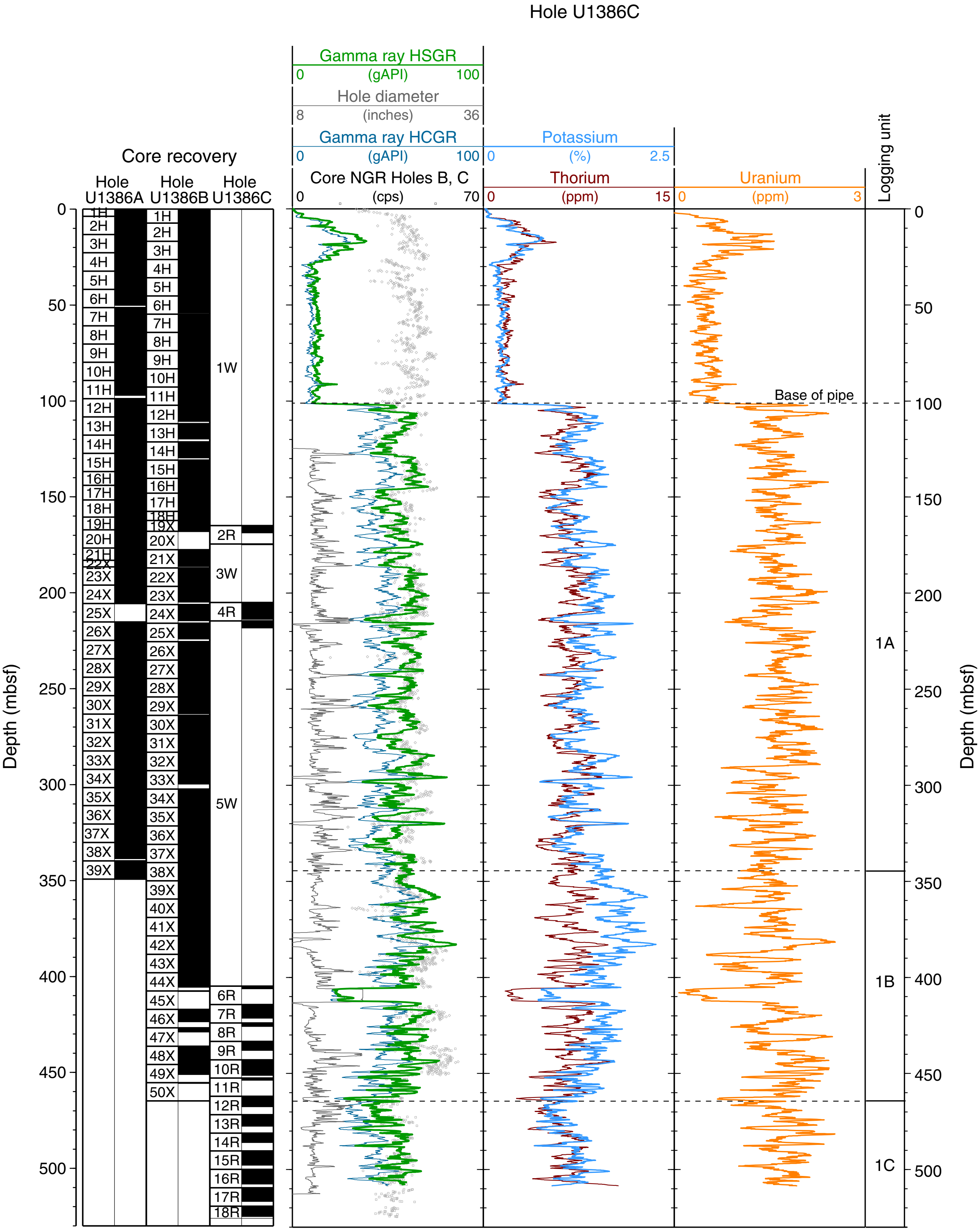

Figure F51. Comparison of High-Resolution Laterolog Array and Dual Induction Tool resistivity logs, Hole U1386C. HSGR = standard (total) gamma radiation, IDPH = deep induction resistivity, IMPH = medium induction resistivity, SFLU = spherically focused resistivity, RLA1–5 = apparent resistivity from computed focusing modes 1–5 (1 = shallowest and 5 = deepest).

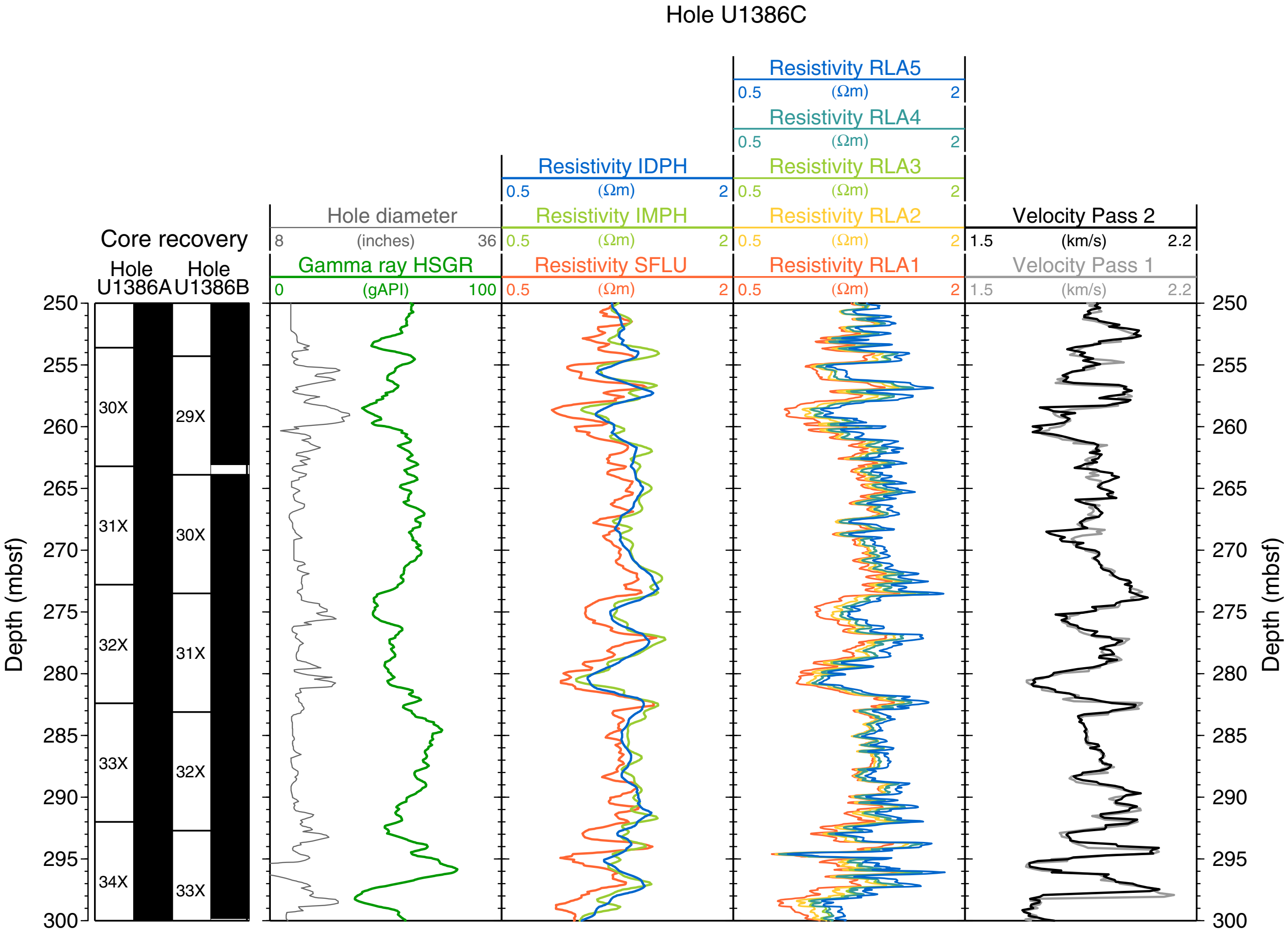

Figure F52. Comparison of lithology and downhole logs, Hole U1386C. HSGR = standard (total) natural gamma radiation, IDPH = deep induction resistivity, RLA1 and 5 = shallow and deep apparent resistivity, FMS = Formation MicroScanner. n.m. = nannofossil mud, s.m. = silty mud, s.s. = silty sand.

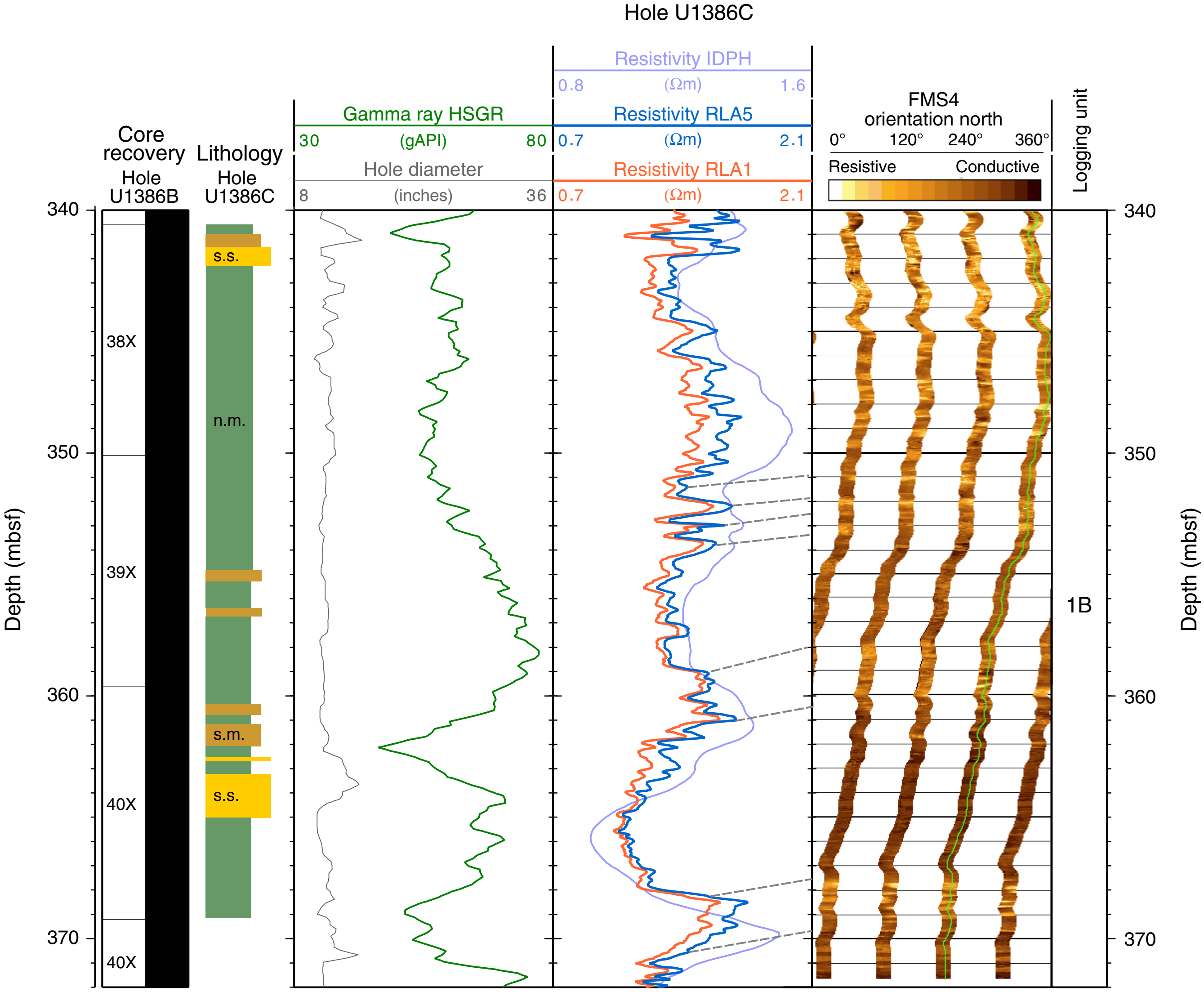

Figure F53. Downhole logs of an example interval with cyclic alternations, Hole U1386C. HSGR = standard (total) natural gamma radiation, IDPH = deep induction resistivity, RHOM = bulk density.

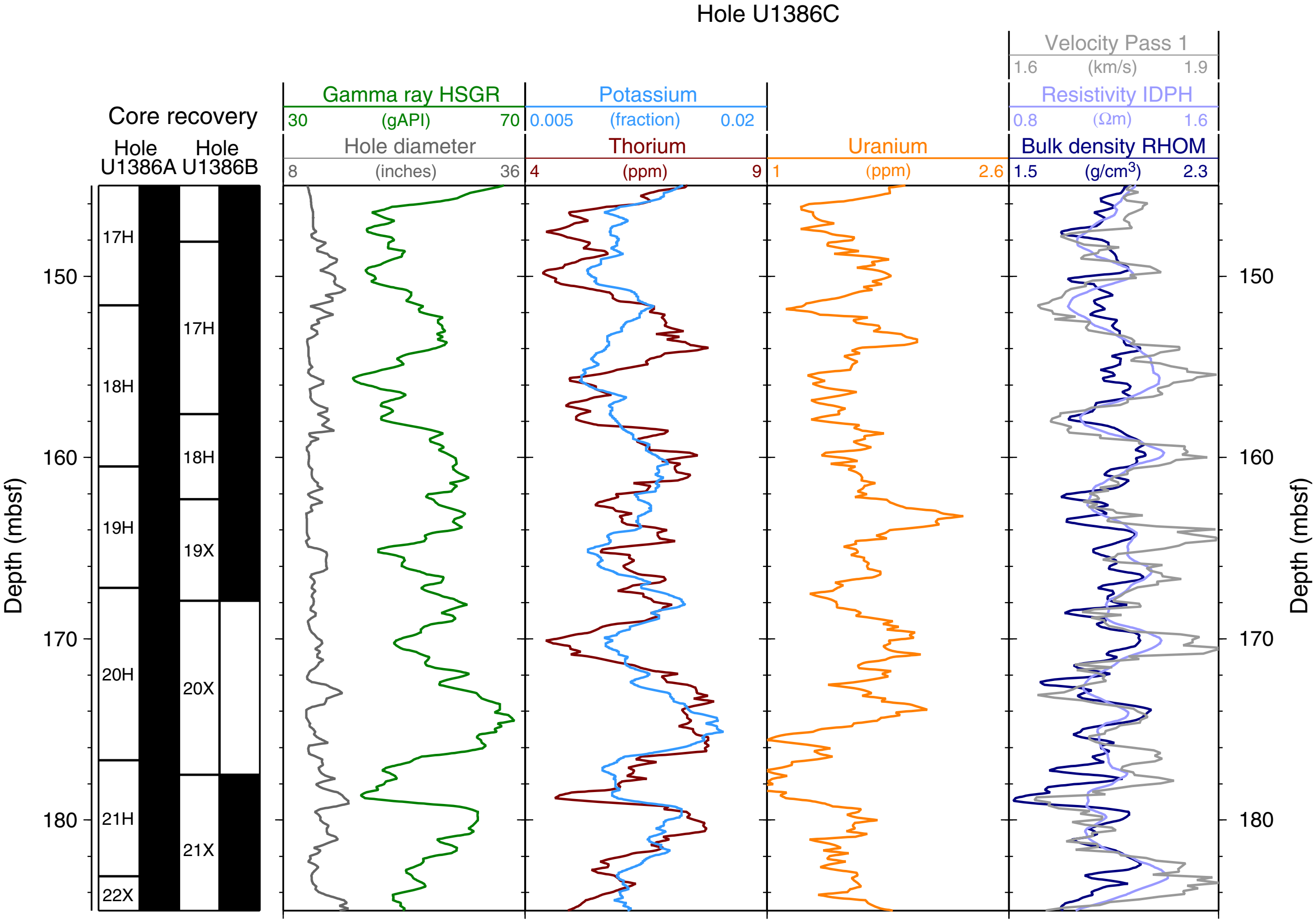

Figure F54. Plot of vertical seismic profile waveforms and one-way traveltime picks, Site U1386.

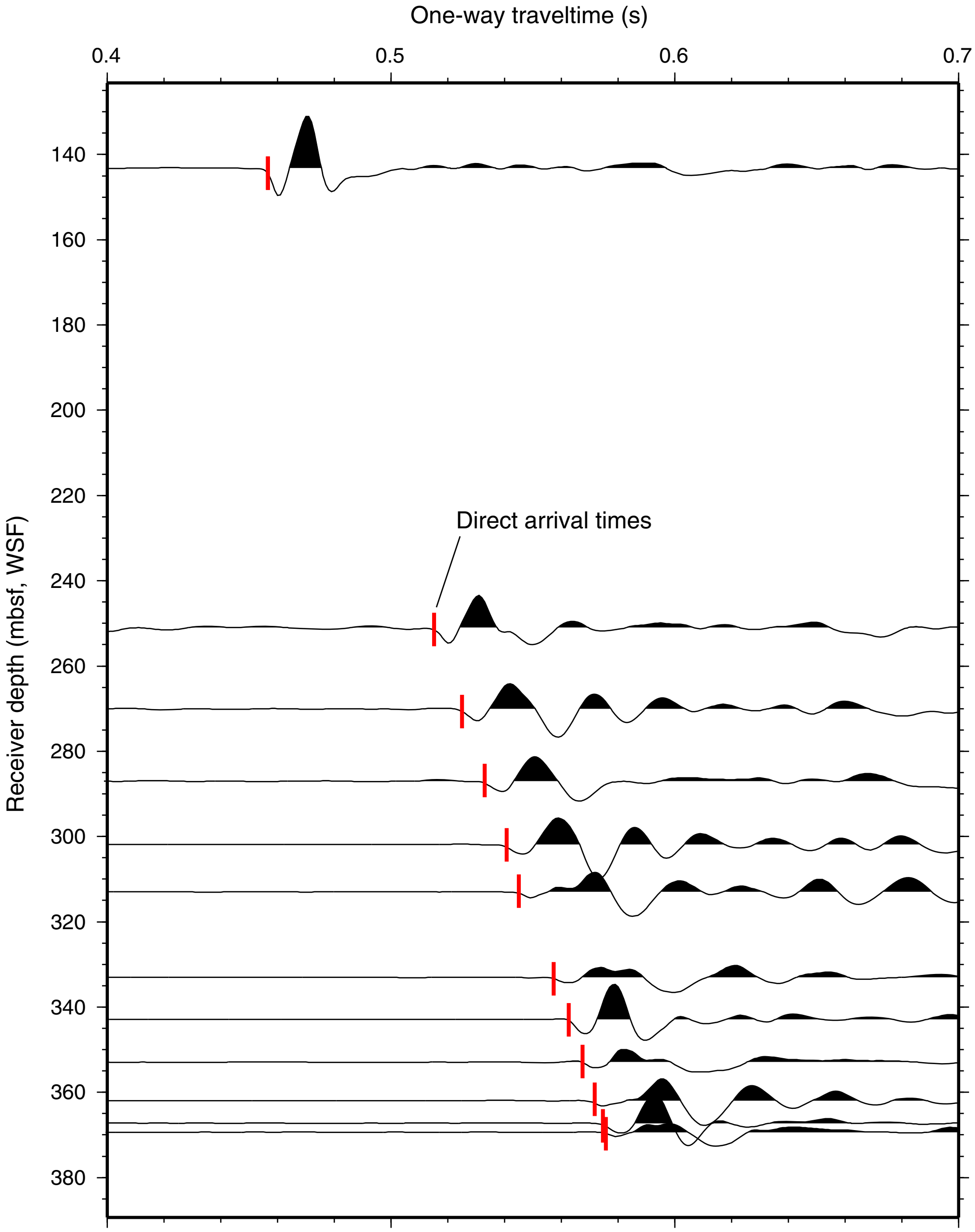

Figure F55. Plots of magnetic susceptibility vs. composite depth, Site U1386. **A.** 0–40 mcd. (Continued on next 14 pages.)

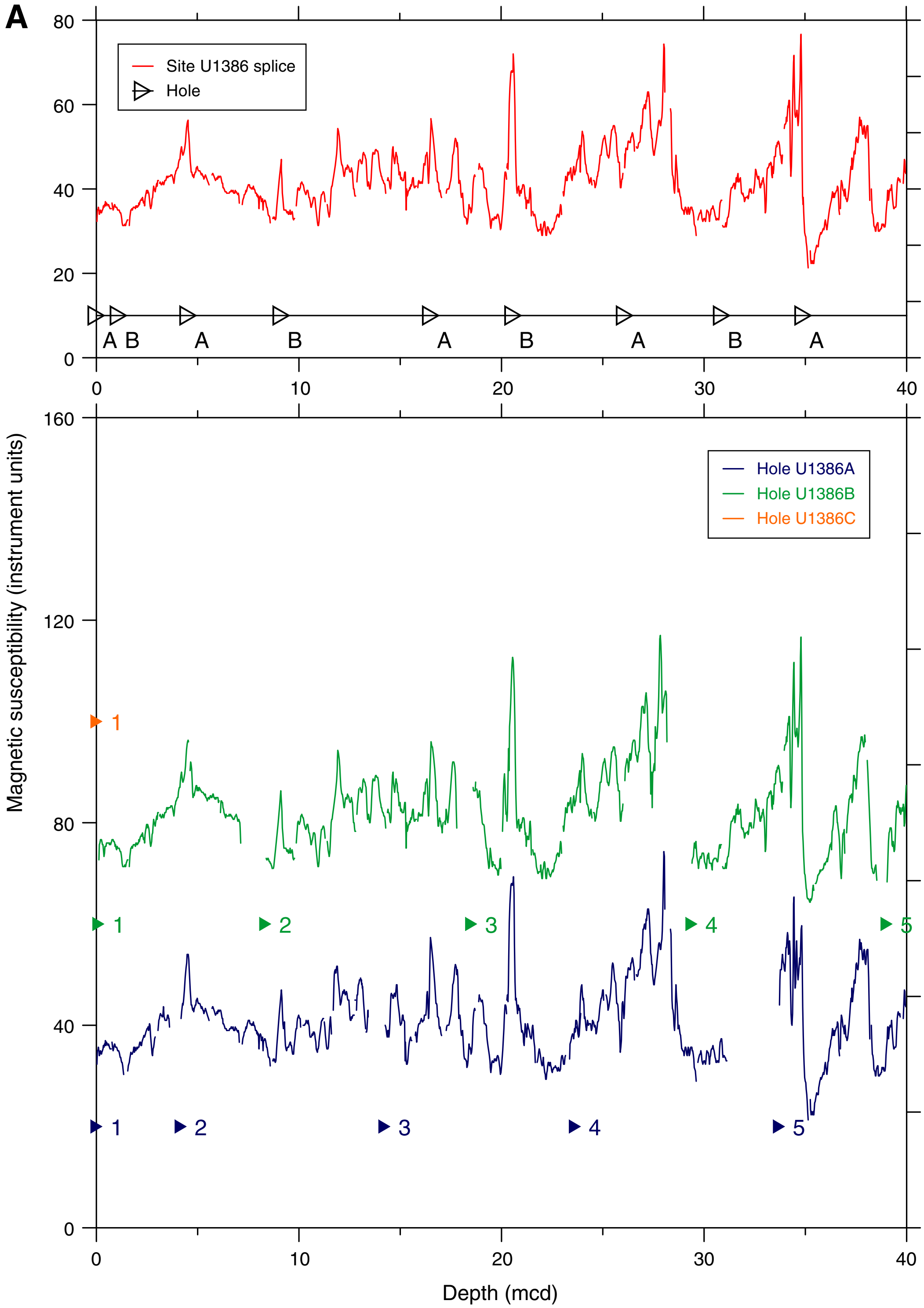

Figure F55 (continued). B. 40–80 mcd. (Continued on next page.)

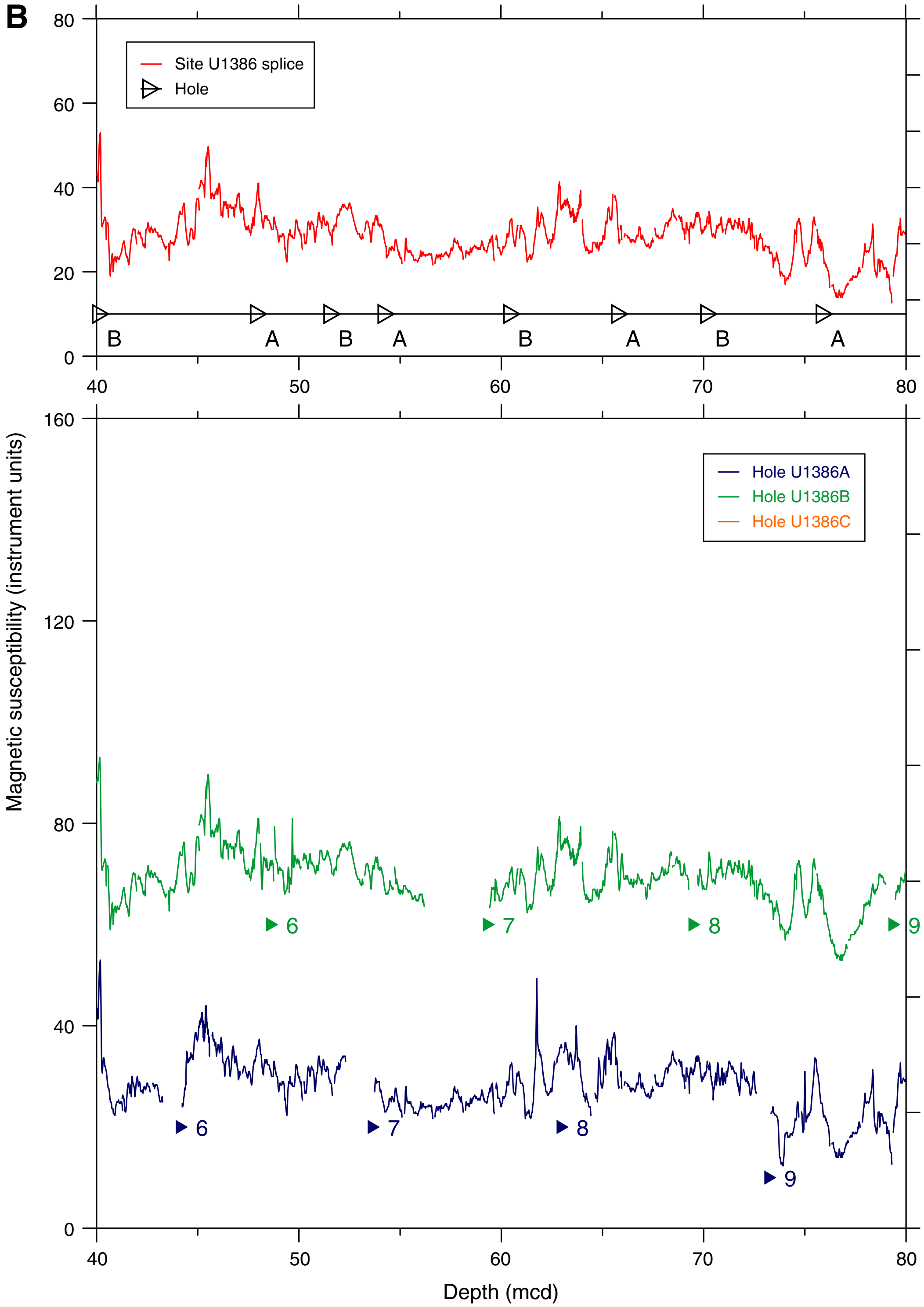

Figure F55 (continued). C. 80–120 mcd. (Continued on next page.)

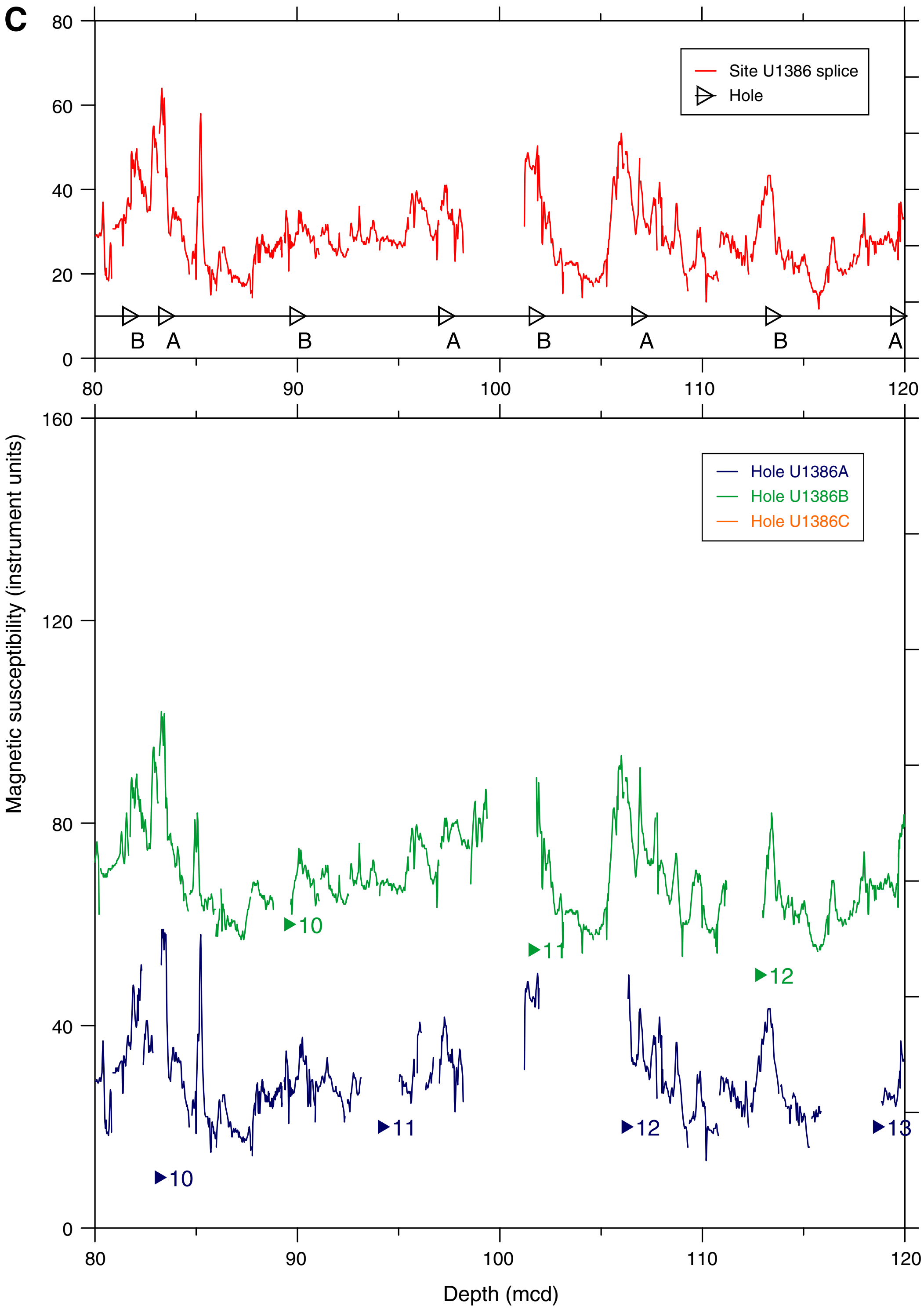

Figure F55 (continued). D. 120–160 mcd. (Continued on next page.)

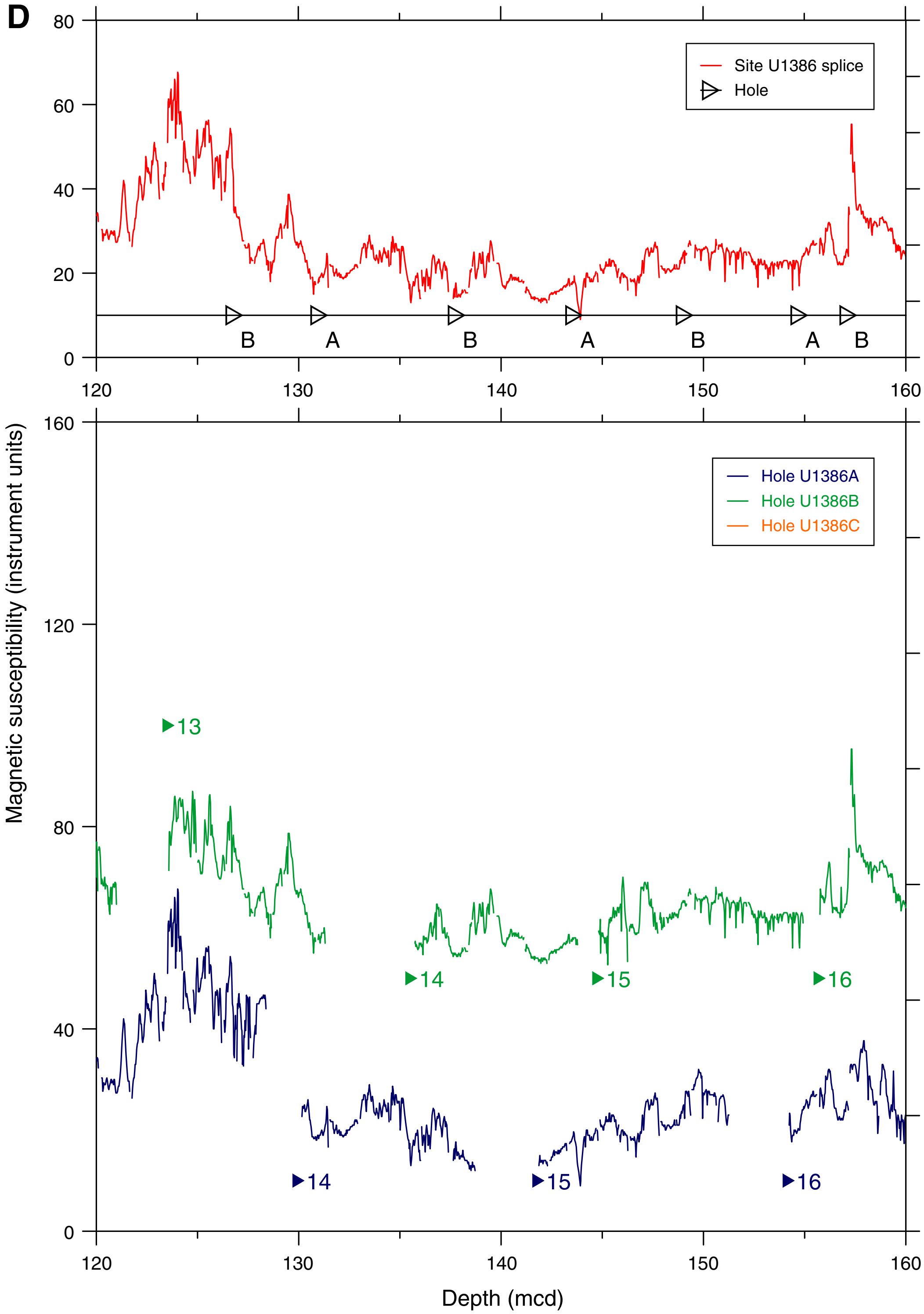

Figure F55 (continued). **E.** 160–200 mcd. (Continued on next page.)

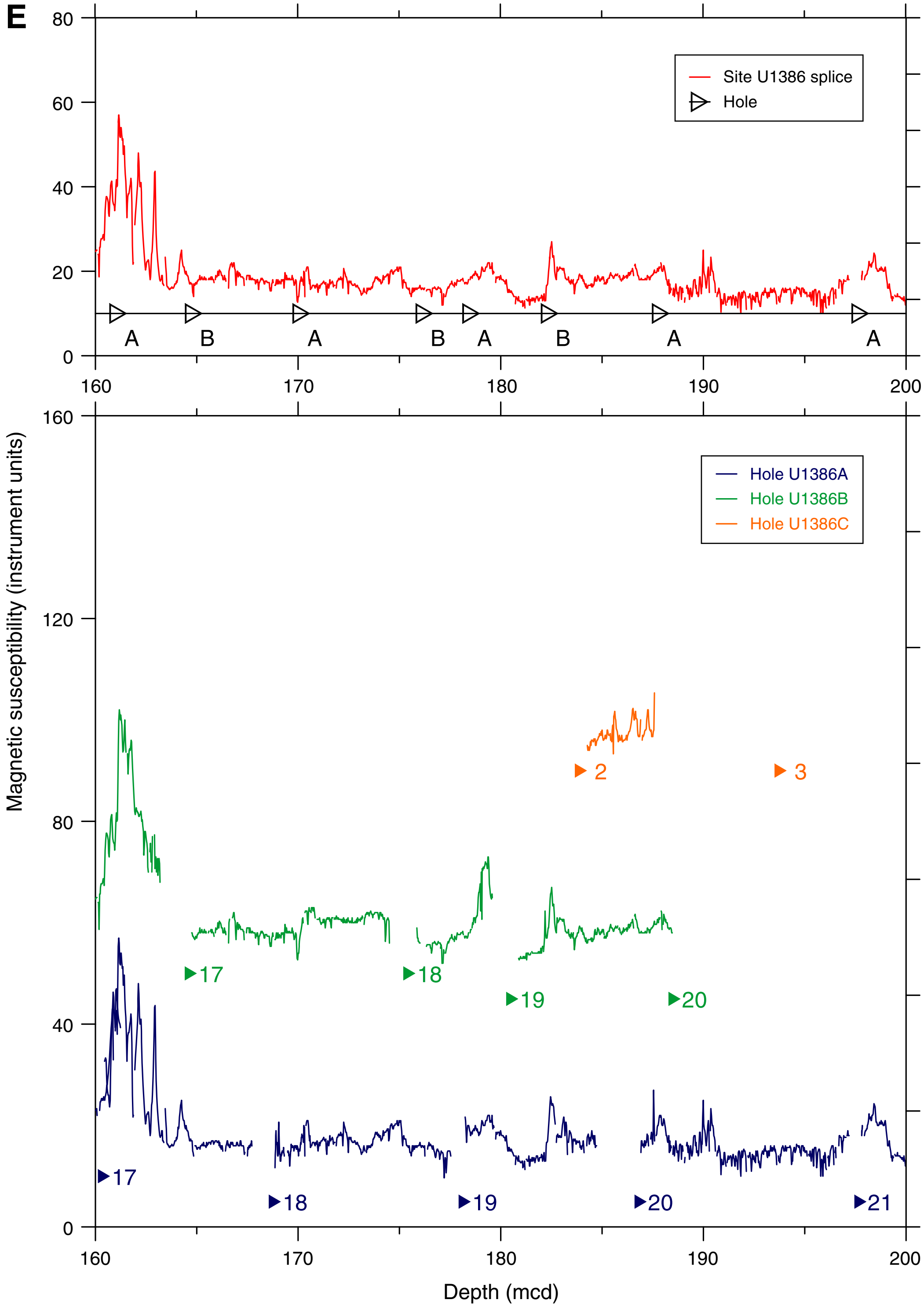

Figure F55 (continued). **F.** 200–240 mcd. (Continued on next page.)

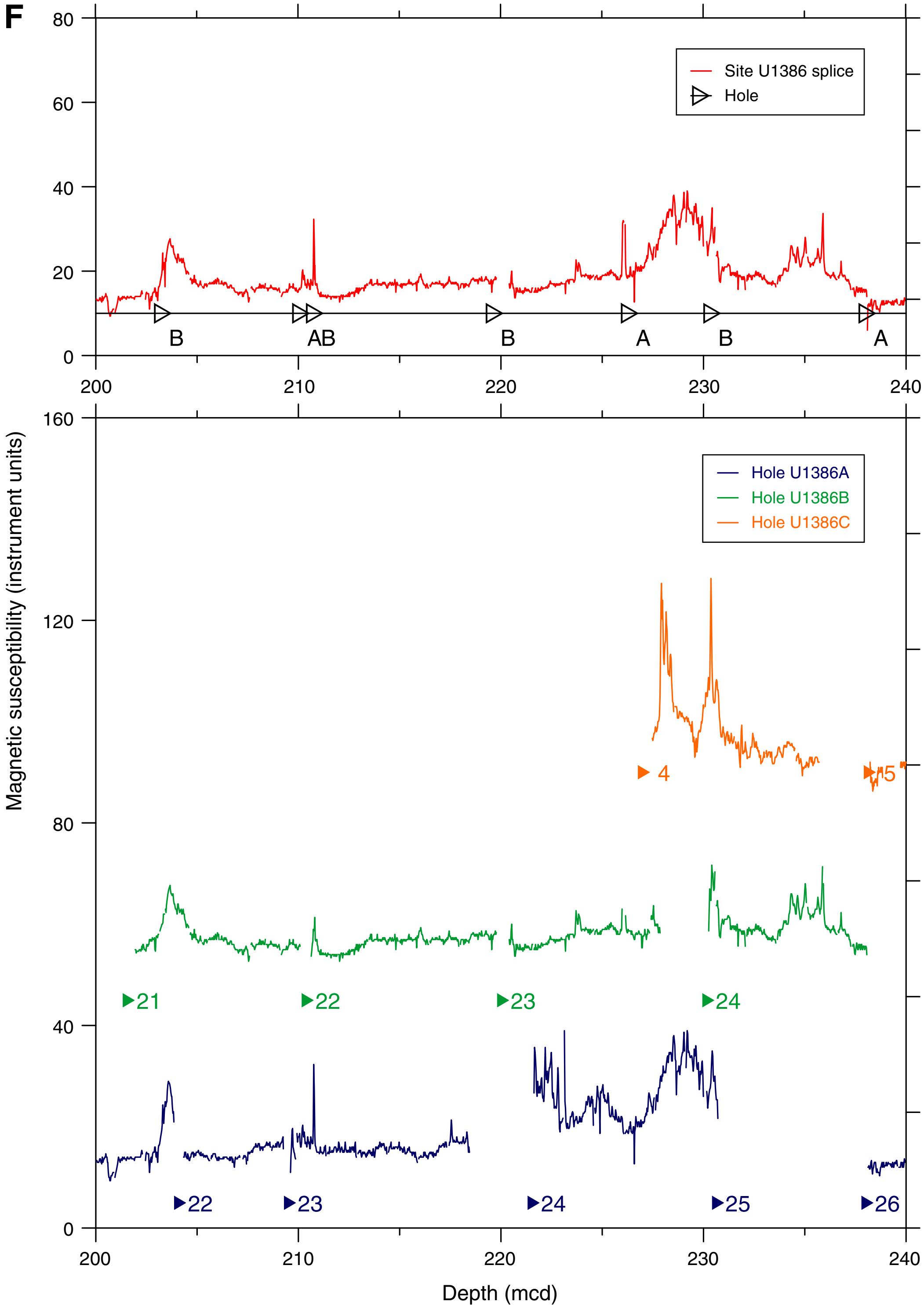

Figure F55 (continued). G. 240–280 mcd. (Continued on next page.)

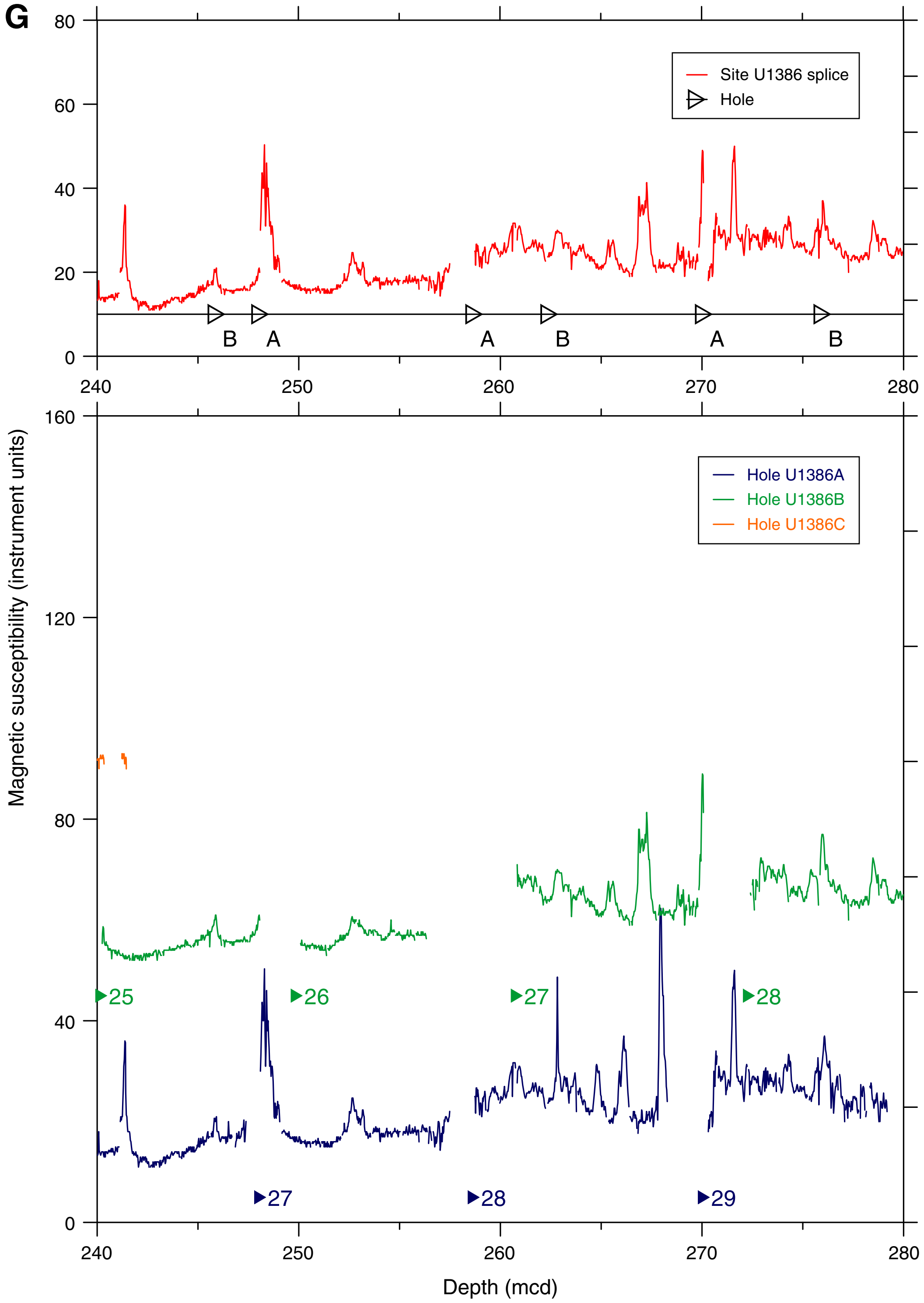

Figure F55 (continued). H. 280–320 mcd, with the Brunhes/Matuyama (B/M) polarity reversals. (Continued on next page.)

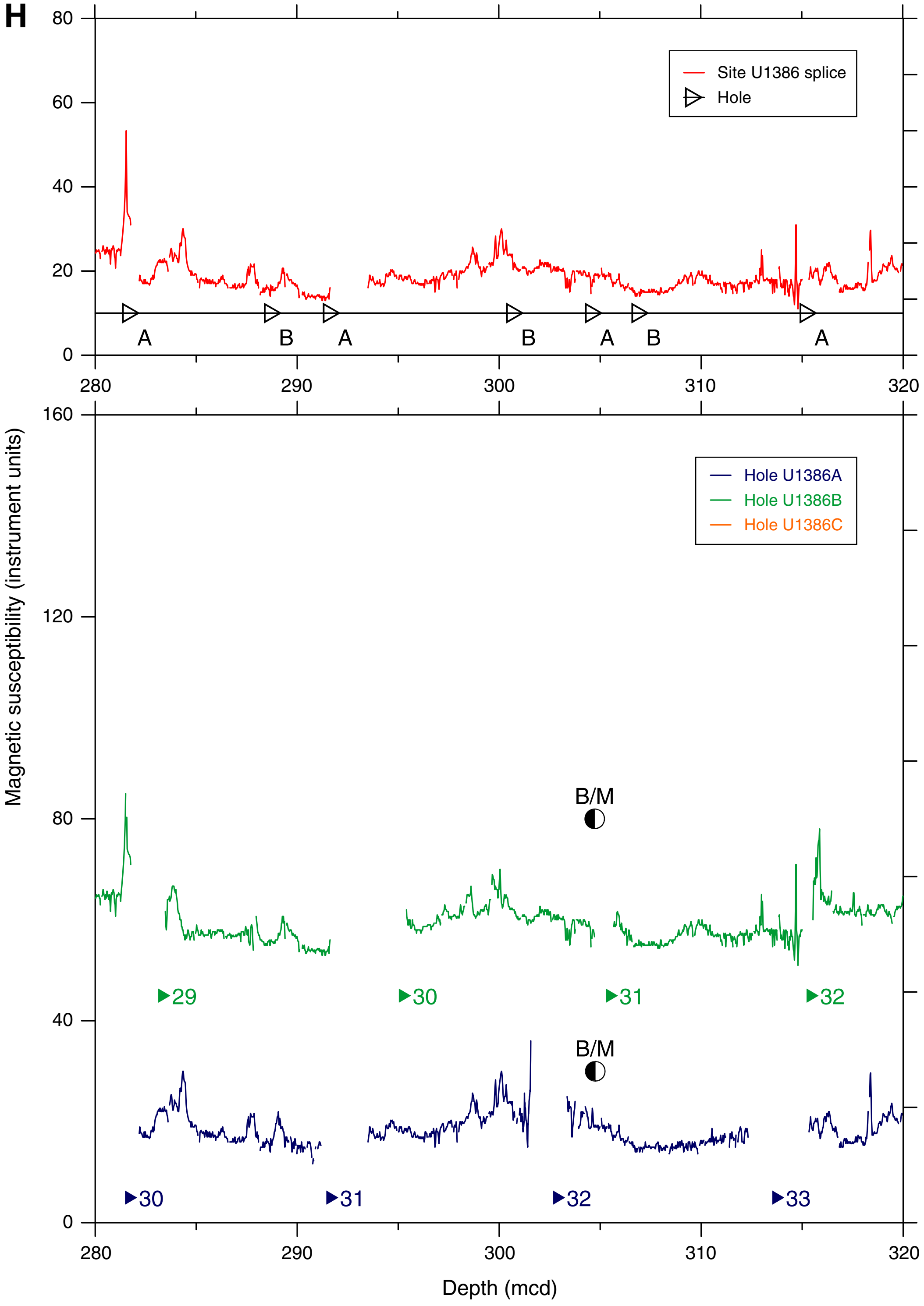

Figure F55 (continued). I. 320–360 mcd. (Continued on next page.)

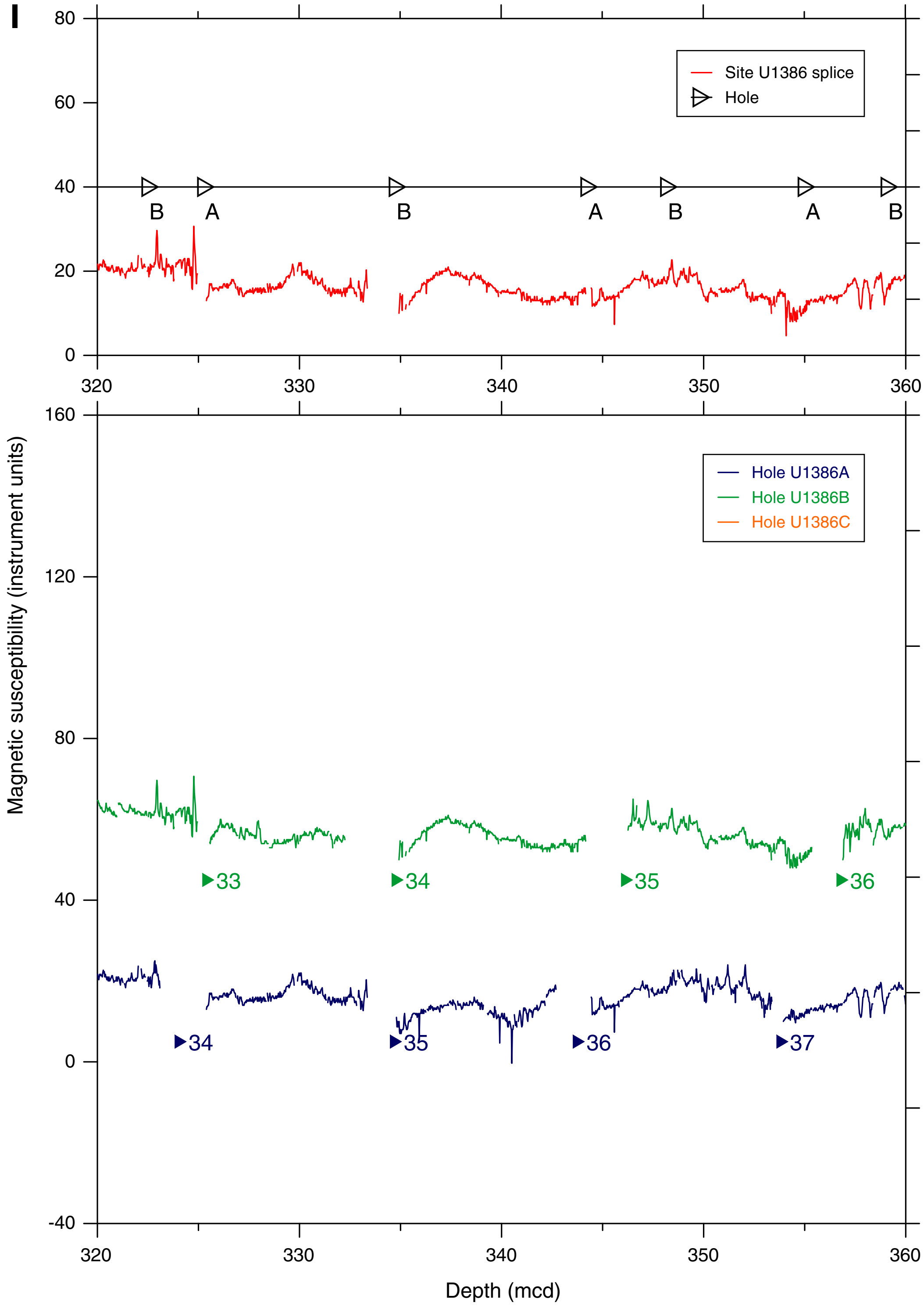

Figure F55 (continued). J. 360–400 mcd, with the estimated depth to the top of the Jaramillo Subchron. (Continued on next page.)

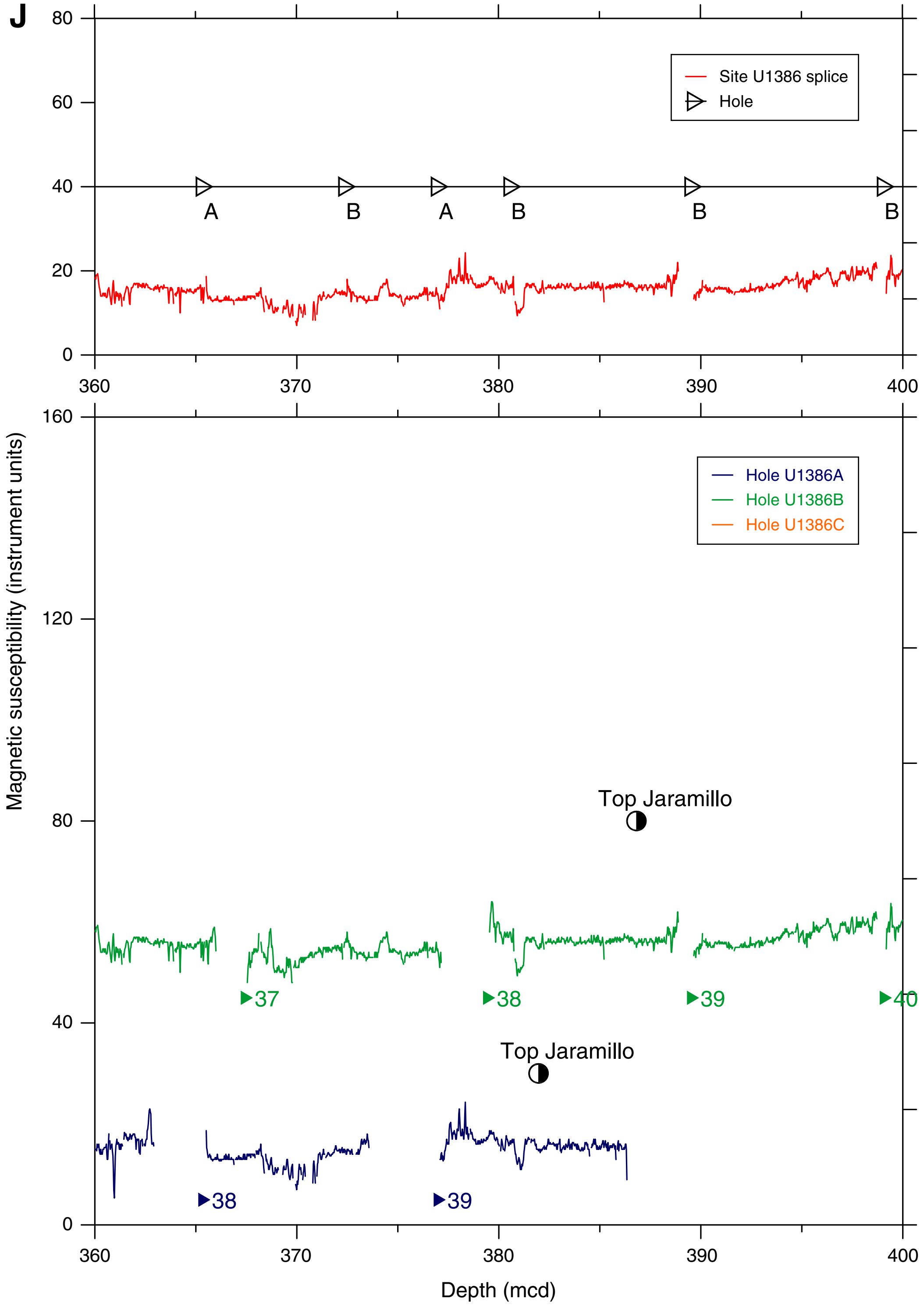

Figure F55 (continued). K. 400–440 mcd, with the estimated depth to the bottom of the Jaramillo Subchron. (Continued on next page.)

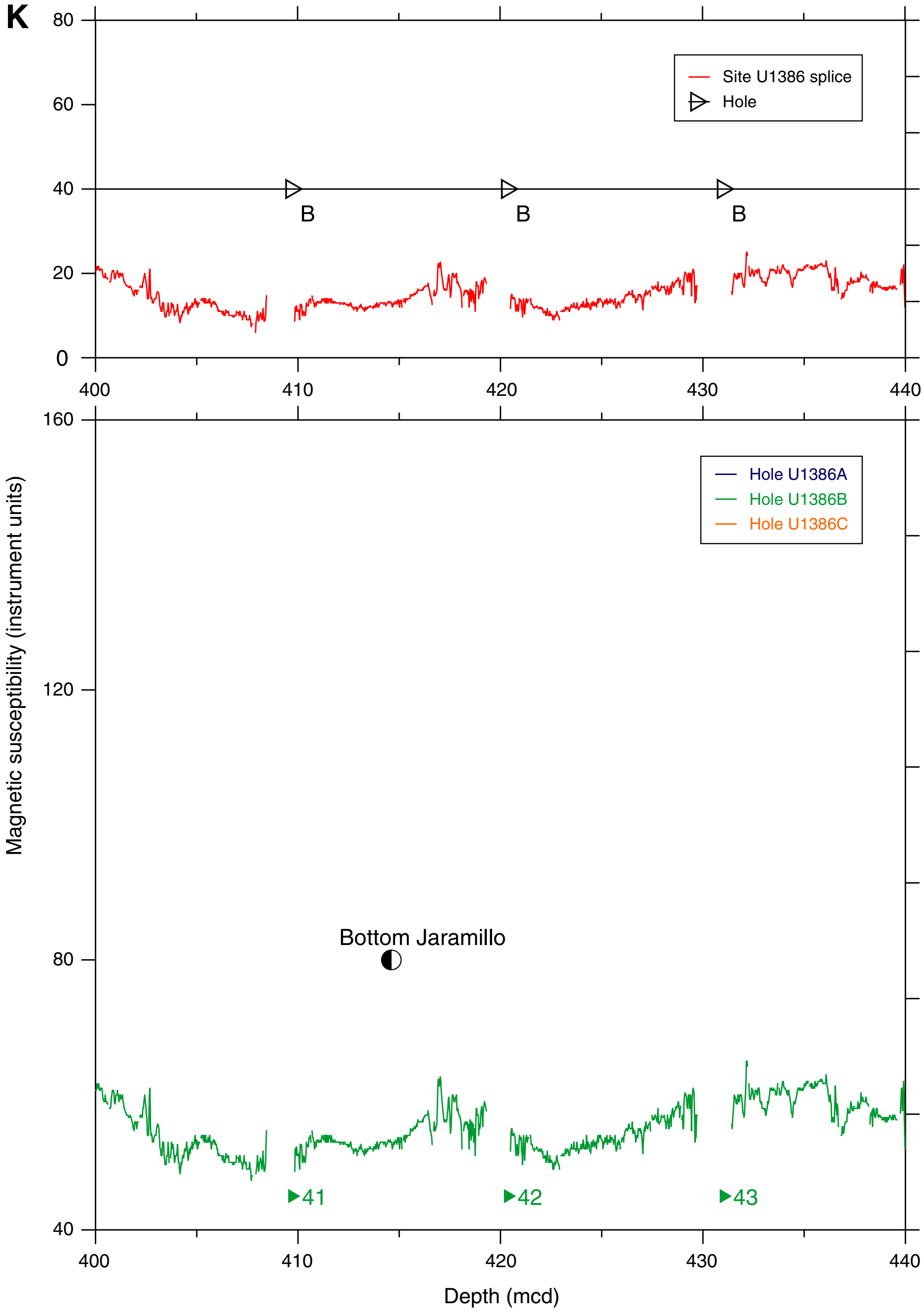

Figure F55 (continued). L. 440–480 mcd. (Continued on next page.)

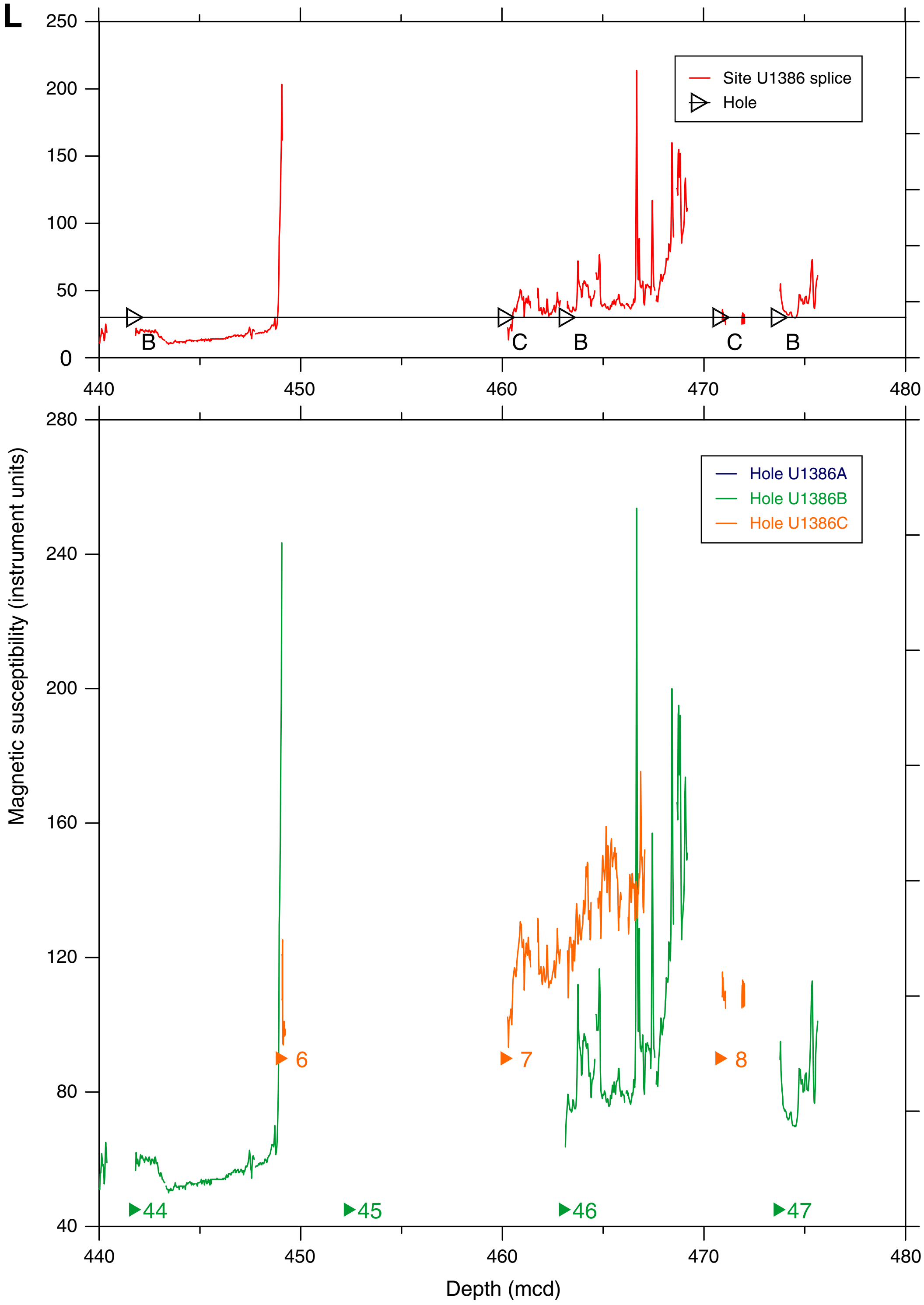

Figure F55 (continued). M. 480–520 mcd. (Continued on next page.)

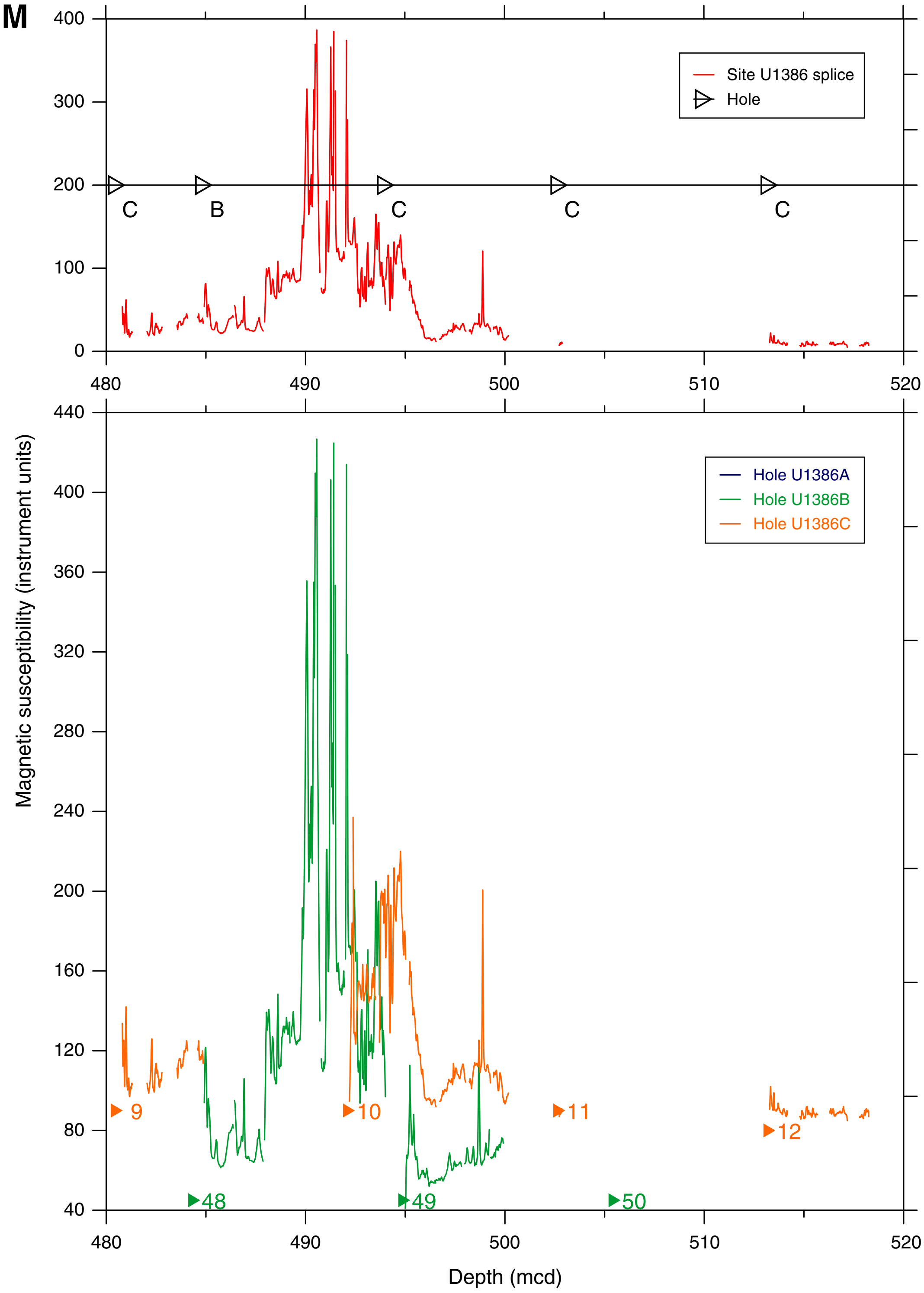

Figure F55 (continued). N. 520–560 mcd. (Continued on next page.)

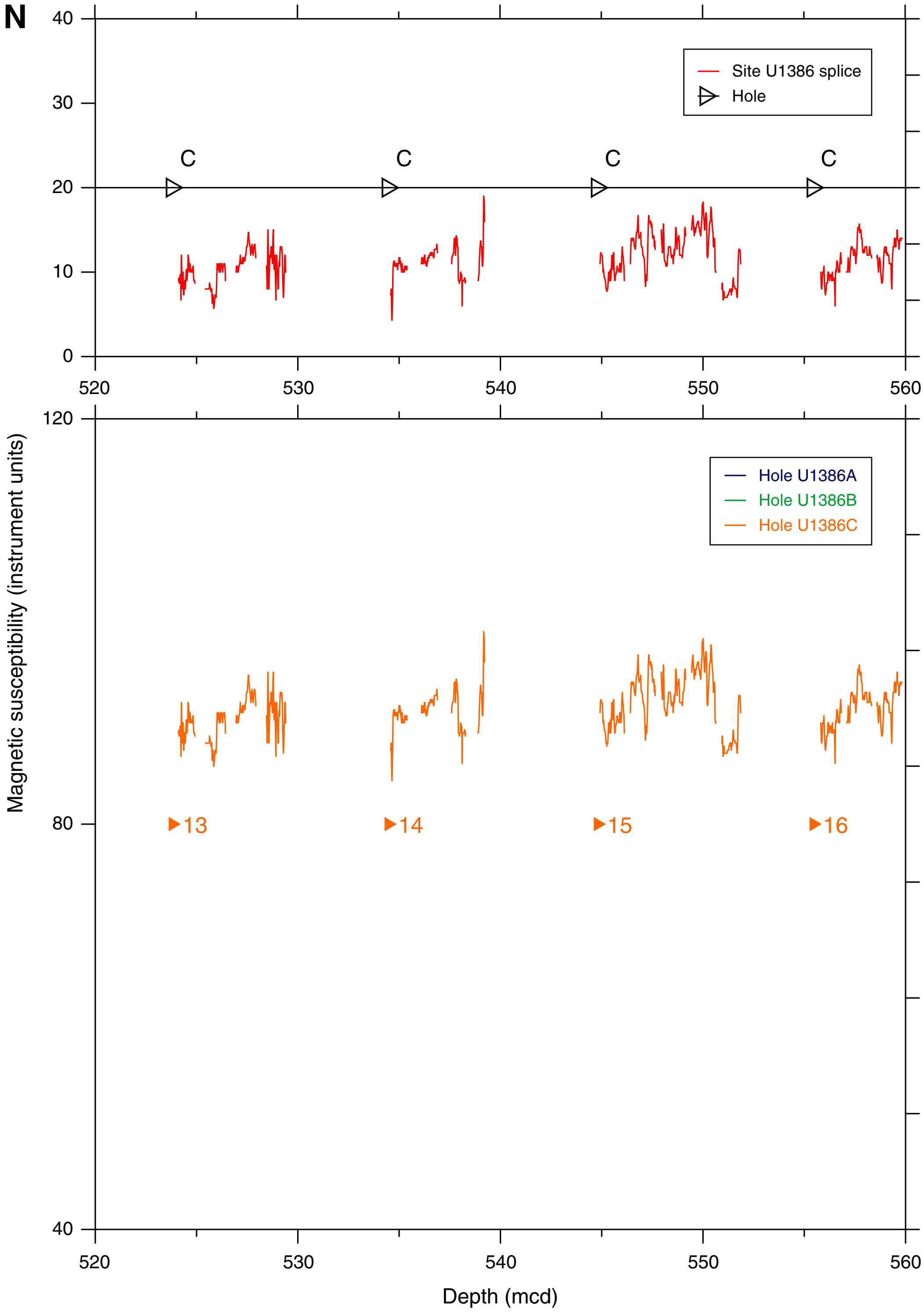

Figure F55 (continued). O. 560–600 mcd.

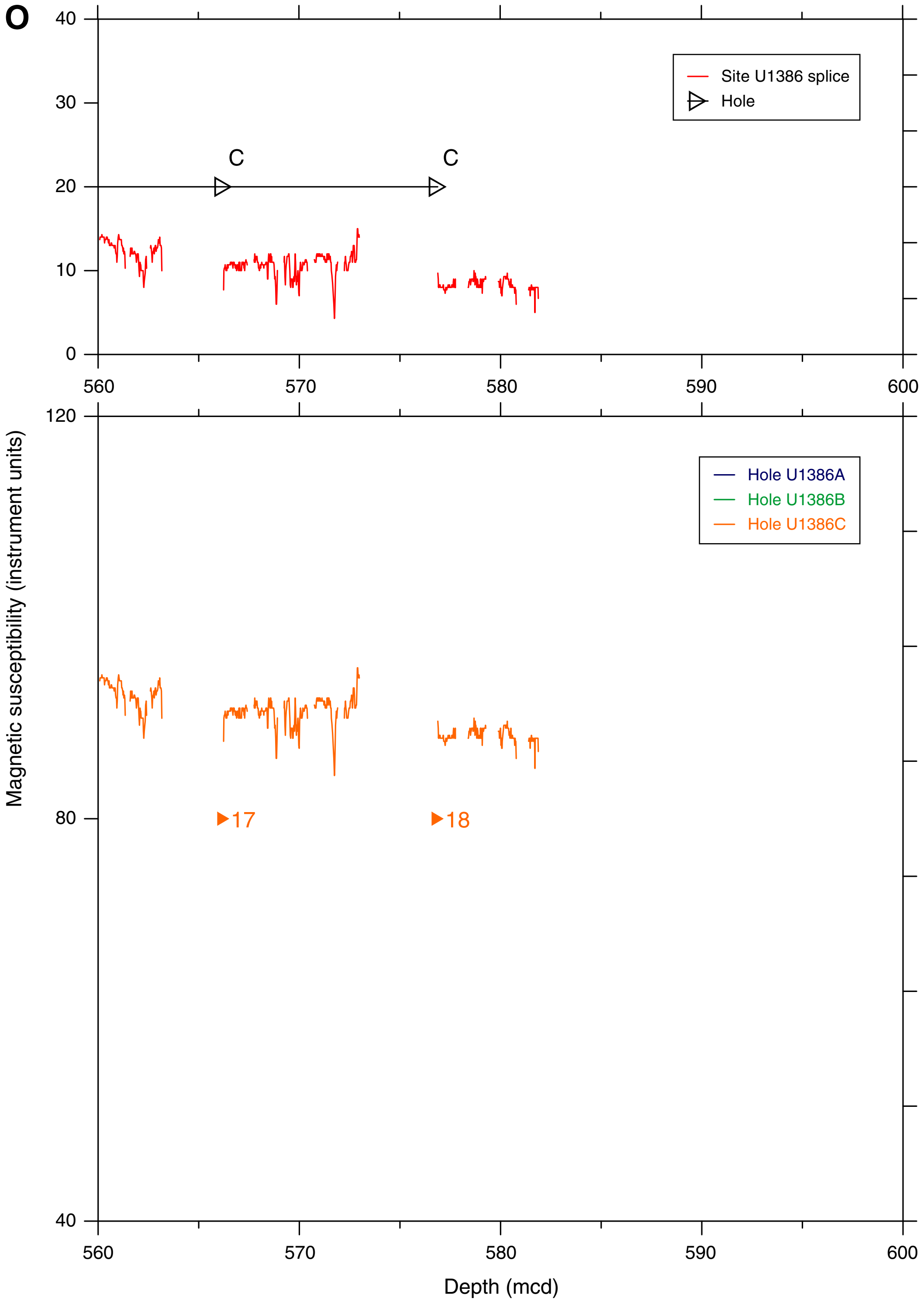

Figure F56. Plots of core top depths for mbsf vs. mcd, Site U1386. Lines fit through the core top depths for each hole give the relative expansion of the mcd scale relative to the mbsf scale.

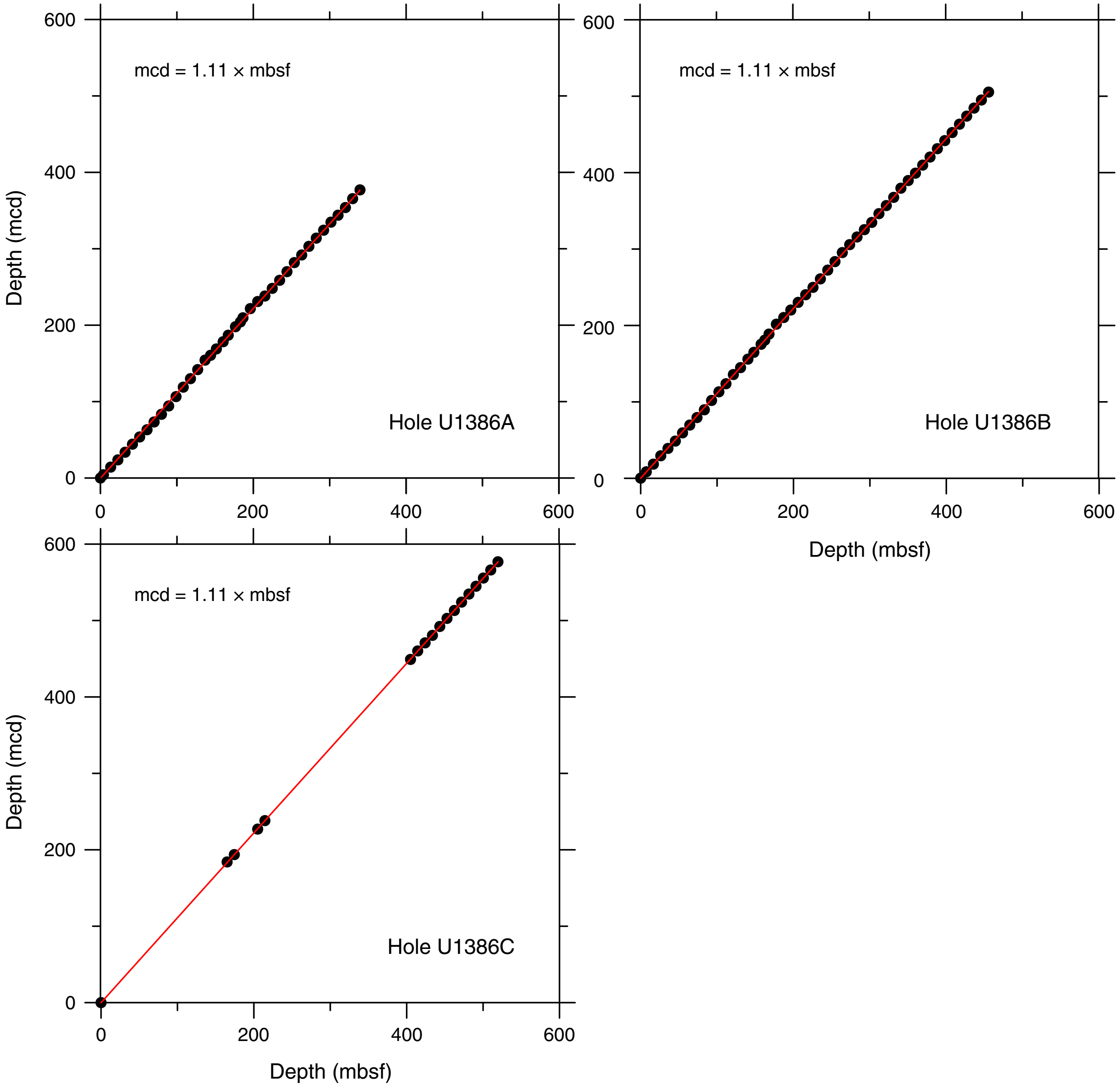

Figure F57. Plot of core top depths for mcd vs. mbsf*, Holes U1386A–U1386C. Line fits through the core top depths of all holes give an estimate of the amount the mcd scale has to be compressed to derive the mbsf* scale (see text).

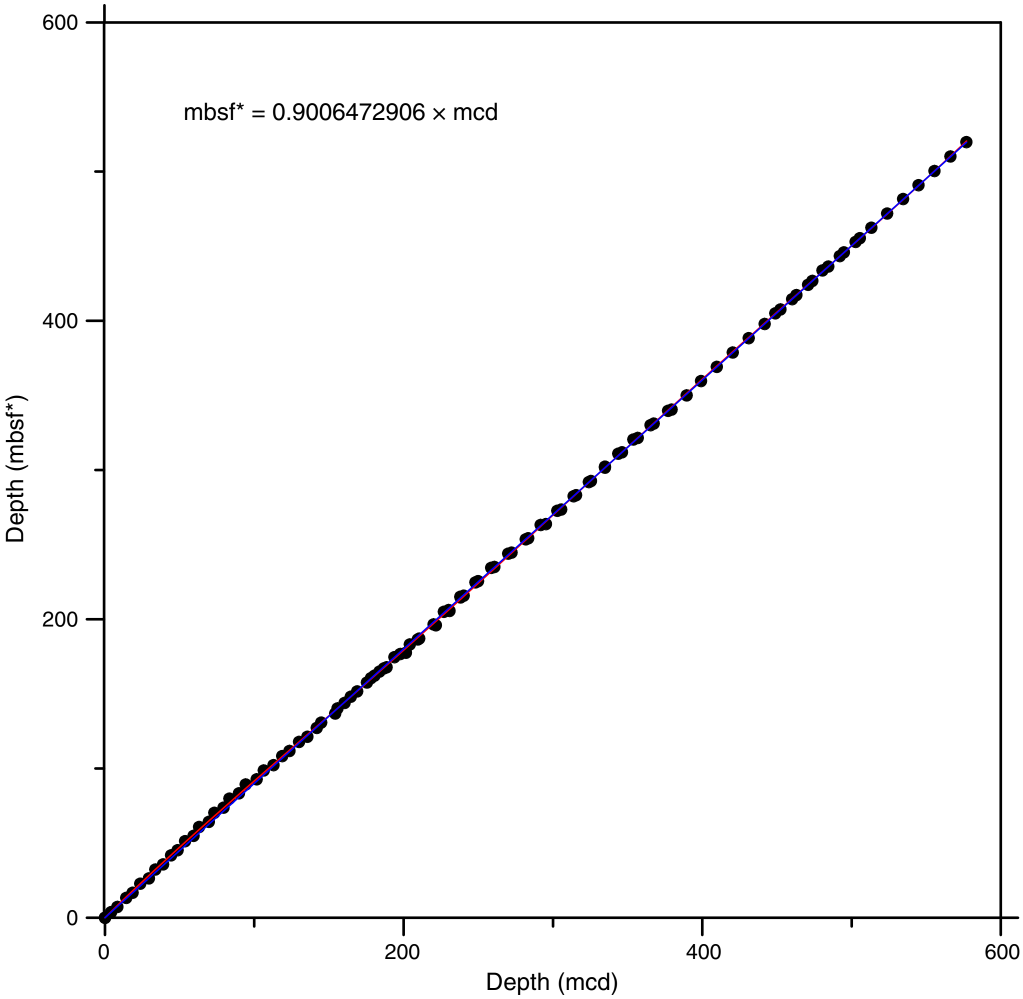

Figure F58. Plots of comparison between the logging standard (total) gamma ray (HSGR) data in Hole U1386C and the (five-point average) natural gamma ray (NGR) data in Holes U1386A and U1386B plotted on the mbsf scale (below) and a corrected mbsf* scale (above).

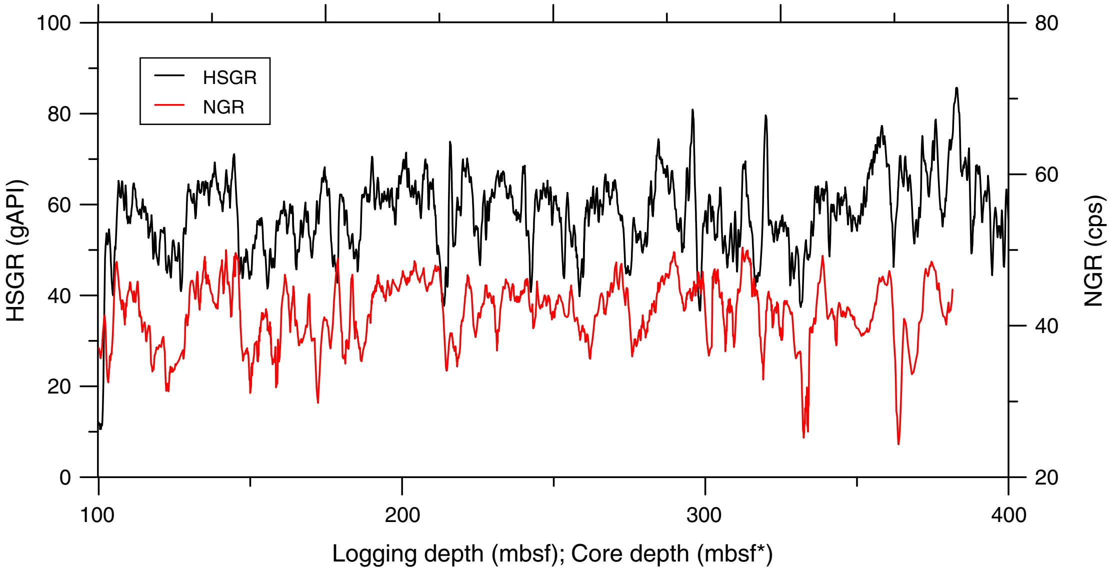

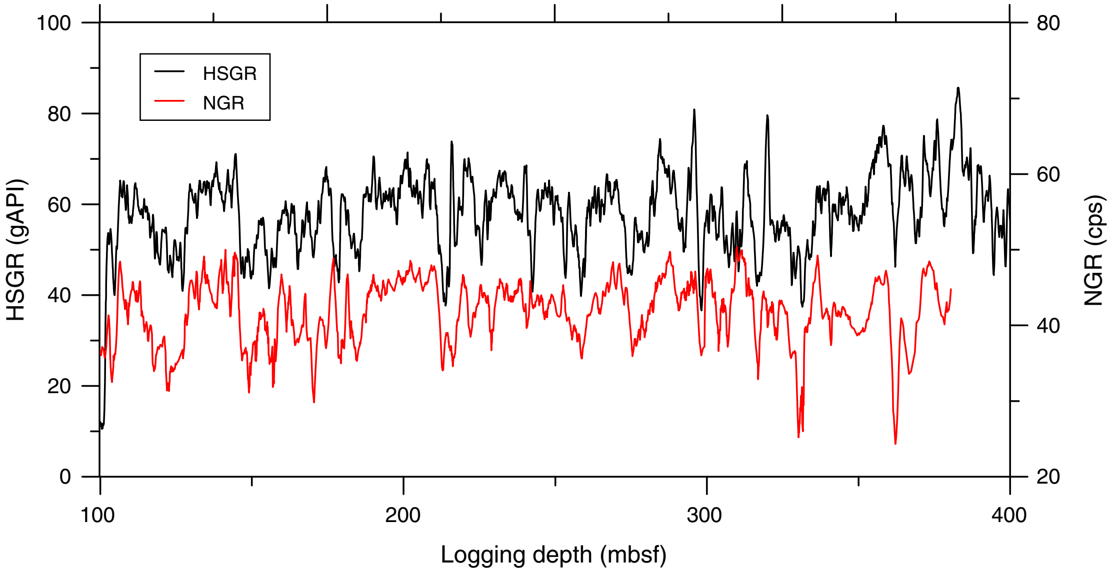

Figure F59. Plot of linear regression fit through 11 tie points between the NGR data in Holes U1386A and U1386B on the mbsf* scale and logging standard (total) gamma ray data in Hole U1386C on the mbsf scale.

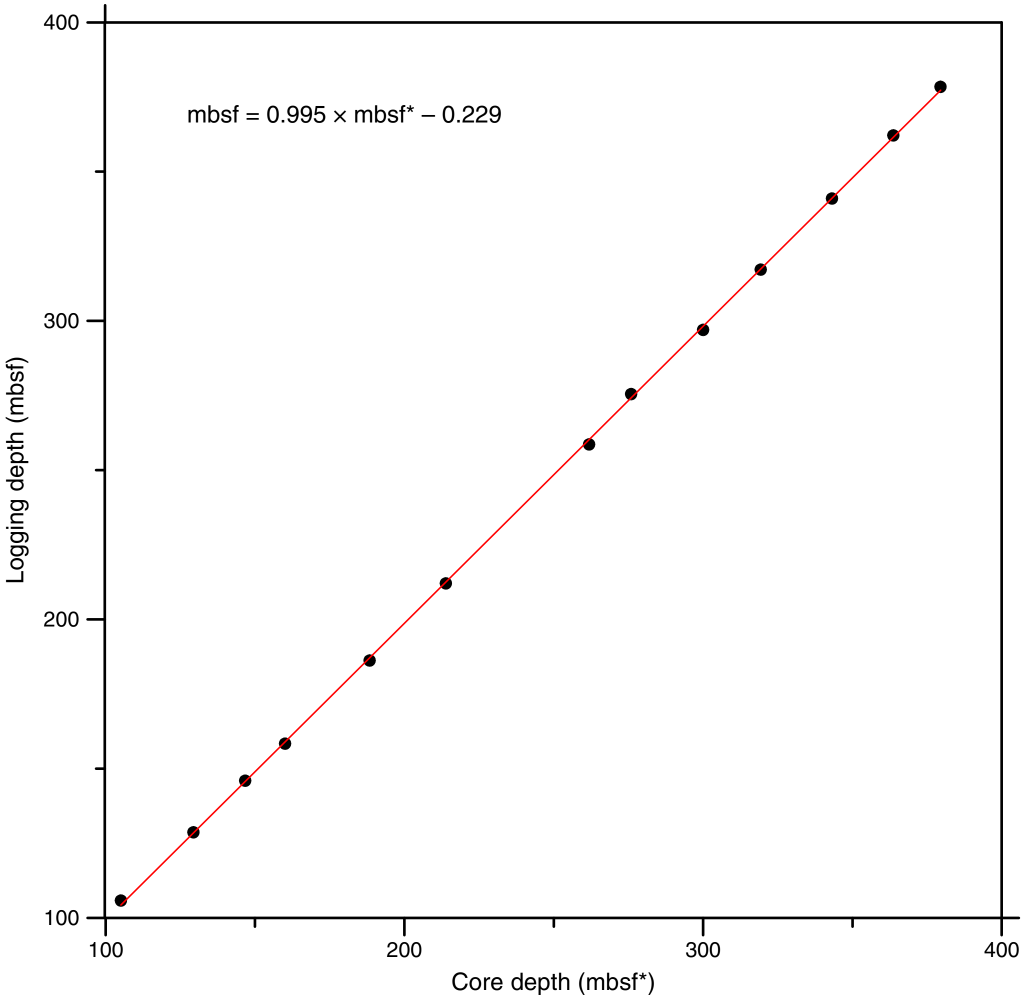

Table T1. Coring summary, Site U1386. (Continued on next two pages.)

Hole U1386A
Latitude: 36°49.6885′N
Longitude: 7°45.3309′W
Time on hole (d): 2.1
Seafloor (drill pipe measurement below rig floor, m DRF): 571.7 (APC mudline)
Distance between rig floor and sea level (m): 11.3
Water depth (drill pipe measurement from sea level, mbsl): 560.7
Total penetration (drilling depth below seafloor, m DSF): 349.3
Total length of cored section (m): 349.3
Total core recovered (m): 347.04
Core recovery (%): 99.35
Total number of cores: 39

Hole U1386B
Latitude: 36°49.6880′N
Longitude: 7°45.3168′W
Time on hole (d): 2.7
Seafloor (drill pipe measurement below rig floor, m DRF): 573.2 (APC mudline)
Distance between rig floor and sea level (m): 11.3
Water depth (drill pipe measurement from sea level, mbsl): 562.2
Total penetration (drilling depth below seafloor, m DSF): 464.9
Total length of cored section (m): 464.9
Total core recovered (m): 421.6
Core recovery (%): 90.69
Total number of cores: 50

Hole U1386C
Latitude: 36°49.6773′N
Longitude: 7°45.3165′W
Time on hole (d): 3.8
Seafloor (drill pipe measurement below rig floor, m DRF): 573.2 (APC mudline)
Distance between rig floor and sea level (m): 11.3
Water depth (drill pipe measurement from sea level, mbsl): 561.9
Total penetration (drilling depth below seafloor, m DSF): 526
Total length of cored section (m): 140.2
Total core recovered (m): 82
Core recovery (%): 58.5
Total number of cores: 15

Site U1386 totals
Number of cores: 104
Penetration (m): 1340.2
Cored (m): 954.4
Recovered (m): 850.64 (89.1%)

			Depth DSF (m)			Depth CSF (m)				
Core	Date (2012)	Time (h)	Top of cored interval	Bottom of cored interval	Interval advanced (m)	Top of recovered core	Bottom of recovered core	Length of core recovered (m)	Curated length (m)	Recovery (%)
339-U1386A-										
1H	11 Nov	1305	0.0	3.8	3.8	0.0	3.80	3.86	3.80	102
2H	11 Nov	1340	3.8	13.3	9.5	3.8	13.54	9.77	9.74	103
3H	11 Nov	1415	13.3	22.8	9.5	13.3	23.27	9.95	9.97	105
4H	11 Nov	1455	22.8	32.3	9.5	22.8	33.17	10.31	10.37	109
5H	11 Nov	1530	32.3	41.8	9.5	32.3	42.23	9.86	9.93	104
6H	11 Nov	1555	41.8	51.3	9.5	41.8	50.36	8.47	8.56	89
7H	11 Nov	1640	51.3	60.8	9.5	51.3	61.25	9.96	9.95	105
8H	11 Nov	1720	60.8	70.3	9.5	60.8	70.67	9.76	9.87	103
9H	11 Nov	1800	70.3	79.8	9.5	70.3	80.18	9.81	9.88	103
10H	11 Nov	1845	79.8	89.3	9.5	79.8	90.28	10.30	10.48	108
11H	11 Nov	1920	89.3	98.8	9.5	89.3	97.18	7.91	7.88	83
12H	11 Nov	2105	98.8	108.3	9.5	98.8	108.74	9.89	9.94	104
13H	11 Nov	2155	108.3	117.8	9.5	108.3	118.36	10.01	10.06	105
14H	11 Nov	2235	117.8	127.3	9.5	117.8	126.92	9.10	9.12	96
15H	11 Nov	2305	127.3	136.8	9.5	127.3	137.01	9.69	9.71	102
16H	11 Nov	2355	136.8	144.0	7.2	136.8	143.95	7.15	7.15	99
17H	1 Dec	0045	144.0	151.6	7.6	144.0	151.64	7.68	7.64	101
18H	1 Dec	0125	151.6	160.5	8.9	151.6	160.57	8.98	8.97	101
19H	1 Dec	0230	160.5	167.2	6.7	160.5	167.28	6.78	6.78	101
20H	1 Dec	0320	167.2	176.7	9.5	167.2	178.05	10.81	10.85	114
21H	1 Dec	0455	176.7	183.1	6.4	176.7	183.12	6.40	6.42	100
22X	1 Dec	0735	183.1	186.5	3.4	183.1	188.62	5.52	5.52	162
23X	1 Dec	0835	186.5	196.0	9.5	186.5	196.27	9.75	9.77	103

Table T1 (continued). (Continued on next page.)

			Depth DSF (m)			Depth CSF (m)				
Core	Date (2012)	Time (h)	Top of cored interval	Bottom of cored interval	Interval advanced (m)	Top of recovered core	Bottom of recovered core	Length of core recovered (m)	Curated length (m)	Recovery (%)
24X	1 Dec	0935	196.0	205.6	9.6	196.0	205.38	9.38	9.38	98
25X	1 Dec	1020	205.6	215.2	9.6	205.6	205.60	0.00	0.00	0
26X	1 Dec	1115	215.2	224.8	9.6	215.2	224.81	9.58	9.61	100
27X	1 Dec	1220	224.8	234.4	9.6	224.8	234.68	9.88	9.88	103
28X	1 Dec	1400	234.4	244.0	9.6	234.4	244.42	10.02	10.02	104
29X	1 Dec	1450	244.0	253.6	9.6	244.0	253.77	9.77	9.77	102
30X	1 Dec	1555	253.6	263.2	9.6	253.6	263.55	9.95	9.95	104
31X	1 Dec	1650	263.2	272.8	9.6	263.2	273.46	10.26	10.26	107
32X	1 Dec	1835	272.8	282.4	9.6	272.8	282.66	9.86	9.86	103
33X	1 Dec	1955	282.4	292.0	9.6	282.4	292.22	9.82	9.82	102
34X	1 Dec	2125	292.0	301.6	9.6	292.0	301.72	9.72	9.72	101
35X	1 Dec	2235	301.6	310.9	9.3	301.6	310.64	9.04	9.04	97
36X	1 Dec	2340	310.9	320.5	9.6	310.9	320.97	10.07	10.07	105
37X	2 Dec	0050	320.5	330.1	9.6	320.5	330.15	9.65	9.65	101
38X	2 Dec	0235	330.1	339.7	9.6	330.1	338.65	8.55	8.55	89
39X	2 Dec	0415	339.7	349.3	9.6	339.7	349.47	9.77	9.77	102
				Advanced total:	349.3					
				Total interval cored:	347.04					
339-U1386B-										
1H	2 Dec	0835	0.0	7.3	7.3	0.0	7.32	7.32	7.32	100
2H	2 Dec	0940	7.3	16.8	9.5	7.3	17.28	9.97	9.98	105
3H	2 Dec	1020	16.8	26.3	9.5	16.8	26.78	9.94	9.98	105
4H	2 Dec	1100	26.3	35.8	9.5	26.3	36.07	9.62	9.77	101
5H	2 Dec	1150	35.8	45.3	9.5	35.8	45.89	10.04	10.09	106
6H	2 Dec	1235	45.3	54.8	9.5	45.3	54.25	8.90	8.95	94
7H	2 Dec	1310	54.8	64.3	9.5	54.8	65.10	10.09	10.30	106
8H	2 Dec	1350	64.3	73.8	9.5	64.3	74.22	9.92	9.92	104
9H	2 Dec	1425	73.8	83.3	9.5	73.8	84.05	10.28	10.25	108
10H	2 Dec	1505	83.3	92.8	9.5	83.3	93.36	10.09	10.06	106
11H	2 Dec	1600	92.8	102.3	9.5	92.8	102.88	10.08	10.08	106
12H	2 Dec	1635	102.3	111.8	9.5	102.3	110.76	8.46	8.46	89
13H	2 Dec	1715	111.8	121.3	9.5	111.8	119.93	8.13	8.13	86
14H	2 Dec	1810	121.3	130.8	9.5	121.3	129.79	8.49	8.49	89
15H	2 Dec	1935	130.8	140.3	9.5	130.8	141.33	10.53	10.53	111
16H	2 Dec	2020	140.3	148.1	7.8	140.3	148.10	7.80	7.80	100
17H	2 Dec	2115	148.1	157.6	9.5	148.1	158.27	10.17	10.17	107
18H	2 Dec	2155	157.6	162.3	4.7	157.6	162.33	4.73	4.73	101
19X	2 Dec	2345	162.3	167.9	5.6	162.3	170.60	8.30	8.30	148
20X	3 Dec	0100	167.9	177.5	9.6	167.9	167.90	0.00	0.00	0
21X	3 Dec	0210	177.5	187.1	9.6	177.5	186.39	8.89	8.89	93
22X	3 Dec	0330	187.1	196.6	9.5	187.1	196.75	9.65	9.65	102
23X	3 Dec	0450	196.6	206.2	9.6	196.6	204.88	8.28	8.28	86
24X	3 Dec	0550	206.2	215.9	9.7	206.2	214.60	8.4	8.40	87
25X	3 Dec	0705	215.9	225.5	9.6	215.9	224.17	8.27	8.27	86
26X	3 Dec	0815	225.5	235.1	9.6	225.5	235.31	9.81	9.81	102
27X	3 Dec	0915	235.1	244.7	9.6	235.1	244.88	9.78	9.78	102
28X	3 Dec	1035	244.7	254.3	9.6	244.7	254.46	9.76	9.76	102
29X	3 Dec	1145	254.3	263.9	9.6	254.3	263.08	8.78	8.78	91
30X	3 Dec	1245	263.9	273.5	9.6	263.9	273.67	9.77	9.77	102
31X	3 Dec	1335	273.5	283.1	9.6	273.5	283.43	9.93	9.93	103
32X	3 Dec	1450	283.1	292.7	9.6	283.1	293.08	9.98	9.98	104
33X	3 Dec	1550	292.7	302.3	9.6	292.7	299.83	7.13	7.13	74
34X	3 Dec	1720	302.3	311.9	9.6	302.3	312.08	9.78	9.78	102
35X	3 Dec	1855	311.9	321.5	9.6	311.9	321.84	9.94	9.94	104
36X	3 Dec	2035	321.5	331.1	9.6	321.5	331.02	9.52	9.52	99
37X	3 Dec	2150	331.1	340.6	9.5	331.1	340.91	9.81	9.81	103
38X	3 Dec	2325	340.6	350.1	9.5	340.6	350.35	9.75	9.75	103
39X	4 Dec	0135	350.1	359.6	9.5	350.1	359.80	9.70	9.70	102
40X	4 Dec	0305	359.6	369.2	9.6	359.6	369.32	9.72	9.72	101
41X	4 Dec	0450	369.2	378.8	9.6	369.2	379.34	10.14	10.14	106
42X	4 Dec	0550	378.8	388.4	9.6	378.8	388.57	9.77	9.77	102
43X	4 Dec	0655	388.4	398.0	9.6	388.4	398.08	9.68	9.68	101
44X	4 Dec	0750	398.0	407.6	9.6	398.0	405.66	7.66	7.66	80
45X	4 Dec	0845	407.6	417.2	9.6	407.6	407.98	0.33	0.38	3
46X	4 Dec	1000	417.2	426.8	9.6	417.2	423.66	6.46	6.46	67
47X	4 Dec	1100	426.8	436.4	9.6	426.8	428.94	2.14	2.14	22
48X	4 Dec	1230	436.4	445.9	9.5	436.4	446.67	10.27	10.27	108
49X	4 Dec	1400	445.9	455.4	9.5	445.9	451.16	5.26	5.26	55

Table T1 (continued).

			Depth DSF (m)			Depth CSF (m)				
Core	Date (2012)	Time (h)	Top of cored interval	Bottom of cored interval	Interval advanced (m)	Top of recovered core	Bottom of recovered core	Length of core recovered (m)	Curated length (m)	Recovery (%)
50X	4 Dec	1705	455.4	464.9	9.5	455.4	455.78	0.38	0.38	4
				Advanced total:	464.9					
				Total interval cored:	421.6					
339-U1386C-										
1W	5 Dec	1305			*****Drilled from 0.0 to 165.0 m DSF without coring*****					
2R	5 Dec	1355	165.0	174.6	9.6	165.0	168.81	3.81	3.81	40
3W	5 Dec	1550	174.6	205.0	30.4	174.6	174.97	0.37	0.37	1.2
4R	5 Dec	1650	205.0	214.6	9.6	205.0	213.91	8.91	8.91	93
5W	6 Dec	0545	214.6	405.0	190.4	214.6	218.42	3.82	3.82	2
6R	6 Dec	0655	405.0	414.6	9.6	405.0	406.43	1.43	1.43	15
7R	6 Dec	0830	414.6	424.2	9.6	414.6	421.75	7.15	7.15	74
8R	6 Dec	0955	424.2	433.8	9.6	424.2	426.08	1.88	1.88	20
9R	6 Dec	1145	433.8	443.4	9.6	433.8	438.55	4.75	4.75	49
10R	6 Dec	1300	443.4	452.9	9.5	443.4	451.64	8.24	8.24	87
11R	6 Dec	1415	452.9	462.4	9.5	452.9	454.11	1.21	1.21	13
12R	6 Dec	1540	462.4	472.0	9.6	462.4	467.91	5.51	5.51	57
13R	6 Dec	1655	472.0	481.6	9.6	472.0	478.09	6.09	6.09	63
14R	6 Dec	1840	481.6	490.9	9.3	481.6	486.59	4.99	4.99	54
15R	6 Dec	2025	490.9	500.5	9.6	490.9	498.41	7.51	7.51	78
16R	6 Dec	2215	500.5	510.1	9.6	500.5	508.30	7.80	7.80	81
17R	7 Dec	0005	510.1	519.7	9.6	510.1	517.33	7.23	7.23	75
18R	7 Dec	0135	519.7	526.0	6.3	519.7	525.19	5.49	5.49	87
				Advanced total:	526.0					
				Total interval cored:	86.19					

DRF = drilling depth below rig floor, DSF = drilling depth below seafloor, CSF = core depth below seafloor. H = advanced piston coring system, X = extended core barrel system, R = rotary core barrel system, W = washed interval. Time is Universal Time Coordinated.

Table T2. Results from coulometric and CHNS analysis on whole-round squeezecake samples, Holes U1386A–U1386C. (Continued on next page.)

Core, section	Depth (mbsf)	Calcium carbonate (wt%)	Inorganic carbon (wt%)	Total carbon (wt%)	Nitrogen (wt%)	Organic carbon (wt%)	C/N
339-U1386A-							
1H-1	0.50	33.214	3.982	5.10	0.08	1.12	14.00
1H-2	2.00	27.663	3.317	4.68	0.10	1.36	13.60
1H-3	3.50	27.655	3.316	4.28	0.07	0.96	13.71
2H-1	4.30	20.908	2.507	4.06	0.06	1.55	25.83
2H-2	5.80	32.344	3.878	4.85	0.05	0.97	19.40
2H-3	7.30	32.587	3.907	4.73	0.05	0.82	16.40
2H-4	8.81	28.371	3.402	4.14	0.06	0.74	12.33
2H-5	10.31	30.707	3.682	4.57	0.05	0.89	17.80
2H-6	11.81	29.983	3.595	4.25	0.04	0.66	16.50
2H-7	12.97	27.863	3.341	4.02	0.07	0.68	9.71
3H-1	14.66	22.937	2.750	4.27	0.08	1.52	19.00
4H-1	24.17	26.200	3.141	3.84	0.05	0.70	14.00
4H-2	25.67	24.977	2.995	3.70	0.05	0.71	14.20
4H-3	27.18	21.598	2.590	3.49	0.04	0.90	22.50
4H-4	28.69	33.991	4.075	5.10	0.08	1.02	12.75
4H-5	30.20	31.888	3.823	4.62	0.06	0.80	13.33
4H-6	31.71	28.815	3.455	4.33	0.09	0.88	9.78
5H-6	41.21	29.869	3.581	4.50	0.09	0.92	10.22
6H-5	49.18	31.635	3.793	4.51	0.06	0.72	12.00
7H-6	60.18	29.834	3.577	4.05	0.04	0.47	11.75
8H-6	69.57	21.877	2.623	3.42	0.07	0.80	11.43
9H-6	79.24	19.945	2.391	2.89	0.06	0.50	8.33
10H-6	88.77	31.104	3.729	4.60	0.07	0.87	12.43
11H-5	94.60	25.718	3.084	3.49	0.04	0.41	10.25
12H-6	107.71	38.237	4.585	5.51	0.08	0.93	11.63
13H-6	117.18	32.017	3.839	4.41	0.05	0.57	11.40
14H-6	126.50	40.714	4.881	5.70	0.08	0.82	10.25
15H-6	136.05	23.410	2.807	3.29	0.06	0.48	8.00
16H-5	143.75	22.203	2.662	3.07	0.04	0.41	10.25
17H-5	151.22	34.082	4.086	4.95	0.07	0.86	12.29
18H-6	160.19	29.668	3.557	4.58	0.10	1.02	10.20
20H-7	176.75	24.590	2.948	3.82	0.09	0.87	9.67
21H-5	182.74	17.035	2.042	2.57	0.07	0.53	7.57
22X-3	187.46	30.347	3.638	4.33	0.08	0.69	8.63
23X-6	194.19	23.450	2.812	3.62	0.08	0.81	10.13
24X-6	204.29	21.523	2.581	3.24	0.08	0.66	8.25
26X-6	223.69	23.944	2.871	3.76	0.08	0.89	11.13
27X-6	233.23	26.100	3.129	3.89	0.08	0.76	9.50
28X-6	242.40	24.961	2.993	3.68	0.07	0.69	9.86
29X-6	251.96	27.228	3.265	4.00	0.06	0.74	12.33
30X-6	261.32	32.861	3.940	4.71	0.06	0.77	12.83
31X-6	270.87	27.527	3.300	4.00	0.06	0.70	11.67
32X-6	280.95	32.697	3.920				
33X-5	289.74	24.072	2.886				
34X-6	300.62	25.786	3.092				
35X-6	309.49	18.086	2.168				
36X-6	318.72	20.783	2.492				
37X-6	328.84	26.748	3.207				
38X-6	338.15	25.980	3.115				
39X-6	348.30	26.194	3.141				
339-U1386B-							
38X-6	349.20	28.820	3.455				
39X-6	357.97	25.985	3.116				
40X-6	368.13	19.633	2.354				
41X-6	377.41	19.457	2.333				
42X-6	387.14	22.422	2.688				
43X-6	396.82	22.786	2.732				
44X-4	403.84	23.242	2.787				
46X-3	421.61	16.449	1.972				
47X-2	428.50	23.868	2.862				
48X-6	443.81	14.586	1.749				
49X-4	450.72	15.530	1.862				

Table T2 (continued).

Core, section	Depth (mbsf)	Calcium carbonate (wt%)	Inorganic carbon (wt%)	Total carbon (wt%)	Nitrogen (wt%)	Organic carbon (wt%)	C/N
339-U1386C-							
2R-1	168.58	33.646	4.034				
4R-6	213.63	28.655	3.436				
7R-1	415.70	14.879	1.784				
9R-1	434.30	22.260	2.669				
10R-1	444.09	10.959	1.314				
11R-1	453.12	26.499	3.177				
13R-2	474.54	27.081	3.247				
13R-4	477.63	15.113	1.812				
16R-6	508.15	31.179	3.738				
17R-5	517.04	33.564	4.024				

Blank cells = no data.

Table T3. Average composition of main lithologies, Site U1386.

	Sand (%)	Silt (%)	Clay (%)	Siliciclastic (%)	Detrital carbonate (%)	Biogenic carbonate (%)
Nannofossil mud	2–5	25–45	55–70	20–40	30–40	30–45
Calcareous silty mud	15–20	40–60	30–50	10–30	30–60	20–40
Silty sand with biogenic carbonate	30–45	40–50	15–30	30–40	30–45	20–30

Table T4. XRD data, Site U1386. (Continued on next page.)

Hole, core, section, interval (cm)	Depth (mbsf)	Total intensity (counts)	Quartz (counts)	Calcite (counts)	K-feldspar (counts)	Plagioclase (counts)	Dolomite (counts)	Chlorite (counts)	Kaolinite (counts)	Illite (counts)	Smectite (counts)	Hornblende (counts)	Augite (counts)	Pyrite (counts)	Aragonite (counts)
339-															
U1386A-1H-1, 50–51	0.50	59,147	27,601	17,245	1,231	2,561	2,559	698	1,360	4,468	447	182	NA	NA	795
U1386A-2H-2, 50–51	5.80	75,296	35,884	15,835	661	3,084	7,056	1,214	2,167	8,121	323	167	784	NA	NA
U1386A-2H-6, 50–51	11.81	72,364	38,979	13,844	697	4,636	3,794	1,002	1,756	6,582	261	165	648	NA	NA
U1386A-3H-1, 136–137	14.66	60,768	33,692	13,066	524	1,822	3,065	NA	2,060	5,391	254	151	743	NA	NA
U1386A-4H-6, 137–138	31.71	53,506	22,381	14,658	526	1,553	1,730	1,215	2,588	7,946	361	140	NA	408	NA
U1386A-5H-6, 137–138	41.21	57,750	17,565	15,784	707	1,730	1,832	2,020	4,065	12,691	782	76	NA	NA	498
U1386A-6H-5, 137–138	49.18	48,183	21,335	15,702	412	1,204	2,005	628	1,441	4,371	386	74	625	NA	NA
U1386A-7H-6, 137–138	60.18	75,937	26,814	13,576	1,082	4,391	5,139	2,047	3,865	17,374	400	615	634	NA	NA
U1386A-8H-6, 117–118	69.57	69,312	26,319	11,042	946	2,702	2,089	2,064	3,976	18,502	576	406	690	NA	NA
U1386A-9H-6, 137–138	79.24	51,831	23,430	10,330	652	1,824	1,493	1,166	2,161	9,302	365	320	788	NA	NA
U1386A-10H-6, 137–138	88.77	69,090	31,254	16,603	830	2,228	4,861	1,189	2,587	8,530	289	117	602	NA	NA
U1386A-11H-5, 137–138	94.60	62,749	26,304	13,151	1,145	2,564	4,629	1,265	2,526	9,438	526	422	779	NA	NA
U1386A-12H-6, 137–138	107.71	60,399	17,994	22,155	552	1,302	2,555	1,381	3,062	9,912	620	207	NA	227	432
U1386A-13H-6, 133–134	117.18	58,804	26,009	17,078	543	1,629	2,144	1,296	2,163	6,857	225	296	564	NA	NA
U1386A-14H-6, 108–109	126.50	46,343	15,070	23,622	328	566	942	611	1,171	3,232	450	118	NA	233	NA
U1386A-15H-6, 120–121	136.05	49,356	21,086	12,208	683	1,296	2,923	976	2,080	6,873	462	151	618	NA	NA
U1386A-16H-5, 100–101	143.75	41,890	20,366	8,696	642	1,319	1,742	767	1,675	5,079	291	144	541	NA	628
U1386A-17H-5, 126–127	151.22	37,938	14,412	16,298	260	625	1,256	457	1,044	2,611	385	65	NA	165	360
U1386A-18H-6, 110–111	160.19	45,847	19,845	16,731	449	1,220	1,427	NA	1,440	3,603	496	214	NA	NA	422
U1386C-2R-3, 58–59	168.58	58,622	32,602	17,655	378	1,113	1,953	737	1,327	2,293	347	217	NA	NA	NA
U1386A-20H-7, 129–130	176.75	42,774	18,436	13,337	533	1,031	2,016	673	1,471	3,714	550	25	612	375	NA
U1386A-21H-5, 137–138	182.74	47,119	26,652	8,483	847	2,089	1,434	830	1,563	3,917	466	132	536	170	NA
U1386A-22X-3, 136–137	187.46	44,219	22,053	13,523	NA	1,156	1,510	520	1,231	2,202	415	147	696	NA	766
U1386A-23X-6, 137–138	194.19	40,849	18,974	12,582	453	951	1,986	551	1,296	3,024	544	129	NA	359	NA
U1386A-24X-6, 79–80	204.29	43,428	21,302	10,965	1,431	1,362	1,375	713	1,160	3,537	564	123	639	257	NA
U1386C-4R-6, 113–114	213.63	42,904	16,975	15,760	474	888	1,268	745	1,348	3,262	484	40	572	1,087	NA
U1386A-26X-6, 96–97	223.69	52,506	26,647	13,780	803	1,676	2,444	694	1,491	3,657	585	235	494	NA	NA
U1386A-27X-6, 139–140	233.23	42,539	21,886	11,854	NA	1,314	1,542	573	1,345	3,043	371	120	NA	NA	491
U1386A-28X-6, 137–138	242.40	52,658	26,846	12,589	758	1,976	2,105	1,006	1,865	4,636	462	415	NA	NA	NA
U1386A-29X-6, 127–128	251.96	55,215	26,359	13,406	1,266	3,624	2,450	937	1,951	4,645	272	305	NA	NA	NA
U1386A-30X-6, 136–137	261.32	64,659	33,065	18,971	606	1,412	2,473	911	1,884	4,227	274	189	NA	NA	647
U1386A-31X-6, 145–146	270.87	47,884	22,722	13,412	422	1,017	2,615	909	1,822	3,716	524	106	619	NA	NA
U1386A-32X-6, 124–125	280.95	57,941	25,994	15,093	640	1,293	4,595	1,125	2,573	5,059	585	280	NA	NA	704
U1386A-33X-5, 134–135	289.74	62,157	25,248	10,840	998	2,079	2,334	2,307	3,968	13,384	532	286	NA	181	NA
U1386A-34X-6, 137–138	300.62	42,515	19,418	13,935	NA	1,394	938	768	1,349	3,294	561	NA	542	316	NA
U1386A-35X-6, 49–50	309.49	43,500	22,242	9,145	942	1,505	963	926	1,357	4,534	627	155	715	389	NA
U1386A-36X-6, 130–131	318.72	68,282	46,850	8,718	1,122	1,979	2,780	770	1,306	3,566	346	337	508	NA	NA
U1386A-37X-6, 94–95	328.94	51,517	27,811	13,508	416	1,131	1,848	874	1,670	2,992	591	58	NA	NA	618
U1386A-38X-6, 55–56	338.15	52,703	19,677	15,883	585	1,494	1,468	1,476	2,514	8,209	769	109	519	NA	NA
U1386A-39X-6, 114–115	348.30	49,394	23,212	13,417	1,607	1,326	2,740	937	1,665	3,351	499	57	NA	NA	583
U1386B-40X-6, 103–104	368.13	34,837	14,000	11,763	587	680	1,150	725	1,170	3,589	683	86	404	NA	NA
U1386B-41X-6, 137–138	377.41	90,129	46,571	10,029	1,378	7,299	5,806	2,052	3,191	12,289	536	445	533	NA	NA
U1386B-42X-6, 137–138	387.14	58,801	23,294	12,533	1,091	1,598	4,696	1,681	3,026	9,326	607	112	549	288	NA
U1386B-43X-6, 132–133	396.82	66,487	43,404	10,692	941	2,871	1,793	732	1,540	3,586	336	81	511	NA	NA
U1386B-44X-4, 134–135	403.84	52,402	23,944	11,304	731	1,356	3,175	1,348	2,644	6,772	455	109	564	NA	NA
U1386B-46X-3, 141–142	421.61	57,817	30,231	7,775	1,044	1,922	4,630	1,203	1,952	7,512	399	346	803	NA	NA
U1386B-47X-2, 50–51	428.50	56,368	30,431	10,253	653	1,678	3,485	937	1,806	5,739	423	215	588	160	NA
U1386B-48X-6, 105–106	443.81	54,851	30,154	7,384	731	2,641	1,613	1,179	1,877	7,528	321	363	910	150	NA
U1386B-49X-4, 51–52	450.72	43,810	25,990	7,591	729	1,973	799	477	1,314	3,518	306	123	721	269	NA

Table T4 (continued).

Hole, core, section, interval (cm)	Depth (mbsf)	Total intensity (counts)	Quartz (counts)	Calcite (counts)	K-feldspar (counts)	Plagioclase (counts)	Dolomite (counts)	Chlorite (counts)	Kaolinite (counts)	Illite (counts)	Smectite (counts)	Hornblende (counts)	Augite (counts)	Pyrite (counts)	Aragonite (counts)
U1386C-14R-4, 59–60	486.49	48,858	24,151	14,119	538	1,549	1,058	829	1,517	4,095	549	NA	NA	NA	453
U1386C-16R-6, 65-66	508.15	48,705	22,900	16,439	707	960	879	579	1,357	2,933	609	64	419	858	NA
U1386C-17R-5, 94-95	517.04	48,080	17,294	20,844	478	1,097	886	711	1,409	4,423	705	NA	NA	233	NA

NA = no peak detected.

Table T5. Thin section description, Site U1386.

Core, section, interval (cm)	Thin section number	Sample type	Description	Lith. unit	Comment
339-U1386B-					
1H-CC, 22–27	3	Sand	Coarse material: abundant shell fragments, abundant foraminifers (planktonic + benthic), some of them are pyritized, sponge spicules	IA	
1H-CC, 22–27	4	Sand	Coarse material: abundant shell fragments, abundant foraminifers (planktonic + benthic), some of them are pyritized, sponge spicules, quartz present		
5H-CC, 26–31	5	Sand	Coarse material: abundant shell fragments, abundant foraminifers (planktonic + benthic), some of them are pyritized, sponge spicules, 40% quartz		
8H-CC, 38–45	7	Sand	Coarse material: abundant shell fragments, abundant foraminifers (planktonic + benthic), some of them are pyritized, sponge spicules, 30%–40% quartz		
14H-CC, 0–8	8	Sand	Abundant foraminifers (planktonic++, benthic) + fragments, pyrite and pyritized tests, 10% quartz	IB	
18H-CC, 22–27	9	Sand	Abundant foraminifers (planktonic, benthic++) + fragments, echinoderm spine fragments, pyrite and pyritized tests, 20%–30% quartz		
24H-CC, 48–53	10	Sand	Abundant foraminifers (planktonic, benthic++) + fragments, echinoderm spine fragments, pyrite and pyritized tests, abundant glauconite and glauconitized tests, 15% quartz		
33X-CC, 29–34	11	Sand	40% quartz, abundant foraminifers (planktonic, benthic++) + fragments, few pyrite	IC	
36X-CC, 31–36	12	Sand	Smaller grain size; 20%–30% quartz, abundant foraminifers and fragments (more difficult to identify)		
44X-CC, 29–34	13	Sand	70% quartz, 10% feldspar (among them plagioclase), opaques, few heavy minerals, 1 subrounded zircon, rare foraminifers		
45X-CC, 5–7	1	Pebble	50% clays, 40% quartz, 5% opaques, 5% micas, foraminifers and calcareous bioclasts present		Guadalquivir blue marls (Tortonian)?
45X-CC, 28–30	2	Pebble	50% clays, 40% quartz, 5% opaques, 5% micas, foraminifers present		Guadalquivir blue marls (Tortonian)?
45X-CC, 28–30	14	Sand	70% quartz, 10% felspars (plagioclase), clays		
47X-CC, 16–21	15	Sand	60% quartz, 10% feldspars (plagioclase), 10%–15% rock fragments, opaques, 1 augite	II	
50X-CC, 33–38	16	Sand	50% clays, 20% quartz, 10% felspars, 20% rock fragments		
339-U1386C-					
7R-4, 138	6	Pebble?	Siliceous sandstone		

Table T6. Biostratigraphic datums, Site U1386.

Event	Reference	Age (Ma)	Hole U1386A depth (mbsf)			Hole U1386B depth (mbsf)			Hole U1386C depth (mbsf)		
			Top	Bottom	Mean	Top	Bottom	Mean	Top	Bottom	Mean
LrO *Emiliania huxleyi* (>4 µm)	Flores et al., 2010	0.01	3.05	3.50	3.28	0.00	7.32	3.66			
FO *Emiliania huxleyi*	Raffi et al., 2006	0.26	97.18	108.74	102.96	74.22	84.05	79.14			
LO *Pseudoemiliania lacunosa*	Raffi et al., 2006	0.46	110.70	111.35	111.03	129.79	141.33	135.56			
Stilostomella extinction	Hayward, 2002; Kawagata et al., 2005	0.58–0.70	244.42	253.73	249.07	254.46	263.03	258.75			
LO *Reticulofenestra asanoi*	Raffi et al., 2006	0.90	265.85	266.75	266.30	273.67	283.43	278.55			
FO *Reticulofenestra asanoi*	Raffi et al., 2006	1.07				379.34	388.57	383.96			
T paracme *Neogloboquadrina pachyderma* (sin)	Lourens et al., 2004	1.21				388.57	398.08	393.33			
LO large *Gephyrocapsa* (>5.5 µm)	Raffi et al., 2006	1.24				407.93	423.66	415.80			
LO *Helicosphaera sellii*	Raffi et al., 2006	1.25				407.93	423.66	415.80	406.43	421.75	414.09
B paracme *Neogloboquadrina pachyderma* (sin)	Lourens et al., 2004	1.37				428.94	446.67	437.81	426.08	438.55	432.32
FO large *Gephyrocapsa* (>5.5 µm)	Raffi et al., 2006	1.61				428.94	446.67	437.81	426.08	438.55	432.32
LO *Calcidiscus macintyrei*	Raffi et al., 2006	1.66				451.16	455.78	453.47	451.64	454.08	452.86
LO *Discoaster brouweri*	Raffi et al., 2006	1.95							454.08	462.85	458.47
FO *Globorotalia inflata*	Lourens et al., 2004	2.09							461.81	462.60	462.21
LO *Globorotalia puncticulata*	Lourens et al., 2004	2.41							461.81	462.60	462.21
LO *Discoaster pentaradiatus*	Raffi et al., 2006	2.51							454.08	462.85	458.47
LO *Discoaster surculus*	Raffi et al., 2006	2.53							454.08	462.85	458.47
LO *Discoaster tamalis*	Raffi et al., 2006	2.80							454.08	462.85	458.47
LO *Sphaeroidinellopsis seminulina*	Hilgen, 1991	3.19							475.45	482.24	478.85
LO *Sphenolithus* spp.	Raffi et al., 2006	3.70							454.08	462.85	458.47
LO *Reticulofenestra pseudoumbilicus* (>7 µm)	Raffi et al., 2006	3.83							454.08	462.85	458.47
LaO *Globorotalia margaritae*	Lourens et al., 2004	3.98							506.52	507.95	507.24
FO *Globorotalia puncticulata*	Lourens et al., 2004	4.52							506.52	507.95	507.24
FO *Ceratolithus acutus*	Raffi et al., 2006	5.34							514.34	515.51	514.93
LO *Discoaster quinqueramus*	Raffi et al., 2006	5.54							515.31	516.76	516.03

LrO = last regular occurrence, LaO = last abundant occurrence, FO = first occurrence, LO = last occurrence, T = top, B = bottom. sin = sinistral, dex = dextral.

Table T7. Abundance of nannofossils, Site U1386. This table is available in an oversized format.

Table T8. Abundance of planktonic foraminifers, Holes U1386A and U1386B. (Continued on next two pages.)

Core, section	Depth (mbsf) Top	Depth (mbsf) Bottom	Pteropod abundance	Planktonic foraminifer abundance	Planktonic foraminifer preservation	*Beella digitata*	*Globigerina bulloides*	*Globigerina calida*	*Globigerina falconensis*	*Globigerinella siphonifera*	*Globigerinita glutinata*	*Globigerinoides conglobatus*	*Globigerinoides ruber* (pink)	*Globigerinoides ruber* (white)	*Globigerinoides sacculifer*	*Globigerinoides trilobus*	*Globorotalia crassaformis* s.l. (dex)	*Globorotalia crassaformis* s.l. (sin)	*Globorotalia hirsuta* (dex)	*Globorotalia hirsuta* (sin)	*Globorotalia inflata*	*Globorotalia menardii* (dex)	*Globorotalia menardii* (sin)	*Globorotalia scitula* (dex)	*Globorotalia scitula* (sin)	*Globorotalia truncatulinoides* (dex)	*Globorotalia truncatulinoides* (sin)	*Globoturborotalita rubescens*	*Globoturborotalita tenella*	*Neogloboquadrina atlantica* (dex)	*Neogloboquadrina atlantica* (sin)	*Neogloboquadrina dutertrei*	*Neogloboquadrina pachyderma* (dex)	*Neogloboquadrina pachyderma* (sin)	*Orbulina universa*	*Pulleniatina obliquiloculata*	*Sphaeroidinella dehiscens*	*Turborotalita humilis*	*Turborotalita iota*	*Turborotalita quinqueloba*	Comments
339-U1386A-																																									
1H-CC	3.81	3.86	B	D	G		D							P	P						F			R									F	F						F	
2H-CC	13.48	13.53	B	D	G		D	P			P			P							F			R		P	R						A		R					P	
3H-CC	23.22	23.27	B	D	G		A	P						P							P					R	B						A							F	
4H-CC	33.11	33.16	B	D	G		F	R		P				A			P				F	P		R			R	P					A		R					R	
5H-CC	42.18	42.23	B	D	G		A	P			P			F	P				P		F			P		R							A		R					R	
6H-CC	50.31	50.36	B	D	G		D				R			P					P	P	R			P									F		R					P	
7H-CC	61.22	61.27	B	D	G		F	P			P			R					R		A			P		R							A	P	R					P	
8H-CC	70.62	70.67	B	D	G		F	P			P			F					R		A					R	P						A		R					P	
9H-CC	80.13	80.18	B	D	G		A	P		P	P			R					R		F			P			P						F	P	R						
10H-CC	90.23	90.28	B	D	G		F	P		R	P			F							A			R		R							A		R					F	
11H-CC	97.13	97.18	B	D	G		F	P			P			F							R			R		P	P		P				A		P					F	
12H-CC	108.69	108.74	B	D	G		A	P		P	R	R	P	A							F		P	P		P	F		P				R		F					P	
13H-CC	118.14	118.19	B	D	G		A			P	P			R			P				F			P		P	R						A		F						
14H-CC	126.87	126.92	B	D	G	P	F		P	P	B			A	P	R	P		P		F	F				P	R					R	F		P	P					
15H-CC	136.96	137.01	B	D	G		A			P	P			P							R			P		P							A	P	P					P	
16H-CC	143.90	143.95	B	A	M		A			P	P			P										P									A	P	R					F	
17H-CC	151.59	151.64	B	D	G		A				P		P	A							F			P		P	P		R				A		R					P	
18H-CC	160.52	160.57	B	D	G		F			P	P			P				P			R			P			P		R				D		R					P	
19H-CC	167.23	167.28	B	D	G		A			P	P			P				P			F			P		P							A		P					P	
20H-CC	177.96	178.01	B	D	G		A			P	P			P							F			P					P				A	P	P					F	
21H-CC	183.05	183.10	B	D	M		F			P	P			P							R					P							A	P	P					F	
22X-CC	188.57	188.62	B	D	G		A			P	P			A			P				R					P			P				A							P	
23X-CC	196.20	196.25	B	D	G		A			P	P			F							A					P							A							P	
24X-CC	205.33	205.38	B	D	M		A							R							F					P	P						F	R	P					R	
26X-CC	224.50	224.55	B	D	G		F	P													F			P		P							F	F	F					F	
27X-CC	234.63	234.68	B	D	G		F							F	R						P			P		R	P						F	F	F						
28X-CC	244.37	244.42	B	D	G		F			P	P			R			R	F			A			R		F							A		F					R	
29X-CC	253.72	253.77	B	A	M		A							R			P	P			F			R		F							A	P	F						
30X-CC	263.50	263.55	B	D	G		F							F							A			R		R	P						F	F	F					R	
31X-CC	273.41	273.46	B	D	G		A							R							R			R	P	R							A	R	R						
32X-CC	282.61	282.66	B	D	G		A				P			R			P				F			P		R							F	A	R					P	
33X-CC	292.17	292.22	B	D	G		A			P				P							R			R		P	R						F	P	F					P	
34X-CC	301.67	301.72	B	D	G		F			P				F				P			F			P		R							A		F					P	
35X-CC	310.59	310.64	B	D	G		A			R				P							R												A	P	F					R	
36X-CC	320.92	320.97	B	A	G		A		P	R				R				P			R					R							A		R					P	
37X-CC	330.10	330.15	B	A	G		F			P	P			R							R					P							R	D	R					P	
38X-CC	338.60	338.65	B	A	G		F			P	P			F							F	P											R	P	B						
39X-CC	349.42	349.47	B	A	G		A			P	P			R				P			R			P		P							A	F	P					P	

Table T8 (continued). (Continued on next page.)

Core, section	Depth (mbsf)		Pteropod abundance	Planktonic foraminifer abundance	Planktonic foraminifer preservation	*Beella digitata*	*Globigerina bulloides*	*Globigerina calida*	*Globigerina falconensis*	*Globigerinella siphonifera*	*Globigerinita glutinata*	*Globigerinoides conglobatus*	*Globigerinoides ruber* (pink)	*Globigerinoides ruber* (white)	*Globigerinoides sacculifer*	*Globigerinoides trilobus*	*Globorotalia crassaformis* s.l. (dex)	*Globorotalia crassaformis* s.l. (sin)	*Globorotalia hirsuta* (dex)	*Globorotalia hirsuta* (sin)	*Globorotalia inflata*	*Globorotalia menardii* (dex)	*Globorotalia menardii* (sin)	*Globorotalia scitula* (dex)	*Globorotalia scitula* (sin)	*Globorotalia truncatulinoides* (dex)	*Globorotalia truncatulinoides* (sin)	*Globoturborotalita rubescens*	*Globoturborotalita tenella*	*Neogloboquadrina atlantica* (dex)	*Neogloboquadrina atlantica* (sin)	*Neogloboquadrina dutertrei*	*Neogloboquadrina pachyderma* (dex)	*Neogloboquadrina pachyderma* (sin)	*Orbulina universa*	*Pulleniatina obliquiloculata*	*Sphaeroidinella dehiscens*	*Turborotalita humilis*	*Turborotalita iota*	*Turborotalita quinqueloba*	Comments
	Top	Bottom																																							
339-U1386B-																																									
1H-CC	7.27	7.32	B	D	G		F	P		R	P			F					P		F			R		R							A		R						
2H-CC	17.22	17.27	B	D	G		F			P				F							F			P		P	R						A	P	R					R	
3H-CC	24.49	24.54	B	D	M		A	P						P					F		F	P					R						F		P						
5H-CC	45.79	45.84	B	D	M		A			P	P			R					R		F			P		F	R						A		R					P	
6H-CC	54.15	54.20	B	D	G		A				R			B					P		F			P									A	P	P					P	
7H-CC	64.84	64.89	B	D	G		D				P								P		R			R									F		F					R	
8H-CC	74.17	74.22	B	D	M		F				P			F				P	P		F			R		R	P						A		P					R	
9H-CC	84.03	84.08	B	D	M		F				F			B							F			F		P							A		P					R	
10H-CC	93.34	93.39	B	D	G		A			P	F													R		F							A	R	F						
11H-CC	102.83	102.88	B	D	G		A				R			F					F		P			R	P								F		P					P	
12H-CC	110.71	110.76	B	D	G		A							P			P				F			R			R						A		R					R	
13H-CC	119.88	119.93	B	D	G		A			P				R			P				F			P		R	P						A		R						
14H-CC	129.71	129.79	B	D	G		F				R			B							F												D	F	R					P	
15H-CC	141.28	141.33	B	D	G		A	P		P	P			R							A			R		R							A		F						
16H-CC	148.05	148.10	B	D	G		A			P	P			R							F	P		P		R			P				A	P	R						
17H-CC	158.22	158.27	B	D	G		A			P	P			R							A	P		P		P	P		P				R		R					B	
18H-CC	162.28	162.33	B	A	G		A	P		P	P			R							F			P		P			P				A		R					P	
19X-CC	170.55	170.60	R	D	G		A		P	R	R			F				P			R			P	P	R	P						A		R					R	
21X-CC	186.34	186.39		D	M		F			P	R			P				P			R			P									D	P	P					R	
22X-CC	196.70	196.75	B	A	G		A				P			P				P			F			P		R	P	P	P				A	P	P					R	
23X-CC	204.83	204.88	B	A	G		F			P				P							F			P									A	P	P					F	
24X-CC	214.55	214.60	B	A	G		F			R	P			P				P			F			P		R			P				A	P	P					R	
25X-CC	224.12	224.17	B	F	M		R			P											R			P		P							R	D						F	
26X-CC	235.26	235.31	B	A	G		P			P	P										A					P							R	P	R					F	
27X-CC	244.83	244.88	B	D	G		A			P	P			P			P		P		A			P		P							A	P	R					R	
28X-CC	254.41	254.46	B	D	G		F			P	P			F							A			R		R	P						F	R	R					P	
29X-CC	263.03	263.08	B	D	G		F			F				F			P	R			F			P		F							A		R					P	
30X-CC	273.62	273.67	B	D	G		F			P	F			P							R			P									F	A	P					R	
31X-CC	283.38	283.43	B	D	G		A				R			F			P	P			F												F	F	F					P	
32X-CC	293.03	293.08	B	D	G		D			R	P			P							F			F	P	P	R						R	R	R					R	
33X-CC	299.78	299.83	B	D	G		A				R			R							F			P		R							F	F	P					F	
34X-CC	312.03	312.08	B	D	G		A			R				A				P			A												F		P						
35X-CC	321.79	321.84	B	D	G		F			P				F				P			A			P		F	R						F	R	F					R	
36X-CC	330.97	331.02	B	D	G		A		P	R				A							A					F							A	P	F					P	
37X-CC	340.86	340.91	B	D	G		A			P	P			A							A	P		P		R			P				A		F	P				P	
38X-CC	350.30	350.35	R	D	G		A		P	R				A							A					F							A		F	P				P	
39X-CC	359.75	359.80	B	D	G		A		F	P	R			A				R			A			P		P							F	R	R						Abundant diatoms and radiolarians; some diatoms are pyritizied

Table T8 (continued).

Core, section	Depth (mbsf)		Pteropod abundance	Planktonic foraminifer abundance	Planktonic foraminifer preservation	*Beella digitata*	*Globigerina bulloides*	*Globigerina calida*	*Globigerina falconensis*	*Globigerinella siphonifera*	*Globigerinita glutinata*	*Globigerinoides conglobatus*	*Globigerinoides ruber* (pink)	*Globigerinoides ruber* (white)	*Globigerinoides sacculifer*	*Globigerinoides trilobus*	*Globorotalia crassaformis* s.l. (dex)	*Globorotalia crassaformis* s.l. (sin)	*Globorotalia hirsuta* (dex)	*Globorotalia hirsuta* (sin)	*Globorotalia inflata*	*Globorotalia menardii* (dex)	*Globorotalia menardii* (sin)	*Globorotalia scitula* (dex)	*Globorotalia scitula* (sin)	*Globorotalia truncatulinoides* (dex)	*Globorotalia truncatulinoides* (sin)	*Globoturborotalita rubescens*	*Globoturborotalita tenella*	*Neogloboquadrina atlantica* (dex)	*Neogloboquadrina atlantica* (sin)	*Neogloboquadrina dutertrei*	*Neogloboquadrina pachyderma* (dex)	*Neogloboquadrina pachyderma* (sin)	*Orbulina universa*	*Pulleniatina obliquiloculata*	*Sphaeroidinella dehiscens*	*Turborotalita humilis*	*Turborotalita iota*	*Turborotalita quinqueloba*	Comments
	Top	Bottom																																							
40X-CC	369.26	369.31	B	A	M		A		P					D							R				P	F	P						F	P	P	P					Very few foraminifers; radiolarians present (at least three different species); pyritic pellets in a shape similar to a coin that could be molds of large-sized diatoms or radiolarians; potentially diatom valves (recrystallized?)
41X-CC	379.29	379.34	B	D	G		F				P			P				P															R	D		P				R	Various types of lithic grains, including basaltic tephra
42X-CC	388.52	388.57	B	D	G		F		P	P				P				P			F			P									D	R						P	
43X-CC	398.03	398.08	B	A	G		D	P	P		R			F				P			R				P	R		P	P				R		P					F	
44X-CC	405.61	405.66	B	B																																					Residue consists of detrital sand with no foraminifers
45X-CC	407.88	407.93	B	B																																					Residue consists of abundant detrital sand with no foraminifers
46X-CC	423.61	423.66	B	P																																					Residue consists of abundant detrital grains; individual specimens of *G. bulloides, G. inflata, N. pachyderma* (dex) and (sin), *G. calida,* and *O. universa* were found
47X-CC	428.89	428.94	B	P	G																																				Residue formed by detrital sands, only two specimens of planktonic foraminifers were found, *N. atlantica* (dex) encrusted and *G. bulloides*
48X-CC	446.62	446.67	B	D	G		A	P			F			F							F									R			F	F	R					R	
49X-CC	451.11	451.16	B	D	G		A			P											F			P									R	A	R					R	
50X-CC	455.73	455.78	B	A	VG		A	P			R			A	F		P	P			F												F	P	P					P	

Abundance: D = dominant, A = abundant, C = common, F = few, P = present, R = rare, B = barren. Preservation: VG = very good, G = good, M = moderate. sin = sinistral, dex = dextral. See **"Biostratigraphy"** in the "Methods" chapter (Expedition 339 Scientists, 2013b) for abundance and preservation definitions.

Table T9. Abundance of planktonic foraminifers, Hole U1386C. (Continued on next page.)

Core, section, interval (cm)	Depth (mbsf)		Preservation	Abundance	*Dentoglobigerina altispira*	*Globigerina apertura*	*Globigerina bulloides*	*Globigerina calida*	*Globigerina decoraperta*	*Globigerina falconensis*	*Globigerina nepenthes*	*Globigerinella siphonifera*	*Globigerinita glutinata*	*Globigerinoides conglobatus*	*Globigerinoides extremus*	*Globigerinoides ruber* (white)	*Globigerinoides sacculifer*	*Globigerinoides trilobus*	*Globorotalia* cf. *crassula*	*Globorotalia crassaformis* s.l. (dex)	*Globorotalia crassaformis* s.l. (sin)	*Globorotalia hirsuta* (dex)	*Globorotalia hirsuta* (sin)	*Globorotalia inflata*	*Globorotalia margaritae*	*Globorotalia menardii* (dex)	*Globorotalia menardii* (sin)	*Globorotalia miocenica*	*Globorotalia puncticulata*	*Globorotalia scitula* (dex)	*Globorotalia scitula* (sin)	*Globorotalia truncatulinoides* (dex)	*Globorotalia truncatulinoides* (sin)	*Globoturborotalita rubescens*	*Globoturborotalita tenella*	*Neogloboquadrina atlantica* (dex)	*Neogloboquadrina atlantica* (sin)	*Neogloboquadrina pachyderma* (dex)	*Neogloboquadrina pachyderma* (sin)	*Orbulina universa*	*Sphaeroidinella dehiscens*	*Sphaeroidinellopsis seminulina*	*Sphaeroidinellopsis subdehiscens*	*Turborotalita quinqueloba*	Comments
	Top	Bottom																																											
339-U1386C-																																													
2R-CC	168.76	168.81	G	D			A					P	R			F					P			F						R	P	R						F		F	P			F	
4R-CC	213.86	213.91	G	D			A						P			A	P				R			F						R		F						F		F				P	
5W-CC	218.37	218.42	M	D			A					P	P			A					R			F						R		R						F						P	
6R-CC	406.38	406.43	M	R			A					P	R	P		A					P			F												F		F		R				P	
7R-CC	421.70	421.75	G	P			A						P	P		F					B			F												R		A						P	
8R-CC	426.03	426.08	G	A			F						P			P								R						P		P				R		D	P	B				R	
9R-CC	438.50	438.55	G	D			A						P			P					P			F						P						P		F	A	R				R	
10R-CC	451.59	451.64	G	P			A	P								F				R	P			A												R		F	P	F					Small pebbles; shell fragments
11R-1, 31–33	453.21	453.52	G	D			A					P	P			R								A						P								A		R					
11R-CC	454.03	454.08	G	D			A						R			P								F						P								D		R				P	Pyritic molds of diatoms
12R-1, 45–47	462.85	462.87	G	F		R	A					P	P		P	R	P		P										F									R		R					
12R-1, 82–84	463.22	463.24		D		A	F		P				P		P	R		P		P									D									F		F					
12R-CC	467.86	467.91	M	D		R	D	P				P			P	P	R		P							P		P	F									A		F		P		P	
13R-3, 43–45	475.43	475.45	P	A		R	F			R			R			R													D									R	P	R					
13R-CC	478.02	478.07	M	R		A	A								P	P	F								P				A									F				P			
14R-1, 62–64	482.22	482.24				F	F					P	P		R	R													D									D	P	F					
14R-3, 39–41	484.99	485.01				F							R		P	R		F		P									A									F		F		P			
14R-CC	486.54	486.59	G	D	P	A	A								F	P	F			P					R				A											P		P			
15R-1, 0–2	490.90	490.92	M	A		A	F			P			P			P		A							P				A									A		P		P			
15R-1, 85–87	491.75	491.77	M	D		F	A						P			R	P	A	P			P							F	P				P				F		R	P	P			
15R-3, 48–50	494.38	494.40				A	A									R		R			R								A									F	P	F		P			
15R-4, 24–26	495.64	495.66	G	F		F	A			P			R		P	R	R	R	R						P				F	P								R		P		P	P		
15R-CC	498.36	498.41	G	D	P	F	A		P			R			F	R	P	A		P					R				A									P		A		R		P	
16R-4, 43–45	505.43	505.45	M	D		R	A						R			R	R	R				P							F					P				F		R		R		P	
16R-5, 0–2	506.50	506.52	G	D		F	F			R			P		F	R		A											A	P								A	P	F			P		
16R-6, 43–45	507.93	507.95	M	D		P	A		P				F			R		R	P						P				R									A	P	R		P			
16R-CC	508.23	508.28	G	F		A	A		P	P	P	P			F	R	R	R							R													P		F		P	P		
17R-1, 0–2	510.10	510.12	M	D		F	A		F		P		P		A			R							R					P								A	P	R					
17R-1, 70–72	510.80	510.82	M	A		P	F	P				F	P																P									A	R	R				P	
17R-3, 27–29	513.37	513.39		A		F	P		R				P		R			P							F				P	P								A	P	F					
17R-4, 55–57	515.15	515.17	M	D		R	A		A		P		P		F			P																				A	P	R		P	P	P	
17R-5, 90–92	517.00	517.02	G	D			F		R		R		A		F	R	P	R							R					P					P			A	P	R		P			
17R-CC	517.28	517.33	G	F		F	A		F		P				F	F		R							A				P									P	P	P	P	P			
18R-1, 58–60	520.28	520.30	M	A		A			P				P		R			P							R					R								A	P	R					
18R-3, 58–60	523.28	523.30				A	A		P						F	R		P							F					R								A	F	F					
18R-4, 18–20	524.38	524.40	M	R		P	F		P	P			R		R	P		R												P								A		F					

Table T9 (continued).

Core, section, interval (cm)	Depth (mbsf)		Preservation	Abundance	*Dentoglobigerina altispira*	*Globigerina apertura*	*Globigerina bulloides*	*Globigerina calida*	*Globigerina decoraperta*	*Globigerina falconensis*	*Globigerina nepenthes*	*Globigerinella siphonifera*	*Globigerinita glutinata*	*Globigerinoides conglobatus*	*Globigerinoides extremus*	*Globigerinoides ruber* (white)	*Globigerinoides sacculifer*	*Globigerinoides trilobus*	*Globorotalia* cf. *crassula*	*Globorotalia crassaformis* s.l. (dex)	*Globorotalia crassaformis* s.l. (sin)	*Globorotalia hirsuta* (dex)	*Globorotalia hirsuta* (sin)	*Globorotalia inflata*	*Globorotalia margaritae*	*Globorotalia menardii* (dex)	*Globorotalia menardii* (sin)	*Globorotalia miocenica*	*Globorotalia puncticulata*	*Globorotalia scitula* (dex)	*Globorotalia scitula* (sin)	*Globorotalia truncatulinoides* (dex)	*Globorotalia truncatulinoides* (sin)	*Globoturborotalita rubescens*	*Globoturborotalita tenella*	*Neogloboquadrina atlantica* (dex)	*Neogloboquadrina atlantica* (sin)	*Neogloboquadrina pachyderma* (dex)	*Neogloboquadrina pachyderma* (sin)	*Orbulina universa*	*Sphaeroidinella dehiscens*	*Sphaeroidinellopsis seminulina*	*Sphaeroidinellopsis subdehiscens*	*Turborotalita quinqueloba*	Comments
	Top	Bottom																																											
18R-4, 60–62	524.80	524.82	M	R		F	A						R		R			P							P													A	P	F					
18R-CC	525.14	525.19	M	R		A	A		P	P		P	R	P	R	P		P							F													A		F		P	P		

Abundance: D = dominant, A = abundant, C = common, F = few, P = present, R = rare. Preservation: G = good, M = moderate, P = poor. sin = sinistral, dex = dextral. See **"Biostratigraphy"** in the "Methods" chapter (Expedition 339 Scientists, 2013b) for abundance and preservation definitions.

Table T10. Abundance of benthic foraminifers, Site U1386. This table is available in an oversized format.

Table T11. Abundance of ostracods, Site U1386. This table is available in an oversized format.

Table T12. Abundance of pollen and spores, Site U1386.

Hole, core, section	Depth (mbsf)		Preservation	Abundance	Exotic counted	*Alnus*	*Anthemis* type	Apiaceae	*Artemisia*	*Asphodelus*	*Aster* type	*Betula*	*Botrychium* type	Brassicaceae	Caryophyllaceae	*Cedrus*	Chenopodiaceae	Cupressaceae	Cyperaceae	*Daphne*	*Ephedra distachya* type	*Ephedra fragilis* type	Ericaceae	*Fraxinus excelsior* type	*Galium* type	*Helianthemum*	*Isoetes*	Liliaceae	Monolete psilate	*Olea*	*Picea*	*Pinus*	*Pistacia*	*Plantago*	Plumbaginaceae	Poaceae	*Quercus* deciduous type	*Quercus* evergreen type	Ranunculaceae	Rosaceae	*Salix*	*Sanguisorba* minor	*Taraxacum*	Taxodiaceae/Cupressaceae	Trilete ornamented	Trilete psilate	*Typha sparganium*	Unidentifiables
	Top	Bottom																																														
339-																																																
U1386A-1H-CC	3.81	3.86	G	A	116				F		F			R		R	F	C			R	F	R				R		R	R		A				R		F					C			F		C
U1386A-5H-CC	42.18	42.23	G	A	88	F	C				C	F	F	F			F		C				F		F		A		F	C		A	F	F		C	F	C		F	F		A			F	F	C
U1386A-8H-CC	70.62	70.67	G	A	50	F	C		A		F			F			C		F			F	C	F			C					A				C	C	C	F	F			C		F			A
U1386A-15H-CC	136.96	137.01	G	A	22		F		A		F	F		F			A	C			A	F	C			F	C		F			A		C		C	F						C					A
U1386A-20H-CC	177.96	178.05	G	A	88		F	F	C		F	F		F	F	C	C	F	F		C	F	F							F		A				C	C	C				F	C		F			C
U1386A-26X-CC	224.5	224.58	M	A	113				F		R						F				F	R	R				R					C			R													C
U1386A-32X-CC	282.61	282.66	G	A	100		F		C	F	F				F		A	C			F		F				F			F		A		F		F	F						A					A
U1386A-35X-CC	310.59	310.64	M	A	60		F		C		C				F		A				A	C										A				C							A					A
U1386B-40X-CC	369.26	369.31	P	A	23		F	F			F			F	F		A		C								A			C		F	F	C		A	C						A					A
U1386B-42X-CC	388.52	388.57	P	A	57		C		C		C				C		A		C	F		F	C				C	F		C		C		F		C	C	C					A	C		F		A
U1386C-9R-CC	438.5	438.55	P	A	73	F	C		A								C		F		C	C	F									A		F		C	F	C					C	A				A
U1386B-50X-CC	455.73	455.78	P	A	106		C		C		C			F	R	R	F		R			F	F				C			A		C				C	F	F					A	R	F	R		A
U1386C-17R-CC	517.33	517.33	P	A	113			R			F						F		R			R					C			F	F	F				C	C	R					C	R		R		A

Preservation: G = good, M = moderate, P = poor. Abundance: A = abundant, C = common, F = few, R = rare. See "Biostratigraphy" in the "Methods" chapter (Expedition 339 Scientists, 2013b) for abundance and preservation definitions.

Table T13. FlexIt tool core orientation data, Site U1386.

Core	Orientation angle (°)	Orientation standard deviation (°)
339-U1386A-		
4H	85	1.0
5H	67	0.5
6H	326	0.4
7H	330	0.7
8H	155	0.4
9H	300	0.9
10H	356	0.3
11H	92	0.0
12H	30	0.8
13H	310	0.5
14H	176	0.7
15H	289	0.4
16H	137	0.1
17H	180	0.8
18H	245	0.4
19H	297	0.1
20H	357	0.3
21H	203	0.1
339-U1386B-		
4H	274	0.7
5H	253	0.2
6H	250	0.2
7H	183	0.2
8H	86	0.3
9H	216	3.2
10H	274	1.3
11H	242	1.2
12H	281	0.8
13H	134	0.7
14H	157	1.3
15H	45	0.4
16H	187	0.3
17H	256	0.2
18H	294	0.3

Table T14. Disturbed intervals, Site U1386. (Continued on next two pages.)

Core, section, interval (cm)	Drilling disturbance	
	Intensity	Comment
339-U1386A-		
1H-1	Moderate	Slightly soupy mudline, extending down to about 15 cm but do not cull data in this interval
1H-1, 147–150	High	IW tube sample
1H-2, 143–150	Void	WR
2H-1, 0–1	Moderate	Void and minor disturbance
2H-1, 143–150	High	IW tube sample
2H-2, 142–150	High	IW tube sample
2H-3, 143–150	High	IW tube sample
2H-4, 143–150	High	IW tube sample
2H-5, 143–150	High	IW tube sample
2H-6, 116–120	Void	WR
3H-1	Negligible	Undisturbed core top
3H-1, 139–147	High	IW tube sample
3H-1, 147–150	Void	Void
3H-2, 141–150	High	IW tube sample
3H-3, 143–150	High	IW tube sample
3H-4, 143–150	High	IW tube sample
3H-5, 145–150	High	IW tube sample
4H-1	Negligible	Undisturbed core top
4H-1, 145–150	High	IW tube sample
4H-2, 145–150	High	IW tube sample
4H-3, 145–150	High	IW tube sample
4H-4, 145–150	High	IW tube sample
4H-5, 145–150	High	IW tube sample
4H-6, 145–150	Void	WR
5H-1	Negligible	Undisturbed core top
5H-1, 142–150	High	IW tube sample
5H-2, 145–150	High	IW tube sample
5H-3, 144–150	High	IW tube sample
5H-4, 145–150	High	IW tube sample
5H-5, 145–150	High	IW tube sample
5H-6, 145–150	Void	WR
6H-1, 0–13	High	Disturbed core top
6H-1, 139–145	High	IW tube sample
6H-2, 145–150	High	IW tube sample
6H-3, 145–150	High	IW tube sample
6H-4, 145–150	High	IW tube sample
6H-5, 140–145	High	IW tube sample
6H-5, 145–150	Void	WR
7H-1	Negligible	Undisturbed core top
7H-1, 141–150	High	IW tube sample
7H-2, 143–150	High	IW tube sample
7H-3, 143–150	High	IW tube sample
7H-4, 143–150	High	IW tube sample
7H-5, 140–150	High	IW tube sample
7H-6, 145–150	Void	WR
8H-1	Negligible	Relatively undisturbed core top
8H-1, 140–150	High	IW tube sample
8H-2, 140–150	High	IW tube sample
8H-3, 140–150	High	IW tube sample
8H-4, 140–150	High	IW tube sample
8H-5, 140–150	High	IW tube sample
8H-6, 130–135	Void	WR
9H-1	Negligible	Undisturbed core top
9H-1, 140–150	High	IW tube sample
9H-2, 142–150	High	IW tube sample
9H-3, 145–152	High	IW tube sample
9H-4, 145–152	High	IW tube sample
9H-5, 140–150	High	IW tube sample
9H-6, 145–150	Void	WR
10H-1	Negligible	Undisturbed core top
10H-1, 142–150	High	IW tube sample
10H-2, 121–125	High	Crack
10H-2, 144–150	High	IW tube sample
10H-3, 141–150	High	IW tube sample
10H-4, 145–152	High	IW tube sample
10H-5, 125–128	High	Crack
10H-5, 145–154	High	IW tube sample

Table T14 (continued). (Continued on next page.)

Core, section, interval (cm)	Drilling disturbance	
	Intensity	Comment
10H-6, 149–156	Void	WR
11H-1, 0–19	High	Disturbed core top
11H-2, 81–88	Void	Void
11H-3, 0–4	High	Void and disturbance
11H-3, 32–45	High	Void and disturbance
11H-3, 91–94	High	Void and disturbance
11H-3, 104–107	High	Void and disturbance
11H-4, 0–8	High	Void and disturbance
11H-4, 82–99	High	Void and disturbance
11H-4, 116–126	High	IW tube sample
11H-5, 140–150	High	IW tube sample
11H-6, 74–145	High	Flow-in
11H-6, 145–150	Void	WR
11H-7, 0–80	High	Flow-in
12H-1	Negligible	Undisturbed core top; expansion cracks become more abundant from Core 12H downhole but are not included
12H-1, 141–150	High	IW tube sample
12H-2, 143–150	High	IW tube sample
12H-3, 142–150	High	IW tube sample
12H-4, 141–150	High	IW tube sample
12H-5, 144–150	High	IW tube sample
12H-6, 147–152	Void	WR
13H-1	Negligible	Undisturbed core top
13H-1, 142–150	High	IW tube sample
13H-2, 143–150	High	IW tube sample
13H-3, 142–150	High	IW tube sample
13H-4, 140–150	High	IW tube sample
13H-5, 140–150	High	IW tube sample
13H-6, 139–145	Void	WR
14H-1, 0–19	High	Disturbed core top
14H-1, 142–150	High	IW tube sample
14H-2, 142–150	High	IW tube sample
14H-3, 143–150	High	IW tube sample
14H-4, 142–152	High	IW tube sample
14H-5, 150–157	Void	WR
15H-1	Negligible	Undisturbed core top
15H-1, 48–55	High	Void and disturbance
15H-1, 142–150	High	IW tube sample
15H-2, 143–150	High	IW tube sample
15H-3, 141–150	High	IW tube sample
15H-4, 143–150	High	IW tube sample
15H-5, 145–154	High	IW tube sample
15H-6, 120–130	Void	WR
15H-7, 35–60	High	Partially crushed core liner
16H-1	Negligible	An undisturbed core top
16H-1, 141–150	High	IW tube sample
16H-2, 141–150	High	IW tube sample
16H-3, 140–150	High	IW tube sample
16H-4, 140–145	Void	WR
16H-5, 74–83	High	Void and disturbance
17H-1	Negligible	Undisturbed core top
17H-1, 140–150	High	IW tube sample
17H-2, 140–150	High	IW tube sample
17H-3, 139–150	High	IW tube sample
17H-4, 143–150	Void	WR
17H-5, 106–111	Void	Void
18H-1, 0–2	Minor	Slightly disturbed core top
18H-1, 52–61	Void	Void
18H-5, 141–150	Void	WR
18H-6, 98–102	Void	Void
19H-1	Negligible	Undisturbed core top
19H-4, 143–150	Void	WR
20H-1, 0–1	Moderate	Slightly disturbed core top
20H-4, 56–61	Void	Void
20H-7, 144–150	Void	WR
21H-1	Negligible	Undisturbed core top
21H-3, 116–150	High	Void and disturbance
21H-4, 0–17	High	Void and disturbance
21H-4, 142–150	Void	WR
22X-3, 145–150	Void	WR

Table T14 (continued).

Core, section, interval (cm)	Drilling disturbance	
	Intensity	Comment
23X-6, 145–150	Void	WR
24X-6, 91–100	Void	WR
26X-6, 111–120	Void	WR
29X-6, 140–150	Void	WR
32X-6, 140–150	Void	WR
35X-3, 140–150	Void	WR
35X-4, 140–150	Void	WR
38X-4, 53–81	Void	Void
38X-5, 140–150	Void	WR
339-U1386B-		
1H-1	Moderate	Slightly soupy mudline, extending down to about 11 cm but do not cull data in this interval
2H-1, 0–1	Moderate	Disturbed core top
3H-1	Negligible	Undisturbed core top
4H-1	Negligible	Undisturbed core top
5H-1, 0–1	Moderate	Disturbed core top
6H-1, 0–11	High	Disturbed core top
7H-1, 0–2	High	Disturbed core top
8H-1, 0–8	Moderate	Disturbed core top
9H-1, 0–4	High	Disturbed core top
10H-1, 0–2	High	Disturbed core top
11H-1, 0–1	High	Disturbed core top
11H-7, 62–65	Void	Void
12H-1, 0–5	High	Disturbed core top; expansion cracks become more abundant from Core 12H downhole but are not included
13H-1, 0–2	High	Disturbed core top
13H-4, 88–93	Void	Void
13H-6, 28–32	Void	Void
14H-1, 0–16	Moderate	Disturbed core top
14H-7, 39–57	High	Void and disturbance
15H-1, 0–1	High	Disturbed core top
16H-1	Negligible	Undisturbed core top
16H-6, 17–26	Void	Void
17H-1, 0–1	High	Disturbed core top
17H-1, 92–95	Void	Void
17H-2, 76–87	Void	Void
17H-7, 129–134	Void	Void
18H-1, 0–31	High	Disturbed core top
18H-1, 54–75	Void	Void
18H-4, 5–33	High	Void and disturbance
19X-1, 0–18	High	Disturbed core top
21X-1, 0–28	High	Disturbed core top
22X-1, 0–16	High	Disturbed core top
23X-1, 0–6	High	Disturbed core top
40X-6, 111–121	Void	WR
43X-6, 140–150	Void	WR
46X-4, 91–100	Void	WR
49X-2, 140–150	Void	WR
339-U1386C-		
2R-1, 0–30	High	Disturbed core top
3W-1, 0–40	High	Totally disturbed
4R-1, 0–40	High	Disturbed core top
6R-1, 0–15	High	Disturbed core top
7R-1, 0–7	High	Disturbed core top
8R-1, 0–16	High	Disturbed core top
9R-1, 0–50	High	Disturbed core top
13R-1, 0–25	High	Disturbed core top
16R-1, 0–28	High	Disturbed core top

IW = interstitial water, WR = whole-round sample.

Table T15. NRM inclination, declination, and intensity data after 20 mT peak field AF demagnetization, Hole U1386A.

Core, section, interval (cm)	Depth (mbsf)	Inclination (°)	Declination (°)	FlexIt-corrected declination (°)	Intensity (A/m)
339-U1386A-					
1H-1	0.00				
1H-1, 5	0.05				
1H-1, 10	0.10				
1H-1, 15	0.15	44.7	147		0.010919
1H-1, 20	0.20	48.4	140.8		0.01435
1H-1, 25	0.25	51.1	137.5		0.01812
1H-1, 30	0.30	52.3	140.6		0.022065
1H-1, 35	0.35	56.6	139.9		0.023288
1H-1, 40	0.40	58.5	139.2		0.026005
1H-1, 45	0.45	56.6	138.2		0.026631
1H-1, 50	0.50	60.1	133.8		0.026922
1H-1, 55	0.55	61.6	136.2		0.024675
1H-1, 60	0.60	56.8	135.3		0.025176
1H-1, 65	0.65	57.1	135.5		0.024774
1H-1, 70	0.70	55.6	135.7		0.024941
1H-1, 75	0.75	53.7	135		0.025091
1H-1, 80	0.80	50.2	135.1		0.023849
1H-1, 85	0.85	50.9	135.1		0.022292
1H-1, 90	0.90	49.1	136.2		0.024592
1H-1, 95	0.95	49	138.2		0.024753
1H-1, 100	1.00	48.3	141		0.024876
1H-1, 105	1.05	49.2	144.9		0.025922
1H-1, 110	1.10	50.2	148.3		0.026138
1H-1, 115	1.15	49.6	148.1		0.025083
1H-1, 120	1.20	48.8	147		0.024842
1H-1, 125	1.25	48.3	141.8		0.027091
1H-1, 130	1.30	50	141.4		0.027875
1H-1, 135	1.35	50.3	135.5		0.029191
1H-1, 140	1.40				
1H-1, 145	1.45				
1H-1, 150	1.50				
1H-2	1.50				
1H-2, 5	1.55				
1H-2, 10	1.60				
1H-2, 15	1.65	50.4	139.2		0.036862
1H-2, 20	1.70	49.7	136.2		0.034952
1H-2, 25	1.75	49.1	135.7		0.033855
1H-2, 30	1.80	48.7	137.3		0.034231
1H-2, 35	1.85	49.4	140.6		0.033883
1H-2, 40	1.90	50.3	141.9		0.032952
1H-2, 45	1.95	50.2	142.2		0.032863
1H-2, 50	2.00	50.1	141.3		0.032646
1H-2, 55	2.05	50	140.7		0.032295
1H-2, 60	2.10	49	140.9		0.031585
1H-2, 65	2.15	48.4	141.1		0.03113
1H-2, 70	2.20	45	137		0.032169
1H-2, 75	2.25	45.7	133.1		0.032263
1H-2, 80	2.30	49	134		0.02986
1H-2, 85	2.35	50	134.3		0.027874
1H-2, 90	2.40	50.4	137.3		0.026607
1H-2, 95	2.45	51.5	137.2		0.024443
1H-2, 100	2.50	53.5	143.4		0.022758
1H-2, 105	2.55	53.3	146.2		0.020715
1H-2, 110	2.60	52.3	147.5		0.019201
1H-2, 115	2.65	50	146.1		0.017657
1H-2, 120	2.70	48.4	146.9		0.014762
1H-2, 125	2.75	49.6	143.7		0.012313
1H-2, 130	2.80	48.7	141.6		0.011377
1H-2, 135	2.85	45.2	144.9		0.011809

Blank cells indicate depth levels where data were either not available (i.e., FlexIt-corrected declination data for nonoriented cores) or removed because of disturbance, voids, or measurement edge effects. Only a portion of this table appears here. The complete table is available in **ASCII.**

Table T16. NRM inclination, declination, and intensity data after 20 mT peak field AF demagnetization, Hole U1386B.

Core, section, interval (cm)	Depth (mbsf)	Inclination (°)	Declination (°)	FlexIt-corrected declination (°)	Intensity (A/m)
339-U1386B-					
1H-1	0.00				
1H-1, 5	0.05				
1H-1, 10	0.10				
1H-1, 15	0.15	62.4	155.6		0.013381
1H-1, 20	0.20	64.8	157.2		0.013709
1H-1, 25	0.25	66.1	176.7		0.015742
1H-1, 30	0.30	58.4	178.9		0.024092
1H-1, 35	0.35	59.5	177.2		0.026421
1H-1, 40	0.40	61	175		0.025855
1H-1, 45	0.45	59.8	171.3		0.026022
1H-1, 50	0.50	59.1	171.5		0.025901
1H-1, 55	0.55	59.7	171.3		0.025696
1H-1, 60	0.60	61.9	171.2		0.025392
1H-1, 65	0.65	60.8	166.3		0.025535
1H-1, 70	0.70	58.7	162.4		0.024687
1H-1, 75	0.75	60.1	162.5		0.024075
1H-1, 80	0.80	59.6	163.2		0.024712
1H-1, 85	0.85	56.7	162.5		0.025833
1H-1, 90	0.90	56.6	162.6		0.026305
1H-1, 95	0.95	56.9	162.5		0.02713
1H-1, 100	1.00	57.5	161.9		0.027617
1H-1, 105	1.05	57.2	160		0.027948
1H-1, 110	1.10	57.9	160.9		0.027493
1H-1, 115	1.15	58.4	161.7		0.027188
1H-1, 120	1.20	59.4	161.8		0.028698
1H-1, 125	1.25	59.1	161.7		0.0314
1H-1, 130	1.30	58.9	165.2		0.032518
1H-1, 135	1.35	60	166.1		0.031924
1H-1, 140	1.40				
1H-1, 145	1.45				
1H-1, 150	1.50				
1H-2	1.50				
1H-2, 5	1.55				
1H-2, 10	1.60				
1H-2, 15	1.65	53.8	145.5		0.033553
1H-2, 20	1.70	54.7	147.3		0.033232
1H-2, 25	1.75	55.3	150.8		0.032486
1H-2, 30	1.80	55.1	153.8		0.032419
1H-2, 35	1.85	55.4	155.7		0.031408
1H-2, 40	1.90	56.1	155.6		0.030699
1H-2, 45	1.95	56	154.6		0.030568
1H-2, 50	2.00	57.3	146.6		0.029694
1H-2, 55	2.05	58.4	142.1		0.028676
1H-2, 60	2.10	59.3	142.5		0.02774
1H-2, 65	2.15	58.8	142.7		0.026949
1H-2, 70	2.20	60.2	144.2		0.024965
1H-2, 75	2.25	60.4	139.8		0.022664
1H-2, 80	2.30	59.8	142.6		0.02247
1H-2, 85	2.35	60.3	149.8		0.021675
1H-2, 90	2.40	59.6	152.3		0.019915
1H-2, 95	2.45	60.1	152.8		0.017193
1H-2, 100	2.50	58.9	147.1		0.015762
1H-2, 105	2.55	56	149.7		0.014297
1H-2, 110	2.60	57.5	151.9		0.012054
1H-2, 115	2.65	58.2	148		0.010888
1H-2, 120	2.70	61.1	146.6		0.011565
1H-2, 125	2.75	62.5	137.8		0.013984
1H-2, 130	2.80	58.8	144.1		0.015199

Blank cells indicate depth levels where data were either not available (i.e., FlexIt-corrected declination data for nonoriented cores) or removed because of disturbance, voids, or measurement edge effects. Only a portion of this table appears here. The complete table is available in **ASCII.**

Table T17. NRM inclination, declination, and intensity data after 20 mT peak field AF demagnetization, Hole U1386C.

Core, section, interval (cm)	Depth (mbsf)	Inclination (°)	Declination (°)	FlexIt-corrected declination (°)	Intensity (A/m)
339-U1386C-					
2R-1	165.00				
2R-1, 5	165.05				
2R-1, 10	165.10				
2R-1, 15	165.15				
2R-1, 20	165.20				
2R-1, 25	165.25				
2R-1, 30	165.30				
2R-1, 35	165.35	15.2	57.5		0.003535
2R-1, 40	165.40	73.1	298.4		0.002474
2R-1, 45	165.45	51.3	235.3		0.001685
2R-1, 50	165.50	63.1	131.5		0.001387
2R-1, 55	165.55	–8	217.2		0.005085
2R-1, 60	165.60	–84.4	294.6		0.006614
2R-1, 65	165.65	–22.3	59.4		0.007111
2R-1, 70	165.70	–14.8	303.6		0.0006166
2R-1, 75	165.75	55.1	240.4		0.001833
2R-1, 80	165.80	54.9	200.3		0.001998
2R-1, 85	165.85	69.3	130		0.001728
2R-1, 90	165.90	54.5	70		0.002004
2R-1, 95	165.95	54.5	34.8		0.002215
2R-1, 100	166.00	52.8	52.6		0.00239
2R-1, 105	166.05	46.8	85.6		0.003262
2R-1, 110	166.10	49.9	71.9		0.002905
2R-1, 115	166.15	67.5	6.8		0.002305
2R-1, 120	166.20	83.9	57		0.002138
2R-1, 125	166.25	58.5	111.2		0.002194
2R-1, 130	166.30	55.5	128.1		0.00213
2R-1, 135	166.35	53.7	113.4		0.001609
2R-1, 140	166.40				
2R-1, 145	166.45				
2R-1, 150	166.50				
2R-2	166.50				
2R-2, 5	166.55				
2R-2, 10	166.60				
2R-2, 15	166.65	70.9	118.9		0.003561
2R-2, 20	166.70	44.3	86		0.003785
2R-2, 25	166.75	47.7	77.8		0.003579
2R-2, 30	166.80	74.7	56.5		0.002208
2R-2, 35	166.85	53.7	124.1		0.002331
2R-2, 40	166.90	67.6	147.4		0.003145
2R-2, 45	166.95	52	272.1		0.002018
2R-2, 50	167.00	75.6	121.8		0.00123
2R-2, 55	167.05	65.5	15.8		0.001305
2R-2, 60	167.10	76.3	271.3		0.001252
2R-2, 65	167.15	38.8	249.6		0.001586
2R-2, 70	167.20	41.7	209.3		0.001382
2R-2, 75	167.25	39.2	131		0.00161
2R-2, 80	167.30	53	90.7		0.001446
2R-2, 85	167.35	68.6	93.6		0.001665
2R-2, 90	167.40	77.5	58.2		0.001637
2R-2, 95	167.45	75.2	41.2		0.001927
2R-2, 100	167.50	82.3	254		0.003798
2R-2, 105	167.55	74.5	28.7		0.007975
2R-2, 110	167.60	74.9	50.2		0.012506
2R-2, 115	167.65	86.4	288		0.007989
2R-2, 120	167.70	69.5	25.2		0.006072
2R-2, 125	167.75	47.5	55.1		0.005126
2R-2, 130	167.80	71.6	161.5		0.001938
2R-2, 135	167.85	44.5	205.6		0.001864

Blank cells indicate depth levels where data were either not available (i.e., FlexIt-corrected declination data for nonoriented cores) or removed because of disturbance, voids, or measurement edge effects. Only a portion of this table appears here. The complete table is available in **ASCII.**

Table T18. Polarity boundaries, Site U1386.

Polarity boundary	Age (Ma)	Depth (mbsf)	
		Hole U1386A	Hole U1386B
Brunhes/Matuyama	0.781	274.6	273.3
T Jaramillo	0.988	344.6	347.9
B Jaramillo	1.072		374.0

T = top, B = bottom.

Table T19. Headspace sample hydrocarbon concentrations, Holes U1386A–U1386C.

Core, section	Depth (mbsf)	Concentration (ppmv)		
		Methane	Ethene	Ethane
339-U1386A-				
1H-3	3.00	6.1	—	—
2H-7	12.47	21.3	—	—
3H-7	22.32	11,684.0	—	—
4H-7	31.85	28,919.0	—	—
5H-7	41.35	47,727.0	—	0.75
6H-6	49.32	38,216.0	—	—
7H-7	60.31	29,135.0	—	—
8H-7	69.70	27,448.0	—	0.48
9H-7	79.37	16,843.0	—	—
10H-7	88.98	8,109.2	—	—
11H-7	96.23	3,303.7	—	—
12H-7	107.87	9,467.0	—	—
13H-7	117.14	3,891.4	—	—
14H-6	125.42	25,855.0	—	1.09
15H-7	136.15	3,942.5	—	—
16H-5	142.75	5,690.2	—	—
17H-5	149.96	7,394.6	—	—
18H-6	159.09	6,230.3	—	—
20H-8	176.96	11,134.0	0.67	0.89
21H-5	181.37	6,795.8	—	—
22X-4	187.60	5,879.1	—	—
23X-7	194.32	12,622.0	—	1.26
24X-7	204.50	8,292.5	0.48	1.44
26X-7	223.93	11,488.0	0.54	1.26
27X-6	231.84	4,766.1	—	—
28X-6	241.03	5,624.7	—	0.75
29X-7	252.19	6,940.0	—	—
30X-6	259.96	5,404.0	0.83	1.04
31X-6	269.42	8,233.9	0.00	1.17
32X-7	281.21	6,719.2	0.00	1.16
33X-5	288.40	5,813.4	0.00	1.00
34X-6	299.25	7,730.9	0.88	2.10
35X-5	307.60	14,535.0	0.84	3.10
36X-6	317.42	8,556.3	0.00	1.62
37X-7	329.01	7,483.9	0.00	2.05
38X-6	337.60	8,314.7	1.06	3.48
39X-7	348.45	5,963.4	0.58	1.99
339-U1386B-				
39X-7	358.10	11,109.0	1.76	6.01
40X-7	368.31	10,204.0	1.44	4.62
41X-7	377.54	5,221.4	—	1.24
42X-7	387.27	5,111.5	0.55	2.36
43X-7	397.00	6,436.2	—	1.20
44X-5	403.95	1,446.6	—	0.75
46X-5	422.70	5,476.8	—	1.42
47X-2	428.00	8,367.9	—	4.89
48X-6	442.76	3,876.2	—	2.11
49X-3	448.90	4,691.9	—	2.94
339-U1386C-				
7R-5	420.60	1,191.4	—	—
8R-2	425.21	2,716.2	—	1.56
9R-4	437.84	2,488.1	—	1.31
10R-6	450.61	5,304.3	—	2.33
11R-1	452.90	3,812.2	—	1.71
12R-3	465.40	3,924.3	0.41	3.40
13R-3	475.00	2,654.1	1.07	5.42
14R-3	484.60	2,658.2	0.79	5.82
15R-5	496.90	4,452.1	0.69	9.31
16R-5	506.50	1,618.9	0.46	2.60
18R-4	524.20	3,968.6	1.31	11.53

— = no data.

Table T20. Interstitial water major and trace elements, Hole U1386A.

Core, section	Depth (mbsf)	Alkalinity (meq/L) TITRA_AUTO	NH_4^+ (µM) SPEC	Ba (µM) 493.409 ICPAES	B (µM) 208.890/ 208.956* ICPAES	Ca^{2+} (mM) 317.933 ICPAES	Cl^- (mM) TITRA_AUTO	Fe (µM) 238.204/ 259.940* ICPAES	Li (µM) 670.784 ICPAES	Mg^{2+} (mM) 279.533 ICPAES	K^+ (mM) 766.491 ICPAES	Si (µM) 250.690/ 251.611* ICPAES	Na^+ (mM) 589.592 ICPAES	Sr (µM) 407.771 ICPAES	SO_4^{2-} (mM) IC
339-U1386A-															
1H-2	2.95	7.651	812	7.196	445.7	8.110	586.8	21.86	33.44	50.50	10.55	209.5	485.7	63.17	20.64
2H-6	12.25	10.000	2560	14.59	476.3	3.673	582.0	NA	25.78	37.47	9.066	187.8	475.3	51.06	0
3H-6	22.32	NA	3121	16.58	462.4	4.315	578.3	15.20	21.51	32.88	8.208	142.5	446.0	55.83	0
4H-6	31.04	5.367	3216	13.17	457.5	6.105	575.4	NA	25.01	34.36	8.774	150.3	477.0	79.01	0
5H-6	40.90	5.375	3224	20.60	434.6	5.225	578.6	NA	25.44	33.06	8.405	197.1	476.2	64.42	0
6H-5	49.26	4.725	3259	28.73	452.9	7.081	571.9	NA	28.98	30.68	7.972	144.3	471.2	87.47	0
7H-6	59.86	4.688	3620	22.67	370.7	5.770	568.8	NA	24.53	30.79	7.896	104.5	475.7	65.60	0
8H-6	69.32	5.317	3778	19.61	390.9	6.178	573.3	NA	25.62	30.78	7.734	140.1	465.2	69.78	0
9H-6	78.97	4.658	3857	22.55	371.1	6.310	570.0	NA	26.31	30.73	7.717	137.9	472.9	72.37	0
10H-6	88.00	3.717	3923	25.03	333.0	5.988	572.3	NA	27.64	28.91	7.483	106.1	476.2	83.60	0
11H-6	96.18	4.298	3385	24.62	414.8	6.218	573.2	NA	32.02	29.28	6.624	156.3	454.3	90.86	0
12H-6	107.41	4.194	3799	22.45	361.8	6.012	571.1	NA	30.45	26.67	6.833	166.6	441.7	88.49	0
13H-6	116.75	4.336	3897	20.67	366.4	6.328	572.6	NA	32.69	29.38	7.497	105.9	475.3	76.72	0
14H-5	123.85	4.419	3838	20.52	341.8	6.402	571.3	NA	28.66	29.60	6.962	152.6	475.8	76.03	0
15H-6	135.91	3.927	3729	23.03	264.3	6.264	568.2	NA	32.01	29.03	6.534	128.2	487.2	89.13	0
16H-4	142.70	3.981	4025	22.23	286.6	5.833	571.8	NA	28.77	27.50	6.900	94.2	463.5	76.44	0
18H-5	158.98	NA	4203	21.89	317.9	6.603	572.3	NA	36.78	29.70	6.785	248.2	482.9	83.61	0
20H-7	175.70	4.908	4625	29.55	192.2	5.337	569.4	NA	48.62	26.87	6.916	121.5	468.4	89.59	0
21H-4	181.31	6.524	4640	28.81	265.1	6.026	569.0	NA	47.45	28.45	6.625	215.4	473.6	85.37	0
22X-3	185.84	7.614	4431	29.48	295.4	6.651	571.2	NA	50.78	28.39	6.181	396.2	463.5	85.89	0
23X-6	194.06	6.470	4257	32.29	250.5	6.548	571.0	NA	53.75	29.18	6.452	230.1	467.9	85.06	0
24X-6	204.42	5.776	4330	35.59	284.4	6.632	566.8	NA	55.03	27.67	5.945	224.0	470.2	95.89	0
26X-6	223.83	5.852	4338	33.47	280.4	8.231	565.6	NA	49.61	26.30	5.845	249.3	484.6	113.30	0
29X-6	251.95	4.340	4635	30.62	312.1	7.895	573.3	NA	43.41	30.51	6.569	182.5	512.2	93.00	0
32X-6	280.89	5.788	4479	38.80	260.4	7.067	573.6	NA	56.95	28.22	5.696	250.8	460.7	92.34	0
35X-3	306.00	8.492	5065	38.33	216.1	8.480	574.5	NA	112.3	28.29	6.266	604.7	476.8	106.20	0
38X-5	337.50	9.325	5027	39.01	252.5	8.300	569.0	NA	140.7	29.84	5.672	426.5	482.3	111.26	0

TITRA_AUTO = automatic titration, SPEC = spectrometer, IC = ion chromatograph, ICPAES = inductively coupled plasma–atomic emission spectrometer, ISE = ion-selective electrode. * = average of results from two wavelengths. NA = not available.

Table T21. Interstitial water oxygen and hydrogen isotopes, Hole U1386A.

Core, section, interval (cm)	Depth (mbsf)	δ^{18}O (‰, VSMOW)	δD (‰, VSMOW)	δ^{18}O* (‰, VSMOW)	δD* (‰, VSMOW)
339-U1386A-					
1H-1, 145–150	1.50	0.90	5.47		
1H-2, 72–78	2.25	0.99	6.00		
1H-2, 145–150	3.00	1.05	7.30		
2H-1, 145–150	5.30	1.06	7.49		
2H-2, 145–150	6.80	0.93	6.83		
2H-3, 145–150	8.30	1.15	8.17		
2H-4, 145–150	9.80	1.21	7.32		
2H-5, 145–150	11.30	1.25	6.91		
2H-6, 57–64	11.90	1.12	7.72	1.19	7.99
2H-6, 145–150	12.45	0.98	8.02		
3H-1, 145–150	14.80	1.26	8.18		
3H-2, 145–150	15.30	1.23	8.39		
3H-3, 145–150	17.81	1.22	8.80		
3H-4, 145–150	19.32	1.23	8.99		
3H-5, 145–150	20.82	1.25	8.99		
3H-6, 72–78	21.57	1.28	8.96	1.30	8.85
3H-6, 145–150	22.32	1.18	8.91		
4H-1, 145–150	24.30	1.22	9.01		
4H-2, 145–150	25.81	1.28	9.12		
4H-3, 145–150	27.32	1.33	10.31		
4H-4, 145–150	28.83	1.44	9.72		
4H-5, 145–150	30.34	1.21	9.89		
4H-6, 72–78	31.09	1.34	9.64		
4H-6, 145–150	31.85	1.40	8.94		
5H-1, 145–150	33.80	1.28	9.42		
5H-2, 145–150	35.31	1.39	8.54	1.28	9.11
5H-3, 145–150	36.82	1.22	10.44		
5H-4, 145–150	38.32	1.37	9.74	1.36	8.56
5H-5, 145–150	39.82	1.30	9.31	1.26	9.97
5H-6, 72–78	40.59	1.24	9.19		
5H-6, 145–150	41.35	1.27	9.48		
6H-1, 145–150	43.25	1.28	9.08		
6H-2, 145–150	44.77	1.18	9.32		
6H-3, 145–150	46.29	1.45	9.27		
6H-4, 145–150	47.81	1.46	9.65		
6H-5, 72–78	48.56	1.40	9.79		
6H-5, 145–150	49.32	1.52	10.49		
7H-1, 140–145	52.80	1.27	9.47		
7H-2, 140–145	54.30	1.08	9.53		
7H-3, 140–145	55.80	1.41	9.74		
7H-4, 140–145	57.30	1.26	9.07		
7H-5, 140–145	58.81	1.24	9.10		
7H-6, 72–78	59.56	1.38	9.59		
7H-6, 145–150	60.31	1.19	8.67		
8H-1, 140–145	62.30	1.19	9.04		
8H-2, 140–145	63.81	1.23	8.43		
8H-3, 140–145	65.34	1.27	8.34		
8H-4, 140–145	66.87	1.27	9.08		
8H-5, 140–145	68.40	1.18	9.83		
8H-6, 72–78	69.15	1.58	9.37		
8H-6, 125–130	69.70	1.22	9.03	1.24	8.84
9H-1, 140–145	71.80	1.11	8.63		
9H-2, 140–145	73.30	1.07	8.50	1.18	8.46
9H-3, 140–145	74.82	1.17	8.12		
9H-4, 140–145	76.35	1.09	8.59		
9H-5, 140–145	77.87	1.15	8.52		
9H-6, 72–78	78.62	1.18	8.68		
9H-6, 145–150	79.37	1.02	8.45		
10H-1, 140–145	81.31	1.15	8.04		
10H-2, 140–145	82.82	1.26	8.51		

* = replicate measurements. VSMOW = Vienna standard mean ocean water.

Table T22. Vertical seismic profile station and traveltime information, Site U1386.

Depth WSF* (m)	Water depth (mbsl)	One-way traveltime (ms)	One-way traveltime, corrected† (ms)	Two-way traveltime (ms)	Two-way traveltime below seabed* (ms)
143.2	705.2	456.5	461.2	922.4	182.4
251.0	813.0	515.5	520.2	1040.4	300.4
270.1	832.1	525.0	529.7	1059.4	319.4
287.0	849.0	533.0	537.7	1075.4	335.4
301.9	863.9	541.0	545.7	1091.4	351.4
313.0	875.0	546.5	551.2	1102.4	362.4
333.0	895.0	557.5	562.1	1124.2	384.2
342.9	904.9	562.5	567.2	1134.4	394.4
352.9	914.9	567.5	572.2	1144.4	404.4
362.0	924.0	572.0	576.6	1153.2	413.2
367.2	929.2	574.5	579.1	1158.2	418.2
369.4	931.4	575.5	580.2	1160.4	420.4

* = seafloor at 562 mbsl, 740 ms two-way traveltime. † = a correction of ~4.7 ms is added to the one-way traveltime.

Table T23. Results from APCT-3 temperature profiles, Site U1386.

Core	Original depth (mbsf)	Tidal sea level height* (m)	Corrected depth (mbsf)	Minimum temperature (°C)	Minimum temperature prior to mudline (°C)	Average temperature at mudline (°C)	In situ temperature (°C)	Thermal resistance (m^2K/W)
339-U1386A-								
4H	32.2	–0.2	33.3	12.93	13.19	13.54	14.20	22.6
7H	60.8	0.5	61.2	12.85	13.85	14.11	15.19	43.6
10H	89.3	0.8	89.4	13.01	13.51	14.30	16.14	67.4
13H	117.8	–0.3	119.0	12.82	14.03	14.20	17.05	93.8
16H	144.0	–0.8	145.7	12.59	13.99	14.20	18.09	114.4
19H	167.2	–0.3	168.4	12.54	13.64	14.01	18.88	131.2
			Average:	12.79	13.70	14.06		
339-U1386B-								
2H	16.8	0.4	17.3	13.44	13.50	13.59	13.56	11.7
5H	45.3	–0.4	46.6	13.34	13.34	13.56	14.85	32.0
8H	73.8	–0.75	75.45	13.84	13.84	14.04	15.75	55.6
11H	102.3	–0.45	103.65	13.92	13.92	14.20	16.67	80.1
14H	130.5	0.25	131.15	13.68	14.06	14.20	17.64	103.5
17H	157.6	0.5	158	13.67	14.05	14.40	18.46	123.6
			Average:	13.65	13.78	14.00		

* = –0.9 m tidal height when mudline Core 339-U1386-1H was taken. In situ temperatures were determined using TP-Fit software by Martin Heesemann. Thermal resistance was calculated from thermal conductivity data (see **"Physical properties"**) corrected for in situ conditions (see **"Downhole measurements"** in the "Methods" chapter [Expedition 339 Scientists, 2013b]).

Table T24. Meters composite depth scale, Site U1386. (Continued on next page.)

Core	Top depth (mbsf)	Top depth (mcd)	Offset (m)
339-U1386A-			
1H	0.00	0.00	0.00
2H	3.80	4.16	0.36
3H	13.30	14.21	0.91
4H	22.80	23.62	0.82
5H	32.30	33.69	1.39
6H	41.80	44.21	2.41
7H	51.30	53.69	2.39
8H	60.80	63.03	2.23
9H	70.30	73.29	2.99
10H	79.80	83.25	3.45
11H	89.30	94.27	4.97
12H	98.80	106.31	7.51
13H	108.30	118.72	10.42
14H	117.80	129.99	12.19
15H	127.30	141.84	14.54
16H	136.80	154.21	17.41
17H	144.00	160.42	16.42
18H	151.60	168.85	17.25
19H	160.50	178.22	17.72
20H	167.20	186.89	19.69
21H	176.70	197.74	21.04
22X	183.10	204.16	21.06
23X	186.50	209.59	23.09
24X	196.00	221.61	25.61
25X	205.60	230.72	25.12
26X	215.20	238.09	22.89
27X	224.80	248.08	23.28
28X	234.40	258.67	24.27
29X	244.00	270.09	26.09
30X	253.60	281.78	28.18
31X	263.20	291.73	28.53
32X	272.80	302.96	30.16
33X	282.40	313.81	31.41
34X	292.00	324.12	32.12
35X	301.60	334.78	33.18
36X	310.90	343.82	32.92
37X	320.50	353.90	33.39
38X	330.10	365.41	35.31
39X	339.70	377.07	37.37
339-U1386B-			
1H	0.00	0.10	0.10
2H	7.30	8.33	1.03
3H	16.80	18.50	1.70
4H	26.30	29.37	3.07
5H	35.80	39.01	3.21
6H	45.30	48.67	3.37
7H	54.80	59.38	4.58
8H	64.30	69.54	5.24
9H	73.80	79.43	5.63
10H	83.30	89.64	6.34
11H	92.80	101.71	8.91
12H	102.30	112.90	10.60
13H	111.80	123.56	11.76
14H	121.30	135.56	14.26
15H	130.80	144.80	14.00
16H	140.30	155.73	15.43
17H	148.10	164.70	16.60
18H	157.60	175.49	17.89
19X	162.30	180.56	18.26
20X	167.90	188.57	20.67
21X	177.50	201.63	24.13
22X	187.10	210.46	23.36
23X	196.60	220.11	23.51
24X	206.20	230.23	24.03
25X	215.90	240.20	24.30
26X	225.50	249.90	24.40
27X	235.10	260.81	25.71

Table T24 (continued).

Core	Top depth (mbsf)	Top depth (mcd)	Offset (m)
28X	244.70	272.33	27.63
29X	254.30	283.42	29.12
30X	263.90	295.33	31.43
31X	273.50	305.58	32.07
32X	283.10	315.51	32.41
33X	292.70	325.49	32.79
34X	302.30	334.85	32.55
35X	311.90	346.21	34.31
36X	321.50	356.87	35.37
37X	331.10	367.52	36.42
38X	340.60	379.52	38.92
39X	350.10	389.61	39.51
40X	359.60	399.16	39.56
41X	369.20	409.81	40.61
42X	378.80	420.47	41.67
43X	388.40	431.12	42.72
44X	398.00	441.78	43.78
45X	407.60	452.44	44.84
46X	417.20	463.10	45.90
47X	426.80	473.75	46.95
48X	436.40	484.40	48.00
49X	445.90	494.95	49.05
50X	455.40	505.49	50.09
339-U1386C-			
1W	0.00	0.00	0.00
2R	165.00	183.95	18.95
3W	174.60	193.81	19.21
4R	205.00	227.05	22.05
5W	214.60	238.21	23.61
6R	405.00	449.05	44.05
7R	414.60	460.21	45.61
8R	424.20	470.86	46.66
9R	433.80	480.53	46.73
10R	443.40	492.17	48.77
11R	452.90	502.72	49.82
12R	462.40	513.26	50.86
13R	472.00	523.92	51.92
14R	481.60	534.58	52.98
15R	490.90	544.90	54.00
16R	500.50	555.56	55.05
17R	510.10	566.21	56.11
18R	519.70	576.87	57.17

Table T25. Splice tie points, Site U1386. (Continued on next page.)

Hole, core, section, interval (cm)	Depth (mbsf)	Depth (mcd)		Hole, core, section, interval (cm)	Depth (mbsf)	Depth (mcd)
339-				339-		
				U1386A-1H-1, 0	0.00	0.00
U1386A-1H-1, 110	1.10	1.10	Tie to	U1386B-1H-1, 100	1.00	1.10
U1386B-1H-3, 142.5	4.43	4.53	Tie to	U1386A-2H-1, 37.5	4.18	4.53
U1386A-2H-4, 46.6	8.78	9.13	Tie to	U1386B-2H-1, 80	8.10	9.13
U1386B-2H-6, 67.67	15.49	16.52	Tie to	U1386A-3H-2, 80.29	15.60	16.52
U1386A-3H-5, 33.38	19.65	20.57	Tie to	U1386B-3H-2, 57.3	18.87	20.57
U1386B-3H-6, 7.29	24.39	26.09	Tie to	U1386A-4H-2, 97	25.27	26.09
U1386A-4H-5, 121.9	30.05	30.87	Tie to	U1386B-4H-1, 150	27.80	30.87
U1386B-4H-4, 95.41	31.81	34.89	Tie to	U1386A-5H-1, 120	33.50	34.89
U1386A-5H-5, 48.64	38.82	40.21	Tie to	U1386B-5H-1, 120	37.00	40.21
U1386B-5H-6, 147.03	44.80	48.01	Tie to	U1386A-6H-3, 83.63	45.61	48.01
U1386A-6H-5, 143.09	49.24	51.65	Tie to	U1386B-6H-2, 147.65	48.28	51.65
U1386B-6H-4, 112.24	50.94	54.32	Tie to	U1386A-7H-1, 62.5	51.93	54.32
U1386A-7H-5, 84.12	58.14	60.53	Tie to	U1386B-7H-1, 115	55.95	60.53
U1386B-7H-5, 32.26	61.28	65.86	Tie to	U1386A-8H-2, 132.72	63.63	65.86
U1386A-8H-5, 117.5	68.05	70.27	Tie to	U1386B-8H-1, 72.5	65.03	70.27
U1386B-8H-5, 40.81	70.74	75.98	Tie to	U1386A-9H-2, 118.28	72.98	75.98
U1386A-9H-6, 92.5	78.80	81.79	Tie to	U1386B-9H-3, 9.75	76.16	81.79
U1386B-9H-4, 40.94	77.93	83.56	Tie to	U1386A-10H-1, 30.82	80.11	83.56
U1386A-10H-5, 74.67	86.60	90.04	Tie to	U1386B-10H-1, 40	83.70	90.04
U1386B-10H-6, 36.28	91.04	97.39	Tie to	U1386A-11H-4, 45.49	92.41	97.39
U1386A-11H-7, 65.59	96.89	101.86	Tie to	U1386B-11H-1, 15	92.95	101.86
U1386B-11H-4, 75.76	98.02	106.93	Tie to	U1386A-12H-1, 62.5	99.43	106.93
U1386A-12H-5, 121.89	106.04	113.55	Tie to	U1386B-12H-1, 64.43	102.94	113.55
U1386B-12H-5, 109.32	109.11	119.72	Tie to	U1386A-13H-1, 100	109.30	119.72
U1386A-13H-6, 54.73	116.40	126.82	Tie to	U1386B-13H-3, 43.2	115.06	126.82
U1386B-13H-6, 38.15	119.25	131.01	Tie to	U1386A-14H-1, 102.5	118.83	131.01
U1386A-14H-6, 20.69	125.63	137.81	Tie to	U1386B-14H-2, 84.62	123.55	137.81
U1386B-14H-7, 19.51	129.35	143.61	Tie to	U1386A-15H-2, 27.09	129.07	143.61
U1386A-15H-5, 120.4	134.52	149.07	Tie to	U1386B-15H-3, 126.9	135.07	149.07
U1386B-15H-7, 112.77	140.73	154.73	Tie to	U1386A-16H-1, 52.5	137.33	154.73
U1386A-16H-2, 145.44	139.75	157.16	Tie to	U1386B-16H-1, 142.5	141.73	157.16
U1386B-16H-4, 102.86	145.70	161.13	Tie to	U1386A-17H-1, 70.52	144.71	161.13
U1386A-17H-3, 143.67	148.43	164.85	Tie to	U1386B-17H-1, 15	148.25	164.85
U1386B-17H-4, 133.46	153.55	170.16	Tie to	U1386A-18H-1, 131.4	152.91	170.16
U1386A-18H-5, 140.22	158.99	176.24	Tie to	U1386B-18H-1, 75	158.35	176.24
U1386B-18H-3, 10.29	160.65	178.54	Tie to	U1386A-19H-1, 32.5	160.83	178.54
U1386A-19H-3, 119.83	164.70	182.41	Tie to	U1386B-19X-2, 34.87	164.15	182.41
U1386B-19X-6, 2.38	169.62	187.89	Tie to	U1386A-20H-2, 27.09	168.20	187.89
U1386A-20H-8, 55	177.51	197.20	Append to	U1386A-21H-1, 0	176.70	197.74
U1386A-21H-5, 89.8	182.27	203.31	Tie to	U1386B-21X-2, 18.93	179.19	203.31
U1386B-21X-6, 101.24	186.01	210.14	Tie to	U1386A-23X-2, 24.07	187.05	210.14
U1386A-23X-2, 91.57	187.73	210.81	Tie to	U1386B-22X-1, 35	187.45	210.81
U1386B-22X-7, 66.51	196.44	219.80	Append to	U1386B-23X-1, 0	196.60	219.69
U1386B-23X-5, 25.04	202.85	226.36	Tie to	U1386A-24X-4, 25.85	200.75	226.36
U1386A-24X-7, 32.3	204.82	230.43	Tie to	U1386B-24X-1, 20	206.40	230.43
U1386B-24X-7, 77.5	214.06	238.09	Append to	U1386A-26X-1, 0	215.20	238.09
U1386A-26X-6, 29.06	223.02	245.91	Tie to	U1386B-25X-4, 121.58	221.62	245.91
U1386B-25X-6, 55.31	223.78	248.08	Append to	U1386A-27X-1, 0	224.80	248.08
U1386A-27X-7, 92.19	234.26	257.54	Append to	U1386A-28X-1, 2.5	234.43	258.70
U1386A-28X-4, 11.94	238.15	262.42	Tie to	U1386B-27X-2, 50.31	236.71	262.42
U1386B-27X-7, 80.25	244.38	270.09	Tie to	U1386A-29X-1, 0	244.00	270.09
U1386A-29X-5, 69.64	249.89	275.98	Tie to	U1386B-28X-4, 16.83	248.35	275.98
U1386B-28X-7, 147.76	254.16	281.78	Append to	U1386A-30X-1, 0	253.60	281.78
U1386A-30X-6, 65.27	260.61	288.79	Tie to	U1386B-29X-4, 87	259.67	288.79
U1386B-29X-6, 150.35	262.55	291.68	Append to	U1386A-31X-1, 0	263.18	291.71
U1386A-31X-7, 134.23	272.26	300.79	Tie to	U1386B-30X-4, 117.84	269.36	300.79
U1386B-30X-7, 58.41	273.26	304.69	Tie to	U1386A-32X-2, 81.88	274.53	304.69
U1386A-32X-4, 11.76	276.83	306.99	Tie to	U1386B-31X-2, 37.21	274.91	306.99
U1386B-31X-7, 121.4	282.94	315.02	Append to	U1386A-33X-2, 0	283.90	315.31
U1386A-33X-7, 20.54	291.21	322.62	Tie to	U1386B-32X-6, 13.03	290.21	322.62
U1386B-32X-7, 113.33	292.56	324.97	Append to	U1386A-34X-2, 0	293.25	325.37
U1386A-34X-7, 51.08	301.26	333.38	Append to	U1386B-34X-1, 0	302.30	334.85
U1386B-34X-7, 149.29	311.63	344.19	Append to	U1386A-36X-2, 0	311.42	344.34
U1386A-36X-4, 94.86	315.37	348.29	Tie to	U1386B-35X-2, 58.03	313.98	348.29
U1386B-35X-7, 42.04	320.79	355.10	Tie to	U1386A-37X-1, 120	321.70	355.10
U1386A-37X-4, 79.44	325.79	359.19	Tie to	U1386B-36X-2, 82.78	323.83	359.19

Table T25 (continued).

Hole, core, section, interval (cm)	Depth			Hole, core, section, interval (cm)	Depth	
	(mbsf)	(mcd)			(mbsf)	(mcd)
U1386B-36X-6, 151.73	330.08	365.44	Tie to	U1386A-38X-1, 2.5	330.13	365.44
U1386A-38X-5, 108.12	337.18	372.49	Tie to	U1386B-37X-5, 18.41	336.06	372.49
U1386B-37X-8, 57.38	340.65	377.07	Tie to	U1386A-39X-1, 0	339.70	377.07
U1386A-39X-3, 60	343.30	380.67	Tie to	U1386B-38X-1, 115	341.75	380.67
U1386B-38X-7, 65	349.99	388.91	Append to	U1386B-39X-1, 1.79	350.12	389.63
U1386B-39X-7, 112.99	359.23	398.74	Append to	U1386B-40X-1, 0	359.60	399.16
U1386B-40X-7, 60.75	368.92	408.47	Append to	U1386B-41X-1, 0	369.20	409.81
U1386B-41X-7, 117.66	378.72	419.33	Append to	U1386B-42X-1, 0	378.80	420.47
U1386B-42X-7, 80	388.07	429.74	Append to	U1386B-43X-1, 0.09	388.40	431.12
U1386B-43X-7, 67.95	397.68	440.40	Append to	U1386B-44X-1, 0	398.00	441.78
U1386B-44X-5, 135.57	405.31	449.09	Append to	U1386C-7R-1, 0	414.60	460.21
U1386C-7R-3, 2.6	417.62	463.23	Tie to	U1386B-46X-1, 12.5	417.33	463.23
U1386B-46X-5, 59.41	423.29	469.20	Append to	U1386C-8R-1, 0	424.20	470.86
U1386C-8R-2, 67.5	425.35	472.01	Append to	U1386B-47X-1, 0	426.80	473.75
U1386B-47X-2, 71.68	428.72	475.66	Append to	U1386C-9R-1, 0	433.80	480.53
U1386C-9R-4, 60	438.16	484.89	Append to	U1386B-48X-2, 0	436.89	484.89
U1386B-48X-8, 149.94	446.02	494.02	Tie to	U1386C-10R-2, 37.6	445.25	494.02
U1386C-10R-6, 87.4	451.42	500.19	Append to	U1386C-11R-1, 0	452.90	502.72
U1386C-11R-1, 110	453.05	502.87	Append to	U1386C-12R-1, 0	462.40	513.26
U1386C-12R-4, 81.8	467.41	518.27	Append to	U1386C-13R-1, 0	472.00	523.92
U1386C-13R-4, 144.3	477.49	529.41	Append to	U1386C-14R-1, 0	481.60	534.58
U1386C-14R-4, 62.9	486.25	539.23	Append to	U1386C-15R-1, 0	490.90	544.90
U1386C-15R-5, 116.3	497.88	551.88	Append to	U1386C-16R-1, 0	500.50	555.56
U1386C-16R-6, 72.5	508.14	563.19	Append to	U1386C-17R-1, 0	510.10	566.21
U1386C-17R-5, 97.5	516.89	573.00	Append to	U1386C-18R-1, 0	519.70	576.87

Table T26. Excluded magnetic susceptibility data, Site U1386.

Core, section, interval (cm)
339-U1386A-
1H-1, 0
1H-1, 75
1H-1, 138
1H-1, 140
1H-1, 143
1H-1, 145
1H-1, 148
1H-1, 150
1H-2, 28
1H-2, 1428
1H-3, 18
1H-3, 64
2H-1, 0
2H-1, 143
2H-1, 145
2H-1, 148
2H-1, 150
2H-2, 2
2H-2, 85
2H-2, 1425
2H-2, 145
2H-2, 1475
2H-2, 150
2H-3, 2
2H-3, 144
2H-3, 147
2H-3, 149
2H-4, 2
2H-4, 144
2H-4, 147
2H-4, 149
2H-5, 1
2H-5, 106
2H-5, 144
2H-5, 146
2H-5, 149
2H-6, 0
2H-6, 108
2H-6, 115
2H-7, 1
2H-7, 312
2H-7, 48
2H-7, 61
2H-7, 61
3H-1, 0
3H-1, 3
3H-1, 138
3H-1, 140
3H-1, 143
3H-1, 145
3H-1, 148
3H-2, 0
3H-2, 135
3H-2, 138
3H-2, 140
3H-2, 143
3H-2, 145
3H-2, 148
3H-2, 150
3H-3, 2
3H-3, 145
3H-3, 147
3H-3, 150
3H-4, 1
3H-4, 4
3H-4, 6
3H-4, 9
3H-4, 11
3H-4, 144
3H-4, 146
3H-4, 149
3H-4, 154
3H-4, 156
3H-4, 159
3H-5, 1
3H-5, 146
3H-5, 148
3H-6, 0
3H-6, 145
3H-7, 2
3H-7, 5
3H-7, 7
3H-7, 10
3H-7, 70
4H-1, 0
4H-1, 145
4H-1, 148
4H-1, 150
4H-2, 2
4H-2, 147
4H-2, 150
4H-3, 1
4H-3, 138
4H-3, 141
4H-3, 146
4H-3, 148
4H-4, 0
4H-4, 3
4H-4, 5
4H-4, 84
4H-4, 10
4H-4, 13
4H-4, 15
4H-4, 18
4H-4, 60
4H-4, 145
4H-4, 148
4H-4, 150
4H-5, 2
4H-5, 147
4H-5, 149
4H-6, 0
4H-6, 1
4H-6, 4
4H-6, 6
4H-6, 9
4H-6, 11
4H-6, 14
4H-6, 16
4H-6, 18
4H-6, 189
4H-6, 21
4H-6, 24
4H-6, 26
4H-6, 29
4H-6, 31
4H-6, 34
4H-6, 36
4H-6, 39
4H-6, 41
4H-6, 44
4H-6, 46
4H-6, 49
4H-6, 51
4H-6, 54
4H-6, 56
4H-6, 59
4H-6, 61
4H-6, 64
4H-6, 66
4H-6, 69
4H-6, 71
4H-6, 73
4H-6, 74
4H-6, 76
4H-6, 78
4H-6, 79
4H-6, 81
4H-6, 84
4H-6, 86
4H-6, 89
4H-6, 91
4H-6, 94
4H-6, 96
4H-6, 99
4H-6, 101
4H-6, 104
4H-6, 106
4H-6, 109
4H-6, 111
4H-6, 114
4H-6, 116
4H-6, 119
4H-6, 121
4H-6, 124
4H-6, 126
4H-6, 129
4H-6, 131
4H-6, 134
4H-6, 136
4H-6, 139
4H-6,141
4H-6, 144
4H-6, 145
4H-6, 146
4H-6, 151
4H-6, 154
4H-7, 1
4H-7, 1
4H-7, 4
4H-7, 6
4H-7, 9
4H-7, 11
4H-7, 14
4H-7, 16
4H-7, 19
4H-7, 21
4H-7, 24
4H-7, 26
4H-7, 29
4H-7, 31
4H-7, 34
4H-7, 36
4H-7, 39
4H-7, 41
4H-7, 44
4H-7, 46.
4H-7, 49
4H-7, 51
4H-7, 54
4H-7, 56
4H-7, 59
4H-7, 61
4H-7, 63
4H-7, 64
4H-7, 66
5H-1, 0
5H-1, 143
5H-1, 145
5H-1, 148
5H-1, 150
5H-2, 2
5H-2, 147
5H-2, 149
5H-2, 152
5H-3, 0
5H-3, 145
5H-3, 148
5H-3, 150
5H-4, 2
5H-4, 147
5H-4, 150
5H-5, 1
5H-5, 4
5H-5, 6
5H-5, 9
5H-5, 146
5H-5, 149
5H-5, 159
5H-6, 1
5H-6, 144
5H-6, 146
5H-7, 2
5H-7, 55
5H-7, 57
6H-1, 0
6H-1, 3
6H-1, 5
6H-1, 70
6H-1, 73
6H-1, 75
6H-1, 78
6H-1, 140
6H-1, 143
6H-2, 0
6H-2, 3
6H-2, 145
6H-2, 148
6H-2, 150
6H-2, 153
6H-3, 1
6H-3, 146
6H-3, 149
6H-3, 151
6H-4, 0
6H-4, 145
6H-4, 148
6H-4, 150
6H-5, 1
6H-5, 141
6H-5, 143
6H-5, 146
6H-6, 1
6H-6, 616
7H-1, 0
7H-1, 3
7H-1, 143
7H-1, 145
7H-1, 148
7H-2, 0
7H-2, 145
7H-2, 148
7H-3, 0
7H-3, 145
7H-3, 148
7H-3, 150
7H-4, 1
7H-4, 144
7H-4, 146
7H-4, 149
7H-5, 2
7H-5, 142
7H-5, 144
7H-5, 147
7H-5, 149
7H-5, 152
7H-6, 2
7H-6, 147
7H-7, 1
7H-7, 31
7H-7, 34
7H-7, 36
7H-7, 39
7H-7, 41
7H-7, 44
7H-7, 46
7H-7, 49
7H-7, 51
7H-7, 54
7H-7, 56
8H-1, 0
8H-1, 3
8H-1, 140
8H-1, 143
8H-1, 145
8H-1, 148
8H-2, 0
8H-2, 3
8H-2, 5
8H-2, 5
8H-2, 133
8H-2, 140
8H-2, 143
8H-2, 145

Only a portion of this table appears here. The complete table is available in **ASCII.**